THE PREDICTION OF THE EMISSION SPECTRA OF FLARES and SOLID PROPELLANT ROCKETS

by

Paul Werner Barnard

Dissertation presented in partial fulfillment of the requirements for the degree of M.Sc.Ing at the University of Stellenbosch, South Africa

Promoters:
Professor J.H. Knoetze
Dr JHS Roodt

April 2003

DECLARATION

I, the undersigned, hereby declare that the work contained in this dissertation is my own original work and that I have not previously in its entirety or in part submitted it at any university for a degree.

P.W. Barnard Date: 29 January 2003

SUMMARY

It was shown in an earlier study that it is possible to predict the spectral radiance of rocket combustion plumes directly from the propellant composition and motor parameters. Little is published in the open literature on this subject, but the current trend is to use determinative methods like computational fluid dynamics and statistical techniques to simulate wide band radiance based on blackbody temperature assumptions. A limitation of these methods is the fact that they are computationally expensive and rather complex to implement.

An alternative modeling approach was used which did not rely on solving all the non-linearities and complex relationships applicable to a fundamental model. A multilayer perceptron based Neural Network was used to develop a parametric functional mapping between the propellant chemical composition and the motor design and the resulting spectral irradiance measured in a section of the plume. This functional mapping effectively models the relationship between the rocket design and the plume spectral radiance.

Two datasets were available for use in this study: Emission spectra from solid propellant rockets and flare emission spectra. In the case of the solid rocket propellants, the input to the network consisted of the chemical composition of the fuels and four motor parameters, with the output of the network consisting of 146 scaled emission spectra points in the waveband from 2-5 microns. The four motor parameters were derived from equations describing the mass flow characteristics of rocket motors. The mass flow through the rocket motor does have an effect on the shape of the plume of combustion gases, which in turn has an effect on the infrared signature of the plume. The characteristics of the mass flow through the nozzle of the rocket motor determine the thermodynamic properties of the combustion process. This then influences the kind of chemical species found in the plume and also at what temperature these species are radiating energy.

The resultant function describing the plume signature is:

$$Plume\ signature = f\{p_1, T_1, A_t, \varepsilon, fuel\ composition\}$$

It was demonstrated that this approach yielded very useful results. Using only 18 basic variables, the spectra were predicted properly for variations in all these parameters. The model also predicted spectra that agree with the underlying physical situation when changing the composition as a whole. By decreasing the Potassium content for example, the model demonstrated the effect of a flame suppressant on the radiance in this wavelength band by increasing the predicted output. Lowering the temperature, which drives the process of molecular vibration and translation, resulted in the expected lower output across the spectral band. In general, it was shown that only a small section of the large space of 2 propellant classes had to be measured in order to successfully generate a model that could predict emission spectra for other designs in those classes.

The same principal was then applied to predicting the infrared spectral emission of a burning flare. The brick type flare considered in this study will ignite and the solid fuel will burn on all surfaces. Since there are no physical parameters influencing the plume as in the case of the rocket nozzles it was required to search for parameters that could influence the flare plume. It was possible to calculate thermodynamic properties for the flare combustion process. These parameters were then reduced to 4 parameters, namely: the oxidant-fuel ratio, equilibrium temperature, the molar mass and the maximum combustion temperature. The input variables for the flares thus consisted of the chemical composition and 4 thermodynamic parameters described above.

The network proposed previously was improved and optimised for a minimum number of variables in the system. The optimised network marginally improved on the pevious results (with the same data), but the training time involved was cut substantially. The same approach to the optimization of the network was again followed to determine the optimal network structure for predicting the flare emission spectra. The optimisation involved starting out with the simplest possible network construction and continuously

increasing the variables in the system until the solution predicted by the network was satisfactory. Once the structure of the network was determined it was possible to optimise the training algorithms to further improve the solution.

In the case of the solid rocket propellant emission data it was felt that it would be important to be able to predict the chemical composition of the fuel and the motor parameters using the infrared emission spectra as input. This was done by simply reversing the optimised network and exchanging the inputs with the outputs. The results obtained from the reversed network accurately predicted the chemical composition and motor parameters on two different test sets.

The predicted spectra of some of the solid propellant rocket test sets and flare test sets did not compare well with the expected values. This was due to the fact that these test sets were in a sparsely populated area of the variable space. These outliers are normally removed from training data, but in this case there wasn't enough data to remove outliers.

To obtain an indication of the strength of the correlation between the predicted and measured line spectra two parameters were used to test the correlation between two line spectra. The first parameter is the Pearson product moment of coefficient of correlation and gives an indication of how good the predicted line spectra followed the trend of the measured spectral lines. The second parameter measures the relative distance between a target and predicted spectral point. For both the solid propellants and the flares the correlation values was very close to 1, indicating a very good solution. Values for the two correlation parameters of a test set of the flares were 0.998 and 0.992.

In order to verify the model it was necessary to prove that the solution yielded by the model is better than the average of the variable space. Three statistical tests were done consisting of the mean-squared-error test, T-test and Wilcoxon ranksum test. In all three cases the average of the variable space (static model) and the predicted values (Neural Network model) were compared to the measured values. For both the T-test and the Wilcoxon ranksum test the null hypothesis is rejected when $t < -t_{\alpha} = 1.645$ and then the

alternative hypothesis is accepted, which states that the error of the NN model will be smaller than that of the static model. The mean squared error for the static model was 0.102 compared to the 0.0167 of the neural net, for a solid propellant rocket test set. A t-test was done on the same test set, yielding a value of –2.71, which is smaller than –1.645, indicating that the NN model outperforms the static model. The Z value for this test set is Z = -11.9886, which is a much smaller than –1.645.

The results from these statistical tests confirm that neural network is a valid conceptual model and the solutions yielded are unique.

Opsomming

In ‘n vroeër studie is bewys hoe dit moontlik is om die spektrale irradiansie van ‘n vuurpyl se verbrandingspluim te voorspel vanaf slegs die dryfmiddelsamestelling en vuurpylmotoreienskappe. In die literatuur is daar min gepubliseer oor hierdie onderwerp. Dit wil voorkom asof meer deterministiese metodes gebruik word om die probleem op te los. Metodes soos CFD simulasies en statistiese analises word tans verkies om wyeband radiansie te voorspel gebaseer op perfekte swart ligaam teorie. ‘n Groot beperking van hierdie metodes is die feit dat die berekeninge kompleks is en baie lank neem om te voltooi.

‘n Alternatiewe benadering is gebruik, wat nie poog om al die nie-liniêre en komplekse verbande uit eerste beginsels op te los nie. ‘n Neurale netwerk is gebruik om ‘n funksionele verband te skep tussen die chemiese samestelling van die dryfmiddel, vuurpylmotor ontwerp en die spektrale irradiansie van die vuurpyl se pluim. Die funksionele verband kan nou effektief die afhanklikheid van die dryfmiddelsamestelling, vuurpylmotor ontwerp en die spektrale uitset modelleer.

Twee datastelle was beskikbaar vir analise: Emissie spektra van vaste dryfmiddel vuurpyle en ook van vaste dryfmiddel fakkels. Die invoer tot die neurale netwerk van die vuurpyle het bestaan uit die chemiese samestelling van die dryfmiddel en 4 vuurpylmotor eienskappe. Die uitvoer van die netwerk het weer bestaan uit 146 spektrale irradiansie waardes in die golflengte band van 2-5μm. Die 4 vuurpylmotor eienskappe is afgelei uit massavloei teorie vir vuurpyl motors, aangesien die uitvloei van die produkgasse ‘n invloed op die pluim van die motor sal hê. Die massavloei het weer ‘n effek op die spektrale handtekening van die pluim. Die eienskappe van die massavloei deur die mondstuk van die vuurpylmotor bepaal die termodinamiese eienskappe van die verbrandingsproses. Die invloed op die verbrandingsproses bepaal weer watter tipe produkte gevorm word en by watter temperatuur hulle energie uitstraal. Die gevolg is dat ‘n funksie gedefinieer kan word wat die pluim beskryf.

Pluim handtekening = f{, temperatuur, mondstuk keël grootte, vernouings verhouding van mondstuk, dryfmiddelsamestelling}

Deur net 18 invoer nodes te gebruik kon die netwerk die irradiansie suksesvol voorspel met ‘n variansie in al die invoer waardes. Deur byvoorbeeld die Kalium inhoud van die dryfmiddel samestelling te verminder het die model die vermindering van ‘n vlam onderdrukker suksesvol nageboots deurdat die irradiansie ‘n hoër uitset gehad het. Die sensitiwiteit van die model is verder getoets deur die temperatuur in die verbrandingskamer te verlaag, met ‘n korrekte laer irradiansie uitset, as gevolg van die feit dat die temperatuur die molekulêre vibrasie en translasie beweging beheer.

Dieselfde benadering is gebruik om die model te bou vir die voorspelling van die fakkels se infrarooi irradiansie. Anders as die vuurpylmotors vind die verbranding in die geval van die fakkels in die atmosfeer plaas. Dit was dus ook nodig om na die termodinamiese eienskappe van die fakkel verbranding te kyk. Verskeie parameters is bereken, maar 4 parameters, naamlik die brandstof-suurstof verhouding, temperatuur, molêre massa en die maksimum verbrandingstemperatuur, tesame met die dryfmiddel samestelling kon die irradiansie van die fakkels suskesvol voorspel.

Die bestaande netwerk struktuur vir die vuurpylmotors is verbeter en geoptimiseer vir ‘n minimum hoeveelheid veranderlikes in die stelsel. Die geoptimiseerde netwerk het ‘n klein verbetering in die voorspellings getoon, maar die oplei het drasties afgeneem. Dieselfde benadering is gebruik om die optimale netwerk vir die fakkels te bepaal. Optimisering van die netwerk struktuur is bereik deur met die eenvoudigste struktuur te begin en die hoeveelheid veranderlikes te vermeerder totdat ‘n bevredigende oplossing gevind is. Na die struktuur van die netwerk bevestig is, kon die oordragfunksies op die nodes verder geoptimiseer word om die model verder te verbeter.

Dit het verder geblyk dat dit moonlik is om die netwerk vir die vuurpylmotors om te draai sodat die irradiansie gebruik word om die dryfmiddel samestelling en motor eienskappe te voorspel. Die netwerk is eenvoudig omgedraai en die insette het die uitsette geword.

Die resultate van die omgekeerde netwerk het bevestig dat dit wel moontlik is om die dryfmiddel samestelling en motor eienskappe te voorspel vanaf die irradiansie.

Die voorspelde spektra van beide die vuurpylmotors en die fakkels het nie altyd goed gekorreleer met die gemete data nie. Van die spektra kom voor in ‘n lae digtheidsdeel van die veranderlike ruimte. Dit het tot gevolg gehad dat daar nie genoeg data vir opleiding van die netwerk in die omgewing van die toetsdata was nie. Hierdie data is eintlik uitlopers en moet verwyder word van die opleidingsdata, maar daar is alreeds nie genoeg data beskikbaar om die uitlopers te verwyder nie.

Dit is nodig om te bepaal hoe goed die voorspelde data vergelyk met die gemete data. Twee parameters is gebruik om te bepaal hoe goed die data korreleer. Die eerste is die “Pearson product moment of coefficient of correlation”, wat ‘n goeie aanduiding gee van hoe goed die voorspelde waardes die gemete waardes se profiel volg. Die tweede parameter meet die relatiewe afstand tussen die teiken en die voorspelde waardes. Vir beide die vuurpylmotors en die fakkels het die toetsstelle ‘n korrelasiewaarde van baie na aan 1 gegee, wat ‘n goeie korrelasie is. Die waardes van die twee parameters vir een van die fakkel toetstelle was onderskeidelik 0.998 en 0.992.

Die model is geverifieer deur te bepaal of die model ‘n beter oplossing bied as die gemiddeld van die veranderlike ruimte. Drie statistiese toetse is gedoen: “Mean-squared-error” toets, T-toets en ‘n “Wilcoxon ranksum” toets. In al drie gevalle word die gemiddelde van die veranderlike ruimte (statiese model) en die voorspelde waardes (Neurale netwerk model) teen die gemete waardes getoets. Vir beide die T-toets en die “Wilcoxon ranksum” toets word die nul hipotese verwerp indien $t < t_a = 1.645$ en dan word die alternatiewe hipotese aanvaar, wat bepaal dat die fout van die neurale netwerk model kleiner is as die van die statiese model. Die “mean-squared-error” van die statiese model was 0.102, in vergelyking met 0.0167 van die neurale netwerk model vir ‘n vuurpylmotor toetsstel. ‘n T-toets is gedoen vir dieselfde toetsstel, met ‘n resultaat van

-2.71, wat kleiner is as –1.645 en aandui dat die neurale netwerk model weereens beter presteer as die statiese model. Die Z waarde uit die "Wilcoxon ranksum" toets is Z=-11.9886, wat baie kleiner is as –1.645.

Die resultate van die statitiese toetse toon dat die neurale netwerk 'n geldige model is en die oplossings van die model ook uniek is.

Acknowledgements

The motivation that was needed to finish this dissertation came at no price. I thank my wife, Marga, for all the support over the past four years and of understanding the late hours of work. My daughter for not seeing or understanding her father for the last two weeks. I dedicate this piece of work to them who love me.

Prof Hansie Knoetze for introducing me to this field, but also for helping me pull through in the end. The patient management of the project is very much appreciated and I hope the dissertation meets your high standards.

Jan Roodt for all the interesting chats and motivation and also the passion for this work.

Camaren Peter for the advice, motivation and helping me read through the long chapters of maths.

TABLE OF CONTENTS

LIST OF FIGURES

LIST OF TABLES

1. Introduction

The development of the infrared or heat-seeking missile, introduced a new threat to aircraft. Since a heat-seeking missile will track the heat signature of the engine's plume, the perfect countermeasure would be a heat source that simulates the engine's heat signature. In order for a countermeasure or flare to be successful in diverting a missile attack it would need to have the same spectral characteristics as the target it's protecting. Detectors used in infrared missiles are sensitive in the 3-5 micron wavelength band; therefore it is the wavelength region of importance in this study. Development of *"two-colour"* detectors with sensitivity in the 1-2 micron wavelength and the 3-5 micron wavelength region, asked for a new generation (more intelligent) flares. These flares would have to match the response of the IR detector in two wavelength regions.

The heat signature generated by these flares is most often caused by a combustion reaction. The materials used in the combustion reaction are high-energy materials with complex chemical compositions. Flares are generally released into the atmosphere or will be tethered and pulled through the air. The gaseous products of these high temperature combustion products are subject to wind drag causing cooling and further reactions between the energetic products of such a combustion reaction. A dramatic change in temperature of the reaction is also possible with a change in the ratio of oxygen to fuel that is available for the reaction and thus will influence the thermal signature of the reaction.

Early warning missile systems work on the same principal. An infrared missile is a passive weapon, which does not interact with a target, as a radar missile would do. The only way of detecting such a missile would be by the plume generated by the solid propellant burning in the motor and generating combustion products with specific infrared spectra. The solid propellants used in such rocket motors are complex mixtures and the combustion products even more so.

Modeling the infrared spectra of these high-energy reactions are challenging. In the past computational fluid dynamic analysis have been used to try and model the plume phenomena of combustion reactions. An alternative modeling approach was used which did not rely on solving all the non-linearities and complex relationships applicable to a fundamental model. A multilayer perceptron based Neural Network was used to develop a parametric functional mapping between the propellant chemical composition and the motor design and the resulting spectral irradiance measured in a section of the plume. This functional mapping effectively models the relationship between the rocket design and the plume spectral radiance.

The ultimate goal of this work is to be able to identify the infrared spectra from a solid propellant fuel or flare. This would greatly enhance the development of flares and solid propellant fuels. Rather than physically developing these high-energy fuels, it would be possible to simulate different composition changes, with a resultant change in infrared signature. A neural network model was thus developed to predict the infrared signature of the flares from the chemical composition. The same approach was followed by Roodt [1], who developed a feedforward neural network in order to predict the infrared spectra of rocket plumes. The same rocket plume spectra were used to optimise a neural network construction. This methodology can now be exploited further towards the stated ultimate goal.

There is a significant difference between the combustion reactions of the solid propellant rocket and a flare. The solid propellant ignites inside a chamber and the combustion products are then driven through a nozzle to generate thrust. The flares considered in this study will ignite and burn while exposed to the atmosphere. In order to build a model to simulate these combustion reactions it was necessary to have input data and measured infrared spectra. The chemical composition of the fuels is a logical input, but more parameters were needed in order to model the infrared spectra accurately. In the case of the solid propellant rockets it was possible to use thermodynamic and physical parameters of the motor as data. The flares only interact with the atmosphere, thus it was necessary to generate thermodynamic data to extract more parameters.

The task defined for this thesis is threefold: Firstly it is necessary to streamline the existing neural network proposed by Roodt [1], in order to determine if it is possible to improve the neural network model. This optimisation of the network is only a first order improvement and not a detailed optimisation of the neural network model.
Secondly it will be shown that it is possible to reverse the neural network by using the spectra from different solid propellant rockets to predict the solid propellant composition and rocket motor parameters.
Thirdly an investigation into whether it is possible to develop a model to predict the infrared spectra of flares will be done. The model used for predicting the flare spectra would be similar to that of the model used for training and testing the solid propellant rockets.

The proposed model (a feedforward network) had to be optimised in order to minimize calculation time, but also to have a model properly representing the problem. The number of variables in the model had to be reduced to generate an optimised neural network. Many statistical models exist nowadays and these will be mentioned as possible solutions. It was only the neural network that could handle this complex problem. The available data were sparse and most statistical models need a lot of data to construct a proper solution.

Several neural networks were trained with different input data, until a conceptual working solution was found. The predicted spectra were then evaluated against the actual measured values. Both neural networks showed good results and were verified as valid models using statistical hypothesis testing.

Reference:

1. Roodt, J., *The Prediction of the emission spectra of solid rocket propellants*, Ph.D. dissertation, Dept. Chemical Engineering, University of Stellenbosch, Chapter 7, (1998).

2. Thermodynamics

2.1. Thermodynamic Fundamentals

2.1.1. Chemical Thermodynamics

Among the most important thermodynamic problems is the calculation of heat and work requirements for physical and chemical processes. This requires the determination of equilibrium conditions for chemical reactions and for the transfer of chemical species between phases.

The application of thermodynamics to any real problem starts with the identification of a particular body of matter as the focus of attention. This quantity is called the *system*, and its thermodynamic state is defined by a few measurable macroscopic properties. These depend on the fundamental dimensions of science, of which length, time, mass, temperature and composition of substance are of interest here [3]. Which thermodynamic parameters will describe the specific system best?

The essential parameters necessary for the evaluation of combustion processes are the equilibrium product temperature and composition. It is useful to define the term "thermodynamic equilibrium" by considering the following:

- *Mechanical equilibrium* – exists when there are no unbalanced forces between the system and its surroundings.
- *Thermal equilibrium* – exists when all parts of the system are at the same temperature, which is the same as the surroundings.
- *Chemical equilibrium* – exists when a system has no tendency to undergo a change in chemical composition.

The approach taken here will be one of *irreversible* thermodynamics and not reversible. For a system to be reversible, the process has to be performed in such a way that both the system and the surroundings can return to their initial state. Such a process is regarded as

a succession of equilibrium states, and must be carried out slowly to conserve the equilibrium. Combustion processes such as the burning of solid propellant in a rocket motor is irreversible. By assuming that each subsystem is in equilibrium (not necessarily with its surroundings), equilibrium thermodynamics can be applied [4].

All chemical reactions are accompanied either by absorption or an evolution of energy, which usually manifests itself as heat. This is in essence a statement of the first law of thermodynamics. It is possible to determine the amount of energy, therefore the temperature and subsequently the product composition from basic principles [1]. From this it is clear that at equilibrium the parameters do not change with time. Thermodynamic parameters found to be independent and suitable for combustion studies are the pressure p, the volume V, and the total number of moles of a chemical species n_i. Nomenclature for all the equations used in this chapter could be found under the heading 2.4

The zeroth law of thermodynamics states that the temperature,

$$T = T(p, V, n_i) \tag{2.1-1}$$

is the same for all systems in equilibrium with each other.

The first law of thermodynamics (conservation of energy) states that the stored energy E, is composed of he following:

- Internal Energy, U
- Kinetic Energy, KE
- Potential Energy, PE

thus,

$$E = U + KE + PE \tag{2.1-2}$$

where

$$E = E(p, V, n_i) \tag{2.1-3}$$

For a closed system, the heat added to the system is,

$$\delta\hat{Q} = dE + \delta\hat{W} \tag{2.1-4}$$

where δW is the work done by the system and equals $p\,dV$. Note that the caret indicates that the variable is not a thermodynamic property and δ indicates an inexact differential, since $\hat{Q}$ and $\hat{W}$ are path-dependent functions. A capital symbol indicates a state or a quantity and a lower case symbol of that symbol incates that it is molar specific.

The second law of thermodynamics states that there exists an absolute scale for temperature and a function called the entropy.

$$S = S(p,\ V,\ n_i) \tag{2.1-5}$$

For a process in a closed system

$$T\,dS \geq \delta Q \tag{2.1-6}$$

where the equality is valid for reversible processes and the inequality valid for irreversible processes.

The third law states that the entropy of a crystal, at the absolute zero temperature, is zero. This is used as a reference value for evaluating entropies of various substances.

For a system at volume V and temperature T, there will be a set of values for n_i at which the system is in equilibrium. The equation of state then becomes

$$p = p(V,\ T,\ n_1^*, n_2^*, ..n_N^*) \tag{2.1-7}$$

The asterisk indicates the equilibrium values. From Dalton's law of partial pressures, we know that for a mixture of thermally perfect gases at non-equilibrium state, the pressure can be expressed as.

$$p = \frac{1}{V}\sum_{i=1}^{N} n_i RT \tag{2.1-8}$$

A single arbitrary chemical reaction may be represented as follow.

$$\sum_{i=1}^{N} \nu_i' M_i \rightarrow \sum_{i=1}^{N} \nu_i'' M_i \tag{2.1-9}$$

From the first law of thermodynamics and (2.1-4) it follows that $dE = \delta\hat{Q} - \delta\hat{W}$ and from (2.1-2), $dE = dU + d(KE) + d(PE)$, which can then be combined as,

$$\delta\hat{Q} = dU + d(KE) + d(PE) + \delta\hat{W} \tag{2.1-10}$$

The term $\delta\hat{W}$ contains the following: *shaft work,* W_s, which is work done to produce an effect on the surroundings. *Viscous work,* W_μ, which is work done to overcome fluid friction effects on the boundary where mass flow occurs. The *flow work* is performed to overcome pressure effects at any point on the boundary where mass flow occurs.

The flow work rate can be expressed as

$$p\frac{dV}{dt} = \frac{p}{\rho}\left(\rho\frac{dV}{dt}\right) = \frac{p}{\rho}\dot{m} \tag{2.1-11}$$

where p is a state function related to V and T by the state function, $p = p(V, T)$.
Assuming that there's no viscous and shaft work, and no kinetic energy or potential energy, the resultant internal energy is equal to,

$$dU = \delta\hat{Q} - pdV \tag{2.1-12}$$

with $\delta\hat{Q}$ representing heat that the system receives from the surroundings and pdV the flow work done by the system.

It is also useful to define the enthalpy of the system, by the equation

$$H = U + pV \tag{2.1-13}$$

If a system undergoes change from one state to another, which is irreversible, between two states of equilibrium, the entropy change for the system is given as

$$S_2 - S_1 > \int_1^2\left(\frac{\delta\hat{Q}}{T}\right) + \int_1^2 d_i S \tag{2.1-14}$$

Change in entropy can be split into two parts:

$$dS = (dS)_e + (dS)_i \tag{2.1-15}$$

where d_eS is the change resulting from interaction between the system and the surroundings, and d_iS the change resulting from an internal interaction (e.g. chemical reaction). In the case of a chemical reaction a resultant change in p, T and n_j will take place. The change in the number of moles of chemical species is described by,

$$dn_j = d_i n_j + d_e n_j \tag{2.1-16}$$

(with the subscript on the d indicates the type of change, as in (2.1-15), and n_j indicates the mole species). From equation (2.1-14) and (2.1-15)

$$dS = \frac{\delta \hat{Q}}{T} + \sum_{j=1}^{N} s_j dn_j \tag{2.1-17}$$

The internal energy can be expressed in the same way

$$dU = \delta \hat{Q} - pdV + \sum_{j=1}^{N} u_j dn_j \tag{2.1-18}$$

Next a new parameter μ_j, is introduced, which represents the chemical potential.

$$\mu_j \equiv u_j - Ts_j \tag{2.1-19}$$

Now by dividing equation (2.1-18) by T and substituting both (2.1-19) and (2.1-18) into (2.1-17) the resultant equation is,

$$\boxed{dS = \frac{1}{T} dU + \frac{p}{T} dV - \frac{1}{T} \sum_{j=1}^{N} \mu_j dn_j} \tag{2.1-20}$$

which is the fundamental equation of chemical thermodynamics for *open irreversible chemical processes.* In differential form,

$$dS = \left(\frac{\partial S}{\partial U}\right)_{V,n_j} dU + \left(\frac{\partial S}{\partial V}\right)_{U,n_j} dV + \sum_{j=1}^{N}\left(\frac{\partial S}{\partial n_j}\right)_{U,V,n'_j} dn_j \qquad (2.1\text{-}21)$$

where the symbol n'_j in the last term indicates that all mole numbers except n_j are held constant for the derivative. By comparing equations (2.1-20) and (2.1-21), we have

$$\left(\frac{\partial S}{\partial U}\right)_{V,n_j} = \frac{1}{T} \qquad (2.1\text{-}22)$$

$$\left(\frac{\partial S}{\partial V}\right)_{U,n_j} = \frac{p}{T} \qquad (2.1\text{-}23)$$

$$-T\left(\frac{\partial S}{\partial n_j}\right)_{U,V,n'_j} = \mu_j \qquad (2.1\text{-}24)$$

Since the enthalpy was defined as $H = U + pV$

$$dU = dH - pdV - Vdp \qquad (2.1\text{-}25)$$

Substituting (2.1-25) into equation (2.1-21), we obtain

$$\boxed{dS = \frac{1}{T}dH - \frac{V}{T}dp - \frac{1}{T}\sum_{j=1}^{N}\mu_j dn_j} \qquad (2.1\text{-}26)$$

Similarly done as with equation (2.1-21), from the differential form

$$-T\left(\frac{\partial S}{\partial n_j}\right)_{H,p,n'_j} = \mu_j \qquad (2.1\text{-}27)$$

Combining both equations (2.1-17) and (2.1-24), the result is

$$\left(\frac{\partial S}{\partial n_j}\right)_{H,p,n'_j} = \left(\frac{\partial S}{\partial n_j}\right)_{U,V,n'_j} \qquad (2.1\text{-}28)$$

The *Gibbs free energy G* is introduced and like *H* is a secondary state variable. This simply means that the system's thermodynamics can already be described by the properties *p, T, V, U* and *S*. The Gibbs free energy is an additional function purely for convenience.

$$G \equiv H - TS = U + pV - TS \tag{2.1-29}$$

In differential form

$$dG = dH - TdS - SdT \tag{2.1-30}$$

which upon substitution into equation (2.1-26) gives

$$\boxed{dG = Vdp - SdT + \sum_{j=1}^{N} \mu_j dn_j} \tag{2.1-31}$$

From the above it is possible to write

$$\left(\frac{\partial G}{\partial p}\right)_{T,n_j} = V \tag{2.1-32}$$

$$-\left(\frac{\partial G}{\partial T}\right)_{p,n_j} = S \tag{2.1-33}$$

$$\left(\frac{\partial G}{\partial n_j}\right)_{p,T,n'_j} = \mu_j = -T\left(\frac{\partial S}{\partial n_j}\right)_{H,p,n'_j} \tag{2.1-34}$$

For a system to be in equilibrium at constant temperature and pressure, the conditions that *dT=0* and *dp=0* are contained. For a system in equilibrium at constant temperature and pressure, equation (2.1-31) would change to:

$$dG = \sum_{j=1}^{N} \mu_j dn_j \tag{2.1-35}$$

Thus if no mass is added and the system is in equilibrium it follows that *dG=0*. This then implies that the Gibbs free energy has an extremum when a system is in equilibrium. From equation (2.1-29), it is obvious that if an irreversible change takes place within the system, it will increase the entropy *S* and thus decrease *G*. The extremum is therefore a

minimum. As molecules react during a chemical process, the number of atoms stays constant. Furthermore from equation (2.1-35) it can be seen that a change in the Gibbs free energy in a reaction depends on the chemical potentials of the reactants. In equilibrium G is an extremum and dG must be zero. This result is useful, and will be used extensively in thermodynamic computations in rocket motors, which is relevant to this study.

Criteria for chemical equilibrium depend upon the condition at which certain thermodynamic properties are held constant. For a constant volume process a new function is introduced, called the *Helmholtz free energy*, which is defined by

$$F \equiv U - TS \tag{2.1-36}$$

F represents the useful work other than pressure-volume work, at constant temperature and volume. Rewriting the first law of thermodynamics

$$dU = \delta \hat{Q} - pdV + d\hat{\xi} \tag{2.1-37}$$

with $d\hat{\xi}$ denoting the work other than pressure-volume work. Work done on the system $d\hat{\xi}$ is positive and work done by the system it is negative. Combining equation (2.1-37) with the second law of thermodynamics, the result is:

$$d\hat{\xi} = dU - TdS + pdV \tag{2.1-38}$$

$$d\hat{\xi} = dF + SdT + pdV \tag{2.1-39}$$

At constant T and V, it is obvious from equation (2.1-39) that $d\hat{\xi} = dF$. Here dF represents the useful work in the system, at constant T and V. Again, if dF is negative then the system will do useful work, and if dF is positive, work has to be done on the system. By the same procedure one can write $d\xi$ in terms of dG,

$$d\hat{\xi} = dG + SdT - Vdp \tag{2.1-40}$$

Here $d\hat{\xi} = dG$ at constant p and T. A system is thus at equilibrium if the general equilibrium criterion, $d\hat{\xi} = 0$, is met.

For open irreversible chemical processes, equation (2.1-20) can be rewritten as

$$\boxed{dF = -SdT - pdV + \sum_{j=1}^{N} \mu_j dn_j} \qquad (2.1\text{-}41)$$

2.1.2. Reference:

1. Glassman, I., *Combustion,* Academic Press, New York, Chapter 1, (1977).

2. Sutton, G.P., *Rocket Propulsion Elements – An introduction to the engineering of rockets,* John Wiley & Sons, New York, 6 th edition, Chapter 3, (1992).

3. Smith, J.M., Van Ness, H.C., *Introduction to Chemical Engineering Thermodynamics,* McGraw-Hill Book Company, Singapore, 4th edition, Chapter 1, (1987).

4. Kuo, K. K., *Principles of Combustion,* John Wiley & Sons, New York, Chapter 1, (1986).

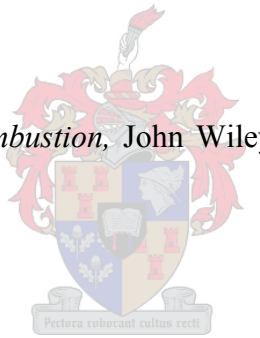

2.2. Rocket Thermodynamics

2.2.1. Introduction

Using the thermodynamic fundamentals deducted from the previous chapter, thermodynamic equations will be developed, which describes the rocket motor. From these equations we will identify and isolate the parameters needed to describe a rocket motor.

The thermodynamic relations established will be used to describe both rocket motors as well as infrared flare devices. Rocket motors are propelled by hot exhaust gases. These gases are usually the products from a combustion reaction of a rocket fuel. The exhaust gases also generate distinct infrared spectra, which is dependent on the type of rocket fuel burned and the design of the rocket motor. The infrared light region is used in many ways to detect and track rockets and flares. The objective is therefore to obtain the equations that justly describes the rocket motor and also the chemical composition of the exhaust gases.

Different types of rocket motors have been developed over the years, but the motor applicable to this study is a *solid propellant rocket motor*. The propellant burned is contained within the combustion chamber or case and is called the *grain* [1]. The solid propellant rocket motor is used mainly as the propulsion device for missiles. The importance of the infrared signal generated by the missile is thus understood, since it is important for a missile not to be detected and also to track a target using the infrared spectra of the target.

2.2.2. Rocket Motor Design

The solid propellant, consisting of a fuel and oxidiser, are located inside the combustion chamber. A schematic illustration of this type of rocket motor is shown in fig 2.2-1.

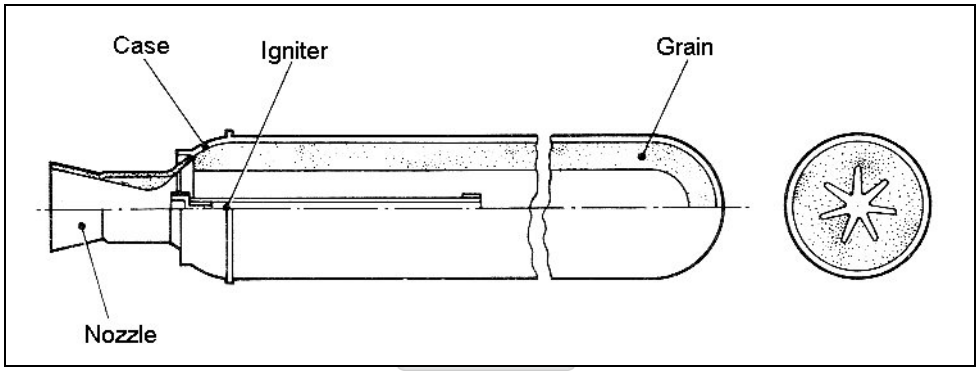

Figure 2.2-1 Schematic diagram of a solid rocket propellant motor [2]

The grain shown here is tubular with igniter inserted into the central cavity of the combustion chamber. After ignition, the hot gases produced flows through this central cavity and are accelerated to a high velocity by means of a nozzle. During combustion the propellant grain burns only on the surface, normally regressive to itself. The grain burns at its *linear regression rate*. The purpose of the combustion chamber is to contain the solid propellant grain, and also to withstand the pressures that build up during combustion of such a fuel.

The geometry of the motor chamber is related to the type of grain used. Geometry of the chamber correspond to the application, e.g. a high gas flow rate is obtained by increasing the ratio of surface burning area of the propellant to the nozzle throat area. [2]

As the combustion reaction products flow through the nozzle, it is thermodynamically expanded to produce thrust. These products are mostly gaseous, but may contain solids or liquids. Assuming the exiting gas to be a perfect gas introduces small errors [3]. It is necessary to know the chemical composition and proportion of the propellants to calculate the composition of the products. The principle of conservation of mass holds for combustion, thus the amount of chemical species must be equal to the amount after a reaction. If n_j is the number of mole's of species j per kg of gas mixture, then

$$n = \sum_{j=1}^{j=N} n_j \tag{2.2-1}$$

where n is the mixture consisting of N different chemical species. The average molecular weight of the mixture is then

$$Mr = \frac{\sum_{j=0}^{N} n_j Mr_j}{\sum_{j=0}^{N} n_j} \tag{2.2-2}$$

2.2.3. Propellant Chemistry

Solid propellants are composed of a fuel and an oxidiser, which when combined reacts to form gaseous products. Solid propellants are divided into two classes: homogeneous and heterogeneous propellants.

Homogeneous propellants generally contain the fuel and oxidiser elements in the same molecule. A propellant base is a pure substance of fuel and oxidiser, of which nitrocellulose and nitroglycerin is the most general. Most homogeneous propellants are double-base, which then consists of both nitrocellulose and nitroglycerin.

Heterogeneous propellants' oxidisers are macroscopic particles, e.g. ammonium perchlorate, which are contained in plastic fuel matrices called binders [9]. Composite propellants have a heterogeneous grain. The oxidiser crystals and a powdered fuel, e.g. Aluminium, are held together by the plastic binder. Another heterogeneous propellant is the composite modified double-base, which is a combination of a composite and double-base. The crystalline oxidiser such as ammonium perchlorate and the powdered fuel are contained in a matrix of nitrocellulose-nitroglycerin. In this study both double-base and composite propellant fuels will be investigated. Basic compositions for both propellants are given in Table 2.2-1. The acronyms used in table 2.2-1 are defined in Appendix A.

Table 2-1

Double-base			***Composite***		
Compound	***%***	*Function*	***Compound***	***%***	*Function*
Nitrocellulose	56%	Structure	**Ammonium Perchlorate**	70%	Oxidiser
Nitroglycerin	25%	Energetic plasticizer			
DOP	3%	Energetic plasticizer	**Al**	16%	Fuel
EC	2%	Stabiliser	**DOA**	1%	Binder / Plasticizer
Pb-Steorate	4%	Ballistic modifier	**Isophoron**	1%	Curing Catalyst
Carbon Black	1%	Opacifier/pigment	**HTPB**	12%	Energetic Binder
Triacetin	10%	Inert plasticizer			

Other than the fuel and the oxidiser, additional ingredients are added to the solid propellant. Each of these ingredients has a different role to play, e.g. as *binder, curing agent,* or *burn-rate catalyst.* These *additives* have many purposes, also in the manufacturing stage of the propellant, where additives are used to control the curing time, improve the rheological properties (easier casting), improving physical properties, etc [10]. The components of solid propellants involved in this study are given in Appendix A.

Different oxidisers have been tested of which ammonium perchlorate is the most widely used in solid propellants. The choice of oxidiser is based on its

- heat of formation, which should be as positive as stability allows,
- density, which should be as high as possible,
- oxydizer content, which should also be as high as possible [9].

Both ammonium and potassium are only slightly soluble in water, a characteristic making them favourable for composite solid rocket fuels. Perchlorate oxidisers produce HCl and other toxic products in a reaction with fuel. Characteristic of double-base solid propellants is the large amount of nitrocellulose plasticized by a liquid ester. High-energy binders, such as HMX (cyclotetramethylene tetranitramine) and RDX (cyclotrimethylene trinitramine) are often included in the propellant matrix in order to achieve specific performance characteristics. This is more often done in double-base propellants, in varying amounts, as required for the specific impulse, burning rate and internal ballistic properties. Propellants use a blend of oxidiser particle sizes, to obtain a high solid packing density and to maximise oxidiser to fuel weight ratio, by using the small particles to fill spaces between bigger particles. It has been shown that the ratio of coarse to fine particles of the oxidiser also influences the burning rate of the propellant.

The high-energy plasticizers or organic binder materials also act as fuels in solid propellant rockets and are oxidised in the combustion process. They are not classified purely as fuels since they also greatly influence other properties of the rocket. The binders, usually a polymer has an effect on motor reliability, mechanical properties, propellant processing complexity, storability and costs. The polymers can be grouped according to their respective effect on propellant processing as

- plastisol binders (PVC)
- oxygen-rich double-base propellant binders (NC)
- prepolymer or monomers for cast composite propellant binders (PBAN, CTPB) polymers from rubber gum stocks [10].

The main fuel used in solid propellants is powdered aluminium. Powdered aluminium is used in composite and composite double-base propellant formulations where during combustion it oxidises into aluminium oxide. Although boron is identified as a high-energy fuel, and it is lighter then aluminium, it is difficult to burn with high efficiency in a combustion chamber because of its high melting point. Beryllium proves to be a better fuel, by burning easier during combustion and improving the specific impulse, but it is highly toxic to both humans and animals. Other high-energy fuels include aluminium hydride (AlH_3) and beryllium hydride (BeH_2), but both have shown to deteriorate due to loss of hydrogen. Add the production cost and the toxicity of BeH_2 and they are not practical fuels [10].

Binders used in composite propellant systems serves to hold together the oxidiser particles as well as the metal particles. However energetic binders were introduced, which act as fuel and binder. At first fuel-rich double-base binders were used, in which the oxidiser particles were mixed, to increase the performance. Later systems included fuels such as powdered aluminium with energetic binders such as HTPB, along with oxidiser, to further increase the performance [9].

Additional additives added to the propellant to control certain characteristics of the fuel (as mentioned earlier), are carbon black and metal salts. Carbon Black is an opacifier, which prevents radiant energy transmission to the interior of the propellant, preventing internal ignition. Potassium compounds (e.g. potassium sulphate), are known as flame suppressants, since they reduce the infrared signal of the exhaust gases.

2.2.4. Thermochemical Modelling

In the evaluation of a combustion process the most important parameters are the equilibrium temperature and composition. When all the heat in a system is used entirely

to raise the product temperature, this equilibrium temperature is called the adiabatic flame temperature [4]. In order to determine these parameters a few assumptions have to be made. The rocket motor will be considered an ideal rocket, which assumes one-dimensional flow. The assumptions made greatly simplifies the mathematics involved and yet measured performance is within 1-10% of calculated ideal values. The following assumptions will hold for the calculations:

- The combustion products form a homogeneous substance. For a solid propellant rocket, the propellant is essentially homogeneous and the burning proceeds at a steady rate.
- The combustion products obey the perfect gas laws. When the temperature achieved in the combustion chamber is high (in excess of about 2500K), the gases are well above their respective saturation conditions and follow the perfect gas law closely.
- Friction and boundary layers are neglected.
- There is no heat transfer to the rocket chamber walls; the process is adiabatic. In most chambers less than 2% of the total energy is transferred to the walls.
- The propellant flow is steady and constant and the start and end of combustion may be neglected, because these processes are short-lived. In tactical missiles the total burn time at a specific profile is often in the order of a few seconds, while the ignition impulse is engineered to be a very short event, often in the order of tens of milliseconds. No shock waves and discontinuities exist in the nozzle flow.
- All the exhaust gases leaving the rocket nozzle have an *axially directed velocity*.
- The *gas velocity, pressure, temperature,* or *density* is uniform across any cross section normal to the nozzle axis.
- Chemical equilibrium is established within the rocket chamber and the composition does not change in the nozzle. Fluctuation in the burning of the propellant is possible, but normally the process proceeds smoothly. This has the effect of ensuring a rather stable pressure and temperature profile in the chamber.
- All the species of the combustion products are gaseous. Any condensed phases (liquid or solid) are considered to be of negligible concentration [1].

The enthalpy for a substance at standard state is given by H_T°. Since the product gases are considered ideal, the perfect-gas equation holds,

$$pV = nR_\circ T \tag{2.2-3}$$

The heat added or in this case evolved from the system, equals the change in enthalpy, $Q = -\Delta H$. This enthalpy is known as the *heat of reaction*. Consider the general reaction,

$$\sum_{i=1}^{N} n_i M_i \rightarrow \sum_{j=1}^{N} n_j M_j \tag{2.2-4}$$

with M_i the chemical symbol for species *i*. The heat of reaction at standard state is then

$$\Delta H_R = \sum_{j=1}^{N} n_j (\Delta H_f^\circ)_{T,M_j} - \sum_{i=1}^{N} n_i (\Delta H_f^\circ)_{T,M_i} \tag{2.2-5}$$

The symbol ΔH_f represents the *heat of formation* for a given substance. The value of this heat of formation of a substance from its elements can be considered to be the heat of one reaction. For an adiabatic process the heat evolved is used to heat the product gases, thus $\Delta H_R = 0$. If the reactants are at temperature, T_1 and the product gases at T_2, it follows that

$$\sum_{j=1}^{N} n_j [\{(H_{T_2}^\circ - H_0^\circ) - (H_{T_0}^\circ - H_0^\circ)\} + (\Delta H_f^\circ)_{T_0}]_j = \sum_{i=1}^{N} n_i [\{(H_{T_1}^\circ - H_0^\circ) - (H_{T_0}^\circ - H_0^\circ)\} + (\Delta H_f^\circ)_{T_0}]_i \tag{2.2-6}$$

If the composition of the product gases were known the flame temperature could be calculated from the equation above. In reality the n_j's are not known and it is obvious that more than just a energy balance would suffice. From equation (2.1-40), the Gibbs free energy were defined as

$$G = G^\circ + nR_\circ T \ln p \tag{2.1-40}$$

For a combustion process it can be written as

$$\Delta G = G_{product} - G_{reactants}$$
$$\Delta G = (cG_C + dG_D) - (aG_A + bG_B)$$
$$\Delta G = [(cG_C^\circ + dG_D^\circ) - (aG_A^\circ + bG_B^\circ)] + R_\circ T \ln p_C^c p_D^d - R_\circ T \ln p_A^a p_B^b$$

(2.2-7)

Since $\Delta G=0$, and

$$-\Delta G^{\circ} = R_{\circ} T \ln \frac{p_C^c p_D^d}{p_A^a p_B^b} \tag{2.2-8}$$

In general, equilibrium can be described by two equivalent formulations – equilibrium constants, or the minimisation of Gibbs free energy. According to Zeleznik and Gordon [6] both formulations reduce to the same number of iteration equations, but the Gibbs free energy method treats each species in the system independently. This property makes it possible to employ this formulation in the *Chemical Equilibrium and Applications* (CEA) computer program. [7]

It has already been established that the perfect gas law holds and all products are considered to be ideal gases. The variables V, n and ρ the volume and number of mole refer to the gas phase only, but the mass includes the condensed phases. From equation (2.1-35) the Gibbs free energy is given by

$$g = \sum_{j=1}^{N} \mu_j n_j \tag{2.1-35}$$

with the chemical potential for species j defined as

$$\mu_j = \left(\frac{\partial g}{\partial n_j} \right)_{p,T,n'_j} \tag{2.1-34}$$

For the condition of minimisation of Gibbs free energy to hold certain constraints has to be maintained, such as the mass-balance constraints:

$$\sum_{j=1}^{N} a_{ij} n_j - b_i^{\circ} = 0 \qquad (i = 1,\ldots,l) \tag{2.2-9}$$

or

$$b_i - b_i^{\circ} = 0 \qquad (i = 1,\ldots,l) \tag{2.2-10}$$

where the stoichiometric coefficients a_{ij} are the number of kilogram-atoms of element i per kilogram-mole of species j, the index l is the number of chemical elements, b°_i is the assigned number of kilogram-atoms of element i per kilogram of total reactants, and

$$b_i = \sum_{j=1}^{N} a_{ij} n_j \tag{2.2-11}$$

is the number of kilogram-atoms of element i per kilogram of mixture.

Define G to be

$$G = g + \sum_{i=1}^{l} \lambda_i (b_i - b_i^{\circ}) \tag{2.2-12}$$

with λ_i as Langrangian multipliers. The conditions for equilibrium then becomes

$$\delta G = \sum_{j=1}^{N} \left(\mu_j + \sum_{i=1}^{\ell} \lambda_i a_{ij} \right) \delta n_j + \sum_{i=1}^{\ell} \left(b_i - b_i^{\circ} \right) \delta \lambda_i = 0 \tag{2.2-13}$$

Approaching both δn_j and $\delta \lambda_i$ independently, the above equation can be reduced to

$$\mu_j + \sum_{i=1}^{\ell} \lambda_i a_{ij} = 0 \qquad (j = 1,\ldots,\mathrm{N}) \tag{2.2-14}$$

and the mass balance equation (2.2-10). From equations (2.1-35) and (2.1-40), the chemical potential can be written as,

$$\mu_j = \begin{cases} \mu_j^{\circ} + RT \ln \dfrac{n_j}{n} + RT \ln P & (j = 1,\ldots,M) \\ \mu_j^{\circ} & (j = M+1,\ldots,N) \end{cases} \tag{2.2-15}$$

where μ_j° for gases (j = 1,…,M) and for condensed phases (j = M+1,…,N) is the chemical potential at standard state. The thermodynamic state of the process can be specified by a further 2 state functions. In this case, for a constant pressure combustion process, the state is described by

$$h = h_0 \tag{2.2-16a}$$

$$P = P_0 \tag{2.2-16b}$$

where h is the specific enthalpy of the mixture and h_0 is the constant equal to the enthalpy of the reactants. The specific enthalpy h can be expressed by

$$h = \sum_{j=1}^{N} n_j H_j^{\circ} \tag{2.2-17}$$

with H_j° as the standard-state molar enthalpy for a species j at temperature T. For an isentropic compression or expansion the thermodynamic state can be specified by the entropy and the pressure.

$$s = s_0 \tag{2.2-18a}$$

$$P = P_0 \tag{2.2-18b}$$

The entropy s is the specific entropy of the mixture and s_0 the entropy of the reactants.

$$s = \sum_{j=1}^{N} n_j S_j^{\circ} \tag{2.2-19}$$

with S_j

$$S_j = \begin{cases} S_j^{\circ} - R \ln \dfrac{n_j}{n} - R \ln P & (j = 1,...,M) \\ S_j^{\circ} & (j = M+1,...,N) \end{cases} \tag{2.2-20}$$

and S_j° is the standard-state molar entropy for species j.

The equations that are required to calculate the composition are not all linear and therefore an iteration process is required. A Newton-Raphson method is used to solve the error for initial estimates of compositions n_j, Langrangian multipliers, λ_i, moles of gaseous species, n, and the temperature T. This requires a Taylor series expansion of the non-linear equations with all the terms with derivatives higher than first order, truncated. Correction variables used are

$\Delta \ln n_j$ (j = 1,…,M)

Δn_j (j = M+1,…,N)

Δn

$$\pi_i = -\lambda_i/RT$$

$$\Delta \ln T \tag{2.2-21}$$

After the equations containing thermodynamic functions were made dimensionless, the Newton-Raphson equations obtained from equations (2.2-14), (2.2-9), (2.2-16a) and (2.2-18a) are

$$\Delta \ln n_j - \sum_{i=1}^{\ell} a_{ij}\pi_i - \Delta \ln n - \frac{H_j^\circ}{RT}\Delta \ln T = -\frac{\mu_j}{RT} \qquad (j = 1,\ldots,\mathrm{M}) \tag{2.2-22}$$

$$-\sum_{i=1}^{\ell} a_{ij}\pi_i - \frac{H_j^\circ}{RT}\Delta \ln T = -\frac{\mu_j}{RT} \qquad (j = \mathrm{M}+1,\ldots,\mathrm{N}) \tag{2.2-23}$$

$$\sum_{j=1}^{M} a_{kj} n_j \Delta \ln n_j + \sum_{j=M+1}^{N} a_{kj} n_j \Delta n_j = b_k^\circ - b_k \qquad (k = 1,\ldots,l) \tag{2.2-24}$$

$$\sum_{j=1}^{M} n_j \Delta \ln n_j - n\Delta \ln n = n - \sum_{j=1}^{M} n_j \tag{2.2-25}$$

$$\sum_{j=1}^{M} \frac{n_j H_j^\circ}{RT}\Delta \ln n_j + \sum_{j=M+1}^{N} \frac{H_j^\circ}{RT}\Delta n_j + \left(\sum_{j=1}^{N} \frac{n_j C_{p,j}^\circ}{R}\right)\Delta \ln T = \frac{h_0 - h}{RT} \tag{2.2-26}$$

$$\sum_{j=1}^{M} \frac{n_j S_j^\circ}{R}\Delta \ln n_j + \sum_{j=M+1}^{N} \frac{S_j^\circ}{R}\Delta n_j + \left(\sum_{j=1}^{N} \frac{n_j C_{p,j}^\circ}{R}\right)\Delta \ln T = \frac{s_0 - s}{R} + n - \sum_{j=1}^{M} n_j \tag{2.2-27}$$

Utilising these equations, it is now possible to obtain the equilibrium compositions, combustion temperature and chamber pressure. These equations are all incorporated into a computer program developed by the NASA Lewis Research centre. It is now an elementary problem of creating an input file for the program. The initial composition of the solid propellant fuel is entered with the heats of formation for each of the species in the fuel.

2.2.5. Rocket Motor Parameters

Utilising the minimisation of Gibbs energy, two parameters were isolated from the thermodynamics of the rocket, namely the chamber pressure and the flame temperature. Souletis and Chastenet [8] found that certain motor functioning parameters have a strong influence on the plume of the rocket. The three parameters identified were the nozzle expansion ratio, nozzle exit radius and the chamber pressure.

The *total impulse* I_t , is the *thrust force F,* integrated over the burning time *t.*

$$I_t = \int_0^t F dt \tag{2.2-28}$$

The *specific impulse* I_s , is the total impulse per unit weight of propellant *w.* With the mass flow rate as $\dot{m}$ and gravitational acceleration as g_o, the specific impulse is

$$I_s = \frac{\int_0^t F dt}{g_o \int \dot{m}\, dt} \tag{2.2-29}$$

Taking into account the assumptions that was made in ***2.2.4***, where the ideal rocket is defined, the decrease of enthalpy between any points *x* and *y*, is equal to the increase in kinetic energy,

$$h_x - h_y = \tfrac{1}{2}\left(v_y^2 - v_x^2\right) = c_p\left(T_x - T_y\right) \tag{2.2-28}$$

where *v* is the velocity at a certain point and c_p the specific heat at constant pressure. The principle of mass conservation states that the mass flow between any two points is equal.

$$\dot{m}_x = \dot{m}_y = \frac{A_x v_x}{V_x} = \frac{A_y v_y}{V_y} \tag{2.2-29}$$

The perfect gas law can also be defined as,

$$p_x V_x = R T_x \tag{2.2-30}$$

where *R* is the universal gas constant divided by the molecular mass of the reaction gases, R_o/M_r. The ratio *k* of the specific heat at constant pressure c_p , and the specific heat at constant volume c_v , is constant for ideal gases as is shown below.

$$k = c_p / c_v$$

$$c_p - c_v = R$$

$$c_p = \frac{kR}{(k-1)} \tag{2.2-31}$$

For an isentropic flow process the following relations hold between two points *x* and *y*.

$$\frac{T_x}{T_y} = \left(\frac{p_x}{p_y}\right)^{\frac{(k-1)}{k}} = \left(\frac{V_y}{V_x}\right)^{k-1} \tag{2.2-32}$$

When flow is stagnated isentropically it is known as the *stagnation condition* and is described by the subscript 0. The isentropic relation for stagnation conditions is

$$\frac{T_0}{T} = \left(\frac{p_0}{p}\right)^{\frac{(k-1)}{k}} = \left(\frac{V}{V_0}\right)^{k-1} \tag{2.2-33}$$

The *Mach number* M, is defined as the ratio of the flow velocity to the *local acoustic velocity* $a = \sqrt{kRT}$.

$$\mathrm{M} = v / a = v / \sqrt{kRT} \tag{2.2-34}$$

Using the relation from (2.2-28) the *nozzle exit velocity* can be found.

$$v_2 = \sqrt{2(h_1 - h_2) + v_1^2} \tag{2.2-35}$$

Substituting for the enthalpy using equations (2.2-31) and (2.2-32)

$$v_2 = \sqrt{\frac{2k}{k-1} RT_1 \left[1 - \left(\frac{p_2}{p_1}\right)^{\frac{(k-1)}{k}}\right] + v_1^2} \tag{2.2-36}$$

This equation holds for any two points within the nozzle. If the chamber cross section area is large compared to the nozzle entry cross section area, then the chamber velocity is relatively small, thus v_1 can be ignored. For an insentropic nozzle the inlet temperature, which is equal to the chamber temperature, is also the stagnation temperature.

$$v_2 = \sqrt{\frac{2k}{k-1} RT_0 \left[1 - \left(\frac{p_2}{p_0} \right)^{\frac{(k-1)}{k}} \right]} \tag{2.2-37}$$

The minimum nozzle area is called the *throat area* A_t. The ratio of the nozzle *exit area* A_2, and the throat area is called the *nozzle area expansion ratio*, $\epsilon = A_2 / A_t$. The mass flow for an isentropic process, as in a rocket nozzle, can be expressed by using equations (2.2-29), (2.2-32) and (2.2-37), between any section x and the nozzle inlet section.

$$\dot{m} = \frac{A_x p_1}{R} \sqrt{2} \left\{ \frac{c_p}{T_1} \left[\left(\frac{p_x}{p_1} \right)^{2/k} - \left(\frac{p_x}{p_1} \right)^{(k+1)/k} \right] \right\}^{\frac{1}{2}} \tag{2.2-38}$$

The maximum gas flow in the nozzle occurs at the throat. A unique gas pressure coinciding with this maximum gas flow exists at the throat of the nozzle, which is the *critical pressure* p_t. If the pressure ratio in a given nozzle $\frac{p_1}{p_t} > \left(\frac{k+1}{2} \right)^{\frac{k}{(k-1)}}$, then it is a supersonic nozzle, which is employed in rockets. It is impossible for a pressure disturbance to travel upstream past the location of sonic or supersonic velocity. Now the flow through the critical section of the nozzle can be written as

$$\dot{m} = \frac{A_t v_t}{V_t} = A_t p_1 \frac{k \sqrt{\left[2/(k+1) \right]^{\frac{(k+1)}{(k-1)}}}}{\sqrt{kRT_1}} \tag{2.2-39}$$

The mass flow through a rocket nozzle is therefore proportional to the throat area A_t, the inlet pressure (or chamber pressure) p_1 and inversely proportional to the nozzle inlet temperature T_1.

The ratio between the nozzle throat area and any downstream area A_t / A_x , can be expressed as

$$\frac{A_t}{A_x} = \frac{V_t v_x}{V_x v_t} = \left(\frac{k+1}{2} \right)^{1/(k-1)} \left(\frac{p_x}{p_1} \right)^{1/k} \sqrt{\frac{k+1}{k-1} \left[1 - \left(\frac{p_x}{p_1} \right)^{(k-1)/k} \right]} \tag{2.2-40}$$

The thrust equation $F = v_2 \dot{m} + (p_2 - p_3)A_2$ can be expanded by substituting for v_2, v_t and V_t.

$$F = A_t p_1 \sqrt{\frac{2k^2}{k-1}\left(\frac{2}{k+1}\right)^{\frac{(k+1)}{(k-1)}}\left[1-\left(\frac{p_2}{p_1}\right)^{\frac{(k-1)}{k}}\right]} + (p_2 - p_3)A_2 \tag{2.2-41}$$

2.2.6. Conclusions

From equation 2.2-37 it is seen that the exhaust velocity of a nozzle is a function of the ratio p_1 / p_2 , the specific heat ratio k, combustion temperature and the gas constant R.
Equation 2.2-41 shows that the thrust is proportional to the nozzle inlet pressure p_1, a function of the pressure ratio across the nozzle p_1 / p_2, and also proportional to both the throat and nozzle outlet area. From the above equation it is possible to state that the shape of the nozzle, i.e. the throat and nozzle outlet cross sectional area, has an effect on the thrust of the rocket. Souletis and Chastenet [8] also shows that both the nozzle expansion ratio and the nozzle exit radius has an effect on the shape of the rocket's plume as well as the intensity along the plume axis. The nozzle exit radius can be substituted by the nozzle throat diameter, since the exit radius is inherent in the expansion ratio. These deductions can be written as follow:

$$v_2 = f\{p_1, p_2, k, R,\}$$
$$F = f\{p_1, p_2, p_3, k, A_t, \varepsilon\}$$

Both k and R are functions depending on the composition of the fuel. The ratio of p_1 / p_2 is a function of the configuration of the nozzle, with p_3 the atmospheric pressure. If one can assume the exhaust velocity and the thrust to be mathematically descriptive of the exhaust plume structure and infrared signature, then

$$Plume\ signature = f\{p_1, T_1, A_t, \varepsilon, fuel\ composition\}$$

It was shown earlier that the combustion temperature T_1, resolves the composition of the exhaust gases and thus also the infrared signature given off by the different components of the gas.

2.2.7. Reference:

1. Sutton, G.P., Rocket Propulsion Elements – *An introduction to the engineering of rockets*, John Wiley & Sons, New York, 6th edition, Chapter 1, (1992).

2. Williams, F.A., Barrère, M. and Huang, N.C., *Fundamental aspects of Solid Propellant Rockets*, Technivision Services, Slough, England, Chapter 1, (1969).

3. Sutton, G.P., Rocket Propulsion Elements – *An introduction to the engineering of rockets*, John Wiley & Sons, New York, 6th edition, Chapter 6, (1992).

4. Glassman, I., *Combustion,* Academic Press, New York, Chapter 1, (1977).

5. Sutton, G.P., Rocket Propulsion Elements – *An introduction to the engineering of rockets*, John Wiley & Sons, New York, 6th edition, Chapter 3, (1992).

6. Zeleznik, F.J. and Gordon, S., *Calculation of Complex Chemical Equilibria,* Industrial and Engineering Chemistry, Vol.60, No.6, (1968).

7. Gordon, S. and McBride, B., *Computer program for Calculation of Complex Chemical Equilibrium Compositions and Applications,* NASA SP-273, 1971, NASA Lewis Research Center, NASA Reference Publication 1311, (1994).

8. Souletis, J. and Chastenet, J.C., *Study of the afterburning flame size and intensity as a function of the motor parameters,* AIAA90-1853, 26th AIAA SAE/ASME/ASEE Joint Propulsion Conference, Orlando, (1990).

9. Williams, F.A., Barrère, M. and Huang, N.C., *Fundamental aspects of Solid Propellant Rockets*, Technivision Services, Slough, England, Chapter 3, (1969).

10. Sutton, G.P., Rocket Propulsion Elements – *An introduction to the engineering of rockets*, John Wiley & Sons, New York, 6th edition, Chapter 11, (1992).

2.3. Flare Thermodynamics

2.3.1. Introduction

Flares have different uses in the industry, but in this study countermeasure flares are considered. The development of countermeasure flares has not been a precise science and different approaches have been employed. The objective of a flare is to simulate the infrared signature of a target e.g. an aircraft, or to confuse the threat (rocket, missile) used to attack the target.

Modern flares burn a solid propellant to produce an infrared signal, which has to match the target's signature. There exists no reliable tool by which the resultant infrared signal of a flare can be predicted form the composition of the solid propellant burned in the flare. The countermeasure flare system differs from the rocket system, in that it is an *irreversible open combustion process.*

2.3.2. Flare Design

Since countermeasure flares were introduced, several designs were developed. Countermeasure flares have several ranges of application, from countermeasures for air

targets to ground targets. These are constantly being improved, because of the constant evolution of threats.

The type of construction ranges from a basic brick of compacted solid propellant, to a flare similar to a solid propellant rocket, where the solid propellant produces both the infrared signature and the necessary propulsion. The brick type flare will ignite and the flare (in this case solid propellant) will burn on all surfaces. The brick is usually encased in a foil, to control the burning rate of the propellant.

Another design resembling a small rocket has been developed. Here a lightweight composite material encloses the flare's solid propellant fuel, which improves the flare's performance. The material selected must be lightweight, yet it must be able to withstand the high pressures and temperature for the duration of the flare's burning time. The baseline design incorporates a stainless steel housing, shroud, fins and a nozzle. [1]

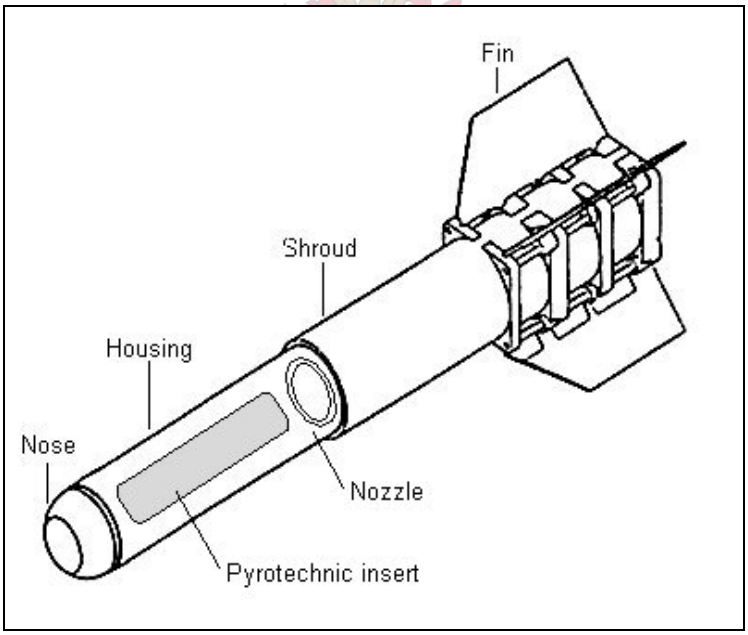

Figure 2.3-1 Baseline flare design [1].

The propellant is enclosed within the stainless steel housing, with the nozzle attached to the end of this housing. At the forward end of the housing a tungsten nose is used to shift the centre of gravity forward. The shroud, which is slightly larger than the housing, fits over the housing, with fins attached on the exterior of the shroud. The self-propelled

flare protects a moving target further by simulating the kinematics of the target to deceive a particular threat. The infrared signal created by a flare should be strong enough to emulate an infrared signal from a motor, but at the same time burning time has to be long enough, and total mass has to stay within a reasonable weight limit [2].

2.3.3. Propellant Chemistry

Conventional countermeasure flares have a basis of magnesium and teflon. These flares emit an infrared irradiance of a typical blackbody. This type of flare easily counters a basic threat deceived by a strong infrared signal, but tracking systems of missile have been upgraded, to distinguish more sharply between the infrared signals of the countermeasure and the target. These flares have become outdated and incapable of deceiving a very capable threat. New generation tracking systems are capable of comparing the signatures of the countermeasure flare and the target in different spectral strips (a bimodal system) and also to analyse the spatial extent of the signatures. Within this environment it has become necessary to formulate a composition for a countermeasure flare to simulate real signatures of aircraft or ground targets. The formulation of pyrotechnic flares using solid propellants (with particles) allows for infrared signals rich in CO_2 and H_2O, which approaches real signatures of aircraft motors, which normally cannot be done [2].

According to research done in India, zirconium-based compositions with a polymeric base were developed to meet the requirements mentioned above and also to prolong the shelf life of the flare. These flares were tailored to produce flame temperatures of 1800-2000°C, with a burning time of 3 – 5 minutes [3].

Countermeasure flares generally contains metallic fuels (Mg, Si, Zr) or alloys and oxidisers contained in a matrix supplied by binders. As with the solid rocket propellants, additives are also contained in this matrix to control the ballistic and manufacturing properties of the flare. The effective performance of the flare compositions depends on the chemical nature of infrared-producing formulations and designs. Teflon based composition emits a higher infrared intensity than barium nitrate-based compositions in the 3-5 μm and 8-14 μm wavelength regions. Particles in the postcombustion products, that have a high temperature, correspond to that of a black body, which radiates continuously in the infrared region. Various parameters influence the infrared irradiance of the combustion products, i.e. an increase in combustion temperature results in an increase in intensity of irradiance in the near infrared region. The particle size distribution of the metal powder (Mg, Si, Al in this case) and oxidiser plays an important role in the burning characteristics of the flare composition [3].

Certain additives are added to the composition to modify the irradiance in a specific infrared wavelength range. These additives can also contribute to a decrease of ultra-violet irradiance in the plume of the flare, since new generation threats compare the flare's signal in different ranges of emitted light. Compositions loaded with less particles are also introduced in order to meet the requirements in the spectral field of UV, visible and infrared. A compromise is made, because less particles in the plume results in lower infrared irradiance levels. Taking into account all these demands, solid propellant was employed to simulate an aircraft's or other infrared targets' motor signatures. The different species constituting the propellant burning all have its own significant function in the fuel. The composition for three different flares are shown in table 2.3-1.

Table 2-2 Chemical composition of flare propellants

Compound	***MF02*** %	***SF2515*** %	***SF289*** %	***Function***
HTPB		11.85	20.24	Energetic binder
IPDI		0.9	2.77	Curing Catalyst
DOA		1	1	Binder / Plasticizer
Tepa			0.3	Bonding agent
Tepan		0.25		Bonding agent
APC	67	69.8	73	Oxidiser
Al		16		Fuel
Fe(AA)		0.0001		Ballistic modifier
Aerosil		0.02		Fuel / Oxidiser
TMP			0.45	Bonding agent
AO 2246			0.24	
MgO			0.09	
Carbon Black			2	Pigment / Opacifier / Burning rate enhancer
MA			0.07	
TPB			0.05	
RDX	20			Energetic Fuel / Oxidiser
Polylite	13			Binder / Inhibitor

The first, ***MF02,*** is a basic flare made up of an oxidiser and fuel contained in a binder. The second, ***SF2515***, contains a metallic fuel as well as several additives. ***SF289*** contains (excluding additives contributing to the manufacture and storage of the propellant) carbon black, which causes particles to be in the combustion products and this results in higher infrared irradiance levels.

From Fig. 2.3-2 it can be seen that the infrared irradiance levels of ***SF289*** exceeds those of ***MF02*** and ***SF2515***.

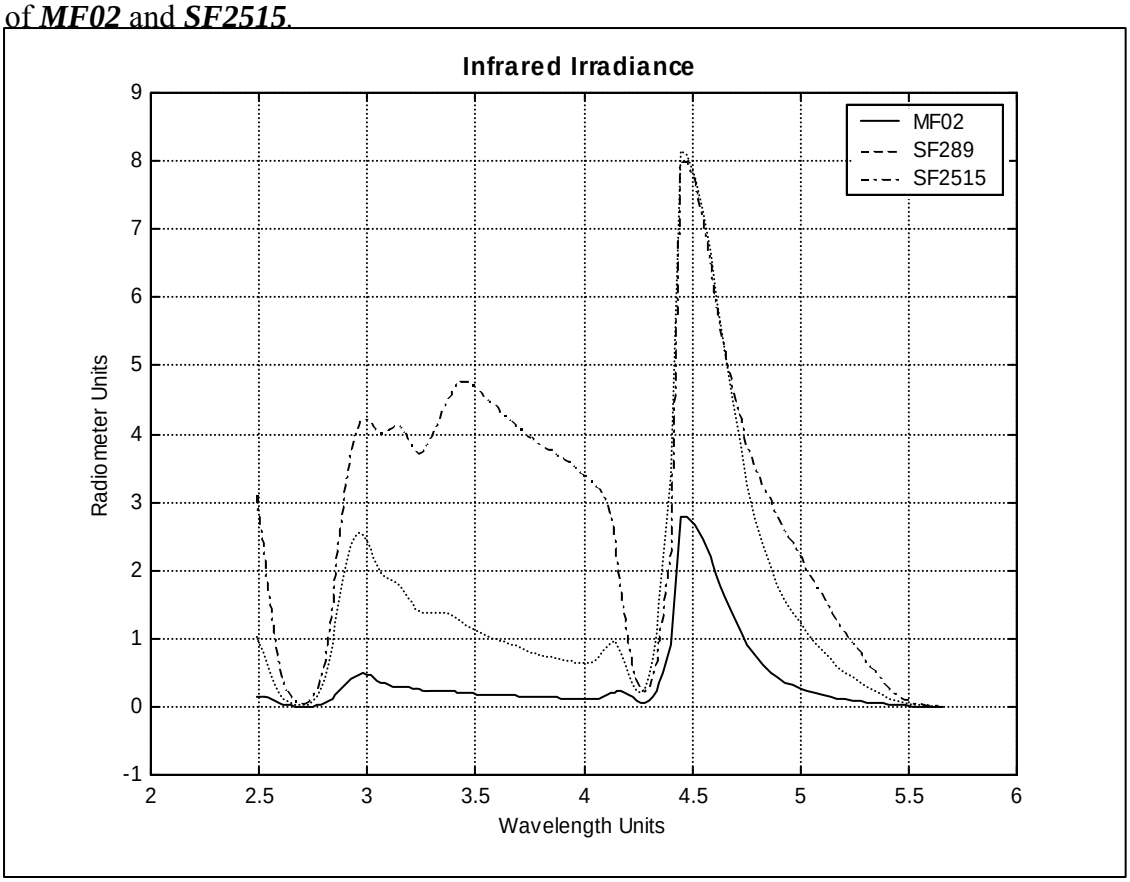

Figure 2.3-2 Measured spectral irradiance for three different flares

2.3.4. Thermochemical Modelling

The same procedure, when considering the thermodynamics surrounding a solid propellant rocket, will be employed for the determination of flares' thermodynamics. There is a difference in the flares' thermodynamics compared to that of solid propellant rockets, in that the combustion process is now an open process and not a closed process. Considering the brick construction for a countermeasure flare, there exists no nozzle through which the combustion products will have to flow. Combustion products leave the surface of the brick of solid fuel in all directions.

For countermeasure flares the products of combustion makes contact in a general direction with the ambient air.
The temperatures of the products are comparable with the combustion products in solid propellant rockets [2].

From equations (2.1-17) and (2.1-18) dU can be written as,

$$dU = TdS - pdV \tag{2.3-1}$$

The system considered is an open system, meaning mass transfer may occur through the systems boundaries. Chemical potential was defined as,

$$\mu_j = \left(\frac{\partial g}{\partial n_j} \right)_{p,T,n'_j} \tag{2.1-34}$$

and the Gibbs free energy,

$$g = \sum_{j=1}^{N} \mu_j n_j \tag{2.1-35}$$

Considering the possible mass transfer, equation (2.3-1) becomes

$$dU = TdS - pdV + \sum_i \mu_i dN_i \tag{2.3-2}$$

where N_i is the number of moles of species i in the equilibrium thermodynamic system.
The relations for the enthalpy and the Helmholtz free energy can be written as,

$$dH = TdS + Vdp + \sum_i \mu_i dN_i \tag{2.3-3}$$

$$dF = -SdT + Vdp + \sum_i \mu_i dN_i \tag{2.3-4}$$

which can be translated as,

$$\mu_i = \left(\frac{\partial H}{\partial N_i}\right)_{S,p,N_j(j\neq i)} = \left(\frac{\partial F}{\partial N_i}\right)_{T,p,N_j(j\neq i)} \tag{2.3-5}$$

T, p and N_i are generally the most readily measured properties. The pressure being the ambient pressure and the fuel composition known, it leaves the temperature to be calculated. From the relation above it can thus be seen that the Helmholtz free energy is the preferred thermodynamic function when it comes to describing an open system. Dependent and independent thermodynamic functions in open thermodynamic systems are the following: [4]

$$\begin{aligned} U &= U\{S, V, N_i\} \\ H &= H\{S, p, N_i\} \\ F &= F(T, p, N_i\} \end{aligned} \tag{2.3-6}$$

Using these functions the *Euler* relation for the internal energy can be written:

$$U = S\left(\frac{\partial U}{\partial S}\right)_{V,N_i} + V\left(\frac{\partial U}{\partial V}\right)_{S,N_i} + \sum_J N_j \left(\frac{\partial U}{\partial N_j}\right)_{S,V,N_i(i\neq j)} \tag{2.3-7}$$

Since *H and F* depend on intensive and extensive variables, their respective Euler relations are deducted using these defining relations:

$$H = U + pV \quad \textit{and} \quad F = H - TS$$

Thus,

$$H = S\left(\frac{\partial U}{\partial S}\right)_{V,N_i} + V\left(\frac{\partial U}{\partial V}\right)_{S,N_i} + \sum_J N_j \left(\frac{\partial U}{\partial N_j}\right)_{S,V,N_i(i\neq j)} + pV \tag{2.3-8}$$

$$F = S\left(\frac{\partial U}{\partial S}\right)_{V,N_i} + V\left(\frac{\partial U}{\partial V}\right)_{S,N_i} + \sum_J N_j \left(\frac{\partial U}{\partial N_j}\right)_{S,V,N_i(i\neq j)} + pV - TS \tag{2.3-9}$$

After evaluating the partial derivatives appearing in the preceding expressions, we find,

$$U = TS - pV + \sum_i \mu_i N_i \tag{2.3-10}$$

$$H = TS + \sum_i \mu_i N_i \tag{2.3-11}$$

$$F = \sum_i \mu_i N_i \tag{2.3-12}$$

Equation (2.3-2), the fundamental equation for an open thermodynamic system and similar to equation (2.1-20), can now be written as:

$$\boxed{dU = \left(\frac{\partial U}{\partial S}\right)_{V,N_i} dS + \left(\frac{\partial U}{\partial V}\right)_{S,N_i} dV + \sum_J N_j \left(\frac{\partial U}{\partial N_j}\right)_{S,V,N_i(i\neq j)} dN_j} \tag{2.3-13}$$

$$\boxed{dS = \left(\frac{\partial S}{\partial U}\right)_{V,n_j} dU + \left(\frac{\partial S}{\partial V}\right)_{U,n_j} dV + \sum_{j=1}^{N} \left(\frac{\partial S}{\partial n_j}\right)_{U,V,n'_j} dn_j} \tag{2.1-21}$$

The same procedure described in 2.2.4 (Thermochemical modelling of rockets) can be followed. There is however differences between the systems.

- The flare combustion reaction is an open irreversible process.
- Since the flare is exposed to ambient air, this excess air or oxygen also acts as oxidiser, where in the case of the rocket no excess air was introduced to the system.
- The type of flare discussed here has no nozzle, meaning no acceleration or change in pressure, affecting the combustion gas temperature is experienced.

The same relations deducted in **2.2.4** are used to determine the temperature during combustion of the flare propellant [5].

$$\Delta \ln n_j - \sum_{i=1}^{\ell} a_{ij}\pi_i - \Delta \ln n - \frac{H_j^\circ}{RT}\Delta \ln T = -\frac{\mu_j}{RT} \qquad (j = 1,\ldots,\mathrm{M}) \tag{2.2-22}$$

$$-\sum_{i=1}^{\ell} a_{ij}\pi_i - \frac{H_j^\circ}{RT}\Delta \ln T = -\frac{\mu_j}{RT} \qquad (j = \mathrm{M}+1,\ldots,\mathrm{N}) \tag{2.2-23}$$

$$\sum_{j=1}^{M} a_{kj} n_j \Delta \ln n_j + \sum_{j=M+1}^{N} a_{kj} n_j \Delta n_j = b_k^\circ - b_k \qquad (k = 1,\ldots,l) \tag{2.2-24}$$

$$\sum_{j=1}^{M} n_j \Delta \ln n_j - n \Delta \ln n = n - \sum_{j=1}^{M} n_j \tag{2.2-25}$$

$$\sum_{j=1}^{M} \frac{n_j H_j^{\circ}}{RT} \Delta \ln n_j + \sum_{j=M+1}^{N} \frac{H_j^{\circ}}{RT} \Delta n_j + \left(\sum_{j=1}^{N} \frac{n_j C_{p,j}^{\circ}}{R} \right) \Delta \ln T = \frac{h_0 - h}{RT} \tag{2.2-26}$$

$$\sum_{j=1}^{M} \frac{n_j S_j^{\circ}}{R} \Delta \ln n_j + \sum_{j=M+1}^{N} \frac{S_j^{\circ}}{R} \Delta n_j + \left(\sum_{j=1}^{N} \frac{n_j C_{p,j}^{\circ}}{R} \right) \Delta \ln T = \frac{s_0 - s}{R} + n - \sum_{j=1}^{M} n_j \tag{2.2-27}$$

The following functions now become important since mass transfer takes place in this open system.

$\Delta \ln n_j$ (j = 1,…,M)

Δn_j (j = M+1,…,N)

Δn

The computer program developed by the NASA Lewis Research centre [5] will again be used for the thermodynamic calculations. The input file for the flares differs from that of rockets since it has to be considered that ambient air or oxygen can act as oxidiser.

```
! 'problem' MF02:
   problem case=mtv hp  p(atm)=1
            r,eq.ratio=0.5,0.75,0.9,1.0,1.1,1.25,1.5,2.0,3.0
! 'reactants' MF02:
   reac
     fuel= APC N 1. H 4. Cl 1. O 4.          wt%=67  h,cal=-70690. t(k)=298.15
     fuel= RDX C 3. H 6. O 6. N 6.           wt%=20  h,cal=15900. t(k)=298.15
     fuel= Polylite  C 10. H 2.824 O 9.765   wt%=13 h,cal=-107900. t(k)=298.15
     oxid= Lug N 79. O 21.                   wt%=100 h,cal=0.  t(k)=298.15
! 'output' MF02:
   output  siunits
! 'end'  MF02
   end



! 'problem' MF02:
   problem case=mtv hp  p(atm)=1
! 'reactants' MF02:
   reac
     oxid= APC N 1. H 4. Cl 1. O 4.          wt%=67  h,cal=-70690. t(k)=298.15
     fuel= RDX C 3. H 6. O 6. N 6.           wt%=20  h,cal=15900. t(k)=298.15
     fuel= Polylite  C 10. H 2.824 O 9.765   wt%=13  h,cal=-107900. t(k)=298.15
! 'output' MF02:
   output  siunits
```

Figure 2.3-3 Input file of MF02 for NASA Lewis program

Different ratios of propellant : air are used to calculate the combustion products and combustion temperature. A second calculation is done, where the air is taken out of the equation and the oxidising agent in the propellant is considered as the only oxygen supplier. The combustion temperature for each propellant : air ratio is then determined along with the combustion products and other thermodynamic properties of the combustion process. These parameters are as follow:

Table 2-3 Thermodynamic properties calculated for the combustion products of a flare

Thermodynamic Property	***Unit***	***Description***
R,EQ.RATIO		Fuel : Air ratio
PHI,EQ.RATIO		
p	Bar	Pressure
ρ	KG/CU M	Density
H	kJ / kg	Enthalpy
U	kJ / kg	Internal Energy
G	kJ / kg	Gibbs free energy
S	kJ / kg K	Entropy
M	(1/n)	
$(\partial \ln V / \partial \ln p)_T$		
$(\partial \ln V / \partial \ln T)_p$		
Cp	kJ / kg K	Heat capacity at constant p
GAMMAs		Ratio of specific heats at constant entropy

SON VEL	M/SEC	Velocity of sound at T and p

Since there exists no physical parameters to thermochemically describe the countermeasure flare discussed here (unlike solid propellant rockets); these properties shown above are used to describe the flare with its combustion properties. The pressure property is not applicable in this case and will only come into play when measuring the infrared signature at a different altitude, where the light absorbing characteristics of the air differs from zero altitude.

2.3.5. Conclusions

The physical parameters that can be used to describe the infrared signature of the plume from the countermeasure flare are the propellant composition and combustion temperature, which can be written as

$$\textit{Plume signature} = f\{T, \textit{fuel composition}\}$$

From the thermochemical calculations done the thermodynamic properties of the combustion products have to be utilised in the process of simulating the infrared signature as is shown below

$$\textit{Plume signature} = f\{T, \textit{fuel composition, thermodynamic properties}\}$$

Combining the propellant composition and thermodynamic information about the combustion products, there now exists a sufficient description of the plume's infrared signature. The use of the thermodynamic properties of the combustion products in predicting the plume signature will be discussed in more detail in subsequent chapters.

2.4. Nomenclature

2.4.1. Thermodynamic Fundamentals

p	Pressure
V	Volume
n_i	Number of moles of a chemical species
E	Stored energy
U	Internal Energy
KE	Kinetic Energy
PE	Potential Energy
S	Entropy
Q	Heat
T	Temperature
R	Universal gas constant
m	Mass flow
μ_j	Chemical potential
G	Gibbs free energy
F	Helmholtz free energy

2.4.2. Rocket and Flare Thermodynamics

M_r	Molecular weight
H_T^o	Enthalpy at standard state
ΔH_R	Heat of reaction
ΔH_f	Heat of formation
a_{ij}	Kilogram-atoms of element *i* per kilogram-mole of species *j*
b°_i	Kilogram-atoms of element *i* per kilogram of total reactants
λ_i	Langrangian multipliers
h	Specific enthalpy
s	Specific entropy
s_o	specific entropy of reactants
H_j^o	Standard-state molar enthalpy for a species *j* at temperature *T*
I_t	Total impulse
F	Thrust force
t	Time
I_s	Specific impulse
g_o	Gravitational acceleration
v	Velocity
C_p	Specific heat at constant pressure
C_v	Specific heat at constant volume
A	Cross-sectional area
k	Ratio of C_p : C_v
M	Machnumber
A_t	Throat area of the missile
N_i	Number of moles of species *i* in a equilibrium system

2.5. Reference:

1. Smaldone, P.L., *Advanced Composite Materials for a high temperature high pressure Flare,* International SAMPE Technical Conference, Vol. 27, pp. 387-396, (1995).

2. Chastenet, J.C. and Bodart, V., *Signatures Discrétion Contre-mesures,* Revue Scientifique et Technique de la Défense, No.3, (1997).

3. Singh, H., *High Energy Material and Development in India,* Journal of Propulsion and Power, Vol. 11, No. 4, (1995).

4. Penner, S.S., *Thermodynamics for Scientists and Engineers,* University of California, San Diego, Addison-Wesley Publishing Company, California, Chapter 14, (1968).

5. Gordon, S. and McBride, B., *Computer program for Calculation of Complex Chemical Equilibrium Compositions and Applications,* NASA SP-273, 1971, NASA Lewis Research Center, NASA Reference Publication 1311, (1994).

Pectora roborant cultus recti

3. Spectroradiometry

Different types of radiation are encountered and it is common practice to describe these radiations by their respective positions in the electromagnetic spectrum. The wavelengths are arranged according to their wavelength or frequency. All radiations obey similar laws of reflection, diffraction and polarisation.

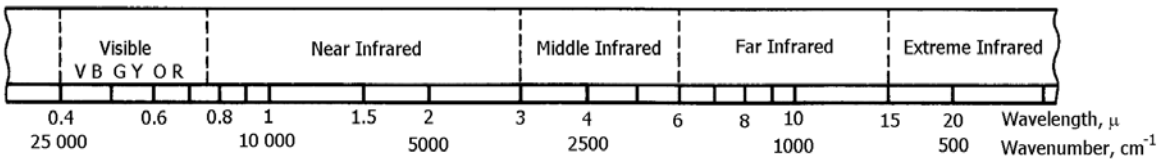

Figure 2.5-1 Electromagnetic Spectrum [1]

The visible and ultra-violet emission seldom exceeds 0.4% of the radiation emitted by combustion processes, while the infrared emission contributes a much greater amount, varying between 2 and 20% of the heat released by combustion[2]. As a consequence, most guidance and targeting systems make use of the infrared region to identify and track potential targets. As was mentioned in the section on flare thermodynamics, modern threats use a method of comparison of different emission regions, thus a flare's emission must compare to that of the target in all electromagnetic regions. However, as a missile tracking a target closes in on a target it often switches to an infrared tracking system. Thus it is important to describe the infrared region of the combustion processes involved when solid propellant burns. The 2 – 5 μm region of the electromagnetic spectrum describes the most distinctive spectral characteristics of a combustion process, because the major resultant combustion species emit energy in this region.

Spectra of atoms consist of sharp lines and those of molecules appear as bands, which are made up of dense lines. These spectra can be used to discriminate between different

atoms and molecules, for different molecular structures result in different molecular spectra. These spectra arise from the emission or absorption of definite quanta of radiation when transitions occur between certain energy levels. [3]

3.1. Radiance spectra

These energy levels represent different orbital states for electrons in atoms. A molecule can also absorb or emit energy in transitions between different electronic energy levels. In addition molecules can change their energy levels in two other ways. These are by changes in the vibrations of the atoms in the molecule and by changes in the molecule's rotation energy. Similar to the electronic transitions, these energy transitions are quantified, so that only certain distinctive levels of vibrational and rotational energy are allowed, which amounts to

$$E_{int} = E_{elec} + E_{vib} + E_{rot} \tag{3-1}$$

with E_{int} as the internal energy of a diatomic molecule. The nomenclature is defined in 3.6. Each electronic state of a diatomic molecule has its own potential energy (E_e) curve. The Schrödinger equation for nuclear motion in a particular electronic state is

$$(\hat{K}_N + E_e)\psi_N \equiv E\psi_N \tag{3-2}$$

where E is the total energy of the molecule, $\hat{K}_N$ the operator for kinetic energy and ψ_N the wave function for nuclear motion. For a diatomic molecule composed of atoms A and B with masses m_A and m_B, the kinetic energy is

$$\hat{K}_N = -\left(h^2 / 2m_A\right)\nabla_A^2 - \left(h^2 / 2m_B\right)\nabla_B^2 \tag{3-3}$$

and $E_e = E_e(R)$, where R is the internuclear distance [4]. The total energy of the molecule is a sum of the translational energy E_{tr}, of the molecule as a whole and the internal energy E_{int}.

$$E = E_{tr} + E_{int} \tag{3-4}$$

The relation for internal energy, which is shown in equation 3-5, is derived from the Schrödinger equation for internal motion.

$$\left[-\left(h^2/2\mu\right)\nabla^2 + E_e(R)\right]\psi_{\text{int}} = E_{\text{int}}\psi_{\text{int}} \tag{3-5}$$

The operator ∇^2 equals $\partial^2/\partial x^2 + \partial^2/\partial y^2 + \partial^2/\partial z^2$, where x, y and z are the coordinates of nucleus to another.

3.1.1. Rotation energy

In the case of a diatomic molecule it is not the motion of an electron around a nucleus, but rather a question of two nuclei rotating around their centre of mass. The rotation of a dumbbell model is equivalent to the rotation of the reduced mass μ at a distance R_e (equilibrium internuclear distance) from the rotation axis. For a rigid rotator the potential energy E_e is zero, reducing the wave equation to [3]

$$\nabla^2\psi_{rot} + \frac{8\pi^2\mu}{h^2}E_{rot}\psi_{rot} = 0 \tag{3-6}$$

This equation can be solved and thus determine the rotational energy of a diatomic molecule as,

$$E_{rot} = \frac{J(J+1)h^2}{2I_e}\ , \quad I_e = \mu R_e^2\ , \quad \mu = \frac{m_A m_B}{m_A + m_B}\ , \quad J = 0, 1, 2, \ldots \tag{3-7}$$

$$E_{rot} = \frac{J(J+1)h^2}{8\pi^2\mu R_e^{\ 2}}\ , \quad E_{rot} = B_e hJ(J+1)\ , \quad B_e = \frac{h}{8\pi^2 I_e} \tag{3-8}$$

I_e is the *equilibrium moment of inertia* and B_e is the *equilibrium rotational constant.* The selection rules for rotational levels is found to be $\Delta J = 0$ or ± 1. An expression for ΔE is then easily derived, between two levels with quantum numbers J and J':

$$\Delta E = h\nu = hB_e[J(J+1) - J'(J'+1)] \tag{3-9}$$

$$\text{thus } \nu = 2BJ \tag{3-10}$$

Spacing between energy levels increases linearly with J. The absorption band of a molecule for pure rotational spectra will consist of lines spaced at an equal distance of $\Delta\nu = \nu - \nu' = 2B$. Pure rotational spectra occur only when the molecule possesses a permanent dipole moment. If the molecule has no dipole moment, its rotation would not result in a change in its electronic field. Rotational energies of polyatomic molecules are more complex, but the principals involved do not differ considerably. The rotational wave function ψ_{rot} depends on the angles θ and ϕ, defining the orientation of the molecule in space, but the vibrational motion is along the internuclear separation.

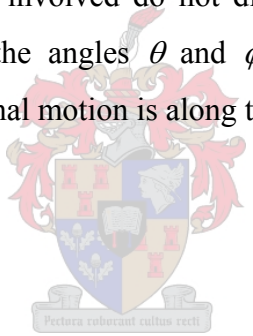

3.1.2. Vibration energy

The vibrational part in the kinetic-energy operator $(h^2/2\mu)\nabla^2$ in (3-5) can be changed to $(h^2/2\mu)\frac{d^2}{dR^2}$. The vibrational wave function ψ_{vib} is a function of R. The vibrational energy can be expressed as $E_{vib} = E_{int} - E_{rot}$ in the Schrödinger equation, yielding the following

$$\left[-\frac{h^2}{2\mu}\frac{d^2}{dR^2} + E_e(R)\right]\psi_{vib}(R) = (E_{\text{int}} - E_{rot})\psi_{vib}(R) \tag{3-11}$$

The potential energy differs for each electronic state. It is also useful to expand the potential energy $E_e(R)$ in a Taylor series about the equilibrium distance R_e.

$$E_e(R) = E_e(R_e) + E_e^{'}(R)(R - R_e) + \tfrac{1}{2}E_e^{''}(R - R_e)^2 + \tfrac{1}{6}E_e^{'''}(R - R_e)^3 + \ldots \qquad (3\text{-}12)$$

When considering a bound state (fig 5-2) with a minimum in E_e at $R=R_e$, the first derivative $E'_e(R_e)$ equals 0. Neglecting the term involving $(R - R_e)^3$ and those with higher powers, the potential energy reduces to

$$E_e(R) \approx E_e(R_e) + \tfrac{1}{2}E_e^{''}(R - R_e)^2 \qquad (3\text{-}13)$$

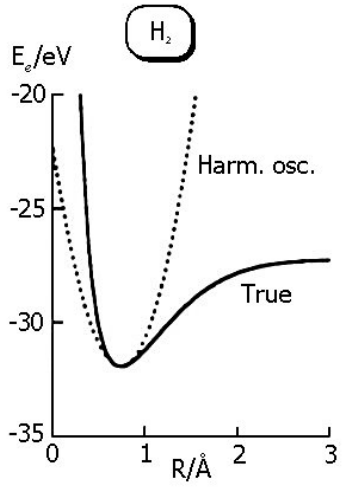

Figure 3.1-1 Harmonic oscillator [4]

In the region near R_e, we find that the electronic energy curve is approximately a parabolic function of $R - R_e$. The quantity $E_e(R_e)$ in (3-12) is a constant for a given electronic state and is called the *equilibrium electronic energy* E_{el}. Now setting $x \equiv R - R_e$, and by rearranging eq. 3-13, the approximate vibrational Schrödinger equation becomes

$$\left[-\frac{h^2}{2\mu}\frac{d^2}{dx^2} + \tfrac{1}{2}E_e^{''}(R)x^2\right]\psi_{vib} = (E_{\text{int}} - E_{rot} - E_{el})\psi_{vib} \qquad (3\text{-}14)$$

which can be written as

$$\frac{d^2\psi}{dx^2} + \frac{8\pi^2\mu}{h^2}\left(E - \tfrac{1}{2}E_e''x^2\right)\psi = 0 \qquad (3\text{-}15)$$

Solving this equation, $E_{vib} = (\upsilon + ½)hv_e$, *with* $\upsilon = 0,1,2,\ldots$

The *equilibrium vibrational frequency* of a harmonic oscillator is then

$$v_e = \frac{1}{2\pi}\left[\frac{E_e''(R_e)}{\mu}\right]^{\frac{1}{2}} \qquad (3\text{-}16)$$

3.1.3. Anharmonicity

The harmonic oscillator is not a good model for molecular vibrations, except at low energy levels, near the minimum of the potential energy curve. It fails to present the fact that a molecule may dissociate if the amplitude of the vibration becomes sufficiently large. The true curve in fig 3-2 and also the curve in fig 3-3 are more realistic and should be used. Two *heats of dissociation* are defined referring to fig 5-3.

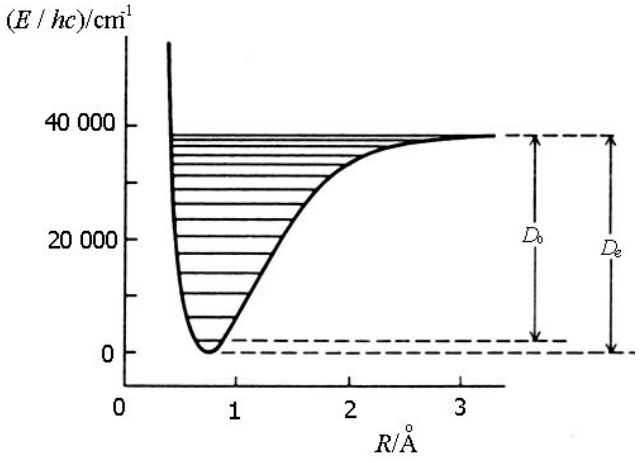

Figure 3.1-2 Ground-electronic-state vibrational levels of H_2 [9]

The *spectroscopic heat of dissociation* D_e, is the height from the asymptote to the minimum. The *chemical heat of dissociation* D_0, is measured from the ground state of the molecule, $\upsilon = 0$, to the onset of dissociation [9]. Therefore it follows from $E_{vib} = (\upsilon + ½)hv_e$ that

$$D_e = D_0 + \tfrac{1}{2}hv_0 \tag{3-17}$$

Actual potential energy curves as in fig 3-3 correspond to anharmonic vibrations. The energy levels corresponding to an anharmonic potential energy curve can be expressed as a power series in $(\upsilon + ½)$,

$$E_{vib} = hv\left[\left(\upsilon + \tfrac{1}{2}\right) - x_e\left(\upsilon + \tfrac{1}{2}\right)^2 + y_e\left(\upsilon + \tfrac{1}{2}\right)^3 - \ldots\right] \tag{3-18}$$

Considering only the first anharmonicity term, with *anharmonicity term,* x_e

$$E_{vib} = hv\left(\upsilon + \tfrac{1}{2}\right) - hvx_e\left(\upsilon + \tfrac{1}{2}\right)^2 \tag{3-19}$$

This entails that the energy levels are not evenly spaced, but lie closer together as the quantum number increases.

3.1.4. Vibration-Rotation interaction

To allow for vibration-rotation interaction another term $-h\alpha_e(\upsilon + ½)J(J + 1)$ has to be added to the energy, where the *vibration-rotation coupling constant* α_e is positive and much smaller than the rotational constant B_e in equation (3-7) [4]. The internal energy of the molecule can thus be summed as follows,

$$E_{\text{int}} = E_{el} + hv\left(\upsilon + \tfrac{1}{2}\right) - hvx_e\left(\upsilon + \tfrac{1}{2}\right)^2 + hB_eJ(J+1) - h\alpha_e(\upsilon + \tfrac{1}{2})J(J+1) \tag{3-20}$$

3.1.5. Rotational and Vibrational spectra

Electronic energy differences are substantially greater than vibrational energy differences, which is in turn greater than rotational energy differences. Rotational spectra

arise from changes in rotational energies. Since these energy transitions are small, the frequencies are quite low and they occur in the far infrared and microwave regions [1]. A diatomic molecule only has pure rotation spectra if it has a non-zero electric dipole moment. This never happens in combustion processes, especially in this case, where the fuel is a complex matrix and the combustion products a mixture of gases.

Changes in a molecule's electronic energy results in absorbency in the ultraviolet region, since the electronic energies involved are so high, which result in high frequencies. A transition with a change in vibrational energy gives the vibration-rotation spectrum of the molecule and absorbs light in the infrared region, from 2-30 μm.

A diatomic molecule only has a vibration-rotation spectrum if the change in dipole moment dp/dR is non-zero at R_e. If a diatomic molecule is homonuclear the dipole change p remains the same; thus a molecule has to be heteronuclear to have an IR vibration-rotation spectrum. The selection rules for diatomic molecule transitions are found to be

$$\Delta J = \pm 1 \tag{3-21}$$

$$\Delta \upsilon = 0, \pm 1, (\pm 2, \pm 3, \ldots) \tag{3-22}$$

Because of selection rule (3-20), it means that there will always be a rotation transition when a vibration transition takes place. Vibrational levels are more widely spaced than rotational levels, therefore the IR vibration-rotation spectrum consists of a series of bands. Each band represents a transition between two particular vibration levels, υ" and υ'. These bands actually consist of a series of lines, each line corresponding to a different change in rotational state. The *band origin* is the hypothetical band where $J = 0$ in both the initial and final states. The wavenumber of the band origin for an absorption transition from level υ" to υ' is

$$\tilde{\nu}_{origin} = 1/\lambda = \nu/c = (E_{\upsilon'} - E_{\upsilon''})/hc \tag{3-23}$$

from equation (3-19) with $J = 0$

$$\tilde{v}_{origin} = \tilde{v}_e(\upsilon' - \upsilon'') - \tilde{v}_e x_e\left[\upsilon'(\upsilon' + 1) - \upsilon''(\upsilon'' + 1)\right] \tag{3-24}$$

$$\tilde{v}_e \equiv v_e / c\,, \qquad \tilde{v}_e x_e \equiv v_e x_e / c$$

The strongest band is the υ = 1 → 0 band, it is called the *fundamental band.* Using (3-24) it is possible to calculate the band origin for each pure vibrational transition.

υ" → υ'	0 → 1	0 → 2	0 → 3
$\tilde{v}_{origin}$	$\tilde{v}_e - 2\tilde{v}_e x_e$	$2\tilde{v}_e - 6\tilde{v}_e x_e$	$3\tilde{v}_e - 12\tilde{v}_e x_e$

The *first overtone* (υ = 0 → 2) is a much weaker band than the fundamental band. Having determined the IR band of origins, it is necessary to deal with the rotational structure of each band. From the selection rule $\Delta J = \pm 1$, each line in the IR band either has a $\Delta J = +1$, or a $\Delta J = -1$, transition. Vibration-rotation with a $\Delta J = +1$, gives the ***R*** branch of the band; transition with a $\Delta J = -1$, gives the ***P*** branch of the IR band.
Again using equation (3-20), but ignoring the vibration-rotation interaction, then

$$\tilde{v} \approx \tilde{v}_e(\upsilon' - \upsilon'') - \tilde{v}_e x_e\left[\upsilon'(\upsilon' + 1) - \upsilon''(\upsilon'' + 1)\right] + \tilde{B}_e J'(J' + 1) - \tilde{B}_e J''(J'' + 1) \tag{3-25}$$

$$\tilde{v} \approx \tilde{v}_{origin} + \tilde{B}_e J'(J' + 1) - \tilde{B}_e J''(J'' + 1) \tag{3-26}$$

For *R* branch lines, $J' = J'' + 1$; thus *v* reduces to,

$$\tilde{v}_R \approx \tilde{v}_{origin} + 2\tilde{B}_e(J'' + 1) \tag{3-27}$$

similarly

$$\tilde{v}_R \approx \tilde{v}_{origin} - 2\tilde{B}_e J'' \tag{3-28}$$

For a more exact representation, the vibration-rotation interaction term can be added. The vibration-rotation interaction constant α_e makes the *R* branch line spacings decrease as *J"* increase and the *P* branch spacings decrease as *J"* increases. A representation of an IR vibration- rotation band can be seen in fig. 3.1-3.

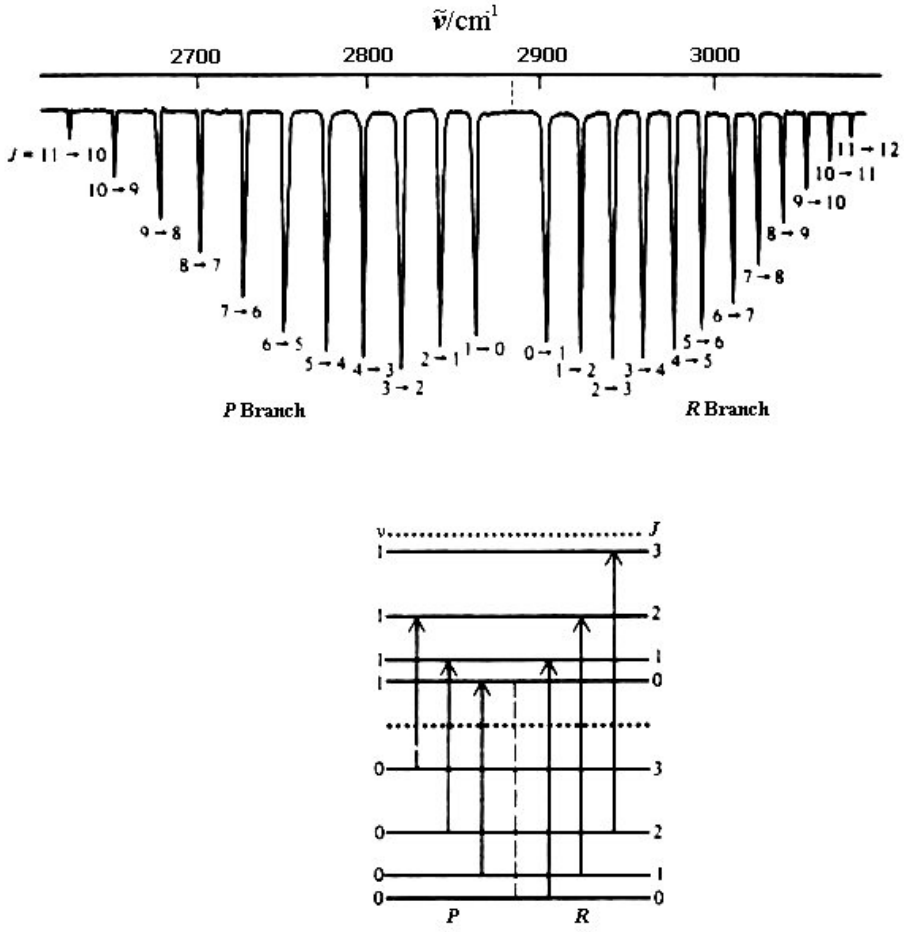

Figure 3.1-3 The gas-phase low-pressure υ = 0 → 1 vibration band of HCl [4]

3.1.6. Spectra of polyatomic molecules

As was stated, IR spectra are the result of a change in dipole moment of a molecule during a vibration-rotation transition. For this reason, there are no vibration spectra from the symmetric vibrations of the molecules of nitrogen, oxygen and argon. Water vapour and carbon dioxide is responsible for the most absorption of radiation by the earth's atmosphere. Both of these molecules are also common products of combustion reactions. Carbon dioxide is a linear polyatomic molecule, with nine degrees of freedom: 3 for translation, 2 for rotation and 4 for vibration [1]. The vibration wave function therefore depends on $3N - 3 - 2 = 3N - 5$ coordinates for a linear molecule, but $3N - 6$ for a non-linear molecule [4].

The four vibrational modes of which two are associated to the same vibration frequency, constitute the fundamental vibration spectra of carbon dioxide.(figure 3-6)

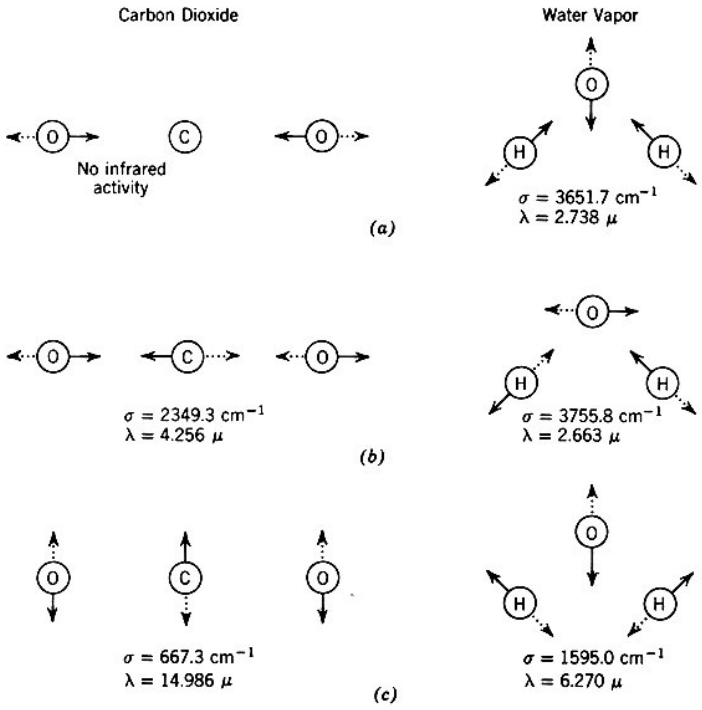

Figure 3.1-4 Vibrational modes of carbon dioxide and water molecules [1]

During the symmetrical stretching mode, the oxygen atoms are symmetrical about the carbon atom, causing no change in the dipole of the molecule and thus no absorption occurs. This vibration is called IR inactive. In another mode the two oxygen molecules move in the same direction with the carbon atom moving the other direction to maintain a fixed centre of gravity. This is the antisymmetrical stretch mode. Both vibrations result in a change of dipole moment and absorption is observed at 4.25μm for the antisymmetrical stretch mode and 15μm for the bending mode. The fourth vibrational mode lies at right angles to that of the bending mode, so that the atoms oscillate in and out of the paper.

The fundamental vibration modes for water are also shown in fig. 3.1-4. Absorption occurs at 2.74, 2.66 and 6.27μ. If a molecule has no symmetry, every fundamental vibration causes a change in dipole moment and a corresponding absorption.
The vibrational spectra observed in practice are always far more complex, with interactions between neighbouring molecules distorting the form of the fundamental vibrations and causing *overtone* bands of the fundamental frequency ($J = 0$) and *combination* bands at various sums or differences of two or more fundamental frequencies [1].

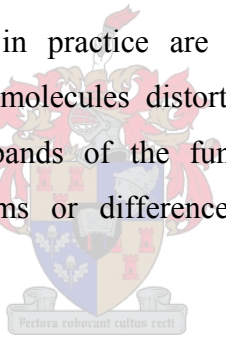

3.2. Blackbody radiation

Kirchhoff introduced his famous law that states that good absorbers are also good radiators. Also introduced was the term *blackbody* to describe a body that absorbs all the incident radiant energy and as a result of this law also acts as the most efficient radiator[1]. The radiation from any system in thermodynamic equilibrium will show a continuous spectrum identical to that of a blackbody at that same temperature [2]. Most small flames show banded spectra, because they are optically thin so that the radiation density is very low for most wavelengths. The flame is losing energy by radiating to the

surroundings and the molecules in the flame tend to lose more energy by radiating energy than by absorption.

It is only because of these optically thin flames that it is possible to utilise the flame spectrum to identify emitting species within the flame. The lack of radiative equilibrium causes difficulties when using the strength of the banded spectrum to estimate the concentration of the species present. The strength of a particular emission band depends on the concentration of the appropriate molecules in excited vibration state and on the rate at which the molecules radiate, or more precisely the *transition probability*.

Planck introduced the fact that molecules' oscillating energies could only increase in discrete quantities *hv*, called the *quantum* of energy.

3.2.1. Thermal Radiation Laws

Planck's law describes the spectral distribution of the radiation from a blackbody as [5]

$$W_\lambda = \frac{2\pi hc^2}{\lambda^5}\frac{1}{e^{ch/\lambda kT}-1}, \tag{3-29}$$

which is usually written as

$$W_\lambda = \frac{c_1}{\lambda^5}\frac{1}{e^{c_2/\lambda T}-1} \tag{3-30}$$

where

W_λ = spectral radiant emittance, W m^{-2} μ^{-1}

h = Planck's constant

k = Boltzmann's constant

The spectral radiance of a blackbody at temperatures ranging from 500°K to 900°K is shown in figure 3.2-1.

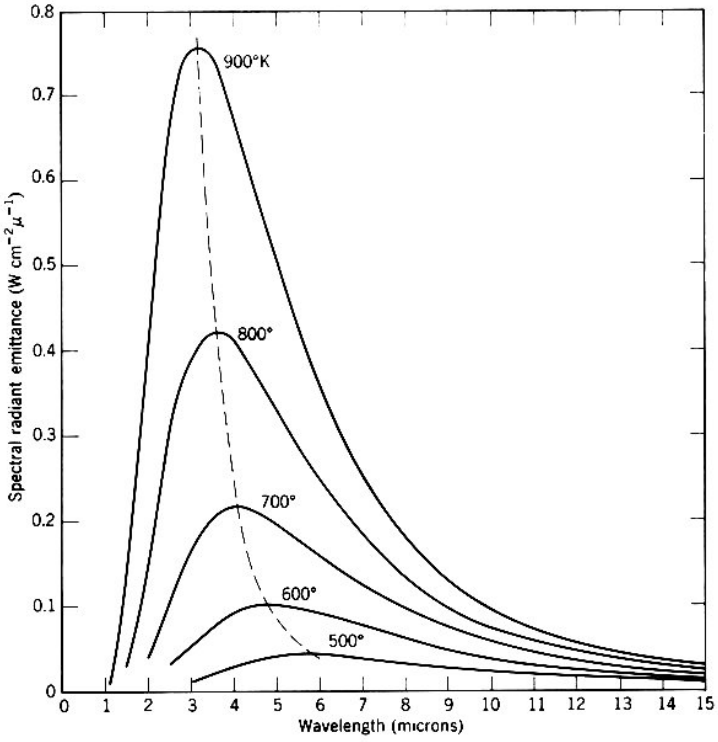

Figure 3.2-1 Spectral radiant emittance of a blackbody at various temperatures [1]

From the figure it is evident that the total radiant emittance, which is proportional to the area under these curves, increases rapidly with temperature. The wavelength of maximum spectral radiant emittance shifts towards shorter wavelengths as the temperature increases. The individual lines never cross; consequently the higher the temperature the higher the emittance at all wavelengths [1].

The form of Planck's law expresses the flux within a spectral interval 1μm wide, radiated into a hemisphere by a blackbody having an area of 1cm^2. The significance of the 1μm spectral interval is of use; the value of an ordinate in fig. 3.2-1 is proportional to the radiant emittance at that wavelength. The absolute value depends on the width of the interval used. Thus a value for spectral radiance is meaningless if the spectral interval is

not specified. Generally radiometric measurements and calculations are referred to as a spectral interval equal to the unit in which the wavelength is measured.

Integrating Planck's law over wavelength limits from zero to infinity gives an expression for radiant emittance, i.e. the total flux radiated to a hemisphere above a blackbody of 1cm^2 in area. This is known as the *Stefan-Boltzmann law,*

$$W = \frac{2\pi^5 k^4}{15c^2h^3}T^4 = \sigma T^4 \tag{3-31}$$

where

W = radiant emittance, [W m^{-2}]

σ = Stefan-Boltzmann constant.[W m^{-2} K^{-4}]

The phenomenon seen in fig. 3.2-1 is restated by this expression in that the radiant emittance increases rapidly; from the Stefan-Boltzmann law it is seen that this increase is proportional to the fourth power of the temperature.

If Planck's expression, equation (3-29), is divided by hc/λ, which is the energy of one photon, the result is the spectral radiant photon emittance,

$$Q_\lambda = \frac{2\pi c}{\lambda^4}\frac{1}{e^{ch/\lambda kT}-1} \tag{3-32}$$

where Q_λ = spectral radiant photon emittance, photon s^{-1} m^{-2} μ^{-1}. The Stefan-Boltzmann law becomes

$$Q = \frac{2\pi k^3}{c^2h^3}\frac{2\pi^3}{25.79436} = \sigma' T \tag{3-33}$$

where

Q = radiant photon emittance, photon s^{-1} m^{-2}

σ' = 1.52041x10^{11} s^{-1} m^{-2} °K^{-3}.

Therefore the rate at which photons are emitted from a blackbody varies as the third power of its temperature, in contrast with the radiant flux.

3.2.2. Emissivity and Kirchhoff's Law

A factor, ε, is introduced to describe a sources that are not a blackbody. This factor ε, called the *emissivity*, is given by the ratio of the radiant emittance W' to that of a blackbody at the same temperature, W:

$$\varepsilon = \frac{W'}{W} \tag{3-34}$$

Three types of sources can be distinguished by the way spectral emissivity varies:

- A blackbody for which $\varepsilon(\lambda) = \varepsilon = 1$
- A *graybody* for which $\varepsilon(\lambda) = \varepsilon =$ constant, but less than unity
- A *selective radiator* for which $\varepsilon(\lambda)$ varies with wavelength.

Figure 5-7 shows the spectral emissivity and spectral radiant emittance for each type of source. A blackbody radiates more flux, either in total or in a certain spectral interval than any other type of source at the same temperature, thus providing a limiting envelope for other types of sources.

As can be seen from fig. 3.2-2 a selective radiator can act as a graybody over a limited spectral interval.

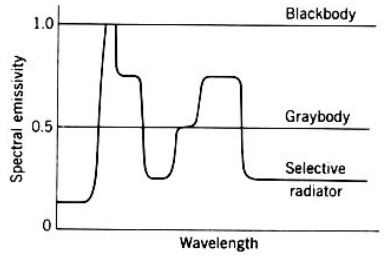

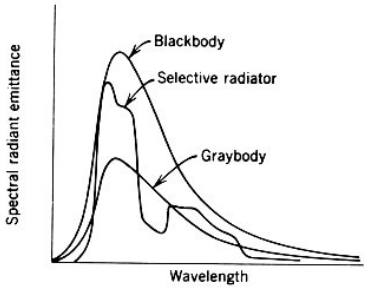

When radiant energy is incident on a surface, three processes can occur:

- a fraction α, may be absorbed
- a fraction ρ, may be reflected
- and a fraction τ, may be transmitted.

Figure 3.2-2 Spectral emissivity and spectral radiant emittance of three types of radiators [1]

Since energy must be conserved, it follows that

$$\alpha + \rho + \tau = 1 \tag{3-35}$$

Since a blackbody absorbs all incident radiant energy, it follows that $\alpha = 1$ and $\rho = \tau = 0$. At a given temperature the ratio of radiant emittance to absorptance is a constant and that it is equal for the radiant emittance of a blackbody at that temperature. Known as *Kirchhoff's law*, it states

$$\frac{W'}{\alpha} = W \tag{3-36}$$

Combining (3-31) and (3-34) gives

$$\frac{\varepsilon\sigma T^4}{\alpha} = \sigma T^4 \tag{3-37}$$

it follows that $\varepsilon = \alpha$ at a particular wavelength. Thus the emissivity at a given temperature is numerically equal to its absorptance at that temperature. This is an important property, since it is often easier to measure reflectance than to measure emissivity directly.

Kirchhoff's law can also be written as [6]

$$\alpha_\lambda E = \varepsilon_\lambda W \tag{3-38}$$

Here the energy absorbed per unit area and unit time is called the irradiance (E).

The conditions under which a gas radiates like a blackbody have been studied by a number of people [7,8]. Gases may act as spectral radiators or band radiators in a certain wavelength region. If the thickness of the layer of gases is increased, there will be a proportional increase in the intensity of the absorption. Because of self-absorption the stronger lines in the absorption band will be restrained; the emissivity cannot exceed 1 and for thermal equilibrium in flame gases the intensities cannot exceed that of a blackbody at the flame temperature. Weaker lines in the absorption band will be

unaffected by the increase in self-absorption and the intensity will increase proportionally with the thickness of the gas body.

The Bunsen flame is a simple example of a burning gas. In this flame, carbon dioxide and water vapour show the strongest absorption bands, and it both of these molecules are also the main products of combustion. In the 2-5μ band, water vapour absorption can be seen around 2.7μ and CO_2 around 2.7μ and 4.4μ. Consequently, if the spectral absorption of a flame is known for a particular set of conditions, the blackbody radiation law can be used to calculate its spectral radiance.

3.3. Radiation Transport

Before an infrared signature reaches the infrared sensor, the radiant flux is selectively absorbed by atmospheric gases, scattered away out of line of sight by small particles. For energy transmitted from a body, the path through the atmosphere can be expressed as

$$\tau = e^{-(a+\sigma)x} \tag{3-39}$$

where x is the path length [12]. The attenuating effect can be separated into two processes,

$$\tau_a = e^{-ax}, \qquad \tau_\sigma = e^{-\sigma x} \tag{3-40}$$

where a is the *absorption coefficient* and σ is the *scattering coefficient*. The absorption is due to gaseous molecules, and the scattering coefficient accounts for scattering by gaseous molecules, haze and fog. Both a and σ can be expected to vary with wavelength. In the infrared portion of the spectrum, absorption is a far more serious problem than scattering [12].

Radiation data, such as emission, absorption and scattering coefficients determine emission and absorption spectra. The spectral radiant emittance W_λ, is the most

important property concerning radiation transport. The total radiance in a direction ϑ is defined as,

$$W(\vartheta) = \int_0^\infty W_\lambda(\vartheta) d\lambda \tag{3-41}$$

The radiance represents the properties of the whole medium; how much is emitted, absorbed or scattered in the surrounding medium before it reaches the control volume. The resultant emittance consists of the following:

$$W_\lambda = W_{emission} - W_{absorption} + W_{scattering\ in} - W_{scattering\ out} \tag{3-42}$$

The radiant flux is a property dependent on time, but since the process characteristic velocity is the speed of light, the radiation field adjusts almost immediately, so that the explicit time variation could be ignored. The decrease in radiance, because of absorption, can be expressed as follow [13].

$$W_{absorption} = a_\lambda(x) W_\lambda(x) dx \tag{3-43}$$

As with the scattering and absorption coefficients, the parameter x, denotes the path of the radiance. Scattering and absorption both have an attenuating effect on the radiance as was mentioned above.

$$W_{scattering\ out} = \sigma_\lambda(x) W_\lambda(x) dx \tag{3-44}$$

Emission incident on the medium increases the radiance detected,

$$W_{emission} = \varepsilon_\lambda(x) W_\lambda(x) dx \tag{3-45}$$

The gain in intensity due to scattering into the ray path is defined with use of the phase function ϕ, where the phase function is described as the scattered radiance in a certain direction divided by the radiance for isentropic scattering [14].

$$W_{scattering\ in} = \frac{\sigma_\lambda}{4\pi} \int_0^{4\pi} W_\lambda(x, \vartheta_i) \phi(\lambda, \vartheta, \vartheta_i) d\vartheta_i \tag{3-46}$$

The resultant equation for radiation transfer is then,

$$\frac{dW_\lambda}{dx} = -a_\lambda W_\lambda(x) - \sigma_\lambda W_\lambda(x) + \varepsilon_\lambda W_\lambda(x) + \frac{\sigma_\lambda}{4\pi}\int_0^{4\pi} W_\lambda(x,\vartheta_i)\phi(\lambda,\vartheta,\vartheta_i)d\vartheta_i \tag{3-47}$$

The radiant energy flux density $F_{\lambda,n}$ crossing an area element dA, is a result of intensities from all directions, i.e. $F_{\lambda,n} = F_{\lambda,x} + F_{\lambda,y} + F_{\lambda,z}$. Considering an angle θ between the ray direction ϑ and the normal to the surface n,

$$F_{\lambda,n} = \int I_\lambda(\vartheta)\cos\theta d\vartheta \tag{3-48}$$

where I_λ is the incident ray's intensity [13]. Oran and Boris consequently derived a formula for flux change from the equations in this section that may be used in Computational Fluid Dynamics type calculations: [14, 15]

$$\nabla \cdot F_n = 4\pi\int_0^\infty \left(-a_\lambda W_\lambda(x) - \sigma_\lambda W_\lambda(x) + \varepsilon_\lambda W_\lambda(x) + \frac{\sigma_\lambda}{4\pi}\int_0^{4\pi} W_\lambda(x,\vartheta_i)\phi(\lambda,\vartheta,\vartheta_i)d\vartheta_i \right) d\lambda \tag{3-49}$$

Both the scattering and absorption coefficients are dependent on the atmospheric properties. Therefore an adequate knowledge of the atmosphere surrounding the flame and in the path of detection, should be known. After these coefficients are known the equations (3-44) and (3-46) can be solved to determine the radiance from the exhaust gases of a rocket engine or flare.

3.4. Measurement of Irradiation

The radiant flux density of a flame, which consists of heated combustion products, can be measured over a distance by a spectroradiometer. The equipment contains collecting optics, spectral filtering devices and a detector set. The voltage change over the detector is directly proportional to the incoming flux density at a given wavelength, which is proportional to the energy at the flame. A material or gas with a temperature sensitive

property is used to generate a voltage signal, when there is a change in the energy reaching the detector [14, 12].

When the radiant energy is exchanged between two bodies, which do not closely face each other, the energy transfer is determined by the geometrical configuration. Consider two elements dA_{source} and $dA_{detector}$, with ϑ as the solid angle into which the flux is radiating. The radiating source is also tilted at an angel θ to the direction of the line-of-sight between the source and the detector as in fig. 3.4-1.

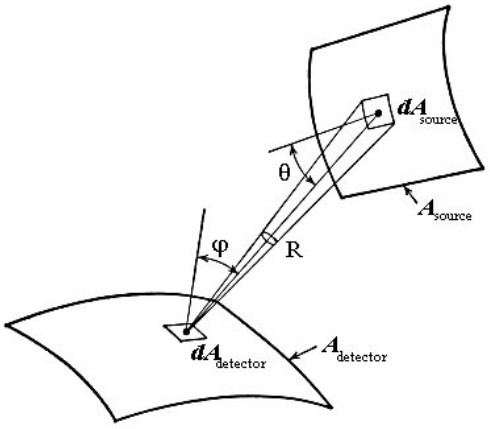

Figure 3.4-1 Field of View or geometrical setup

From the figure an equation can be deducted, showing that the radiance is independent of the direction, as show in equation 3-50. This is true if the source is perfectly diffuse or *Lambertian* [16].

$$W_\lambda = \frac{d^2 F_\lambda}{dA_{\det ector} \cos\theta \, d\vartheta} \tag{3-50}$$

The irradiance is the radiant flux density incident upon a surface,

$$E_\lambda = \frac{dF_\lambda}{dA_{\det ector} \cos\varphi} \tag{3-51}$$

thus the irradiance incident on the detector area can now be expressed as the radiation from the source.

$$E_\lambda = \Omega_{\text{det}\,ector} W_\lambda \tag{3-52}$$

Here $\Omega_{detector}$ is the *view-factor* or the field-of-view (FOV), of the detecting system. This factor can be expressed as follow [12].

$$\Omega_{\text{det}\,ector} = \frac{1}{\pi r^2} \int_{Asource} \cos\theta \cos\varphi \, dA_{source} \tag{3-53}$$

If the source is smaller than the FOV of the detection system, the solid angle is replaced by the ratio of the source area divided by the distance between the detector and the source, *R*, to give:

$$E_\lambda = \frac{A_{source}}{R^2} W_\lambda \tag{3-54}$$

In the equations used above, it is assumed that the radiance measured from the source is without losses. The background and ray path generate enough energy to influence the measured irradiance. Furthermore the atmosphere also acts as a filter, because of absorption and scattering which attenuates the radiation signal, which needs to be accounted for.

3.5. Conclusion

The study of flame spectra can predict some of the intermediary species, which are present and about the methods by which they are formed, removed and give up energy. In order to understanding the complexities of the problem, care would need to be taken in the interpretation of the observational medium and surroundings.

It is possible to decipher the structure of simpler molecules using their respective infrared spectra. More complicated fuel compositions made up of complicated polymers cannot be evaluated in this way. Major infrared bands can be identified, but not to the extent that will make it possible to identify specific combustion reactants. It is clear that there exists a relationship between the infrared irradiance of the combustion products and their reactants. A model incorporating this relationship needs to be developed to properly predict the irradiance spectra for combustion flames.

3.6. Nomenclature

3.6.1. Radiance spectra

E_{int}	Internal energy of a diatomic molecule
E_{elec}	Electronic energy of a diatomic molecule
E_{vib}	Vibrational energy of a diatomic molecule
E_{rot}	Rotational energy of a diatomic molecule
E_e	Potential energy of a diatomic molecule
E_{el}.	Equilibrium electronic energy
E	Total energy of a diatomic molecule
$\hat{K}_N$	Operator for kinetic energy
ψ_N	Wave function for nuclear motion of a diatomic molecule
ψ_{vib}	Vibrational wave function
ψ_{rot}	Rotational wave function
m_A	Atomic mass
R	Internuclear distance
R_e	Equilibrium internuclear distance
E_{tr}	Translational energy of a diatomic molecule
h	Planck's constant
μ	Reduced mass
I_e	Equilibrium moment of inertia
B_e	Equilibrium rotational constant
J	Rotational quantum number
ν_e	Equilibrium vibrational frequency
ν	Vibrational frequency
D_e	Spectroscopic heat of dissociation
D_0	Chemical heat of dissociation
x_e	Anharmonicity term
υ	Energy level number ($\upsilon = 0$ is the ground state for the molecule)
α_e	Vibration-rotation coupling constant
dp/dR	Dipole moment

3.6.2. Blackbody radiation

W_λ	Spectral radiant emittance
h	Planck's constant
k	Boltzmann's constant
T	Temperature
W	Radiant emittance
σ	Stefan-Boltzmann constant
Q_λ	Spectral radiant photon emittance
Q	Radiant photon emittance
λ	Wavelength
ε	Emissivity
α	Coefficient of absorption
ρ	Coefficient of scattering
τ	Coefficient of transmission
E	Irradiance
$F_{\lambda,n}$	Radiant energy flux density
I_λ	Incident ray's intensity
$\Omega_{detector}$	view-factor or the field-of-view (FOV)

3.7. Reference:

1. Hudson, R.D., *Infrared System Engineerin*g, John Wiley & Sons, New York, Chapter 2, (1969).

2. Gaydon, A.G., *Spectroscopy of Flames,* Chapman & Hall Ltd., London, Chapter 9, (1957).

3. Moore, W.J., *Physical Chemistry,* Longmans, Green and Co., London, 3rd edition, Chapter 11, (1960).

4. Levin, I.N., *Physical chemistry,* McGraw-Hill Inc., New York, 4th edition, Chapter 21, (1995).

5. Planck, M, *Theory of Heat Transfer,* New York: Dover, (1959).

6. Wyatt, C.L., *Radiometric System Design,* Macmillan Publishing Company, New York, Chapter 10, (1987).

7. Finkelnburg, W., *Conditions for Blackbody Radiation of Gases,* J.Opt.Soc.Am., Vol. 39-2, No. 185, (1949).

8. Bell, E.E., Burnside and P.B., Dickey, F.P., *Spectral Radiance of Some Flames and heir Temperature Determination,* J.Opt.Soc.Am., Vol. 50-12, No. 1286, (1960).

9. Gaydon, A.G., *Spectroscopy of Flames,* Chapman & Hall Ltd., London, Chapter 1, (1957).

10. Weissman et al., *J. Chem. Phys.,* Vol. 39, No. 2226, (1963).

11. Hudson, R.D., *Infrared System Engineerin*g, John Wiley & Sons, New York, Chapter 4, (1969).

12. Simon, I., *Infrared Radiation,* E. van Nostrand Company, Inc., New Jersey, Chapter 6, (1966).

13. Kondratyev, K. Ya., *Radiation in the atmosphere,* Academic Press, Inc., New York, Chapter 1, (1969).

14. Roodt, J., *The Prediction of the emission spectra of solid rocket propellants*, Ph.D. dissertation, Dept. Chemical Engineering, University of Stellenbosch, Chapter 7, (1998).

15. Oran, E.S. and Boris, J.P., *Numerical Simulation of Reactive Flow,* Elsevier, New York, Chapter 12, (1987).

16. Pinson, L.J., *Electro-Optics,* John Wiley & Sons, New York, Chapter 2, (1985).

4. Spectroradiometric Measurements

This chapter is included as background and describes the measurement process in attaining the infrared emission spectra used in this study.

4.1. Measurement Locations

The Infrared group of the Defencetek division, CSIR, did the measurements. The data that was recorded for both the solid propellants and the flares were done by Roodt[1] and his team. Two venues were used for the measurements. Both these sites were located in a winter rainfall area, in the area of 33°S and 18°E. The first site was located 1 km from the ocean at an abandoned airstrip. On this site, proper range measurements could be made and an infrastructure existed. Power was supplied and access control could be applied for safety reasons. Several conditions need to be complied to and recordings need to be taken, for correct measurements such as [1]

- Measurements were taken at least 45 minutes after sunset.
- The measurements were performed against a clear sky background.
- Humidity and temperature recordings were made, to simulate the atmospheric absorption band for calculations.
- The radiometer was calibrated before and after tests, to determine the response function change over the measurement period.

Measurements were started at a distance of 500m, but were then reduced to 350m, 250m and then 200m. Operational knowledge was gained during each firing, so that the expected radiance levels could be predicted with success. The humidity of the atmosphere caused problems for water started condensing on the optical system of the radiometer, when the wind was blowing from the ocean.

A second site was decided upon after the problems with the humidity. This site, a runway, was located 10km from the ocean and just above sea level. At this location the optical instruments were not influenced by the humidity. All the conditions and necessary recordings were met. The test was again done against a clear night sky, with the exhaust plume facing downwind, to cut down a build up of combustion products and smoke on the measurements. The atmospheric path between the radiometer and the component being tested, was close to horizontal. The radiometer was about 1.1m high and the test unit 0.2 degrees higher in the line of sight.

Since 1994 it was possible to record the infrared images of the plumes in the 2-5μm region from 50m. The humidity, barometric pressure and temperature were continuously recorded at this test unit, which was situated just outside of the field of view (FOV) of the spectroradiometer. The data could then be used to adjust the spectral measurements, by compensating for certain atmospheric changes over the span of a measurement period. A testing period may run from 21:00 to 3:00, during which time the atmospheric properties may change drastically.

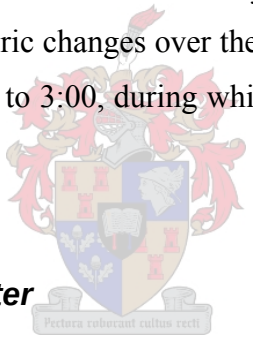

4.2. The Spectral Radiometer

The spectral radiometer used in the setup, employ reflective collective optics in a Newtonian telescopic configuration. Irradiation enters the setup and is reflected from the primary mirror to the secondary mirror. The secondary mirror in turn, redirects the incoming irradiation towards a field stop aperture, in front of a circular variable filter (CVF). The CVF filters the irradiation before it passes through a mechanical frequency modulator (chopper). The irradiation is then reflected by a third mirror onto a liquid nitrogen cooled indium-antimonide (InSb) detector.

The field stop aperture determines the field of view (FOV) of the system. The frequency modulator, the CVF's rotation speed and the field stop aperture are controlled by computer. The signal produced by the detector is conditioned and passed through an

analogue to digital converter to a central computer, from where the signal is displayed and processed. A diagram showing the layout of the spectral radiometer is shown in fig.4.2-1 [1].

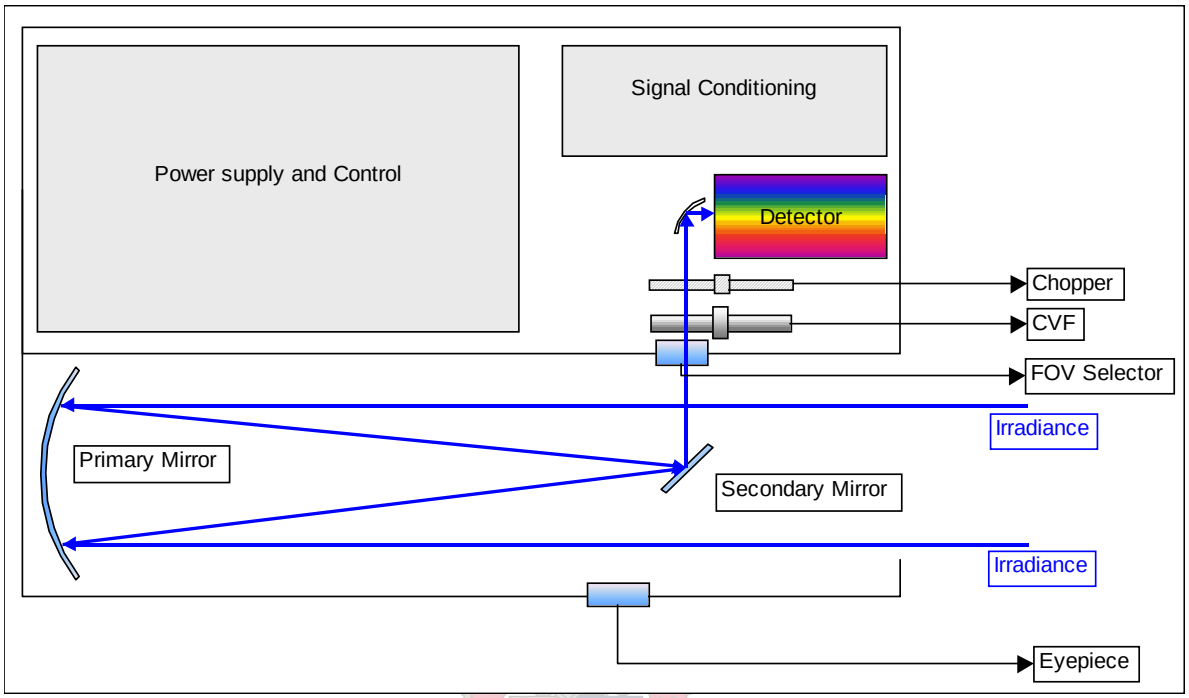

Figure 4.2-1 A schematic diagram of the spectroradiometer [1]

The signal output received by the computer is in radiometer units, scaled linearly between 0.001 and 10. Signals with an output smaller than 0.001 fall within the noise limit of the detector system. The optimal modulator frequency for this detector set was determined in the laboratory and that setting was used for all measurements. The CVF has 320 filter positions, but only 146 of these positions fall in the detection range of the InSb detector. The rotation time for the CVF was set at 0.5 seconds, which means that two to four full spectra can be recorded during one firing. The aperture stop was set to enable a FOV of 28μsr for most measurements. [1]

4.3. Processing of Recorded Data

Data captured at both the mentioned venues are used in this study. The data was captured at different distances, reporting a difference in the intensity of the spectra recorded. This can be solved by using a spectral (wavelength dependent) distance scaling function

$$S = \frac{R_x^2 \tau_y A_{py}}{R_y^2 \tau_x A_{px}} \tag{4-1}$$

where R is the distance at which the measurement was done, A represents the projected areas of the plume in the field of view at that specific distance and τ is the atmospheric transmittance for each recording. Each spectral point, outside the main absorption bands, is then multiplied by S [1].

4.3.1. Atmospheric Correction

The atmospheric correction of the signal, caused by transmittance through the atmosphere, can be done using a transmittance code such as LOWTRAN 7 or MODTRAN [2]. These models are complex and require a large amount of input information to adequately model a given situation. Considering the measurements were done over a horizontal path, the most important parameters are surface meteorological observations, such as the temperature, humidity, height above sea level, height above ground level, barometric pressure, line of sight range, and the aerosol concentration. Being close to the ground, the amount of water precipitated (i.e. humidity), strongly regulates the atmospheric transmittance process. This in turn effects the transmission of radiant flux through the atmosphere [3].

In the 2-5 μm spectral band strong absorption by water and carbon dioxide molecules make the calculation complex [4]. The effect of the absorption by H_2O and CO_2 can be seen in fig. 4.3-1. The absorption by these molecules causes the transmittance to approach zero, which results in the correction factor S, becoming large, due to division by small numbers.

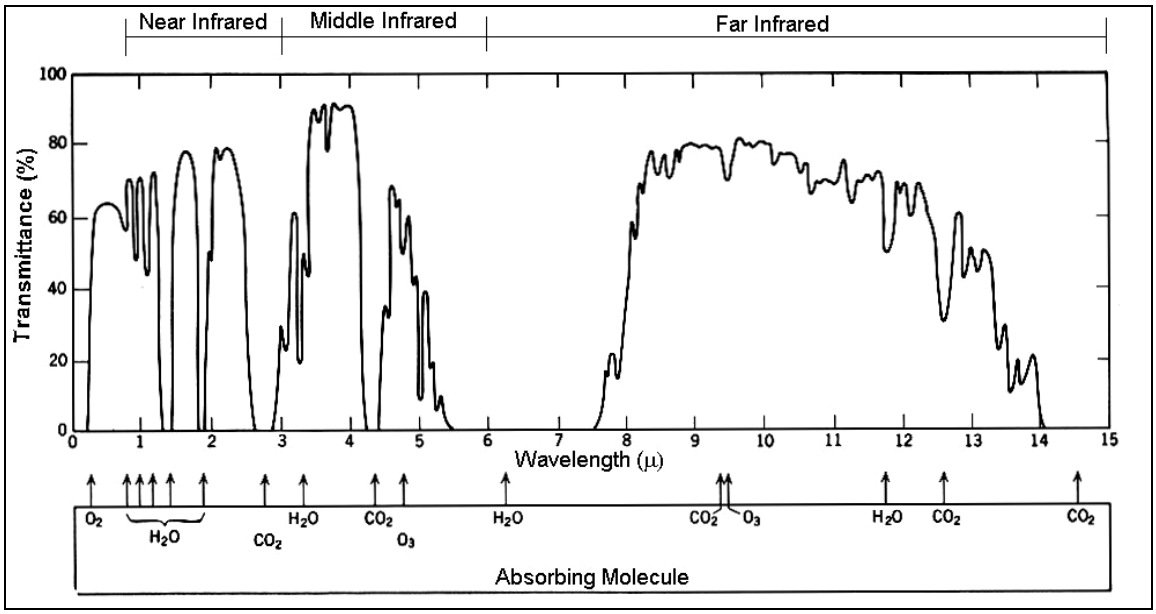

Figure 4.3-1 Transmittance of the atmosphere at sea level containing 17mm of precipitated water [4]

Another way of solving this problem is by using the atmospheric extinction (discussed in the previous chapter). It was seen that the attenuating effect of the atmosphere on transmittance could be expressed as

$$\tau = e^{-(a+\sigma)x} \tag{3-36}$$

where x is the path length [5]. The two factors, a and σ, can be combined to give the extinction coefficient γ, which can then be used as follow

$$F_R = F_{source} e^{-\gamma R} = F_{source} \tau_R \tag{4-2}$$

with F as radiation flux and R as the range of the measurement.

4.3.2. Area Correction

This parameter is calculated by comparing the projected FOV for each path length, and the portion of the plume subtending this area. Close to the nozzle of a rocket motor, the plume consists of a core of hot unmixed gases, enveloped in a thin mixing region, where the combustion products mix with the surrounding atmosphere. In the case of a "brick

type" flare, the core of hot unmixed gases surrounds the whole flare. This is however not the case when a static test is done. The flare is static when ignited, therefore the combustion products accumulate around the flare and move upward.

An afterburning flame can develop in the plume, if at least a moderate amount of oxidiser is present in the flare. According to Souletis and Chastenet [6], the afterburning flame of a rocket motor is dependent on the motor working parameters, but is also connected to the propellant composition. The afterburning flame raises the temperature in that region of the plume, consequently increasing the radiance produced. In the case of flares, no motor parameters exist, which indicates that afterburning is dependent on the propellant composition [7].

At a certain point downstream, in the plume of rocket engines, the combustion products start to mix with the atmosphere; a decrease of gas speed and an expansion to atmospheric pressure is noticed. Because of this rapid cooling of the plume species and condensation, the plume signature approaches a graybody at a much lower temperature than that of the chamber flame temperature [1]. In practice, flares will also move through the atmosphere, but will not be propelled and burn at atmospheric pressure. Mixing will occur, with the same cooling results as with a rocket engine, but at a slower rate.

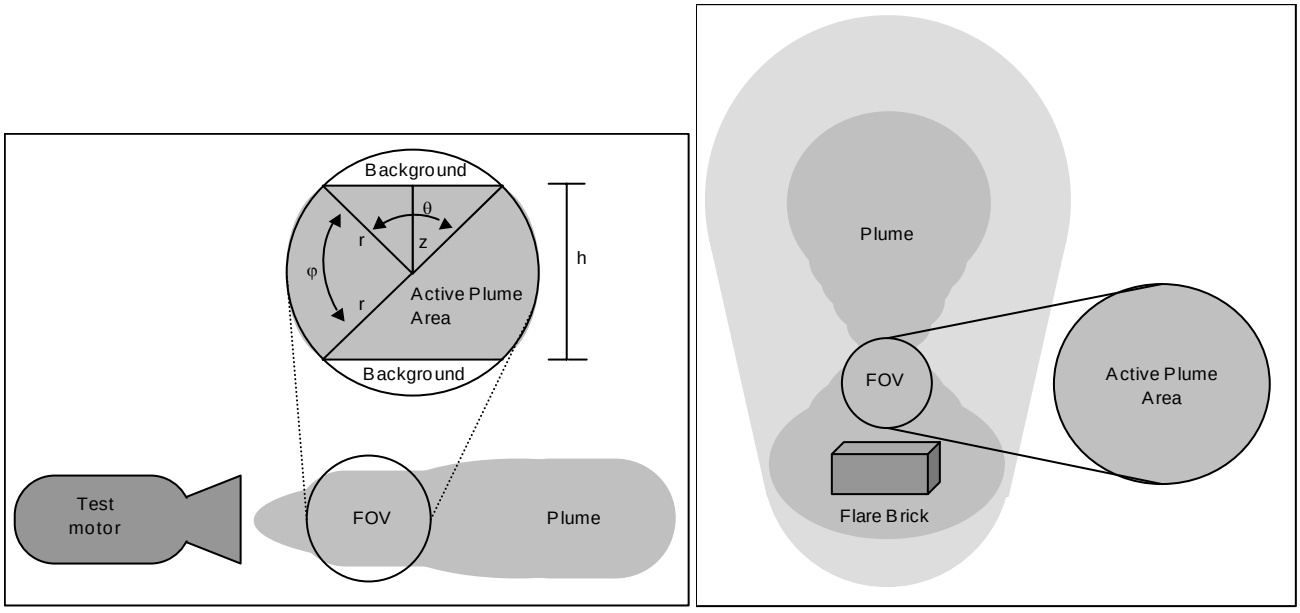

Figure 4.3-2 Calculation of the plume area subtended by the radiometer FOV

It is assumed that the plume will fill a portion of the FOV as in fig. 4.3-2. The "background" is those areas not filled by a significant radiative part of the plume. It is further assumed that the background does not contribute energy to the irradiance measured, since it is a clear, cold night sky. The circle shows the FOV of the radiometer, while the grey part is the portion of the plume filling the FOV.

The line *z* forms the base of an isosceles triangle with side length *r*, which is the radius of the FOV. The height of the triangle is *h/2*, half the height of the plume. The angle subtended by the triangle is denoted by θ. The segment of the circle that forms the leftmost limit of the plume area is subtended by angle φ. If A_θ is the area of the isosceles triangle and A_φ the area of the left active circle segment, the total active plume area A_T is: [1]

$$\begin{aligned} A_T &= 2\left(A_\theta + A_\varphi\right) \\ &= 2\left(\frac{hz}{4} + \int_0^{\varphi'}\int_0^{r'} r\,dr\,d\varphi\right) \\ &= 2\left(\frac{h\cdot 2\sqrt{r'^2 - h^2/4}}{4} + \int_0^{\varphi'}\int_0^{r'} r\,dr\;d\varphi\right) \end{aligned}$$

$$\text{with } \varphi' = \pi - \arccos\left(1 - \frac{z^2}{2r'^2}\right) \qquad (4\text{-}3)$$

The distance between the radiometer and the plume determines the radius of the FOV. A FOV of 28μsr yields a FOV radius of 0.6m at a distance of 200m.

The firing and subsequent spectral measurements of the flares differed from that of the rocket engines. The flare was mounted on a grill and then ignited. There was no air movement over the flare brick, causing the combustion products and smoke to accumulate above the flare. The radiometer FOV was aimed at a space right above the brick; hence the FOV was filled completely with the plume of the burning flare.

4.3.3. Scaling the Data

The scaling of measurements on some data sets, according to equation (4-1), correlated well with the recorded signatures at specific distances for specific motor designs and propellant compositions. The noted differences were within the range of the variation between measurements for a specific session. This was only true for range differences smaller than 50m. For measurements done at distances greater than 250m, it was difficult to reconstruct the IR spectra of stealth formulations, since the signature was polluted by radiometer noise. Only IR spectra measured at distances between 150m and 250m were used, which was then scaled to 200m.

4.4. Spectral Recordings of Solid Rocket Propellants

Eighteen different solid propellant rocket fuels were fired and their different IR signatures were recorded. Two classes of fuels were examined, of which 6 were double-base and 12 were composite fuels. For each fuel fired, a set of recordings was done to create a set of signatures. These signatures are not identical and showed some deviation from the average measured signal.

These signatures are presented in the following figures. The mean for each set of signatures were calculated and then plotted with the deviation band. The standard deviation was calculated for each spectral point and then added to that spectral point yielding the upper deviation line and subtracted to give the bottom deviation line. *DB1* is an example of a double-base solid rocket propellant and *C1* an example of a composite propellant.

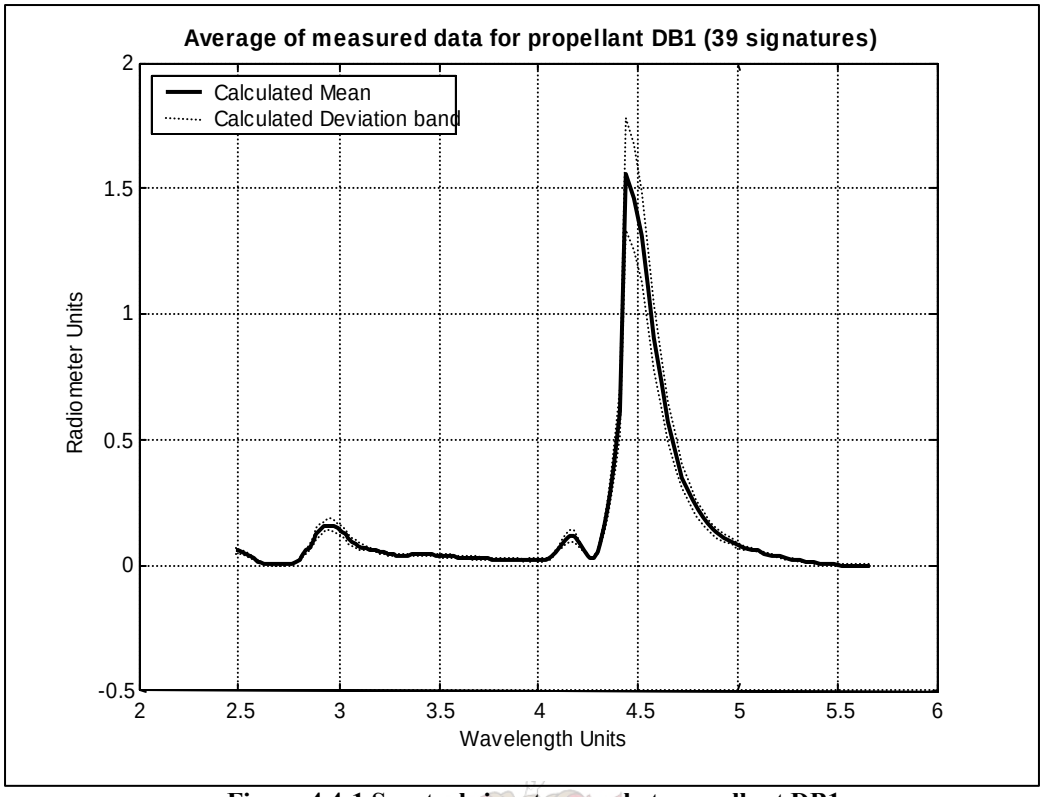

Figure 4.4-1 Spectral signature rocket propellant DB1

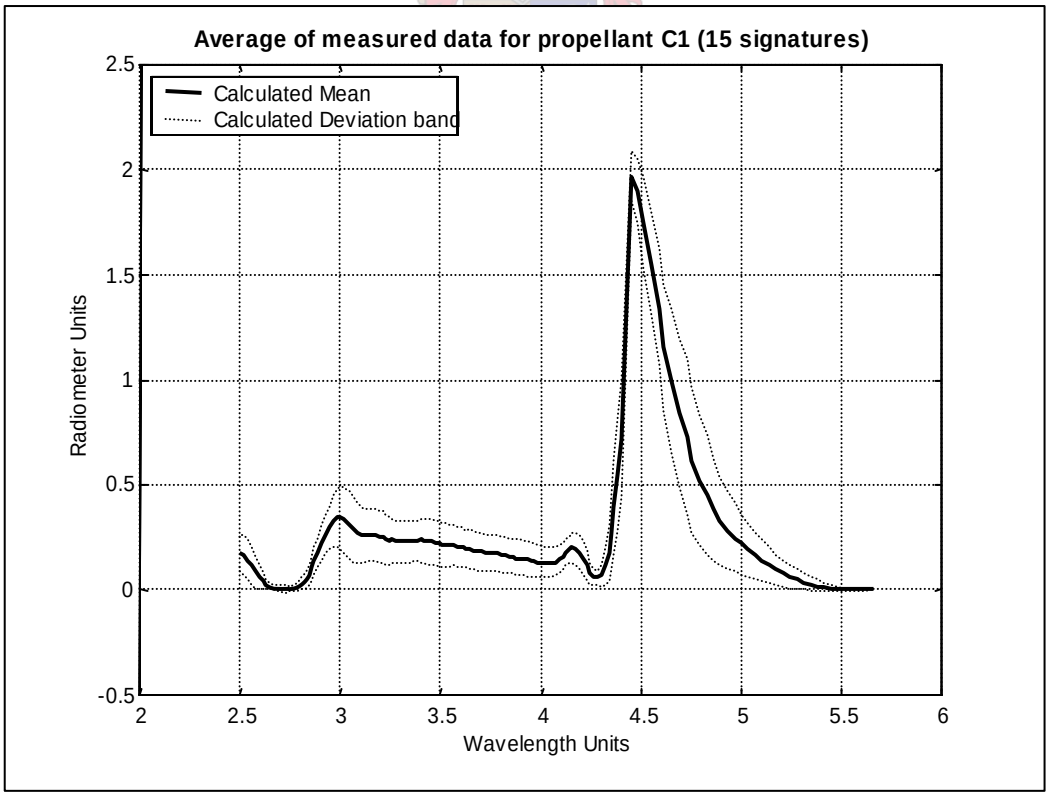

Figure 4.4-2 Spectral signature rocket propellant C1

The spectral signatures for all the solid rocket propellants are recorded in Appendix B. From the figures it is clear that each propellant has its own specific irradiance spectral signature. It was shown earlier that the plume of a rocket engine is dependent on the chemical composition of the fuel burnt as well as several motor working parameters; the aim is to find a model predicting these spectra using these parameters.

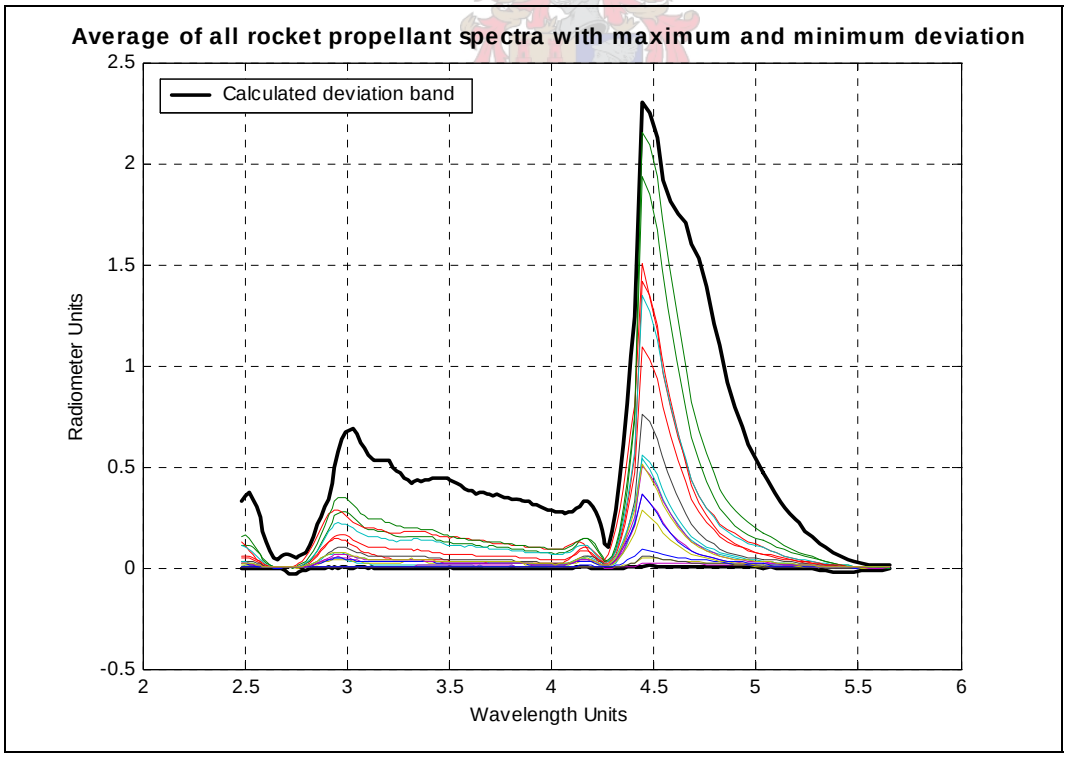

Figure 4.4-3 Average spectra signatures of all the rocket propellants

Figure 4.4-3 represents the mean of the measurements for each solid propellant recorded. The dark lines on the border indicate the maximum and minimum recorded mean values for all the measurements done. This enclosed area is termed the variable space for the model. From figure 4.4-3 it can be seen that the overall deviation band is quite large. Consequently, this dataset will be difficult to model. A different number of measurements were recorded for each propellant, which will have to be standardised before it can be used for modelling. Therefore, 10 signatures were picked for each propellant, with signatures deviating considerably from the calculated mean, discarded. This reduced the deviation for every set, but also for the overall dataset. In the case of *DB2* only 4 recordings were made, hence they were copied with noise added to generate 10 signatures.

4.5. Spectral Recordings of Flare Propellants

As was mentioned earlier, the "brick type" flare has no physical parameters whereby to describe it, except the chemical composition of the propellant that burns. Thermochemical calculations showed that various thermodynamic properties of the combustion products could be determined. These properties will be used to attempt and predict the irradiance spectral plume of flares.

The spectral measurements done for the flares differ from that of the rocket engines, because of the combustion products and smoke accumulating in the FOV of the radiometer. The accumulation can result in the radiometer measurement becoming saturated if the smoke does not move upwards. The irradiance spectra in fig. 4-4 are the measurements made during the firing of a single flare. It can be seen that a lag time exists when the flare is ignited until it burns on all surfaces. As the flare ignites the irradiance measured increases until all the surfaces are burning. The bottom most curves,

represent this ignition phase, in contrast to the topmost curves which represent the full burning flare.

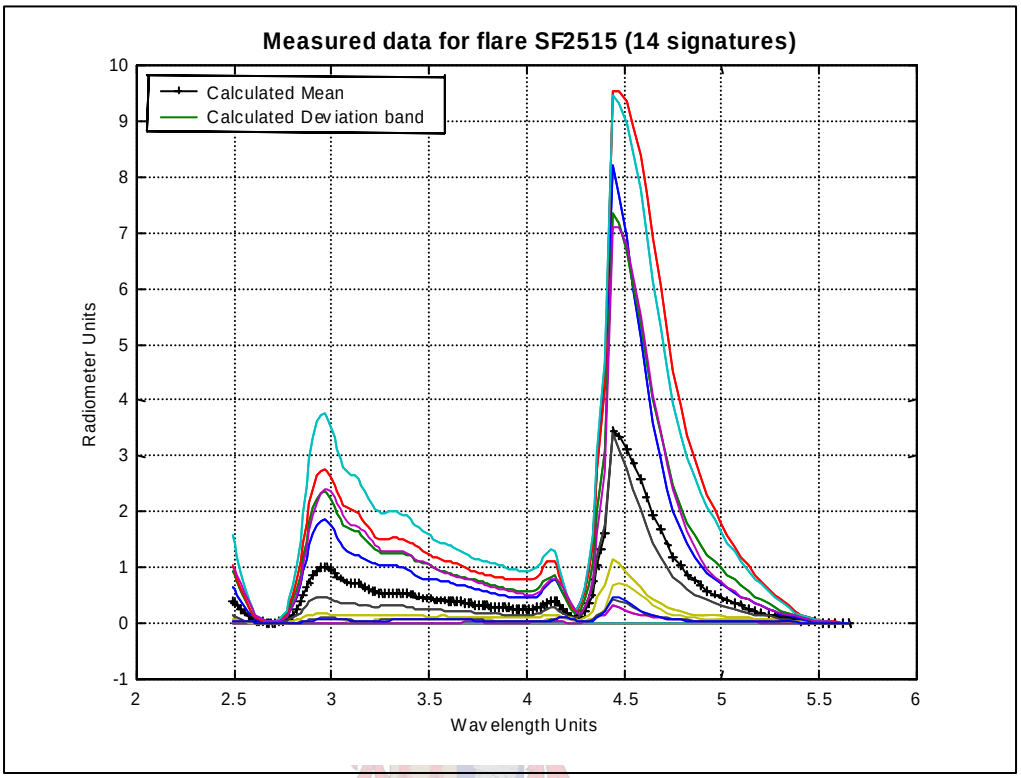

Figure 4.5-1 Measured data for flare SF2515 showing increasing irradiance as time elapsed

The accumulation of smoke and gases that occur, demand that these ignition and saturation curves be dropped. In some cases, only three signature curves describe the state when all the surfaces are burning, which means that these curves again have to be copied to supply a standardised set of signatures. Only 5 signatures and not 10 will be used as a standard set of signatures. Three examples of such standardised sets follow. All the standardised sets for the flares discussed in this study are shown in Appendix C.

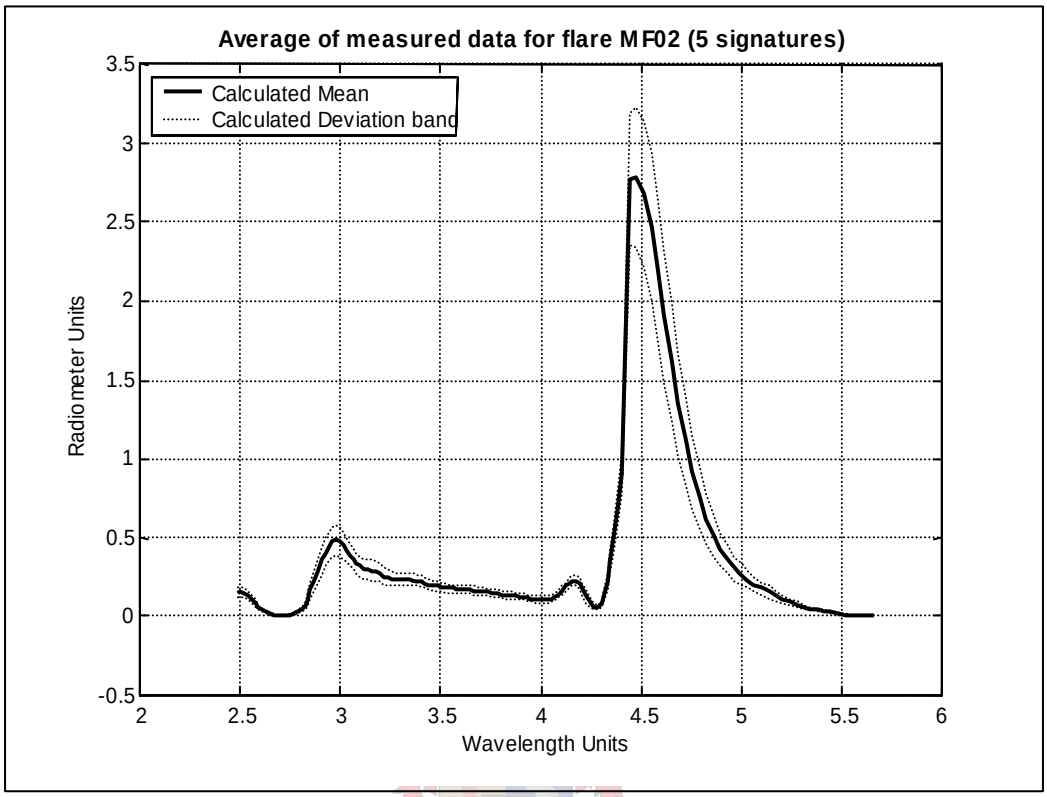

Figure 4.5-2 Spectral signature flare propellant MF02

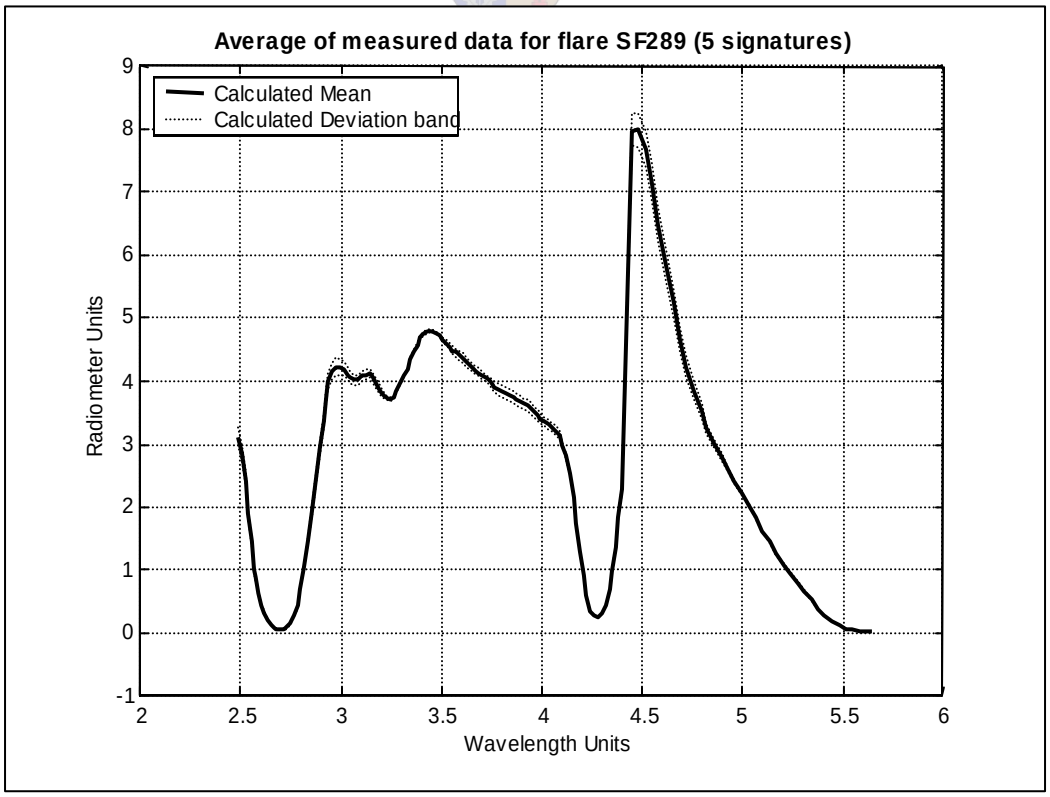

Figure 4.5-3 Spectral signature for flare propellant SF289

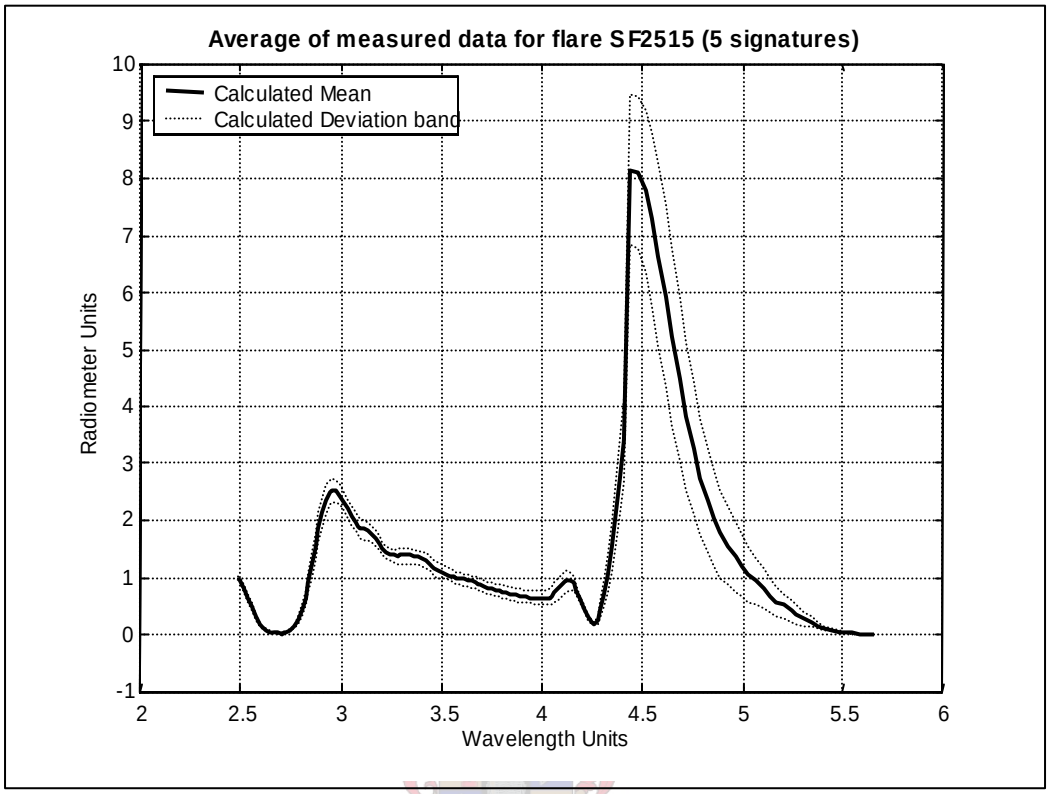

Figure 4.5-4 Spectral signature for flare propellant SF2515

Figure 4.5-4 represents the mean of the measurements for each flare recorded, with the dotted lines indicating the maximum and minimum recorded mean values for all the measurements done. . It clearly shows the improvement on the deviation when the ignition and saturation curves are dropped. The following figure shows the deviation band for all the flares:

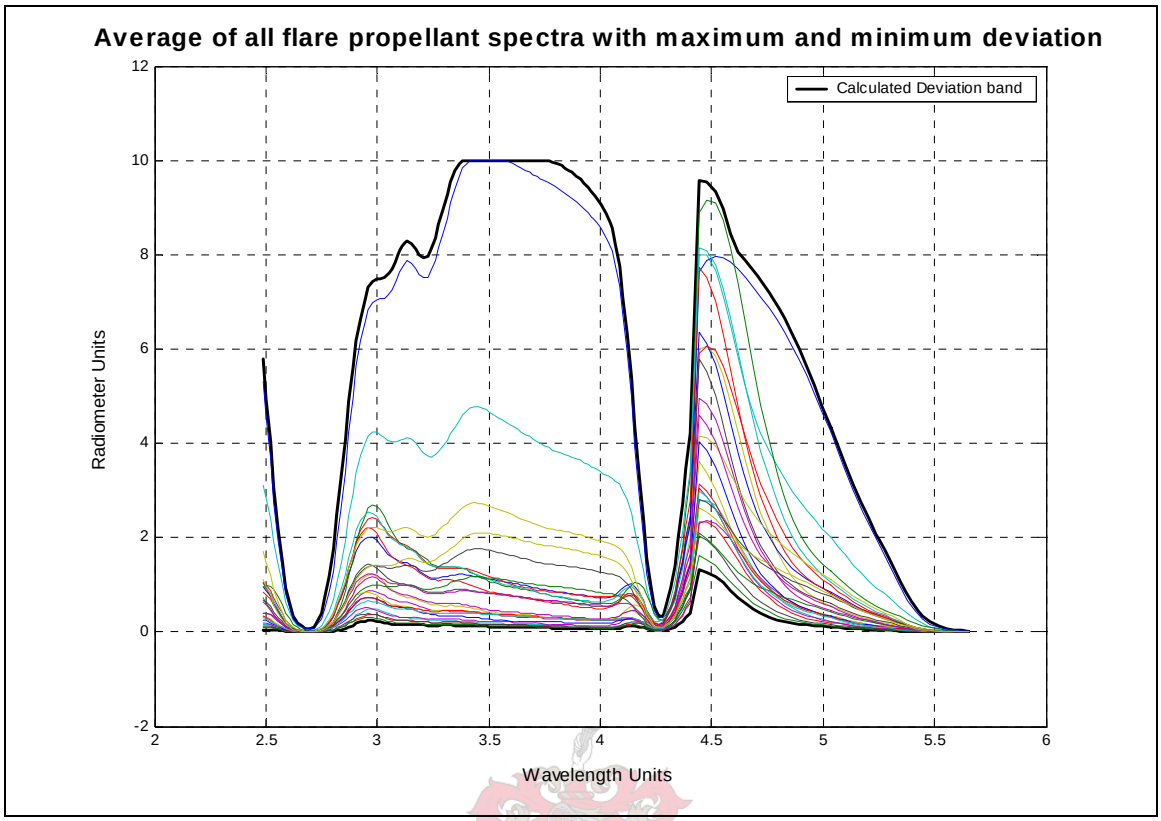

Figure 4.5-5 Average spectra signatures of all the flare propellants

The topmost curve is that of SF915. This flare did saturate the radiometer measurement when tested, but was kept as part of the dataset, to see if a model would be able to accommodate an offshoot dataset. It causes the deviation band to become large, but the density of data is not very high, so it should not influence a model. This dataset cannot be used as a test for the model, since the density of data is so low.

Now that the spectra of the rockets and the flares are set, the aim from here on is to develop a model connecting the respective parameters to the infrared plume spectra.

4.6. Reference:

1. Roodt, J., *The Prediction of the emission spectra of solid rocket propellants*, Ph.D. dissertation, Dept. Chemical Engineering, University of Stellenbosch, Chapter 7, (1998).

2. Thomas, M.E. and Duncan, D.D., *Atmospheric Transmissio*n, The Infrared & Electro-Optical Handbook, Vol. 2, SPIE Press, 2nd edition, Chapter 1, (1996).

3. Kondratyev, K. Ya., *Radiation in the atmosphere,* Academic Press, Inc., New York, Chapter 1, (1969).

4. Hudson, R.D., *Infrared System Engineerin*g, John Wiley & Sons, New York, Chapter 4, (1969).

5. Simon, I., *Infrared Radiation,* E. van Nostrand Company, Inc., New Jersey, Chapter 6, (1966).

6. Souletis, J. and Chastenet, J.C., *Study of the afterburning flame size and intensity as a function of the motor parameters,* AIAA90-1853, 26th AIAA SAE/ASME/ASEE Joint Propulsion Conference, Orlando, (1990).

7. Chastenet, J.C. and Bodart, V., *Signatures Discrétion Contre-mesures,* Revue Scientifique et Technique de la Défense, No.3, (1997).

5. Modelling of Radiation Spectra

A model is a conceptual representation of a system and should be able to generalise and extrapolate results if unknown variables are introduced. For a model to be effective, the known data space should be large enough to generalise or predict for new variables tested [1]. The known data space contains all the variables defined in the data sets, as described in the previous chapter. In order to predict unknown variables, it should fall within the known data space to expect a solution. An empirical model cannot extrapolate beyond the limits of the known data space, and furthermore an empirical model is never a precise solution due to approximations and assumptions.

Three types of models are identified: detailed, phenomenological and empirical models [2]. A detailed model is derived from first principals, making it computationally intensive. The number of variables that have to be accounted for in this study and the complexity of the problem makes it very difficult to derive a model from first principals. In some cases, when a process cannot be described by a mathematical function, experimental data is used to set up an empirical model. New modelling techniques are designed each day, but care should be taken as to which processes they are applied to. Once a model is decided upon it should be tested thoroughly with test data before it can be considered as a suitable solution. In this case it is necessary to consider an empirical model, where experimental data is used to build the model. Once the model is built, it will be tested using independent statistical tests.

5.1. Model Design

The goal of this study was to develop a model to predict the infrared irradiance plume spectra, within the 2-5μm bandwidth of rocket motors and flares from parameters that describe the plume thermodynamically. Furthermore it was necessary to identify thermodynamic properties that sufficiently describe the combustion process. It was shown that the chemical composition of the solid propellant being burned forms an integral part of any thermodynamic calculations relating to

the plume. Motor operating parameters were identified to describe the plume of a solid propellant rocket motor [3]. In the case of the "brick type" flare considered in this study, it was apparent that there were no physical parameters describing the flare that could be related to the spectral contents of the plume. Thermodynamic parameters were determined, using a thermochemical program, which returns properties of the combustion products of the combustion process.

In the case of the rockets, the *input space* of the model is defined by parameters consisting of the chemical composition and the motor operating parameters and the thermodynamic properties of the combustion products for the flares. The IR spectra consisting of irradiance intensities at 146 wavelength positions (composing a continuous band) are defined as the *output space*. A graphical representation describing the model follows:

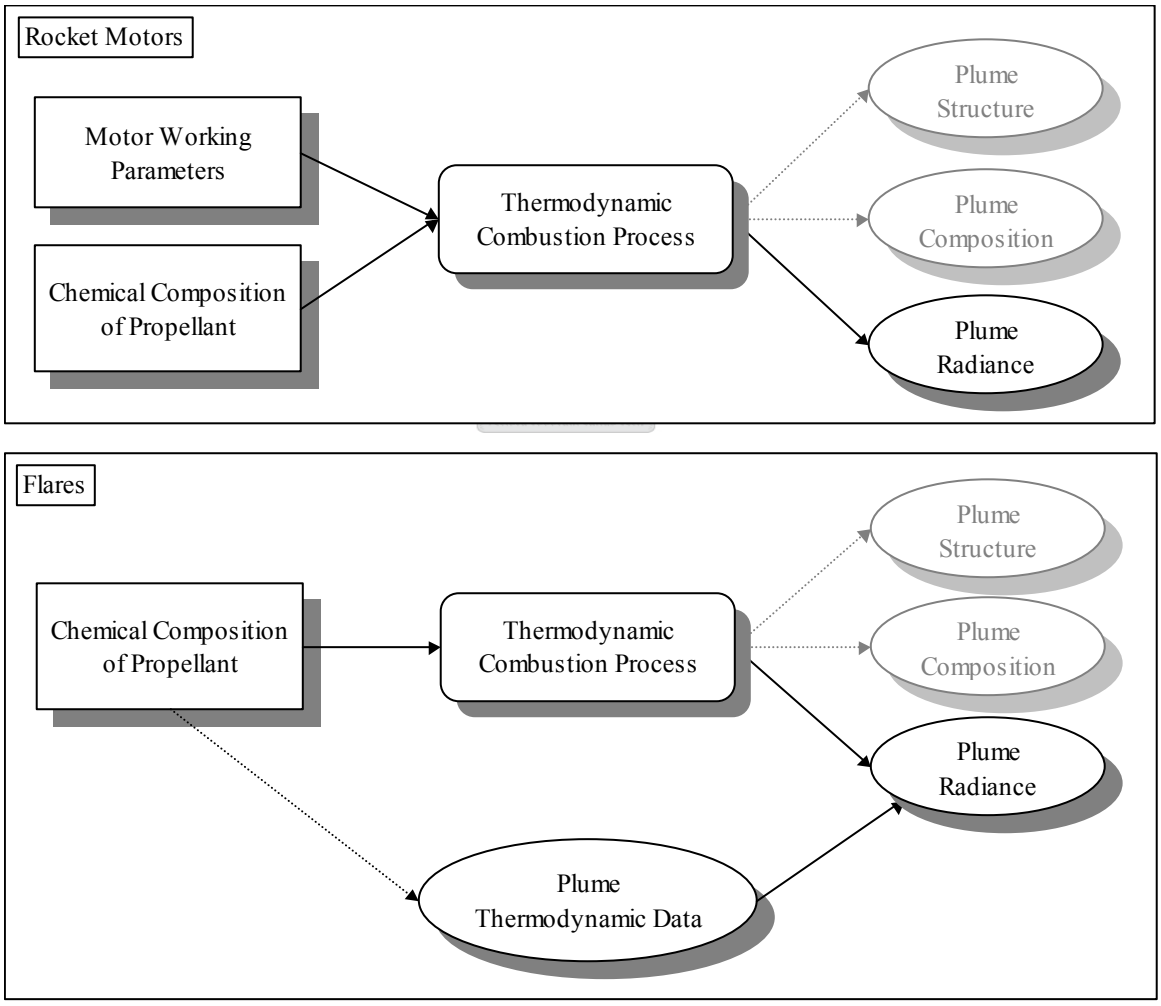

Figure 5.1-1 Graphical representation of the model

From fig.5.1-1 it is seen that the thermodynamic data of a flare's plume, is a result of the combustion process and properties of the plume. The motor operating parameters of the rocket motor are not exhibited in the properties of the plume. The processes and properties shown in fig.5.1-1 have been discussed in previous chapters.

5.1.1. Rocket Motor operating Parameters

The motor operating properties of the rocket motor has been established as follow:

$$Plume\ signature = f\{p_1, T_1, A_t, \varepsilon, fuel\ composition\}$$

- T_1 as the chamber temperature
- p_1 the chamber pressure
- A_t the nozzle throat area
- ε the nozzle expansion ratio.

According to Roodt[4] the nozzle throat diameter could be used instead of the area, since the area is a direct function of the diameter. The four motor operating parameters decided upon are thus the temperature, pressure, nozzle throat diameter and nozzle expansion ratio.

5.1.2. Thermodynamic Properties of Flare's Plume

The properties taken into account have been discussed in ***2.3.4***. A total of 14 parameters were identified, which moderately enlarge the input space. More attention will be paid to these parameters in later chapters.

5.1.3. Chemical Composition of Propellant

The infrared irradiance measurements of 18 solid rocket propellants and motor combinations were deemed to give consistent spectra to use in the model. Six of these propellants are categorised as

double-base (DB) propellants and twelve as composite (C) propellants. The flares cannot be categorised, but the infrared spectra of 25 flare formulations' could be measured with confidence. The propellant compositions for the rocket motors and the flare compositions are shown in table 5-1.

Table 5-1 Composition of solid propellants [mass%]

	DB1	DB2	DB3	DB4	DB5	DB6	C1	C2	C3	C4	C5	C6	C7	C8	C9	C10	C11	C12
NC25	42.8	32.6	55.85	35.98	42.8	42.8												
AP							70	68	68	86	84	82	86.2	70	82.5	80	81	86
SiC										1	1		1					1
TiO_2	0.6				0.6	0.6												
DOP			3.46															
Fe_2O_3								2							0.75			0.2
KAFI					3.6													
Al					0.4		16	16	16			4		16	4	4	4	
DOA							1	1	1	1.95	1.95	0.24	1.92	1	2	2.5	2	1.92
IPDI							0.88	0.88	0.88	0.72	0.72	1.49	0.71	0.88	0.7	1.52	1.32	0.71
CuO		0.3		0.25														
KNO_3				4.5	6	6												
RDX	20	20.1		15	10													
Compound 7	3.8	1.5		1.65	3.8	3.8												
EC	2.2	1.3	2.1	1.25	2.2	2.2												
HTPB							12.12	12.12	12.12	10.33	10.33	10.87	10.17	12.12	10.05	11.48	11.68	10.17
Pb-Steorate	0.5	1.2	3.79	0.9	0.5	0.5												
K_2SO_4									2		2							
C-Black	0.1	0.3	0.51	0.25	0.1	0.1										0.5		
DEP		0.68		0.51														
Cu-SAL-CU		0.32		0.24														
TA		8.9	9.67	8.91														
NGU						14												
NG	30	32.8	24.63	30.56	30	30												
	100	**100**	**100**	**100**	**100**	**100**	**100**	**100**	**100**	**100**	**100**	**99**	**100**	**100**	**100**	**100**	**100**	**100**

Table 5-2 Composition of flares [mass%]

HTPB	MF01	MF02	MF03	MF04	MF05	MF06	MF07	SF280	SF289	SF298	SF913	SF914	SF915	SF916	SF917	SF2515	SF2524	SFDB1	SFDBRAl1	SF930	SF932	SF933	SF935	SF937	SF939
IPDI								10.56	20.24	10.78	12.84	12.84	16.51	11.91	10.02	11.85	10.06	15	15	12.71	17.34	17.28	17.05	16.79	
DOA								0.84	2.77	0.82	0.91	0.91	1.29	0.84	0.71	0.9	0.67	1.4	1.4	1.04	1.41	1.47	1.7	1.96	
DTBHQ								3	1	2	1	1	1.9	1	1.92	1	1.92			1	1	1	1	1	
Tepa								0.1		0.1			0.1												
Tepan									0.3																
Tepanol											0.25	0.25		0.25		0.25				0.25	0.25	0.25	0.25	0.25	
HX752															0.15		0.15								
AP coarse (1)								0.3		0.3			0.1												
AP coarse (2)	80	67	67	67	67	67	76										34.48								
AP fine								24	36.5	28	44.22	46.9	5	53.2	56.84	49	30.17			54.5	56	56	53.9	51.1	60
AN								44	36.5	40	22.78	20.1	13.5	22.8	24.36	20.8	21.55			25.5	14	23	23.1	21.9	
Al																									
Mg								15		16	5	5		5		16			5						
SiC													60												
Fe_2O_3															1		1								
$SrCO_3$										2			1.5												
Oksamide														5	5										
Hexamine											13														
Tetrasiclin e						20						13								5	10	1	3	7	10
Fe(AA)													0.1												
Aerosil																0.0001									
TMP																0.02									
AO 2246									0.45																
MgO									0.24																
C-Black									0.09																
MA									2																
TPB									0.07																
NG/TA (80:20)									0.05																
RDX																			18						
MP200		20		10														43	35.6						
Prussian Blue																		40.6	25						
Lecithin								2																	
Polylite								0.2																	
TNT	20	13	13	13	13	13	14																		30
NTO			20	10																					
Cianuric acid					20																				
S							10																		
□	100	100	100	100	100	100	100	100	100	100	100	100	100	100	100	100	100	100	100	100	100	100	100	100	100

The full chemical names for the abbreviations used for the components of the propellants are given in Appendix A. It is easy to see that there are many 0 inputs in table 5-1. This is not acceptable as an input space for a model. Not enough significant data is fed to the model, resulting in a large zero input vector, thus minimising the possibility to obtain a solution. In addition, if too many zeros were part of the input vector the network could be overly sensitive to modifications of the input space. Roodt[4] has shown that by using the elemental molar sums, and not the components, a smaller zero vector could be obtained. The molar sum for the atom C in the fuel *DB1* is calculated by adding the number of C atoms in all the components that contains C. The propellant *DB1* contains 42.8% of a component: NC25. It is convenient to write the chemical formula for this compound as $C_6 H_{7.579} O_{9.833} N_{2.416}$. The carbon contribution to 100kg of the propellant from this component is calculated as follows:

$$C_{kmol} = \frac{\%NC25 \times C_n}{Mr(NC25)} \tag{5-1}$$

$$Mr(NC25) = (C_n \times C_{atom\ num}) + (H_n \times H_{atom\ num}) + (O_n \times O_{atom\ num}) + (N_n \times N_{atom\ num}) \tag{5-2}$$

The elemental composition of the components and their molar masses are shown in table 5-3.

An example of the calculation of the elemental molar sums of *DB2* is shown in table 5-4. The value in the fraction column indicates the fraction of the component in the fuel and the molar mass is that of the component.

Table 5-3 Elemental composition of rocket propellant components

	C	H	O	N	Al	Cu	Cl	K	Pb	S	Si	Ti	F	Fe	Molar mass of Components
NC25	6	7.579	9.833	2.416											**270.86**
AP		4	4	1			1								**117.49**
SiC	1										1				**40.10**
TiO_2			2									1			**79.90**
DOP	26	34.4	7												**458.95**
Fe_2O_3			3											2	**159.70**
KAFI								1					1		**58.10**
Al					1										**26.98**
DOA	22	42	4												**370.57**
IPDI	12	18	2	2											**222.29**
CuO			1			1									**79.55**
KNO_3			3	1				1							**101.10**
RDX	3	6	6	6											**222.12**
Compound 7	14	10	8			1			1						**576.97**
EC	17	20	1	2											**268.36**
HTPB	1	1.5058	0.0058												**13.62**
Pb-Sterate	12	25	3						1						**424.52**
K_2SO_4			4					2		1					**174.26**
C-Black	1														**12.01**
DEP	12	14	4												**222.24**
Cu-SAL-CU	14	10	6			1									**337.78**
TA	9	14	6												**218.21**
NGU	1	4	2	4											**104.07**
NG	3	5	9	3											**227.09**

Table 5-4 Example of calculation of the elemental molar sums for *DB2*

DB2	C	H	O	N	Al	Cu	Cl	K	Pb	S	Si	Ti	F	Fe	Fraction	Molar mass of Components
NC25	6	7.579	9.833	2.416											32.6	**270.86**
AP																**117.49**
SiC																**40.10**
TiO_2																**79.90**
DOP																**458.95**
Fe_2O_3																**159.70**
KAFI																**58.10**
Al																**26.98**
DOA																**370.57**
IPDI																**222.29**
CuO			1			1									0.3	**79.55**
KNO_3																**101.10**
RDX	3	6	6	6											20.1	**222.12**
Compound 7	14	10	8			1			1						1.5	**576.97**
EC	17	20	1	2											1.3	**268.36**
HTPB																**13.62**
Pb-Steorate	12	25	3						1						1.2	**424.52**
K_2SO_4																**174.26**
C-Black	1														0.3	**12.01**
DEP	12	14	4												0.68	**222.24**
Cu-SAL-CU	14	10	6			1									0.32	**337.78**
TA	9	14	6												8.9	**218.21**
NGU																**104.07**
NG	3	5	9	3											32.8	**227.09**
Σ for element	**91.00**	**111.58**	**53.83**	**13.42**		**3.00**			**2.00**						**100**	

The resultant input space for the solid rocket propellants consists of 18 variables, of which 14 are chemical composition variables, and the motor operating parameters are 4 in number. The same calculations were done for the flares, which can be seen in Appendix D. The complete input spaces for both the rockets and the flares can be found in Appendix D.

5.1.4. Infrared Irradiance Spectra

The output space of the model is composed of the measured irradiance spectra. The irradiance was measured at 146 filter positions with varying intensity at each of these filter positions. The spectra shown in Appendix B and C can be transformed into 146 points of intensity, although it appears as a continuous band. The output space thus consist of 146 variables.

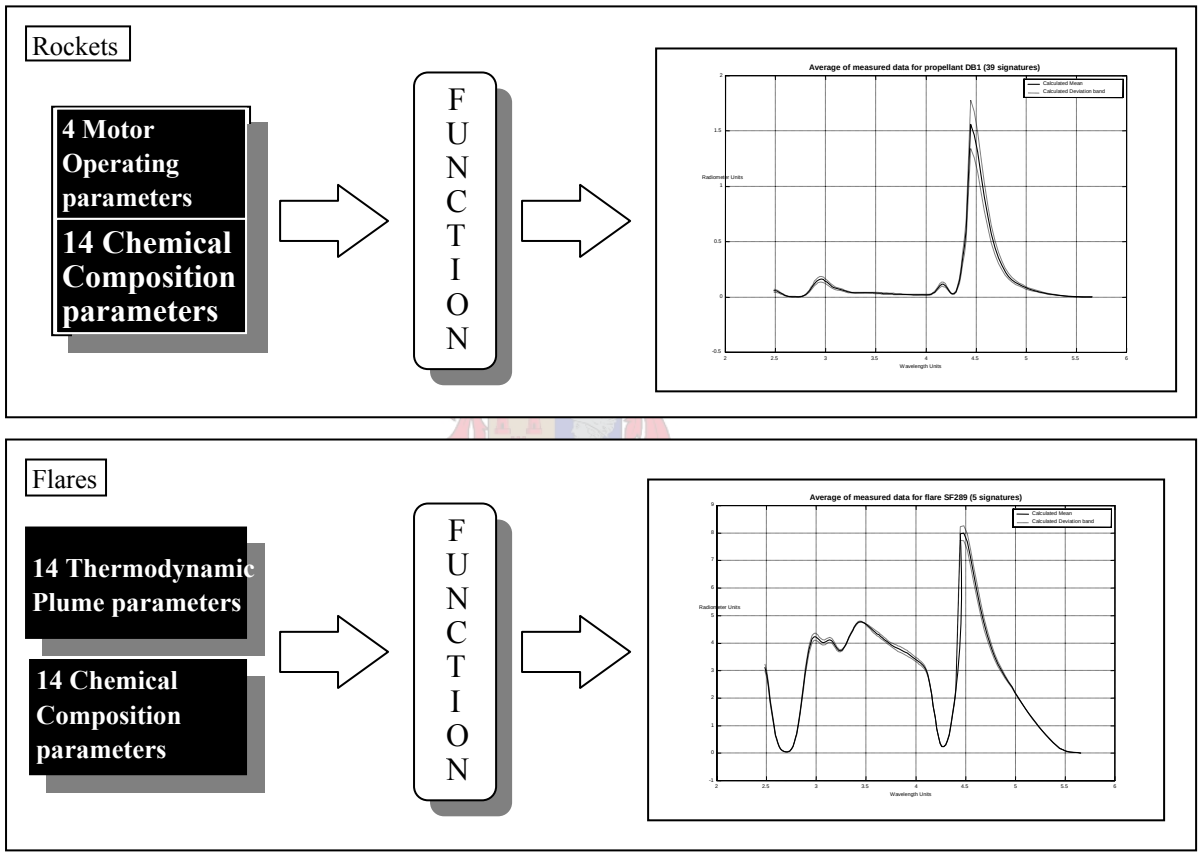

Figure 5.1-2 Layout of the suggested model

5.2. Model Complexity

It was shown that the thermodynamic combustion process could be described by non-linear equations. A combustion reaction such as a complex propellant burning inside a rocket chamber, involves several chemical species and many different reactions taking place. These non-linear equations are linearised and iteratively solved using a thermochemical program.

Models involving spectroscopy are difficult to solve. The energy distribution of the emission of a simple complex molecule is already very complicated and difficult to describe theoretically. The combustion products resulting from solid propellant burning, contains a multitude of molecules, which may be changing phase or reacting with other molecules. It would be impossible to calculate the spectral lines for each molecule in the plume, if keeping in mind that interaction of molecules alters the spectral signatures of those molecules. This is a complex problem, which cannot be solved readily. Using the thermodynamic equations set in Chapter 2, the NASA thermochemical program[5] is used to determine the temperature along with the equilibrium species in the combustion products. The thermodynamic properties of the combustion products along with the composition of the products are all given in an output file.


```
 THERMODYNAMIC EQUILIBRIUM COMBUSTION PROPERTIES AT ASSIGNED PRESSURES
  CASE = mtv
              REACTANT                    WT FRACTION      ENERGY      TEMP
                                           (SEE NOTE)     KJ/KG-MOL      K
  OXIDANT     APC                          1.0000000   -295766.960    298.150
  FUEL        RDX                           .6060606     66525.600    298.150
  FUEL        Polylite                      .3939394   -451453.600    298.150

  O/F=    2.03030  %FUEL= 33.000000  R,EQ.RATIO=  .827805  PHI,EQ.RATIO=  .569877

  THERMODYNAMIC PROPERTIES

  P, BAR            1.0133
  T, K           2660.19
  RHO, KG/CU M    1.2892-1
  H, KJ/KG       -1836.97
  U, KJ/KG       -2622.92
  G, KJ/KG       -29454.9
  S, KJ/(KG)(K)    10.3819

  M, (1/n)          28.142
  (dLV/dLP)t      -1.02100
  (dLV/dLT)p         1.4963
  Cp, KJ/(KG)(K)     5.2061
  GAMMAs             1.1186
  SON VEL,M/SEC      937.7

  MOLE FRACTIONS

  *CO               .04407
  *CO2              .16299
  *CL               .03641
  CLO               .00011
  CL2               .00005
  *H                .00556
  HCL               .12383
  HOCL              .00002
  HO2               .00002
  *H2               .01310
  H2O               .32097
  *NO               .00860
  *N2               .15196
  *O                .00906
  *OH               .03340
  *O2               .08983
```

Figure 5.2-1 Section of the output file of flare composition MF02

In the case of the rockets only the temperature and pressure values are of importance, since the nozzle expansion ratio and the nozzle throat diameter are physically measured parameters.

Up to now most of the efforts into modelling plume characteristics went into CFD (computational fluid dynamic) techniques, where the plume structure is generated as a three dimensional model. Such a model is a grid of cells in a three dimensional space, with each point having allocated values, such as temperature, position and mass flow rate at the point, etc. This process must be combined with reaction kinetics and turbulent flow models into one model if a plume is to be modelled correctly [6,7]. Instead of using CFD techniques, the data will be modelled using statistical and neurocomputing methods, which is easier to develop and test.

5.3. Statistical Models

The problem studied is unique in the sense that several variables have to be included into the model, with not too many data sets available. The immediate response is to decrease the variables using statistical methods. A classic method to implement is Principal Component Analysis (PCA).

5.3.1. Principal Component Analysis

PCA linearly transforms a set of variables into a substantially smaller set of uncorrelated variables, containing most of the information of the original set of variables. A small set of uncorrelated variables is easier to understand and work with, than a large set of correlated variables. If these variables are correlated, and especially if they are highly correlated, it could be transformed to a small set of variables, which are known as the *principal components*. This is a useful and widely used technique to reduce the

dimensionality of the variable space. PCA can also be used to visualise multivariate data sets, and identify outlying or atypical observations.

In order to analyse data, it is customary to *standardise* the data. This is done by subtracting the mean value of each variable from the observations, i.e. and then dividing the result by the standard deviation of the variable observations.

$$(x_i - \mu) / \sigma \tag{5-3}$$

The configuration of the data is important, rather than the frame of reference with regard to which the points have been plotted. The axes can therefore be rotated, without altering the configuration of the data points, or changing the results of the analysis, but creating a new plane in which to view the data [8].

The axes are turned so that the sum of squares of the perpendicular displacements (observations) is minimised, instead of the horizontal and vertical displacements typically minimised in regression procedures. The best selection of the first principal component would therefore maximise the variance of the points projected onto it. Once the first principal component (which maximises the variance) is found, the following line (second principal component) at right angles to the first principal component is searched for. The spread of points projected on the second principal should also be as large as possible. This process terminates when p mutually orthogonal lines have been found.

The following figure represents how a 3 dimensional data space can be reduced to a two dimensional space.

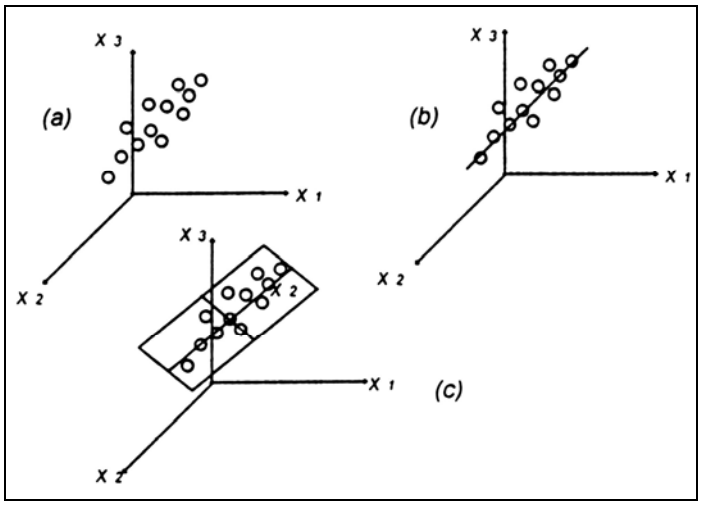

Figure 5.3-1 Geometric representation of the steps in PCA: (a) Data points in the observations space, (b) First principal component, (c) Plane defined by the first two principal components [8]

Since variance forms the basis from which the principal components are derived, a measure of adequacy of the projection of the *n* sample points into the subspace defined by the first r principal components might be related to the variance of the projected points. Each eigenvalue of the covariance matrix, which represents the principal components, gives the variance of the points with respect to the corresponding component.

The criticism against PCA is the fact that important data may be 'lost'. By using PCA the variance of the 146 infrared intensity points, from the irradiance measurements, can typically be covered by 16 new variables or principal components. The model to be designed has to be sensitive towards increases in certain species in the solid propellant. For instance, potassium compounds are known for suppressing the plume flame, thus suppressing the irradiance intensity in a certain part of the IR band. This phenomenon will not be noted if that part of the spectrum was 'lost' to PCA reduction.

5.3.2. Regression Analysis

Another popular and easy modelling technique is that of regression analysis. This is a method that fits curves to data based on the least squares principal and is not dependent on the probability distributions of the variables involved. The appeal of linear regression models is based on the fact that these models are easy to interpret if the probability distributions of the variables are normal. Since the processes considered in this study are non-linear, linear regression is not a feasible solution.

Multiple linear regression can also be used to fit models with non-linear structures to data. For example a curvilinear relationship between the response variable Y and a single explanatory variable x, may be represented by polynomial

$$Y_i = \beta_0 + \beta_1 x_i + \beta_2 x_i^2 + \ldots + \beta_{p-1} x_i^{p-1} + e_i \qquad (5\text{-}4)$$

The powers of x_i are simply treated as distinct variables. It is not advisable to use more than three of four terms in practice, since

- The ability of the model to generalise may be compromised, due to the large number of parameters involved.
- It may be implausible to describe the underlying relationship relating Y and x with a high order polynomial, and an alternative formulation may be more appropriate [9].

5.3.3. Cluster Analysis

According to Fukunaga[10] pattern recognition may be considered a problem of estimating density functions in a high-dimensional space and dividing that space into regions of categories and classes. Analysts are always looking for a natural multivariate structure among observations. The method most commonly used to accomplish this goal is cluster analysis, which aims to group individuals or objects that are more homogeneous than objects in other groups [8].

When considering a system with 146 variables, it is not possible to visualise the data on a 146 virtual plane axis. The number of variables can be reduced using PCA, and then cluster analysis could be applied. Again it needs to be said that data would be lost, and cluster analysis would still prove troublesome with a 16 variable system.

5.4. Neurocomputing Architectures

The problem faced in this study is essentially one of finding a relational description between the input space, chemical and thermochemical parameters, and the output space, which is an infrared spectral signature. This could loosely be described as pattern recognition. Many neural networks (NN) are utilised for pattern recognition. Other available pattern recognition techniques (statistical, static, Artificial Intelligence) are often unable to deal with the complexities inherent in many important applications [12]. Neural networks offer specific processing advantages, making it the technology of choice in multiple application areas, for example:

- *Adaptive Learning* - The ability to learn how to do tasks based on the data given for training or initial experience.
- *Self-organisation* – A neural network can create its own organisation or representation of the data it receives during learning and operation.
- *Real-time operation* – Neural net computations may be carried out in parallel. Hardware devices are now designed and manufactured which take advantage of this capability.

Adaptive learning is the most attractive feature of NN's, since a NN can learn how to perform certain tasks by undergoing training with illustrative examples. By training a NN, it is possible to discern between patterns, which were not included in the training data. This is referred to as generalisation.

5.4.1. Neural Networks

Problems handled by neural networks are varied but in this study, it will be used for modelling. Standard modelling techniques demand the mathematical function beforehand. The 'fitting' of a curve, which is the essential goal, requires the function parameters to be determined on the basis of the best agreement between the measured input and calculated output. The advantage of a NN is that it requires no understanding of the functionality of the problem: the non-linearity of the process and a large number of variable parameters (weights) ensure that the net would be able to adapt to any relation between the input and the output [13]. It should be noted that the performance of the net is best if the measured data covers the variable (deviation) space evenly, with adequate density over the entire region.

5.4.2. Neurons

A NN consists of neurons arranged in a network. A network consists of at least one layer of neurons. The neurons are connected with lines, called weights. The input to this network is typically real numbers, preferably scaled, between either 0 and 1, or –1 and 1, depending on the application [14].

Each neuron contains an input side and an output side, as seen in fig.5.4-1. The input side receives all the inputs, from the previous layer or external environment, along the 'lines', called weights. The function linking the quantities, is a sum of products of the entering signals s_i and weights w_i. Thus,

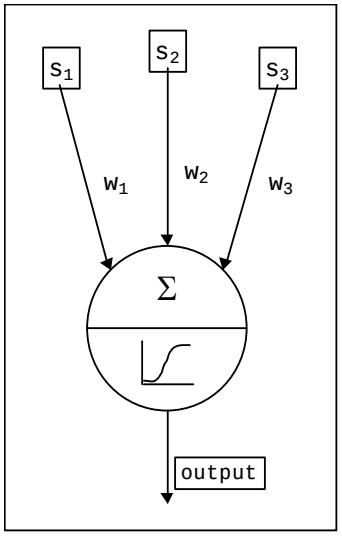

$$\text{Neuron input} = s_1w_1 + s_2w_2 + \ldots + s_mw_m \quad (5\text{-}5)$$

The group of input signals can be combined into a multivariate signal, a multidimensional vector **X**, where

$$\mathbf{X}(x_1, x_2, \ldots, x_m) = (s_1, s_2, \ldots, s_m) \quad (5\text{-}6)$$

The same could be done for the weights,

$$\mathbf{W} = (w_1, w_2, \ldots, w_m) \quad (5\text{-}7)$$

Figure 5.4-1 Diagram of neuron

The neuron input is then a dot product of $\mathbf{W} \cdot \mathbf{X}$, which can be seen as a linear function:

$$y = ax + b \tag{5-9}$$

with y as the neuron output and ax as $\mathbf{W} \cdot \mathbf{X}$. A scalar constant b is introduced which can be regarded as the offset. This offset is known as the *bias*, with a signal value of one. This changes the neuron input to

$$\text{Neuron input} = s_1 w_1 + s_2 w_2 + \ldots + s_m w_m + w_{m+1} + 1 \tag{5-10}$$

On the output side of the neuron, a non-linear transformation of the input signal takes place. The input signal can become either very large, positively or negatively. The signal therefore needs to be 'squashed' (depending on the transfer function), which is done with a transfer function. The transfer function should be continuous and be confined to a specified interval. Several transfer functions have been identified and are in use. The most widely used and (in this case) applicable function, is the sigmoidal function. Another transfer function usually found on an output neuron, is a linear function called the threshold logic.

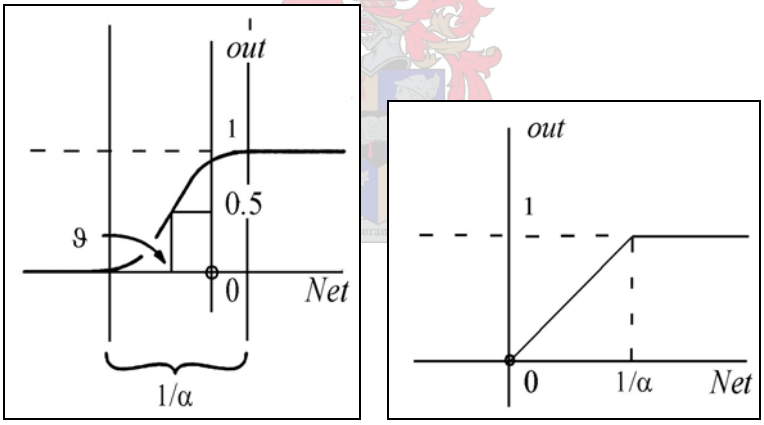

Figure 5.4-2 Transfer functions

The sigmoidal function can be written as

$$Output = \frac{1}{1 + e^{-\alpha(Net\ Input + \vartheta)}} \tag{5-11}$$

with α defined as the steepness and ϑ as $w_{m+1}.1$. The reciprocal width in the linear transfer function is defined as 1/α.

After each epoch the projected output is compared to the true output and the error recorded. The weights need to be updated after each epoch, in order to improve the predicted output. This can be done using the *delta rule,* which states that in order to improve the decision vector the correction $\Delta\mathbf{W}$ should be proportional to a certain parameter δ, (which is proportional to the error), and to the input **X**, for which the wrong answer was obtained.

$$\Delta w = \eta\left(-\frac{\partial E}{\partial W}\right) = -\eta\delta X \tag{5-12}$$

with δ as the as the correction constant and η as the learning rate.

These neurons are now connected into a network. A basic network model is shown figure 5.4-3. For the purpose of this thesis the input layer is not counted as a layer, as it is not an active layer.

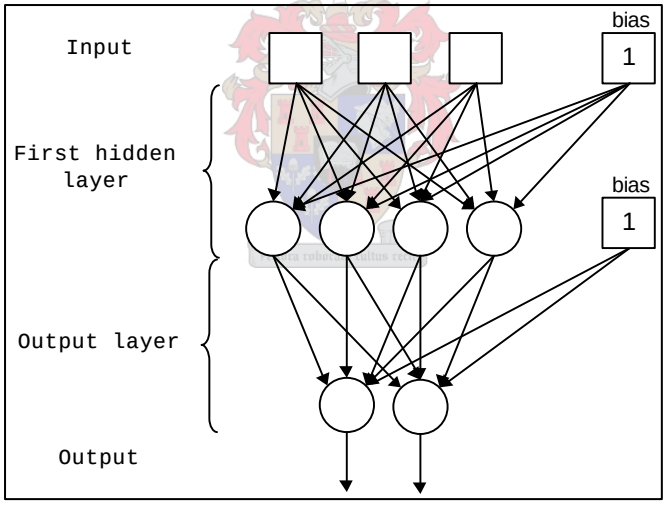

Figure 5.4-3 Basic neural network

5.5. Suggested Network Model

Neurons can be arranged into different kinds of networks. However, Maren[12] states that feedforward networks excel at pattern recognition. Roodt[15] constructed a feedforward network to predict the irradiance spectra for the rocket problem. This network consisted of 18 input parameters identified for the solid rocket propellant, with 146 hidden layer neurons and 146 irradiance outputs.

The network was allowed full interaction between input and output neurons, for the network to be sensitive for changes to the input. It is also necessary for the network to be able to predict changes to certain parts of this specific spectrum band. The reason is that a change in the aluminium content of the propellant has an effect across the irradiance spectrum, but differs for each wavelength. The effect of changing the oxygen or carbon content of the propellant is only visible in certain bands of the IR spectrum. The proposed network setup is shown in fig. 5.5-1.

The same basic structure will be used when analysing the flare problem, but the structure will be tweaked in order to optimise it for the problem at hand. The problem statement also requires the issue to be reversed, thus using the spectral signature to predict the chemical composition of the flare and the solid propellants. The network construction and training of the data is discussed in detail in the next chapters.

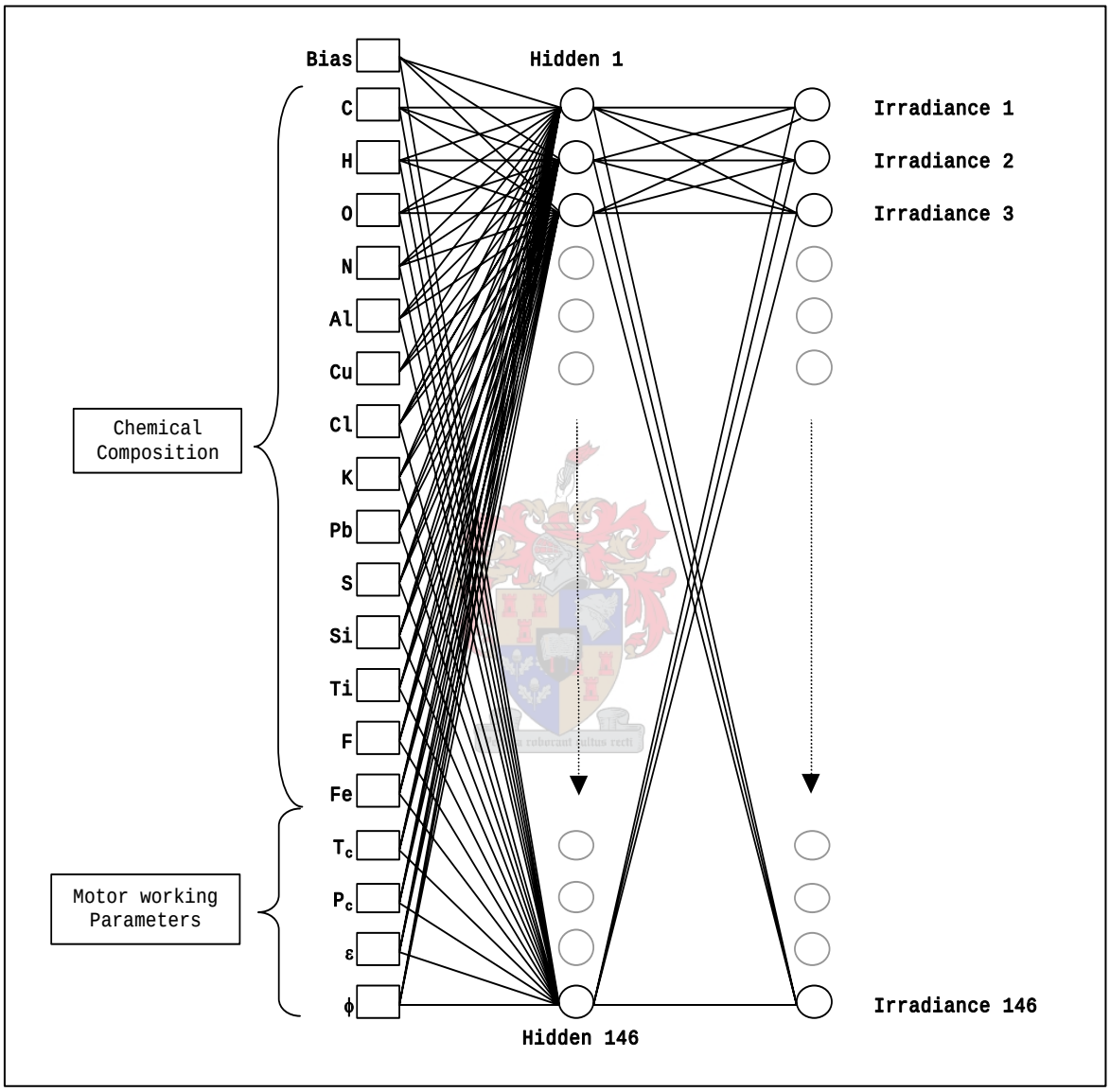

Figure 5.5-1 Proposed network setup for predicting IR irradiance of rockets

5.6. Reference:

1. Cherkassky, V., *Statistical, Neural Network and Fuzzy Methods for function Estimation,* Presented at WCNN-96, San Diego, (1996).

2. Oran, E.S. and Boris, J.P., *Numerical Simulation of Reactive Flow,* Elsevier, New York, Chapter 1, (1987).

3. Chastenet, J.C., *Post-combustion des jets de moteurs à propergol solide,* La Recherche Aérospatiale, Vol. 5, No. 325, (1995).

4. Roodt, J., *The Prediction of the emission spectra of solid rocket propellants*, Ph.D. dissertation, Dept. Chemical Engineering, University of Stellenbosch, Chapter 7, (1998).

5. Gordon, S. and McBride, B., *Computer program for Calculation of Complex Chemical Equilibrium Compositions and Applications,* NASA SP-273, 1971, NASA Lewis Research Center, NASA Reference Publication 1311, (1994).

6. Vaitekunas, D.A., Alexan, K., Lawrence, O.E., *SHIPIR/NTCS: a naval ship infrared signature countermeasure and threat engagement simulator,* SPIE, Vol. 2744, No. 411, (1999).

7. Chastenet, J.C. and Bodart, V., *Signatures Discrétion Contre-mesures,* Revue Scientifique et Technique de la Défense, No.3, (1997).

8. The MathWorks, *Statistics Toolbox User's Guide*, The MathWorks, Inc., Natick, United States, Multivariate Statistics, (2002).

9. Milton, J.S. and Arnold, Jesse C., *Introduction to Probability and Statistics*, McGraw-Hill, Inc., Singapore, Third Edition, Chapter 12, (1995).

10. Fukunaga, K., *Introduction to Statistical Pattern Recognition*, Academic Press, Inc. San Diego, Chapter 1, (1990).

11. The MathWorks, *Statistics Toolbox User's Guide*, The MathWorks, Inc., Natick, United States, Multivariate Statistics, Cluster Analysis, (2002).

12. Maren, A.J., Harston, C.T., Pap, R.M., *Handbook of Neural Computing Applications*, Academic Press, Inc., San Diego, Chapter 1, (1990).

13. Zupan, J., Gasteiger, J., *Neural Networks for Chemists*, VCH Verlagsgesellschaft, Weinheim, Chapter 2, (1993).

14. Zupan, J., Gasteiger, J., *Neural Networks for Chemists*, VCH Verlagsgesellschaft, Weinheim, Chapter 1, (1993).

15. Roodt, J., *The Prediction of the emission spectra of solid rocket propellants*, Ph.D. dissertation, Dept. Chemical Engineering, University of Stellenbosch, Chapter 6, (1998).

6. Modelling of Rocket Plume Infrared Spectra

6.1. Previous Work

Work done by Roodt[1] established the neural network (NN) model shown in the previous chapter. It was, however, not a straightforward problem and in solving it, various characteristics of the model were examined.

The first NN structure used for training contained only the chemical composition of the propellants as input space. The reasoning behind this being that each propellant should have a characteristic set of plume species and concentrations. From the IR spectra of the different propellant compositions, it could be seen that each propellant has a significant IR signature. The aim was for the NN to be able to learn the trend of these signatures. The infrared (IR) spectra of the rocket plumes could not be predicted adequately with this particular NN structure.

The input space was then extended by introducing thermodynamic properties of the combustion products. These properties would describe the 'energy content' of the plume.

Table 6-1 Thermodynamic properties introduced for extending input space

Pressure	Temperature	Gas Density	Molecular Mass	k (C_p / C_v)
Velocity of gas	Enthalpy	Internal Energy	Gibbs Free Energy	Entropy

The additional thermodynamic parameters in table 6-1, were included in the input space, consisting of 24 component composition values and 4 motor operating parameters (including a bias). It was then incorporated into a NN with one hidden layer, consisting of 120 neurons, and 146 neuron output layer. Using this NN it was possible to predict a test set reasonably accurately. A test set is a dataset of a propellant that was not included when the NN was trained. This test set should be in a region of adequate density in the

variable (deviation) space of the whole data set. In the case of the rocket propellants, DB2 and C10 were identified as appropriate test sets. These were not included in the input data fed to the NN.

Certain thermodynamic properties from table 6-1 are merely derivatives of each other, therefore they do not contribute to information on the plume. Another approach would be to use similar inputs to the thermochemistry program, and then predict the IR spectra directly from these parameters. The parameters identified for use in this new input space, was shown earlier as the temperature, pressure, nozzle expansion ratio and nozzle throat diameter.

Now that the motor working parameters were set, it was important to properly represent the chemical species the propellant is made up from. The current input space consists of the component composition. This input space was then reduced to an elemental composition, as explained in the previous chapter. The input space now consists of 14 chemical composition parameters and 4 motor working parameters.

The input to a NN should be scaled correctly, so that certain inputs (with big numerical values) do not incorrectly influence the network.

Table 6-2 Scaling of input space [1]

Feature	***Standard Net***
Chamber Pressure (MPa)	No scaling
Temperature (K)	K/1000
Expansion Ratio	ε/10
Throat Diameter (cm)	No scaling
Σ K	No scaling

A setup as set out in table 6-2, was decided upon, with good results. However, this model did not respond well to a change in the pressure. The irradiance dropped when the

pressure was increased, which does not agree with theory. The inverse of the pressure was used instead, thus increasing the dynamic range of the pressure parameter. Potassium compounds are known as flame suppressants, thus reducing the irradiance of the plume. The sign of the total potassium content was changed to negative, improving the prediction of the *'K' sensitive net*. These two NN's were then used for predicting the IR spectra of the different propellant compositions, with success. A summary of these networks' setup is given in table 6-3.

Table 6-3 Scaling of motor working parameters in Roodt's neural networks [1]

Feature	***Standard Net***	***'K' sensitive net***
Chamber Pressure (MPa)	1/p	1/p
Temperature (K)	K/1000	K/1000
Expansion Ratio	ε/10	ε/10
Throat Diameter (cm)	No scaling	No scaling
Σ K	No scaling	-1

The input and output spaces were then connected to a network as follow:

Table 6-4 Summary of network configuration

No. neurons in Input layer	18
No. neurons in Hidden layer	146
No. neurons in Output layer	146
Training Function	Backpropagation
Hidden layer Transfer function	Hyperbolic tangent sigmoidal
Output layer Transfer function	Linear

Roodt[1] further showed that the optimum training point to be at 200 iterations per training data set. The phenomenon overtraining occurs when measured noise is trained as part of the model. Overtraining can take place due to noise in the training data, too many free parameters (weights) and when the model is trained too long.

6.2. Refining the Existing Model

In order to streamline the neural network model suggested by Roodt[1], the structure and training algorithm used were evaluated. One of the tasks for this thesis was to reduce the number of hidden nodes in the original network. The focus will thus be to reduce the number of hidden nodes (while maintaining a working model) and not to generate a final optimised model.

6.2.1. Measure of Correlation

It is desirable to obtain an indication of the strength of the correlation between the predicted and measured line spectra. Comparing the spectra visually, it is possible to see if there is any correlation, but presents no real measure of how good the fit is. Therefore two parameters were used to test the correlation between two line spectra. Although both parameters are a measure of the linear correlation between two variables, it was found that it could be applied in this case. The first parameter is the *Pearson product moment of coefficient of correlation:*[2]

$$r = \frac{n(\sum XY) - (\sum X)(\sum Y)}{\sqrt{[n\sum X^2 - (\sum X)^2][n\sum Y^2 - (\sum Y)^2]}} \tag{6-1}$$

with X as the target space, Y the predicted space and n the number of observations. If this expression is squared (r_p^2), it is known as the coefficient of determination. Furthermore it was found that r_p^2 gave an indication of how good the predicted line spectra followed the trend of the measured spectral lines.

The second parameter is also a parameter measuring relative distance between a target and a predicted spectral point,

$$R^2 = 1 - \frac{\Sigma(X-Y)^2}{(n-1)(\sigma_{target})^2} \tag{6-2}$$

σ = standard deviation

which indicates the error between the predicted and target line spectra. In the case of this parameter becoming negative it means that the predicted curve flipped over to the negative side. Even though this measure would indicate that the predicted curve has a good "fit" it can't account for the fact that it is impossible to measure negative irradiance

spectra and these negative correlation values will be ignored. These parameters will further on be used to verify the strength of correlation between two IR line spectra.

6.2.2. Reducing the Network Structure

The structure set by Roodt consisted of 18 input nodes, 146 hidden nodes and 146 output nodes. This results in (18x146)+(146x146) = 23962 weights or variables the system has to be trained for. Although the model responded well to tests done, it would be mathematically correct if the number of variables could be decreased. Tests were done, starting with 2 hidden nodes, and doubling the number of nodes after each test. It was found that with 16 hidden nodes the strength of correlation of Roodt's NN could be reproduced. A network with 16 hidden nodes contains (18x16) + (16x146) = 2624 weights. This considerably reduces the variables the system has to be trained for, and it also reduces the training time.

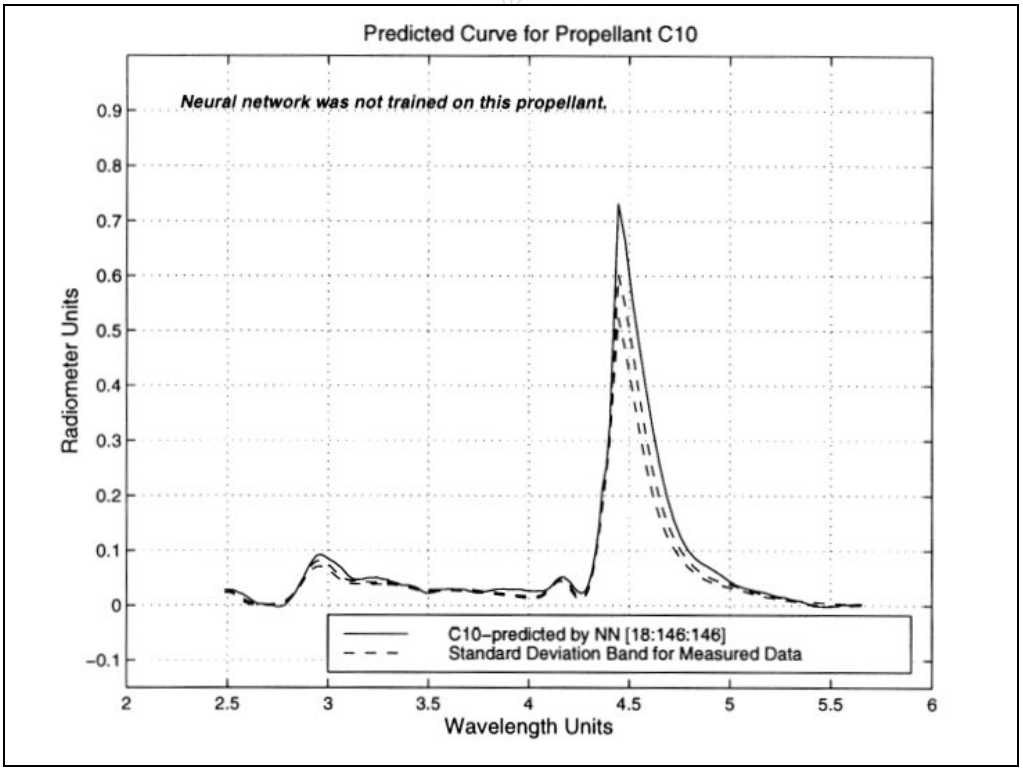

Figure 6.2-1 Curve predicted for C10 propellant using Roodt's[1] 146 hidden nodes

From figures 6.2-1 and 6.2-2 it is apparent that the NN with 16 hidden nodes, matches the performance of the NN with 146 hidden nodes.

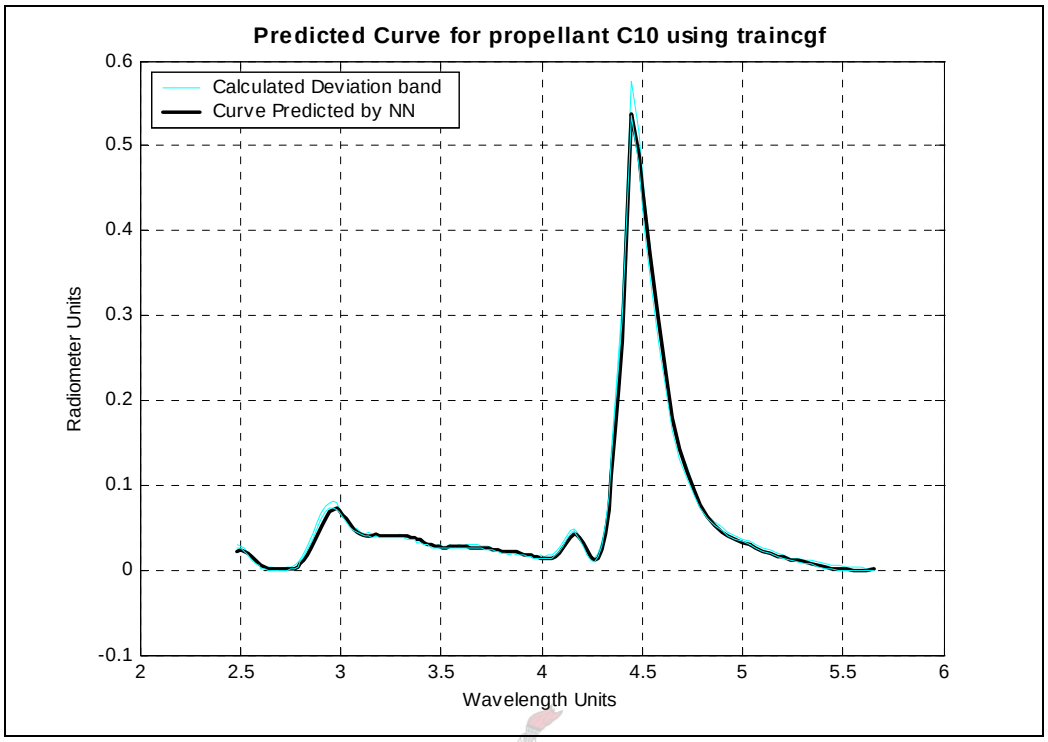

Figure 6.2-2 Curve predicted for C10 propellant using 16 hidden nodes

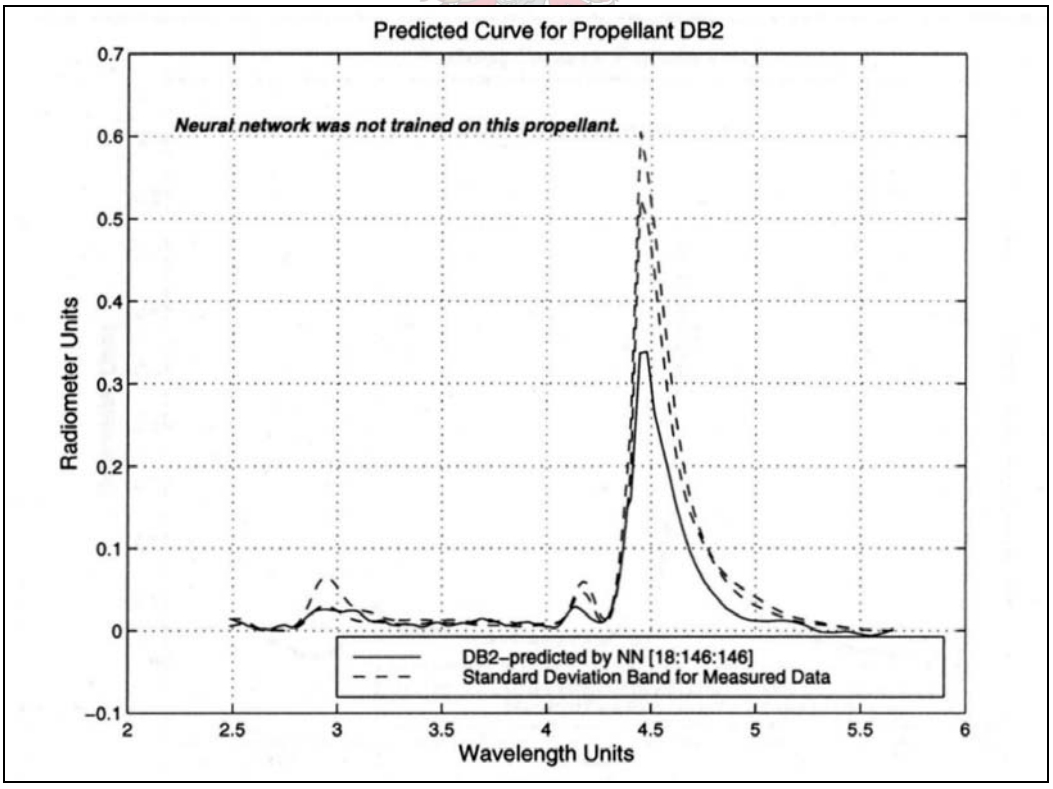

Figure 6.2-3 Curve predicted for DB2 propellant using Roodt's[1] 146 hidden nodes

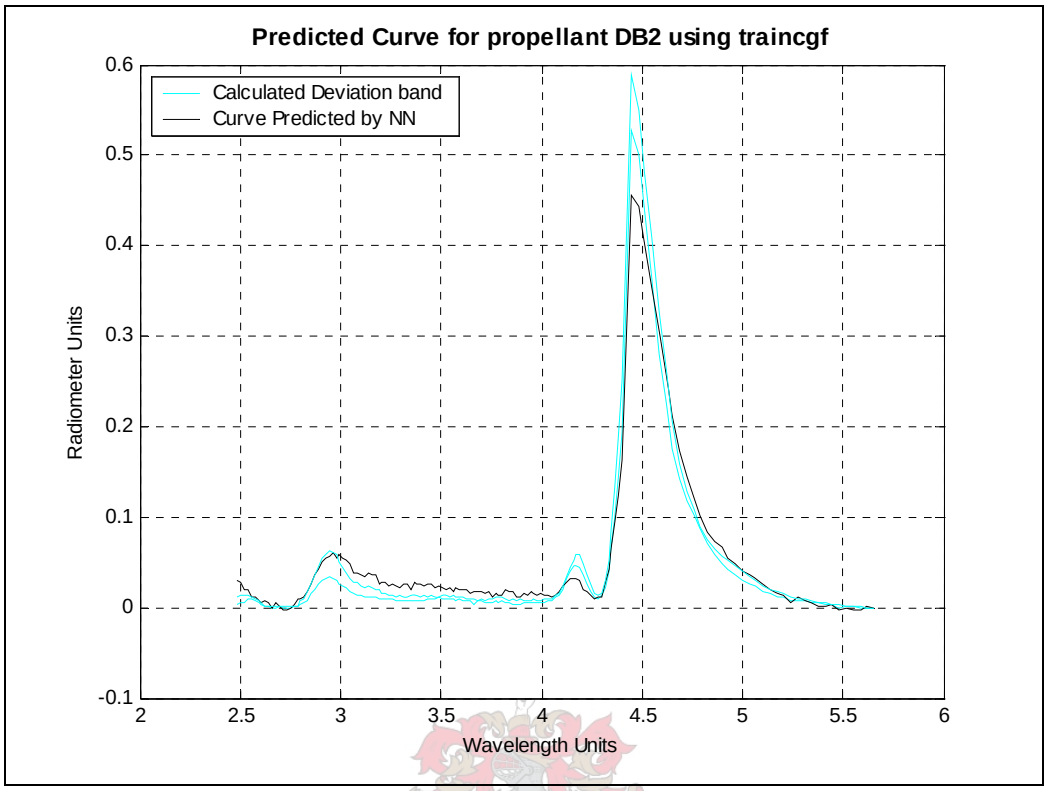

Figure 6.2-4 Curve predicted for DB2 propellant using 16 hidden nodes

From figures 6.2-3 and 6.2-4 it is apparent that the NN using 16 hidden nodes outperforms the NN using 146 hidden nodes in the case of DB2. The motor operating parameters were not scaled as described in table 6-3. Instead the parameters were scaled as in table 6-5.

Table 6-5 Scaling of Motor operating parameters for NN using 16 hidden nodes

Feature	***Standard Net***
Chamber Pressure (MPa)	No scaling
Temperature (K)	K/1000
Expansion Ratio	ε/10
Throat Diameter (cm)	No scaling
Σ K	No scaling

The network configuration used is as follows:

Table 6-6 Network configuration for NN with 16 hidden nodes

Feature	***NN_{16}***	***Matlab function***
No. neurons in Input layer	18	
No. neurons in Hidden layer	16	
No. neurons in Output layer	146	
Training Function	Scaled conjugate gradient backpropagation [3]	trainscg
Performance function	Mean squared error	mse
Hidden layer Transfer function	Hyperbolic tangent sigmoidal	tansig
Output layer Transfer function	Linear	purelin

The networks were trained using *Matlab's* neural network toolbox. The objective function is the method of updating the weights after each epoch, thus minimising the error. The performance function is the sum squared error [3].

The method used for reducing the hidden nodes is a very robust method, but the main goal in streamlining the model was to find the network with the least number of hidden nodes that will generate a satisfactory model. The two solid propellants used as test sets when reducing the network structure are typical of the class of solid propellant, in this case double-base and composite fuels. Various tests were done to confirm that a conceptual working model exists when using 16 hidden nodes. The predicted curves in figures 6.2-2 and 6.2-4 are examples of such tests. It would be worthwhile to further optimise the number of hidden nodes (and various pruning tools exist), but it was not asked for in this study.

6.2.3. Refining the Network Configuration

Several training functions can be used for feedforward training of a network. Eight training functions were identified, which were applicable to this problem and are shown in table 6-7. The first two functions in table 6-7 could not be used, since the memory (RAM) requirements, could not be met. All of these training functions are described in detail in *Matlab's Neural Network Toolbox User's Guide* [3], but will not be discussed here.

Along with 2 performance functions, namely the mean squared error *(mse)* and sum squared error *(sse),* the training functions were tested for each propellant, i.e. each propellant were used as test set. This was done in order to see if there is one training function to model the whole variable space and not just two test sets.

Table 6-7 Training functions tested for all

Matlab function	***Training Function***
trainlm	Levenberg-Marquardt backpropagation
trainbfg	BFGS quasi-Newton backpropagation
traincgb	Powell-Beale conjugate gradient backpropagation
traincgf	Fletcher-Powell conjugate gradient backpropagation
traincgp	Polak-Ribiere conjugate gradient backpropagation
traingdx	Gradient descent, momentum & adaptive learning backpropagation
trainoss	One step secant backpropagation
trainscg	Scaled conjugate gradient backpropagation

The testing ran for 20 iterations per training data set, because it was only necessary to see which training functions are inclined to a solution. Since the weights of the network are initialised with a random function, each test was repeated three times. The two correlation coefficients were then used to test the strength of the correlation. In table 6-8 the darker shading represents a strong correlation for both coefficients, while the cells lightly shaded present a weak correlation with one of the correlation coefficients. From

this table it is possible to get an idea of which training function will be the best solution for the problem.

It is possible to further optimise the training algorithms themselves as most of these algorithms have parameters that could be modified to influence the training the network. Again the goal of this thesis was to find a conceptual working model and not necessarily the optimum network model. For example: in the case of the scaled conjugate gradient backpropagation algorithm the steepness of the transport function (Hyperbolic tangent sigmoidal) could be varied to further optimise the network. Even though only 20 epochs were used during the training of the networks mentioned in table 6-8 and repeated only 3 times, it was only done to see what training algorithms responded best to the model. In no way is the number of epochs used in training the network enough to generate proper results and this is also not implied here. Training of proper test sets took place over at least 200 epochs.

Table 6-8 Testing the different training functions for each propellant

DB1		***Trainscg***			***Traincgb***			***traincgf***			***traincgp***			***traingdx***			***trainoss***			***Maximum***
mse	*Rsq2*	0.393	0.992	0.977	0.994	0.951	0.890	0.862	0.996	0.998	0.834	0.713	0.991	0.837	0.049	0.427	0.976	0.980	0.824	0.998
	rsquare	-0.133	0.852	0.047	0.437	0.560	0.709	-0.001	0.933	0.736	-1.347	0.079	0.499	0.573	-0.161	-0.010	-1.708	0.252	0.798	0.933
sse	*Rsq2*	0.973	0.995	0.816	0.993	0.104	0.000	0.998	0.992	0.796	0.267	0.979	0.988	0.967	0.156	0.814	0.732	0.950	0.040	0.998
	rsquare	0.313	0.638	0.428	0.522	-0.197	-0.204	0.691	0.510	-0.077	-0.114	-0.458	0.687	0.307	-0.039	0.105	0.023	0.074	-0.188	0.691

DB2		***Trainscg***			***traincgb***			***traincgf***			***traincgp***			***traingdx***			***trainoss***			***Maximum***
mse	***Rsq2***	0.224	0.996	0.975	0.007	0.997	0.960	0.872	0.959	0.965	0.920	0.876	0.606	0.075	0.939	0.974	0.983	0.821	0.996	***0.997***
	rsquare	-11.916	0.697	0.859	-0.615	0.939	0.707	0.644	0.214	0.254	-2.535	-7.752	0.572	-0.306	0.606	-3.834	0.862	0.207	0.929	***0.939***
sse	***Rsq2***	0.955	0.956	0.960	0.994	0.993	0.935	0.801	0.933	0.974	0.993	0.571	0.973	0.256	0.929	0.870	0.626	0.961	0.967	***0.994***
	rsquare	0.607	0.639	0.241	0.758	0.679	-4.742	0.280	0.108	0.861	-2.046	-1.450	0.956	-0.074	0.675	0.835	-0.669	0.672	-0.488	***0.956***

DB3		***Trainscg***			***traincgb***			***traincgf***			***traincgp***			***traingdx***			***trainoss***			***Maximum***
mse	*Rsq2*	0.110	0.048	0.010	0.366	0.187	0.430	0.120	0.320	0.533	0.286	0.431	0.017	0.019	0.174	0.362	0.000	0.431	0.287	0.533
	rsquare	-2.E+04	-2.E+04	-2.E+03	-7.E+02	-4.E+04	-2.E+03	-1.E+04	-5.E+04	-1.E+04	-1.E+05	-8.E+02	-9.E+03	-4.E+02	-5.E+02	-5.E+02	-4.E+03	-3.E+03	-3.E+03	-412.233
sse	*Rsq2*	0.242	0.555	0.514	0.406	0.103	0.419	0.000	0.197	0.290	0.275	0.226	0.043	0.079	0.110	0.006	0.224	0.252	0.066	0.555
	rsquare	-1.E+04	-6.E+04	-4.E+03	-6.E+04	-3.E+03	-2.E+02	-2.E+02	-4.E+02	-3.E+05	-3.E+02	-2.E+03	-2.E+01	-3.E+04	-8.E+03	-1.E+04	-2.E+03	-2.E+03	-2.E+04	-20.963

DB4		***trainscg***			***traincgb***			***traincgf***			***traincgp***			***traingdx***			***trainoss***			***Maximum***
mse	*Rsq2*	0.843	0.862	0.858	0.542	0.890	0.919	0.792	0.781	0.819	0.468	0.637	0.534	0.750	0.759	0.379	0.803	0.820	0.879	0.919
	rsquare	-52.176	-71.841	-6.103	-48.912	-8.067	-0.859	-26.440	-101.07	-359.705	0.332	0.185	0.528	-27.856	-42.662	-1.097	-50.644	-964.53	-20.183	0.528
sse	*Rsq2*	0.790	0.540	0.818	0.884	0.870	0.856	0.778	0.796	0.897	0.831	0.715	0.689	0.708	0.697	0.792	0.894	0.831	0.838	0.897
	rsquare	-1.236	-0.070	-50.255	0.547	-229.499	-14.479	-49112	-94.615	-6.544	-21.016	0.165	-188.476	-5.791	-8.309	-315.500	-39.443	-116.03	-1.828	0.547

DB5		***trainscg***			***traincgb***			***traincgf***			***traincgp***			***traingdx***			***trainoss***			***Maximum***
mse	*Rsq2*	0.937	0.450	0.846	0.023	0.835	0.731	0.181	0.629	0.754	0.058	0.652	0.856	0.842	0.847	0.161	0.539	0.763	0.407	0.937
	rsquare	0.896	-101.530	-631.779	-1.922	-123.160	-46.115	-1.300	-5.880	-38.991	-1063.7	-1059.26	-842.095	-528.54	-512.38	-2533.60	-1458.1	-164.5	-2.255	0.896
sse	*Rsq2*	0.209	0.709	0.328	0.039	0.884	0.688	0.005	0.669	0.388	0.704	0.883	0.731	0.169	0.042	0.221	0.453	0.696	0.186	0.884
	rsquare	-286.409	-46.441	0.150	-3.534	-1352.71	-16.163	-16.375	-13.607	-701.386	0.490	-2213.64	-3401.44	-941.95	-129.26	-33.225	-339.6	-140.51	-84.700	0.490

DB6		***trainscg***			***traincgb***			***traincgf***			***traincgp***			***traingdx***			***trainoss***			***Maximum***
mse	*Rsq2*	0.275	0.927	0.941	0.919	0.928	0.912	0.920	0.783	0.907	0.929	0.873	0.392	0.522	0.904	0.907	0.877	0.881	0.915	0.941
	rsquare	-288.401	-36.950	-2.301	-150.683	-4.160	-80.779	-239.64	-1.637	0.743	-5.043	-402.884	-18.233	-67.423	-11.142	-44.122	-29.541	-0.650	-76.389	0.743
sse	*Rsq2*	0.833	0.895	0.940	0.904	0.938	0.879	0.886	0.879	0.919	0.916	0.767	0.392	0.490	0.917	0.341	0.817	0.921	0.484	0.940
	rsquare	-14.057	-603.894	0.933	-1839.74	-6.804	-170.291	-0.152	-46.344	-57.311	-193.36	-448.162	0.040	-184.93	-86.292	-3.971	-362.89	-141.78	-152.81	0.933

C1		***trainscg***			***traincgb***			***traincgf***			***traincgp***			***traingdx***			***trainoss***			***Maximum***
mse	*Rsq2*	0.997	0.997	0.994	0.997	0.996	0.997	0.995	0.998	0.997	0.997	0.996	0.996	0.998	0.998	0.997	0.998	0.998	0.998	0.998
	rsquare	0.991	0.992	0.945	0.988	0.968	0.995	0.981	0.996	0.978	0.984	0.991	0.933	0.994	0.984	0.988	0.997	0.966	0.991	0.997
sse	*Rsq2*	0.998	0.996	0.998	0.996	0.997	0.996	0.997	0.996	0.991	0.996	0.999	0.998	0.988	0.993	0.995	0.994	0.997	0.997	0.999
	rsquare	0.976	0.876	0.984	0.960	0.995	0.863	0.587	0.880	0.976	0.923	0.896	0.994	0.967	0.971	0.983	0.937	0.989	0.996	0.996

C2		***trainscg***			***traincgb***			***traincgf***			***traincgp***			***traingdx***			***trainoss***			***Maximum***
mse	*Rsq2*	0.863	0.249	0.948	0.031	0.933	0.907	0.892	0.984	0.850	0.701	0.962	0.745	0.067	0.890	0.834	0.920	0.676	0.909	0.984
	rsquare	-2.754	-89.729	-39.810	-14.972	-12.639	-47.952	-11.361	-1.007	-131.260	-31.574	-10.587	0.425	-11.028	-4.690	-54.798	-10.992	-6.300	0.362	0.425
sse	*Rsq2*	0.286	0.317	0.927	0.826	0.938	0.823	0.596	0.934	0.285	0.945	0.805	0.872	0.871	0.156	0.919	0.971	0.891	0.595	0.971
	rsquare	-78.756	-159.242	-39.824	-61.044	-36.124	-80.597	-6.459	-73.870	-86.580	-19.984	-12.066	-11.050	-6.666	-3.849	-13.925	-15.499	-21.300	-10.096	-3.849

C3		***trainscg***			***traincgb***			***traincgf***			***traincgp***			***traingdx***			***trainoss***			***Maximum***
mse	*Rsq2*	0.954	0.983	0.989	0.998	0.990	0.778	0.986	0.952	0.974	0.013	0.996	0.909	0.931	0.966	0.945	0.883	0.989	0.987	0.998
	rsquare	0.915	-0.350	0.891	0.989	0.969	0.515	-0.549	0.262	0.101	-1.124	0.985	0.502	0.921	0.460	0.597	0.586	0.512	0.896	0.989
sse	*Rsq2*	0.695	0.007	0.994	0.983	0.925	0.988	0.970	0.831	0.991	0.989	0.998	0.989	0.766	0.845	0.989	0.996	0.772	0.972	0.998
	rsquare	0.668	-1.087	0.360	0.732	0.876	0.482	0.707	0.402	0.680	0.937	0.990	0.920	-0.063	0.502	-4.055	-1.304	0.627	0.763	0.990

C4		***trainscg***			***traincgb***			***traincgf***			***traincgp***			***traingdx***			***trainoss***			***Maximum***
mse	*Rsq2*	0.979	0.983	0.996	0.943	0.915	0.984	0.874	0.948	0.973	0.872	0.981	0.836	0.955	0.961	0.828	0.972	0.986	0.991	0.996
	rsquare	0.325	0.262	0.784	-24.619	-6.286	0.158	0.856	0.179	0.753	-36.076	-5.550	0.646	0.527	0.165	0.278	-2.796	0.792	0.432	0.856
sse	*Rsq2*	0.355	0.985	0.995	0.988	0.922	0.990	0.965	0.922	0.979	0.971	0.982	0.970	0.755	0.969	0.659	0.918	0.990	0.850	0.995
	rsquare	-1.203	0.931	0.712	0.471	0.921	-1.131	-0.768	0.707	0.001	-1.152	0.569	0.718	-1.491	0.845	-0.962	-6.118	-0.307	0.718	0.931

C5		***trainscg***			***traincgb***			***traincgf***			***traincgp***			***traingdx***			***trainoss***			***Maximum***
mse	*Rsq2*	0.692	0.936	0.956	0.959	0.928	0.997	0.972	0.962	0.984	0.096	0.836	0.539	0.771	0.363	0.910	0.744	0.950	0.965	0.997
	rsquare	-45.025	-21.414	-16.052	-35.283	0.441	0.753	-0.024	-18.639	-2.937	-0.942	-7.035	-88.902	0.719	-0.691	-41.356	-58.912	0.875	0.961	0.961
sse	*Rsq2*	0.932	0.946	0.947	0.746	0.897	0.895	0.701	0.788	0.857	0.961	0.000	0.859	0.771	0.860	0.340	0.133	0.970	0.309	0.970
	rsquare	-0.017	0.771	0.914	-93.151	-115.733	-38.740	0.558	-0.669	-118.420	0.946	-0.538	0.710	-16.983	0.673	-0.125	-40.651	-1.318	-1.737	0.946

C6		***trainscg***			***traincgb***			***traincgf***			***traincgp***			***traingdx***			***trainoss***			***Maximum***
mse	*Rsq2*	0.849	0.994	0.990	0.997	0.974	0.998	0.990	0.990	0.996	0.991	0.997	0.925	0.938	0.996	0.992	0.995	0.993	0.993	0.998
	rsquare	0.835	0.975	0.942	0.991	0.906	0.937	0.981	0.729	0.921	0.918	0.790	-0.980	0.860	0.978	0.983	0.977	0.668	0.926	0.991
sse	*Rsq2*	0.993	0.977	0.871	0.993	0.997	0.998	0.996	0.982	0.969	0.981	0.995	0.995	0.811	0.993	0.993	0.779	0.995	0.961	0.998
	rsquare	0.936	0.845	0.452	0.973	0.997	-0.044	0.858	0.933	0.835	0.875	0.935	0.978	0.799	0.993	-0.623	0.652	0.845	0.905	0.997

C7		***trainscg***			***traincgb***			***traincgf***			***traincgp***			***traingdx***			***trainoss***			***Maximum***
mse	*Rsq2*	0.991	0.986	0.941	0.950	0.922	0.995	0.905	0.995	0.994	0.992	0.983	0.986	0.986	0.984	0.983	0.742	0.995	0.991	0.995
	rsquare	0.972	0.958	-0.870	0.175	0.784	0.749	0.829	0.975	0.984	0.774	0.733	0.396	0.971	0.939	0.762	0.007	0.995	0.971	0.995
sse	*Rsq2*	0.991	0.997	0.995	0.520	0.997	0.989	0.984	0.903	0.562	0.993	0.974	0.964	0.969	0.991	0.982	0.872	0.985	0.710	0.997
	rsquare	0.877	0.967	0.976	-1.912	0.980	0.790	0.929	0.777	-4.683	0.903	0.658	0.672	0.604	0.990	0.974	-0.034	0.933	0.533	0.990

C8		***trainscg***			***traincgb***			***traincgf***			***traincgp***			***traingdx***			***trainoss***			***Maximum***
mse	*Rsq2*	0.996	0.996	0.996	0.996	0.997	0.995	0.996	0.998	0.995	0.998	0.996	0.997	0.991	0.992	0.994	0.984	0.995	0.996	0.998
	rsquare	0.990	0.993	0.987	0.986	0.993	0.926	0.939	0.934	0.927	0.993	0.984	0.863	0.983	0.976	0.963	0.810	0.945	0.984	0.993
sse	*Rsq2*	0.997	0.996	0.994	0.996	0.996	0.995	0.986	0.995	0.996	0.995	0.997	0.997	0.992	0.991	0.987	0.977	0.993	0.996	0.997
	rsquare	0.995	0.986	0.856	0.940	0.925	0.934	0.846	0.950	0.965	0.920	0.922	0.994	0.969	0.942	0.953	0.938	0.931	0.993	0.995

C9		***trainscg***			***traincgb***			***traincgf***			***traincgp***			***traingdx***			***trainoss***			***Maximum***
mse	*Rsq2*	0.961	0.809	0.217	0.989	0.303	0.967	0.767	0.952	0.894	0.314	0.002	0.806	0.344	0.836	0.246	0.014	0.348	0.746	0.989
	rsquare	0.828	0.706	-0.415	-1.696	-2.536	0.594	0.246	0.280	0.775	-0.134	-0.292	-23.894	-1.219	0.740	-7.483	-6.608	-2.297	0.464	0.828
sse	*Rsq2*	0.944	0.340	0.864	0.988	0.874	0.985	0.982	0.966	0.823	0.831	0.807	0.751	0.983	0.871	0.596	0.973	0.967	0.301	0.988
	rsquare	0.867	-0.194	0.696	-2.192	-4.485	0.125	0.950	0.395	0.467	0.790	0.667	0.428	-0.726	-0.783	0.188	-1.010	0.920	0.175	0.950

C10		***trainscg***			***traincgb***			***traincgf***			***traincgp***			***traingdx***			***trainoss***			***Maximum***
mse	*Rsq2*	0.993	0.994	0.993	0.992	0.996	0.994	0.991	0.993	0.991	0.993	0.993	0.990	0.984	0.992	0.986	0.987	0.976	0.991	0.996
	rsquare	0.939	0.895	0.986	0.916	0.984	0.988	0.990	0.985	0.974	0.987	0.938	0.988	0.968	0.983	0.876	0.986	0.974	0.988	0.990
sse	*Rsq2*	0.993	0.995	0.997	0.994	0.995	0.995	0.990	0.990	0.996	0.992	0.995	0.991	0.963	0.989	0.986	0.989	0.994	0.993	0.997
	rsquare	0.985	0.971	0.981	0.938	0.961	0.984	0.945	0.927	0.993	0.981	0.987	0.944	0.954	0.844	0.602	0.976	0.950	0.964	0.993

C11		***trainscg***			***traincgb***			***traincgf***			***traincgp***			***traingdx***			***trainoss***			***Maximum***
mse	*Rsq2*	0.996	0.999	0.999	0.996	0.998	0.999	0.987	0.999	0.997	0.999	0.998	0.984	0.984	0.997	0.995	0.999	0.992	0.998	0.999
	rsquare	0.966	0.915	0.995	0.940	0.985	0.991	0.985	0.979	0.953	0.975	0.954	0.983	0.963	0.927	0.718	0.955	0.975	0.997	0.997
sse	*Rsq2*	0.996	0.996	1.000	0.988	1.000	0.998	0.994	0.999	0.992	0.998	0.998	0.999	0.984	0.995	0.989	0.998	0.999	0.999	1.000
	rsquare	0.990	0.988	0.873	0.945	0.975	0.985	0.965	0.939	0.988	0.976	0.987	0.980	0.904	0.961	0.828	0.983	0.975	0.971	0.990

C12		***trainscg***			***traincgb***			***traincgf***			***traincgp***			***traingdx***			***trainoss***			***Maximum***
mse	*Rsq2*	0.996	0.992	0.991	0.995	0.988	0.994	0.931	0.994	0.998	0.993	0.982	0.935	0.982	0.967	0.996	0.989	0.998	0.996	0.998
	rsquare	0.995	0.991	0.807	0.824	0.876	0.823	0.865	0.893	0.881	0.692	0.808	0.776	0.903	0.855	0.990	0.986	0.983	0.981	0.995
sse	*Rsq2*	0.996	0.999	0.998	0.975	0.998	0.995	0.983	0.996	0.987	0.991	0.992	0.993	0.928	0.983	0.976	0.865	0.995	0.984	0.999
	rsquare	0.886	0.891	0.956	0.289	0.937	0.798	0.910	0.991	0.982	0.962	0.813	0.981	0.592	0.882	0.975	0.622	0.819	0.940	0.991

The average mean squared error for each of the training algorithms under evaluation is shown in table 6-9. These averages were taken over all the solid propellants and all three trained networks. The training function with the best overall correlation is the Fletcher-Powell conjugate gradient *(traincgf)* backpropagation function.

Table 6-9 Average mse values for training algorithms

trainscg	traincgb	traincgf	traincgp	traingdx	trainoss
0.666574	0.670046	0.690185	0.605857	0.628674	0.683852

The performance of all the training algorithms are comparable, which would suggest that the type of algorithm used for training the network does not have such great influence on the performance of the network. The further optimisation of a specific training algorithm may yield an improved performance of the neural network, but this is beyond the scope of this thesis.

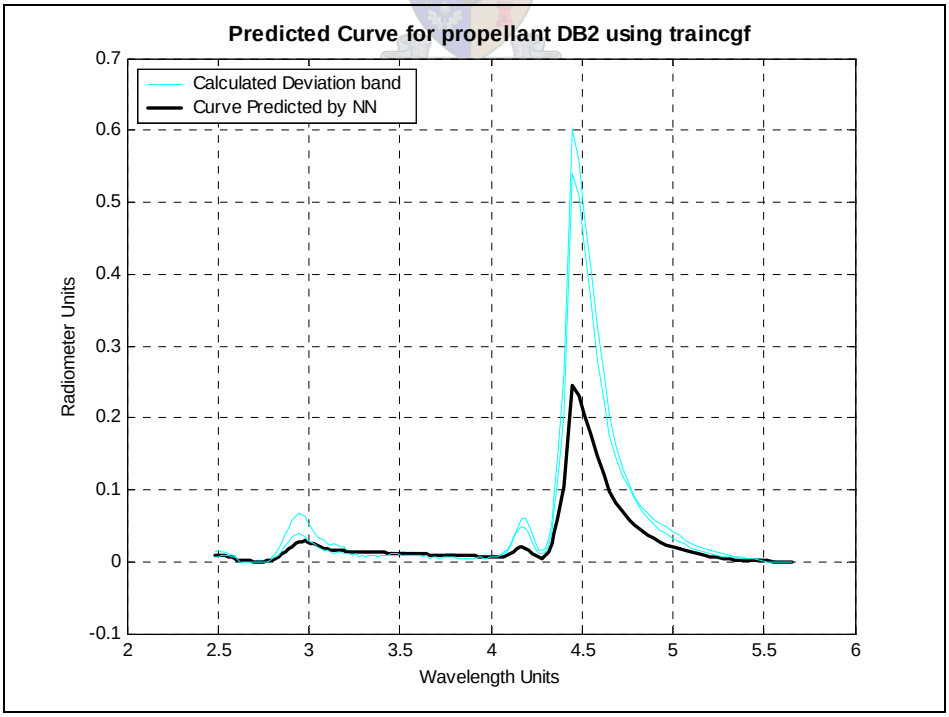

Figure 6.2-5 Predicted curve for DB2 using the Fletcher-Powell conjugate gradient function

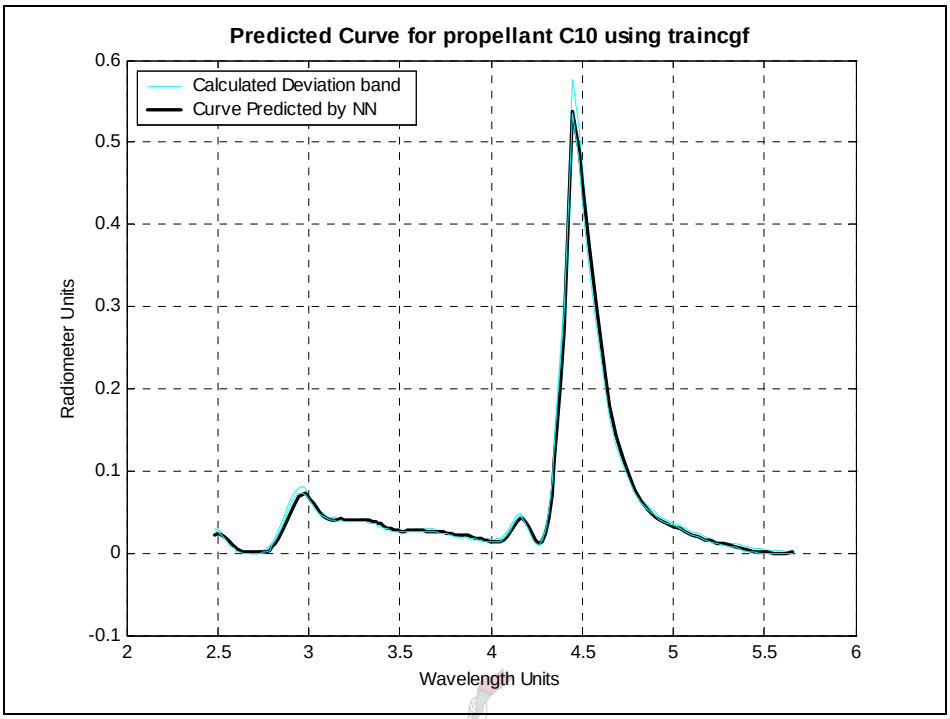

Figure 6.2-6 Predicted curve for C10 using the Fletcher-Powell conjugate gradient function

Although the solution for *DB2* is not as good as in fig. 6.2-4, it confirms a possible solution after 20 iterations per training data set. The predicted curve for *C10* in fig. 6.2-6, shows a good correlation with the measured curve. Considering the variable space of all the propellants IR spectra, it is possible to explain the poor correlation seen with some propellants. A good example is that of *DB3*, which could not be correlated to any degree, with the lesser number of training iterations. Another way of looking at the variable space is to plot the euclidean distances between the propellants. The euclidean distance is defined as:

$$d_{ij} = \left\{ \sum_{k=1}^{p} \left| x_{ik} - x_{jk} \right|^2 \right\}^{1/2} \tag{6-3}$$

where d_{ij} denotes the distance between propellants i and j [4], x_{ik}, the data point k of propellant i and p the number of observations .

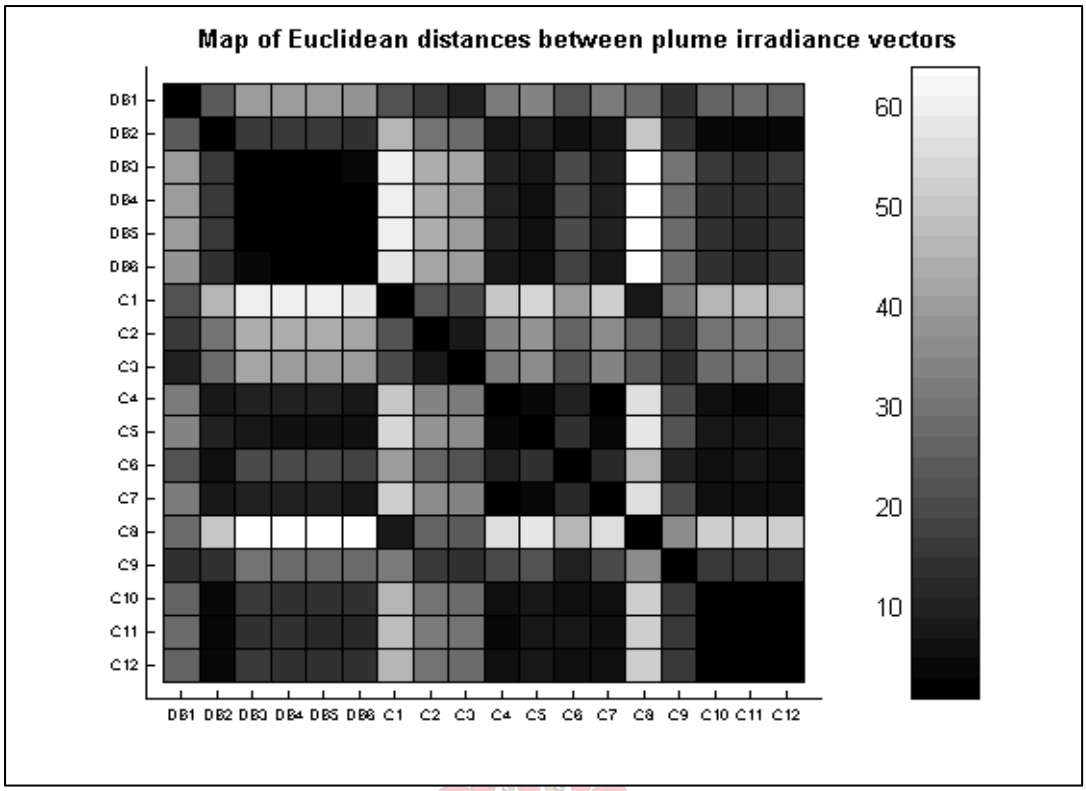

Figure 6.2-7 Map of Euclidean distances between plume irradiance vectors

The Euclidean distances of the irradiance spectra are plotted as a map in figure 6.2-7. On the diagonal each propellant is compared to itself, so the distance is zero and the block is coloured black. If the distance is large, the two vectors are vastly different which indicates that the propellants differ substantially. A large distance is indicated with a white block.

The map of euclidean distances clearly indicates the two classes of propellant. On the contrary to table 6-8, the map of euclidean distances indicates *DB3* to correlate well with the other propellants in the double-base class. If the input space of the network, i.e. the chemical composition along with the motor operating parameters were to be considered, a different plot of euclidean distances is found in fig.6.2-8.

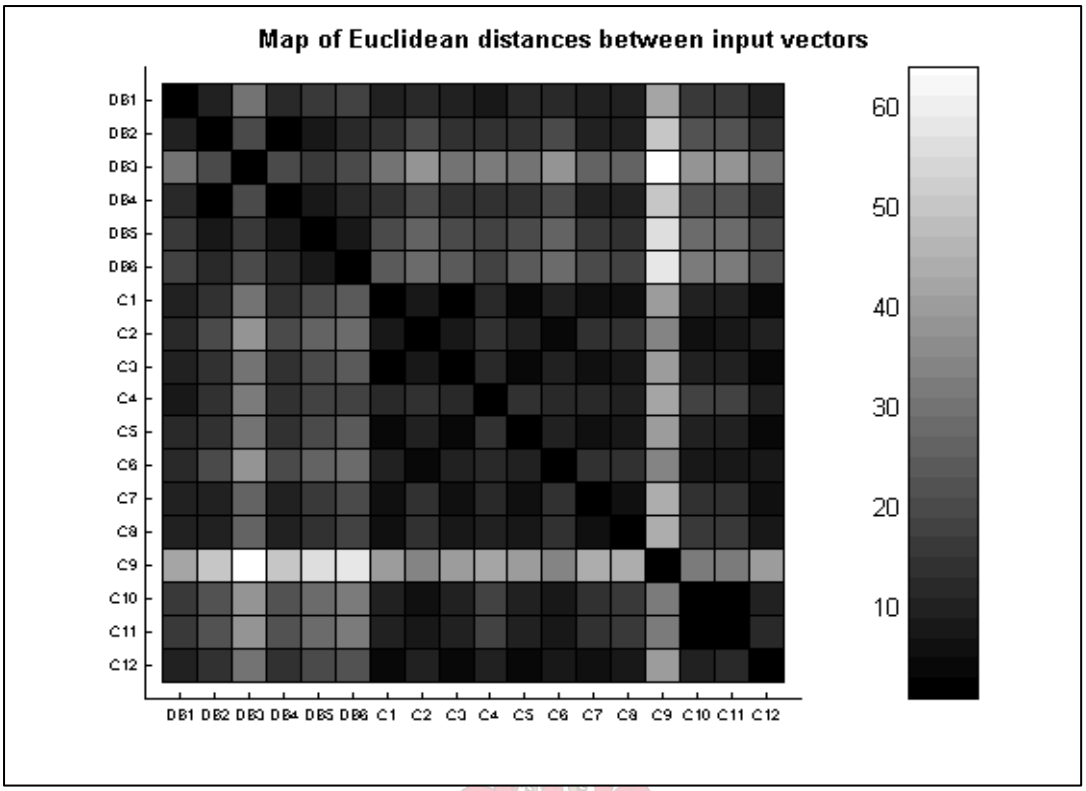

Figure 6.2-8 Map of Euclidean distances between input vectors

From this plot it is clear that *DB3* and *C9* occupy sparsely populated areas in the variable space. Figure 6.2-8 would suggest that the predicted curve of *C9* would not correlate as well with the measured spectra, compared to the other composite class propellants. On the contrary this is not the case, as can be seen in fig.6.2-22. A test set needs to be in an adequately populated area of the variable space, for the NN to be able to predict its IR spectra successfully, yet *C9* is predicted well and *DB3* not. The reason for this is that a NN can only extrapolate to a degree beyond the limits of the variable space, but can interpolate [5]. This is reflected by the fact that the map of euclidean distances, which indicates correlation between the propellants input space, and table 6-8, which shows if and how good a possible solution exists for each propellant, compares with each other. All the solid propellants were tested and plotted against their respective measured spectra, illustrating the generalization performance of the model.

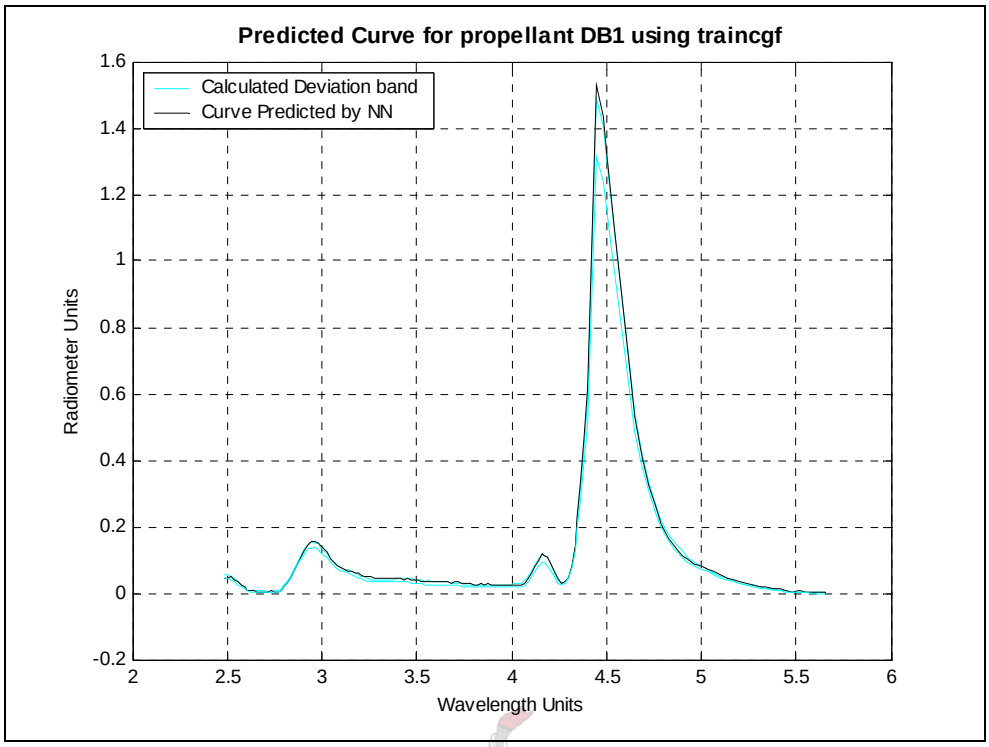

Figure 6.2-9 Irradiance predicted for propellant DB1

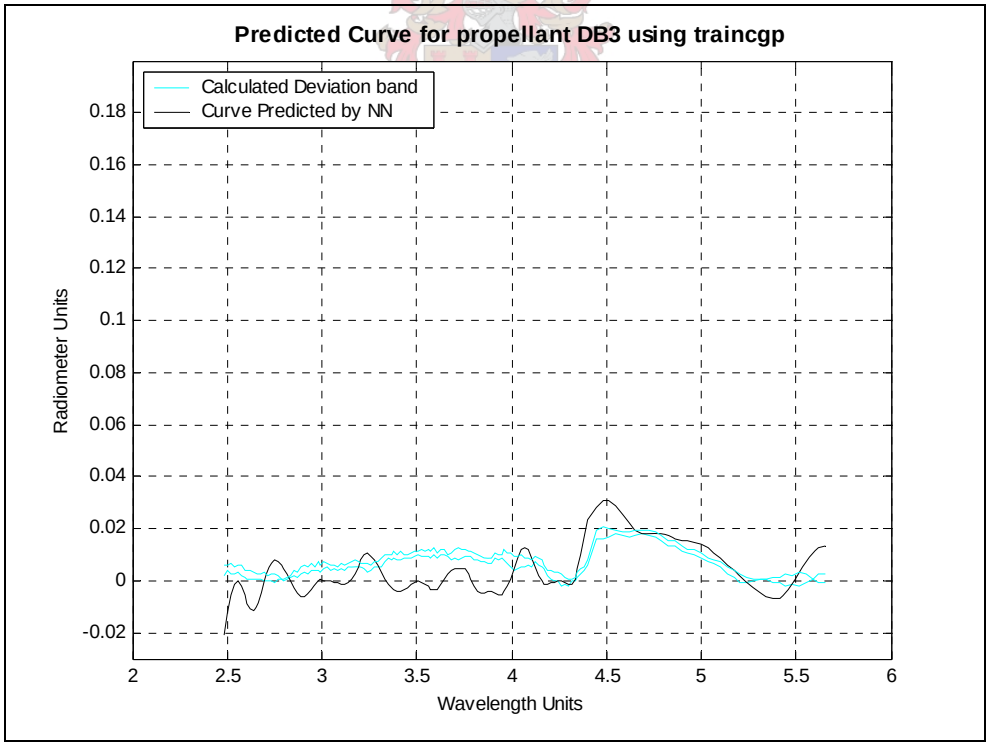

Figure 6.2-10 Irradiance predicted for propellant DB3

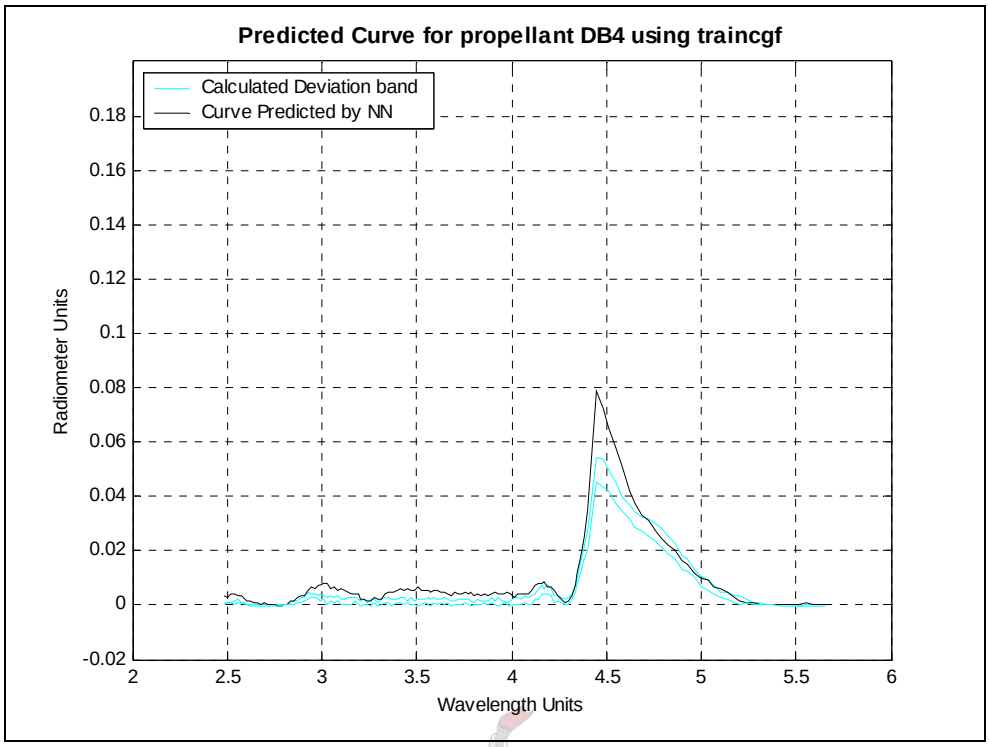

Figure 6.2-11 Irradiance predicted for propellant DB4

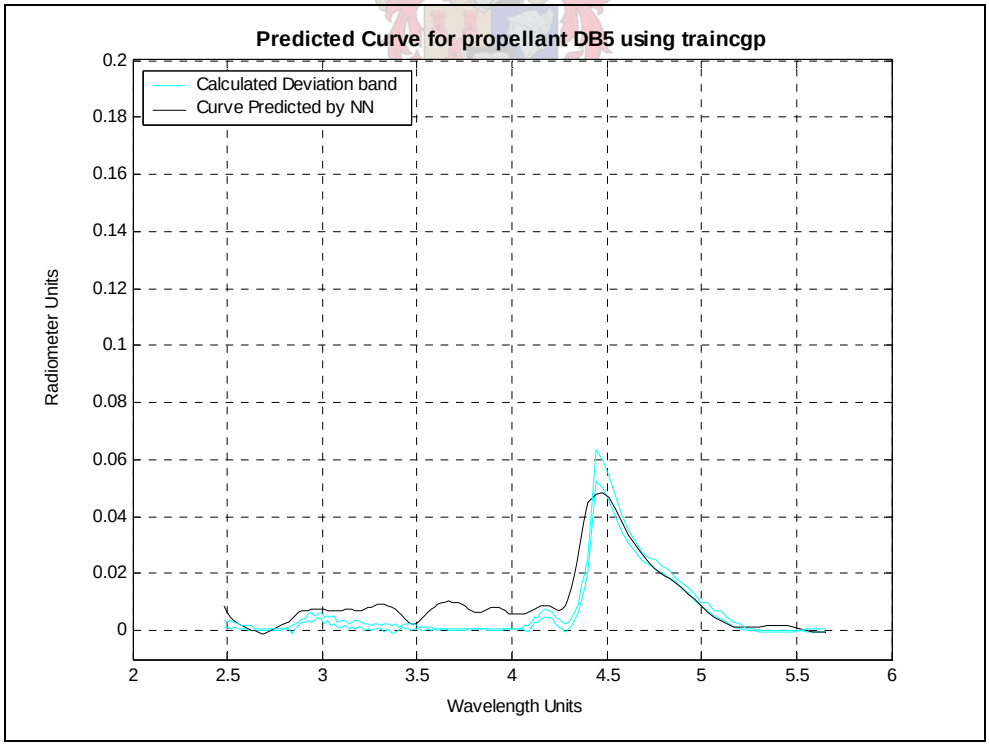

Figure 6.2-12 Irradiance predicted for propellant DB5

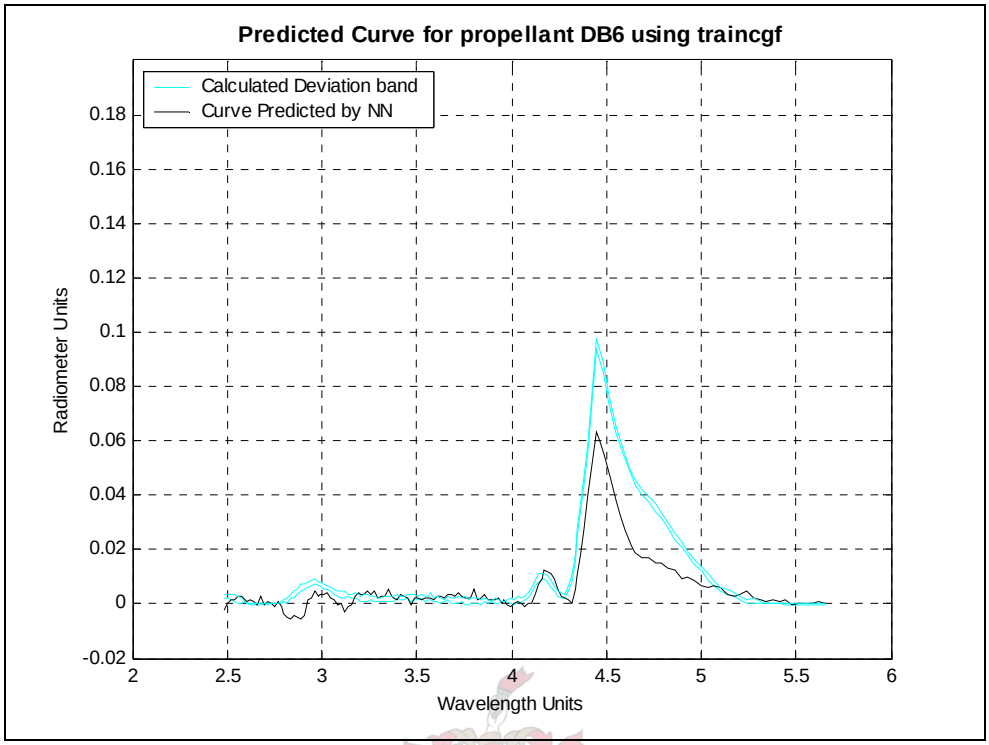

Figure 6.2-13 Irradiance predicted for propellant DB6

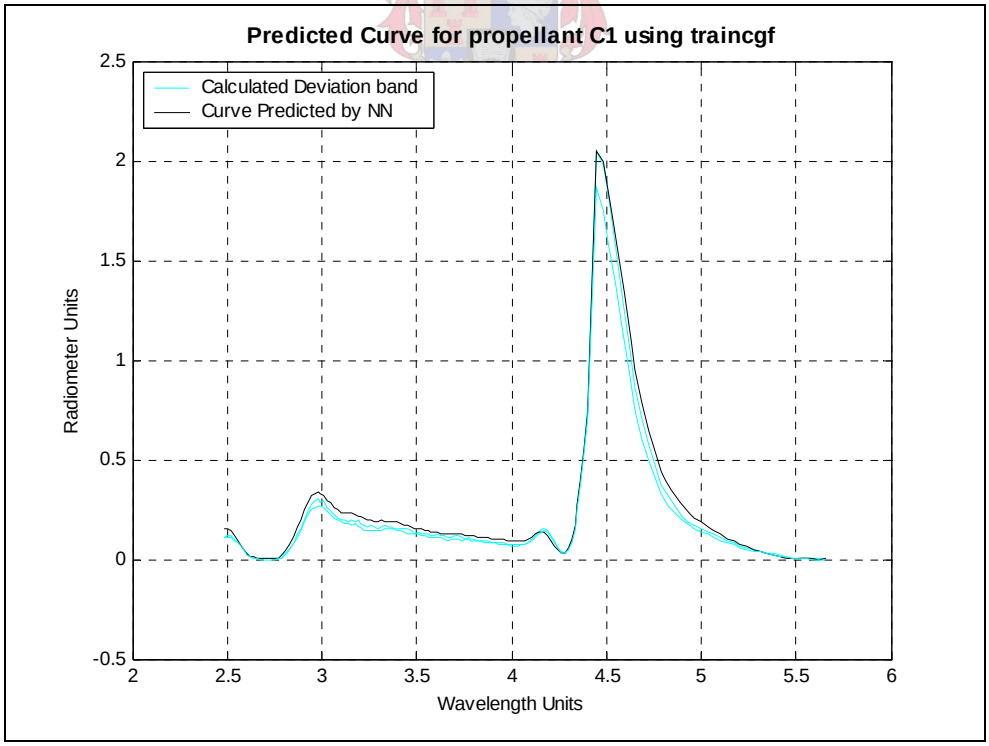

Figure 6.2-14 Irradiance predicted for propellant C1

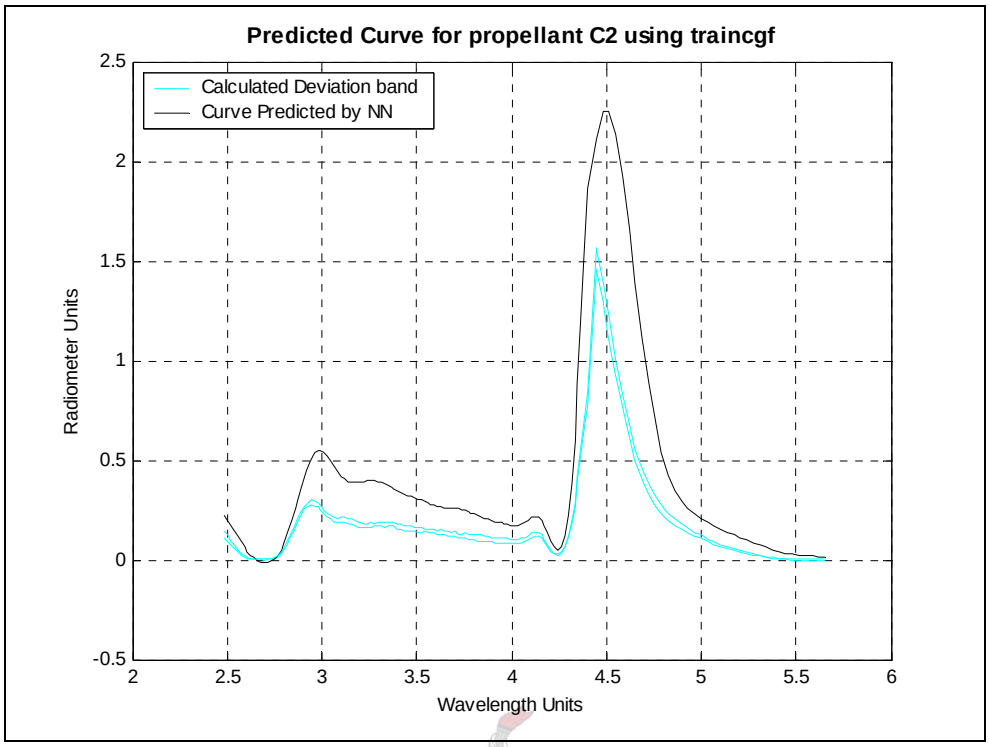

Figure 6.2-15 Irradiance predicted for propellant C2

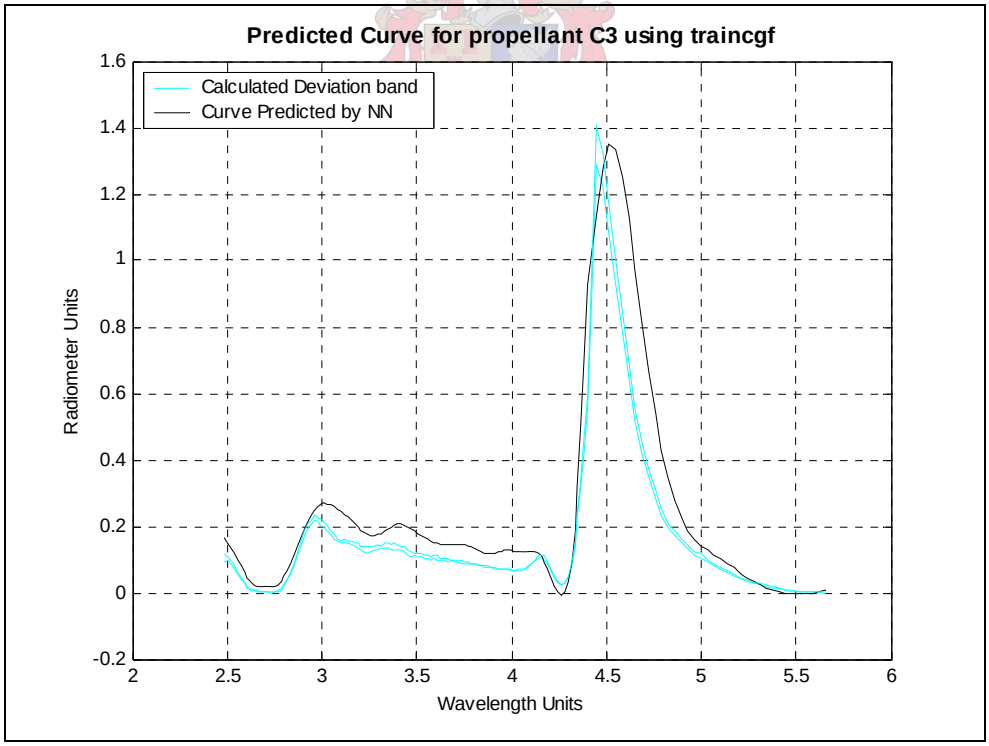

Figure 6.2-16 Irradiance predicted for propellant C3

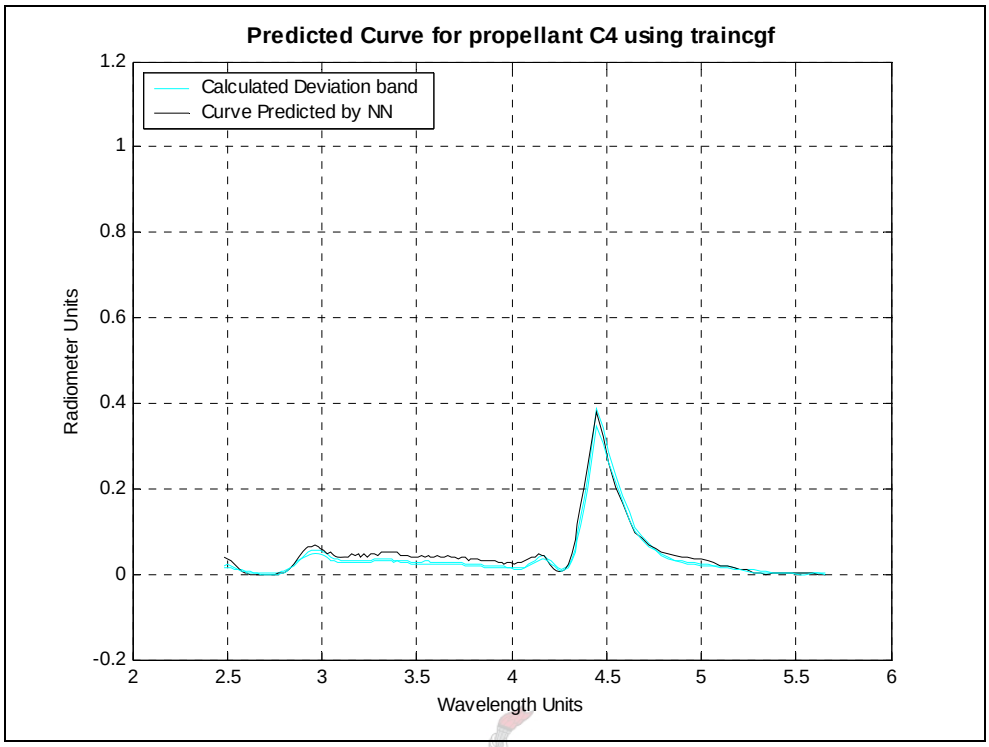

Figure 6.2-17 Irradiance predicted for propellant C4

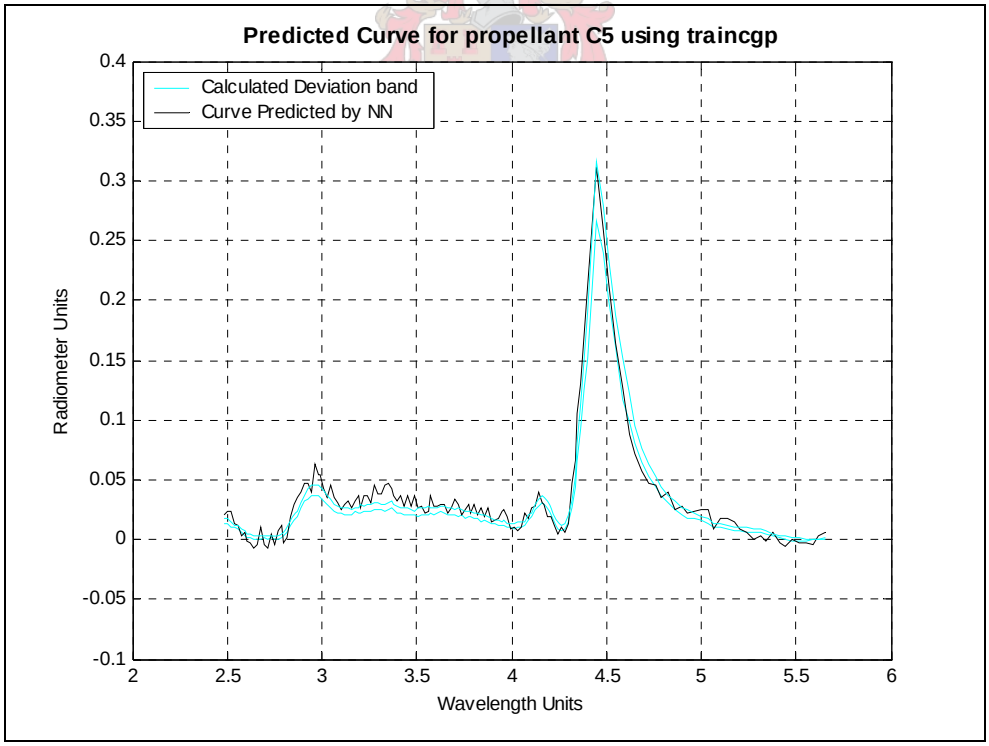

Figure 6.2-18 Irradiance predicted for propellant C5

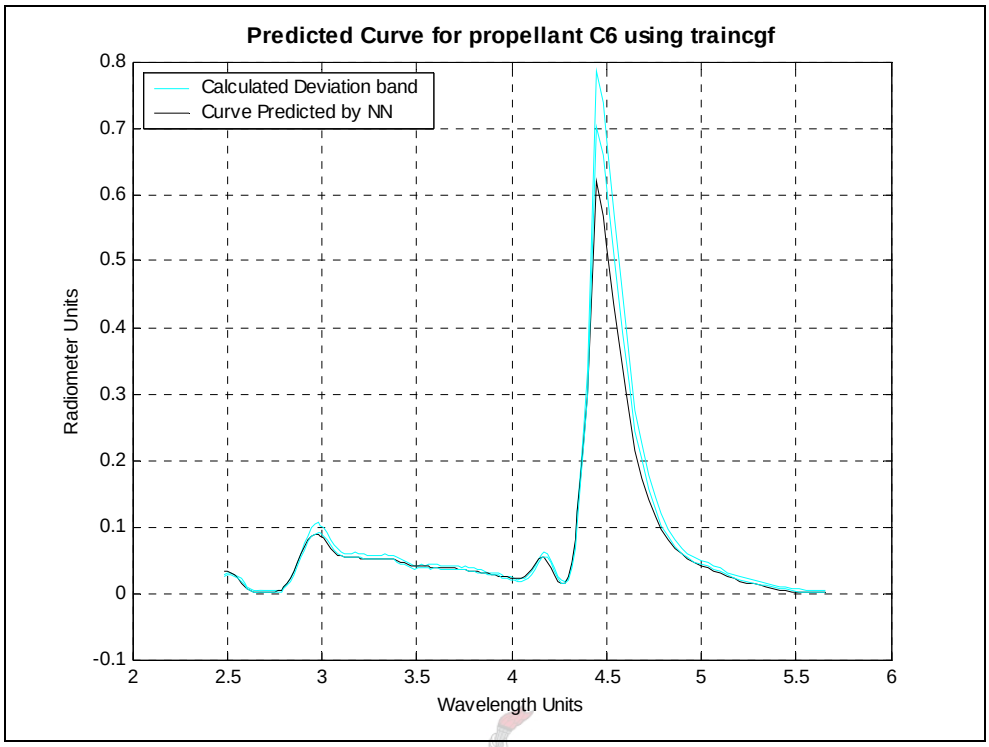

Figure 6.2-19 Irradiance predicted for propellant C6

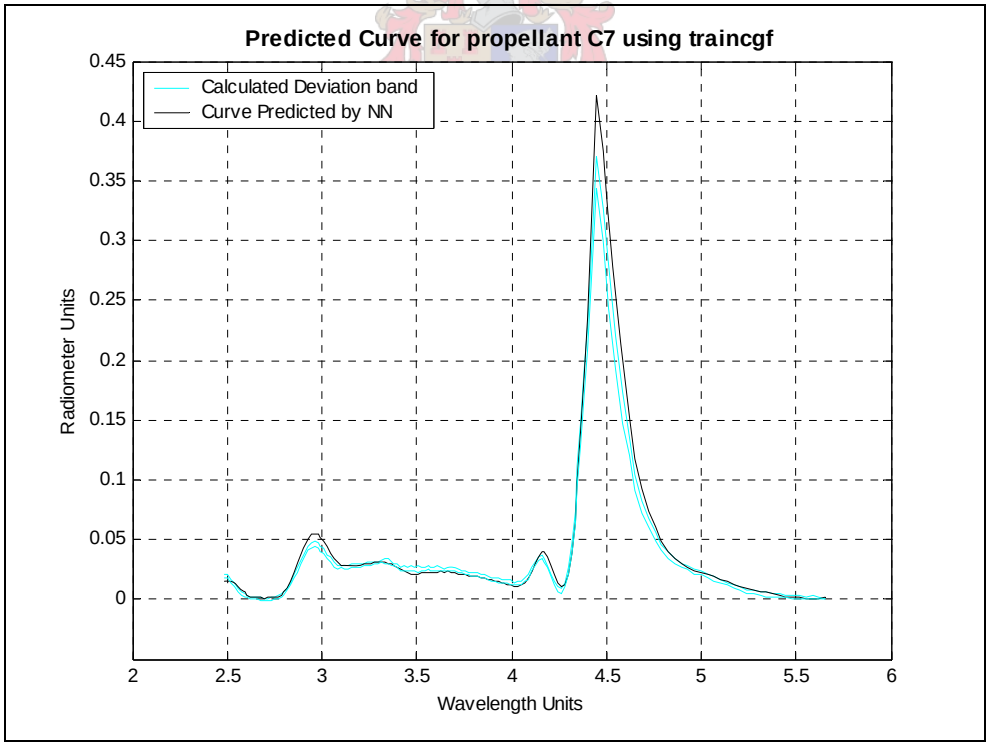

Figure 6.2-20 Irradiance predicted for propellant C7

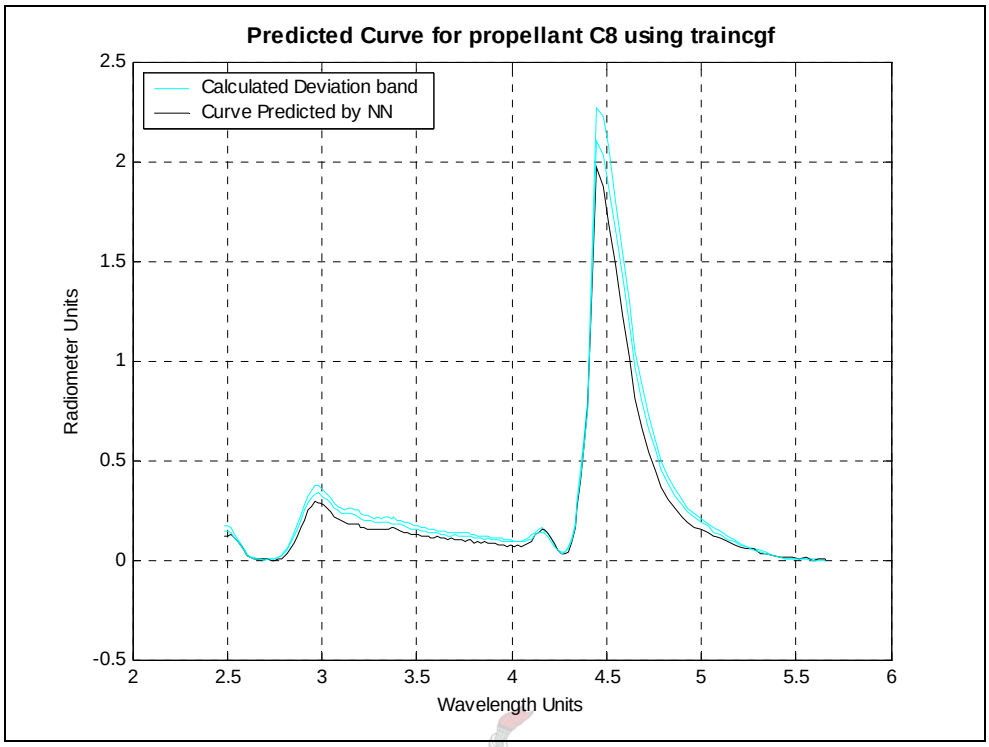

Figure 6.2-21 Irradiance predicted for propellant C8

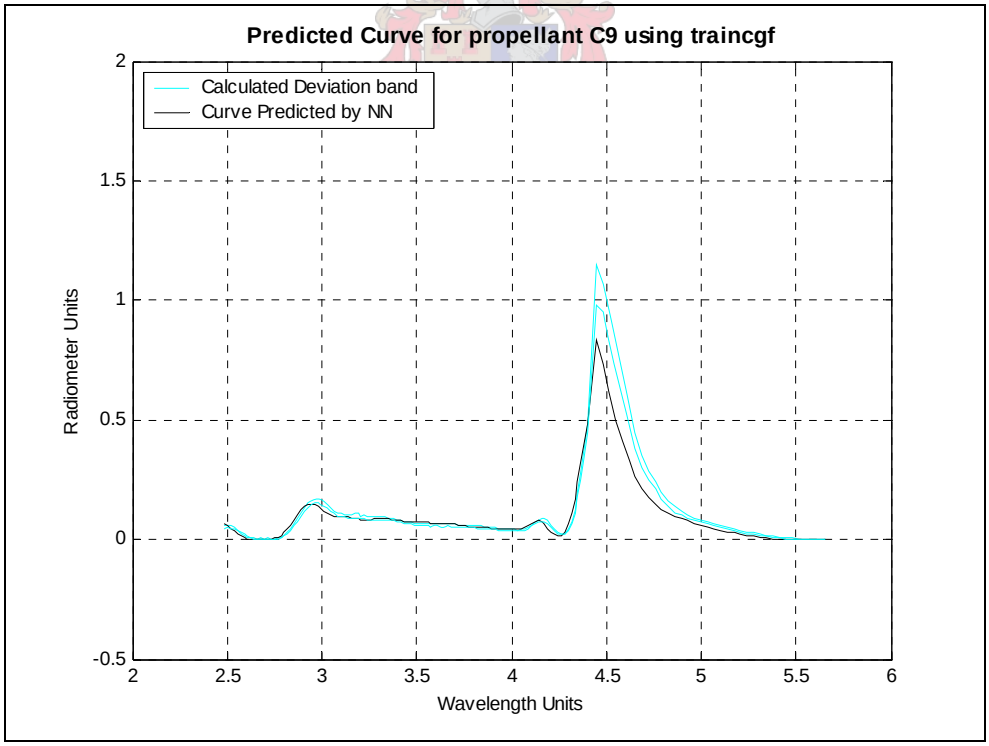

Figure 6.2-22 Irradiance predicted for propellant C9

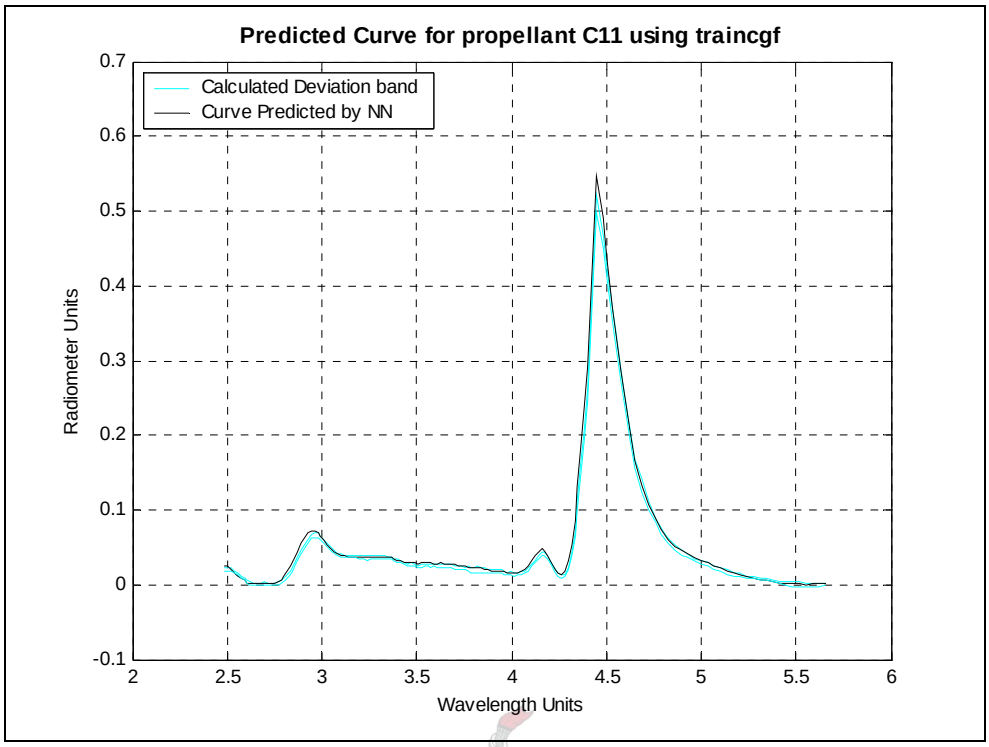

Figure 6.2-23 Irradiance predicted for propellant C11

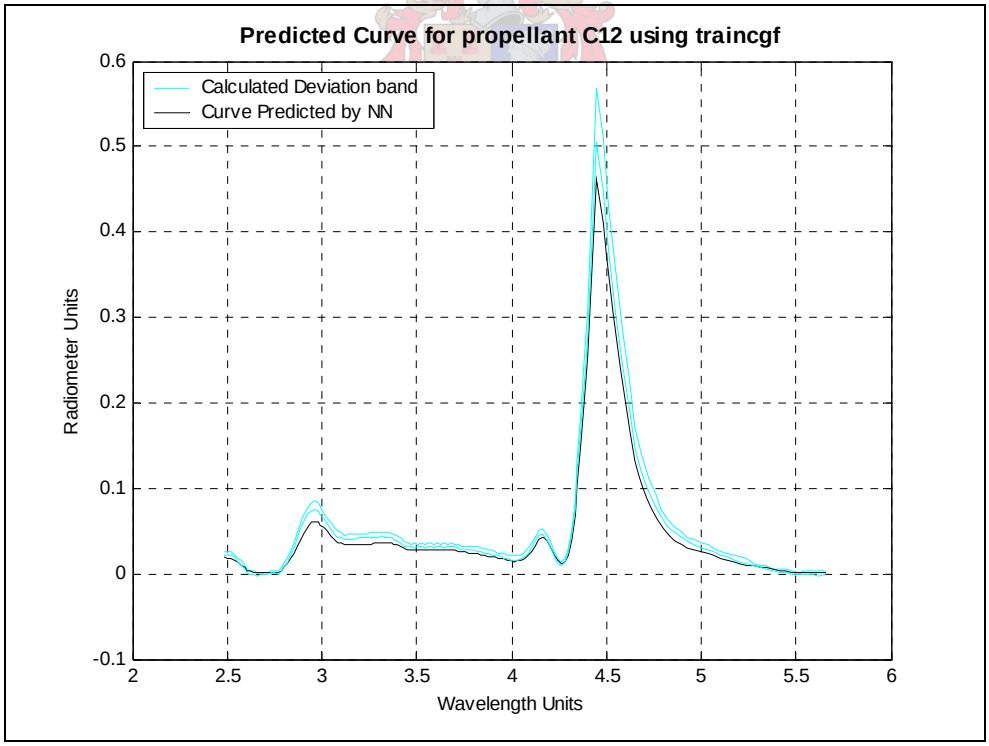

Figure 6.2-24 Irradiance predicted for propellant C12

It is clear that in most of the cases the shape of the predicted curve matches that of the measure IR spectra. The prediction for the test set *DB2* in fig.6.2-4 was not as good as would be expected, but the trend of the curve is predicted correct.

The large peak at wavelength 4.4 is due to CO_2 gas radiating strongly. The largest standard deviation in the spectral band is detected here. This could serve as reason why certain predicted curves do not always correlate well with the height of this peak. Another important part of the spectral recording is the characteristic peaks in the wavelength band 2.5 – 4.0, which is the result of water and metals radiating. These peaks are also important in pattern recognition (and characteristic of a propellant) and therefore the complete curve should be modelled correctly. It was found that these features are predicted accurately in position and in proportion to the CO_2 peak in terms of the overall height and shape of each spectrum.

It has been shown that the model cannot correctly predict the curve for *DB3* and to a degree *DB4* and *DB5*. *DB3* has a low chamber temperature (<1900 K) with a small throat diameter (small mass flow), thus the measured irradiance is very low compared to the other propellants. This motor design differs appreciably and it was shown when the input spaces were compared in fig. 6.2-8. However the model does succeed in predicting the low irradiance measured, if not the correct trend.

The flame suppressant effect of potassium compounds on the irradiance levels is clearly seen in the plot of *DB4*. *DB4* resembles *DB2*, except for the added potassium, which results in a much lower average irradiance recording. The model predicts the curve for *DB4* reasonable well, showing that the model is able to predict changes in the potassium input.

In the composite class of propellants, all the propellants are predicted accurately, except for *C2* and *C3*. The map of euclidean distances for inputs shows *C1, C2* and *C3*, to closely resemble each other, yet the map of the irradiance vectors show them to differ remarkably. The only noted difference in input of *C2* is that it contains iron and that of

C3 contains potassium. Only two other compositions contain iron, but in much smaller quantities, therefore the model is not capable to correctly predict *C2*'s irradiance curve. *C3* contains potassium, which lowers irradiance levels as with *DB4*. The model succeeds in predicting this trend to a certain degree. In the 3 – 4 micron wavelength band, the trend is not correctly predicted, but resembles that of *C1*. This could be due to the fact that the chamber pressure for *C3* is lower than that of *C1*, which also lowers the irradiance levels; this follows from work done in chapter 2 [6].

The model generally predicts the curves well, but it needs to be tested for a change in input, to determine if the model is sensitive for changes in input.

6.2.4. Performance of the Model

The two test sets *C10* and *DB2* were used to test for changes to the input.

- *The chamber pressure and temperature*

If the chamber pressure and temperature are increased, the plume temperature should increase, with a consequent increase in irradiance [6].

- *The throat diameter*

If the throat diameter is increased, the gas flow is increased and the cooling in the plume will be reduced. The optical depth of the plume also increases slightly, with a resulting increase in irradiance [1].

- *The amount of aluminium*

If the aluminium content is decreased, the amount of solids in the plume may be reduced. Since solids act as blackbody radiators the optical density will decrease, lowering the irradiance.

- *The amount of flame suppressant*

Potassium compounds acts as flame suppressants. Thus an addition of potassium will cause the irradiance to drop in the infrared wavelength band of interest.

The tests employed here are not to be seen as sensitivity testing, but rather an exercise to see whether it is possible to predict the spectral responses expected from experience. For example in decreasing the throat diameter, the plume actually becomes smaller and thus radiates less energy. The tests shown here were the ones where the effect of changes to the input could be seen best. The parameters that are changed here are the parameters most often controlled in developing solid propellants.

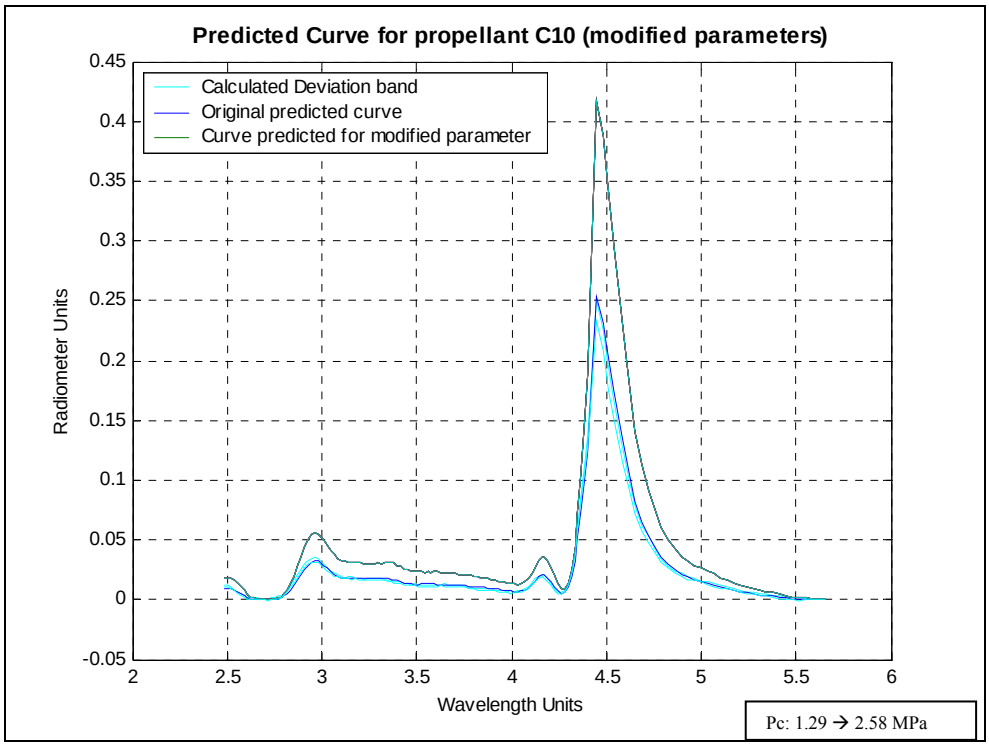

Figure 6.2-25 Curve predicted for a change in pressure for C10

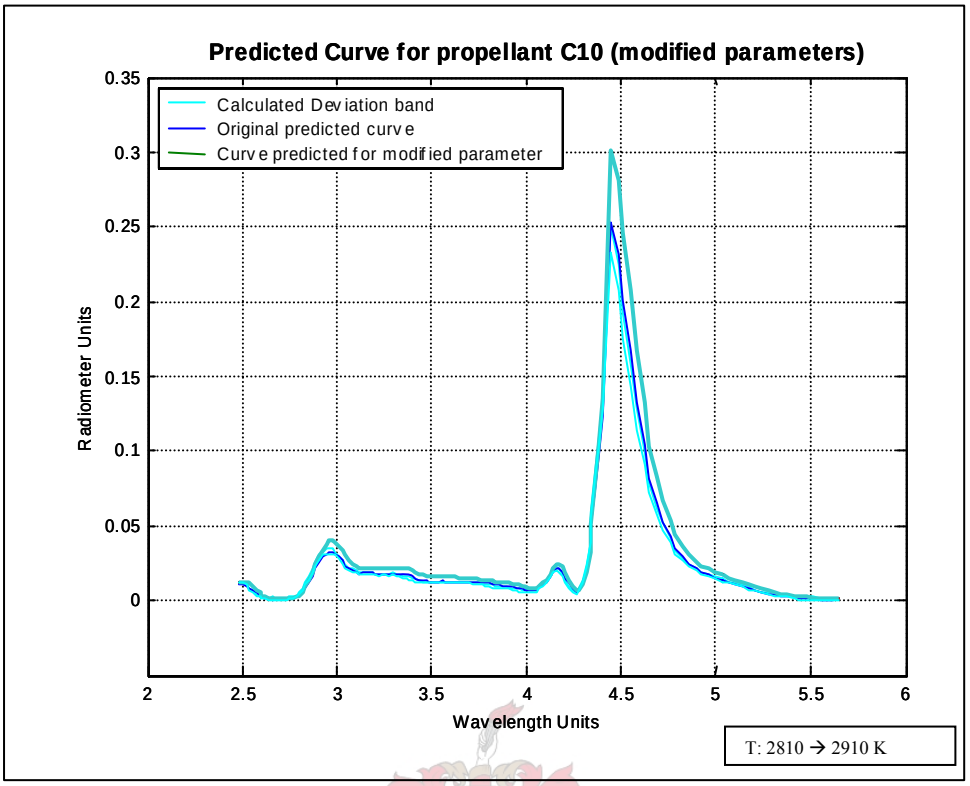

Figure 6.2-26 Curve predicted for a change in temperature for C10

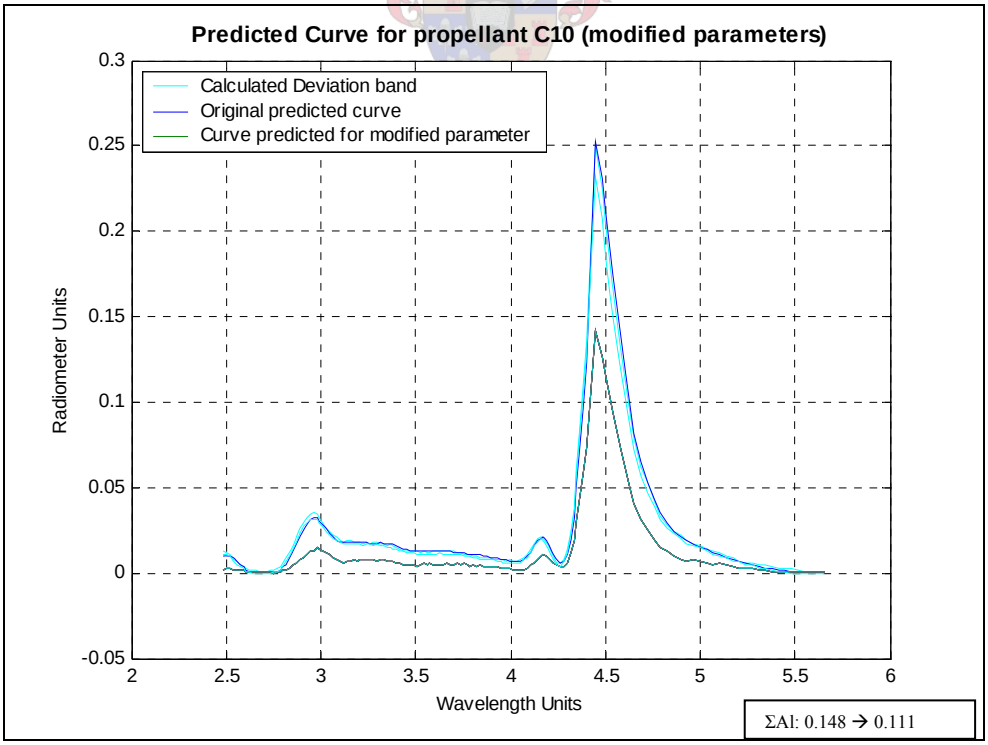

Figure 6.2-27 Curve predicted for a change in Aluminium content for C10

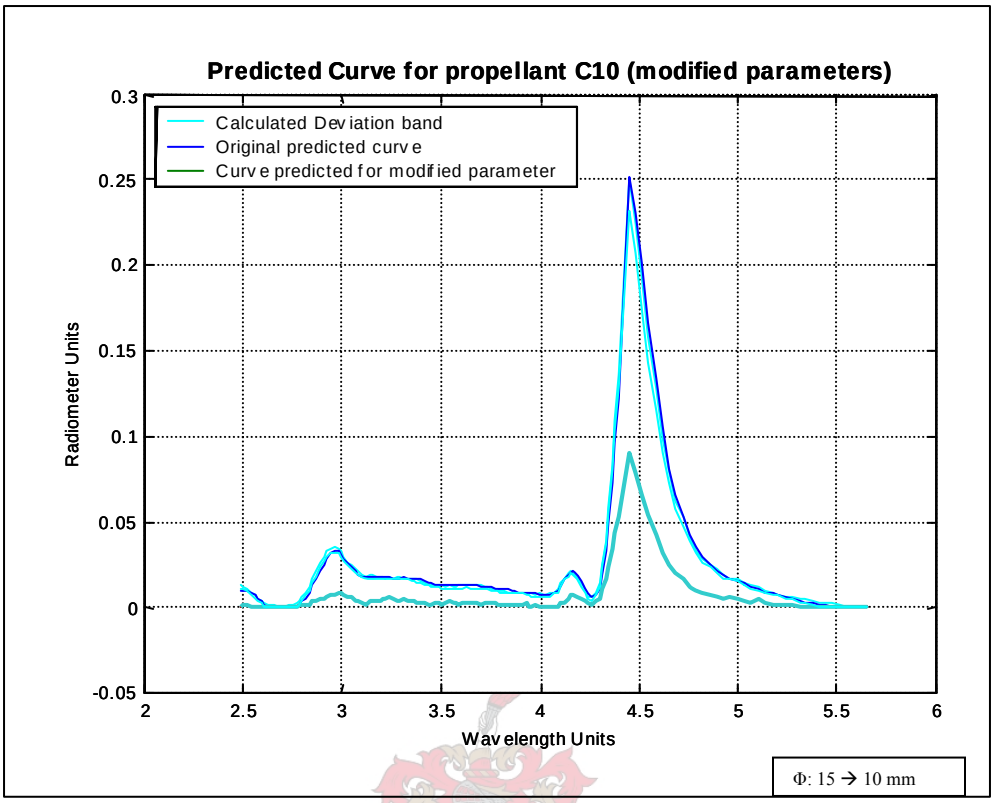

Figure 6.2-28 Curve predicted for a change in throat diameter for C10

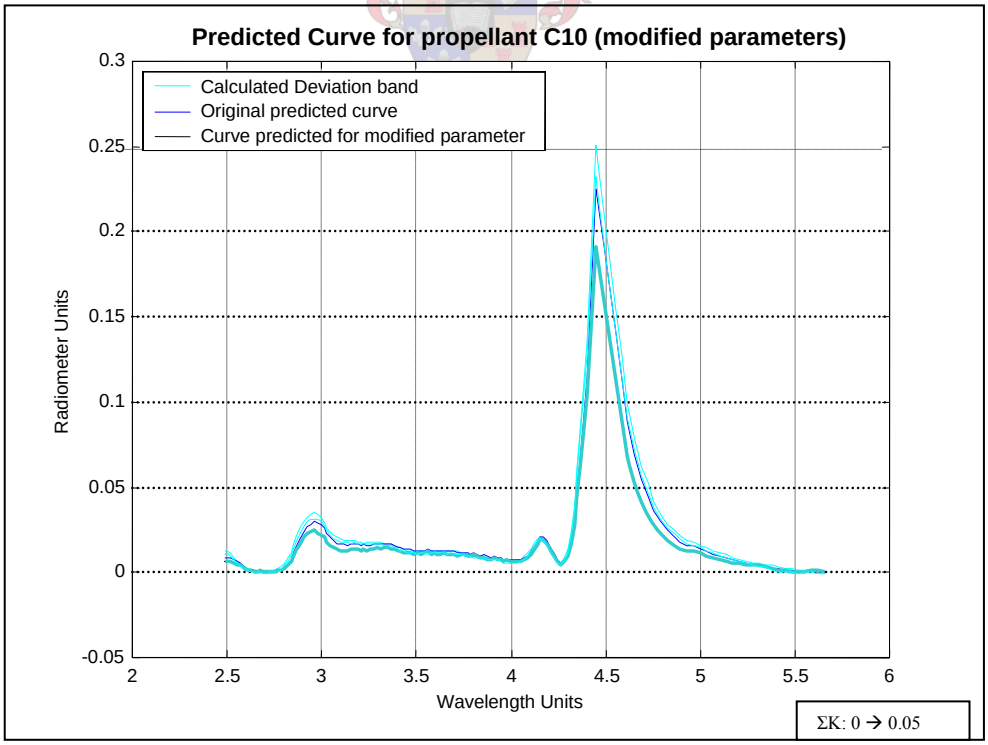

Figure 6.2-29 Curve predicted for a change in potassium content for C10

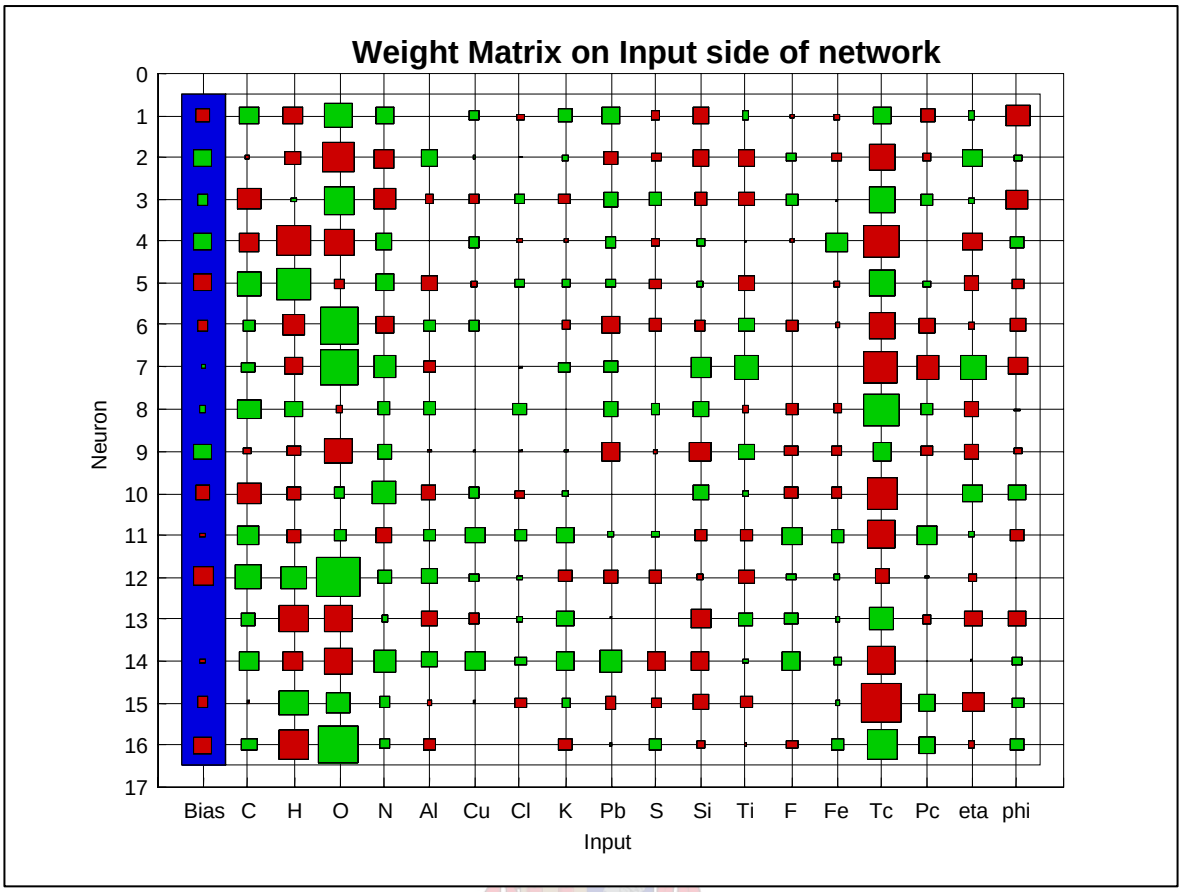

Figure 6.2-30 Weight matrix of the input side of the network

6.3. Discussion of Results

It was shown that the model is capable of predicting the correct trend for most of the propellants. Only for the propellants on the edge of the variable space (or in sparsely populated areas in the variable space), the model could not predict the correct trend. The model is proficient in predicting variations in temperature, pressure, throat diameter, aluminium and potassium content.

The R^2 evaluation parameters for each of the propellant test sets are shown in table 6-10. The values in table 6-10 imply that the neural network generated a good working model. The average R^2 for all the test sets is 0.957, which indicates that overall the predicted spectra correlated well with the measured values. It is only DB3, in fig.6.2-10, that

shows poor correlation, which could be due to various factors, i.e. the net was not trained long enough or the net needed more hidden nodes.

Table 6-10 R2 values for each of the test sets

	R^2
DB1	1.000
DB2	0.988
DB3	0.539
DB4	0.978
DB5	0.897
DB6	0.953
C1	0.998
C2	0.971
C3	0.955
C4	0.985
C5	0.980
C6	0.997
C7	0.996
C8	0.999
C9	0.991
C10	0.997
C11	0.998
C12	0.999

By plotting the euclidean distance between the measured spectral points and the predicted values, it is possible to view the solution relative to the goal. The smaller the value of the distance between the two spectral bands, the better the solution is.

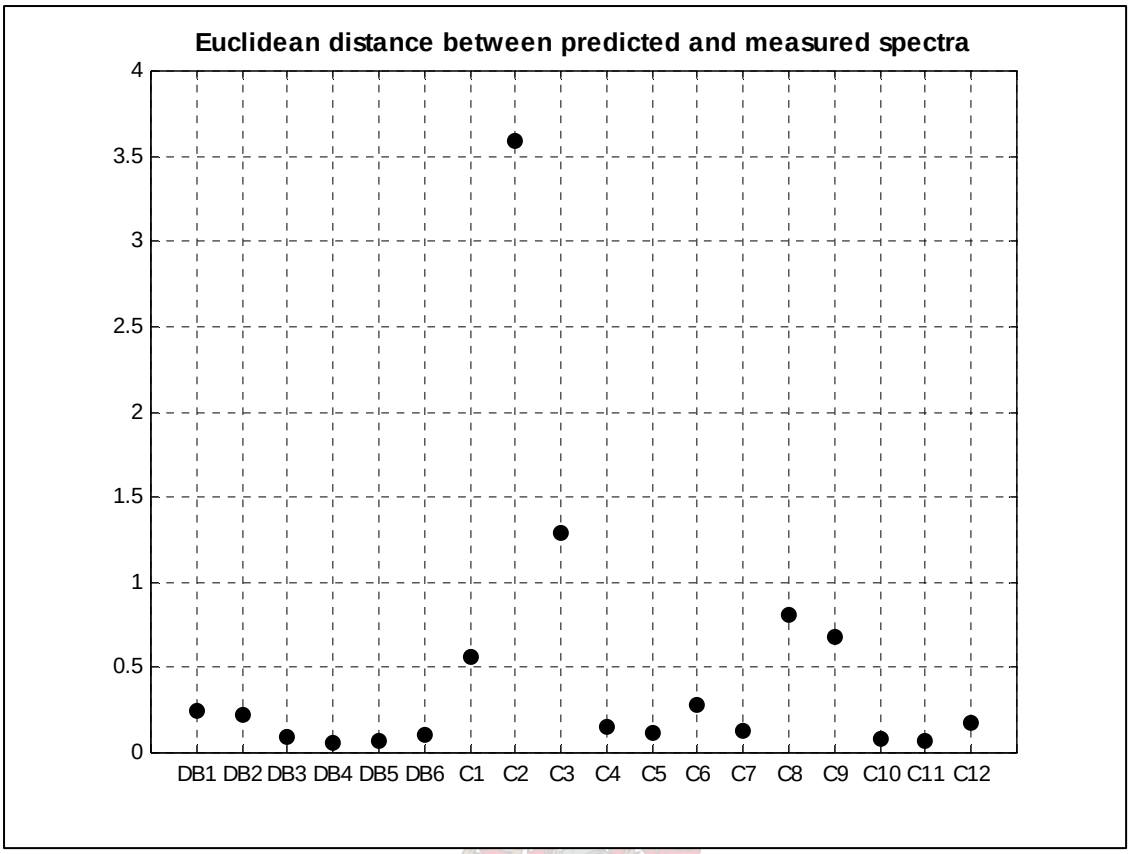

Figure 6.3-1 Comparing the predicted and measured IR spectra in terms of Euclidean distance

In fig 6.3-1 there are 5 points with a value bigger than 0.5. Keeping in mind the fact that the spectral band has a dimensionality of 146, fig. 6.3-1 shows that the solution for these 5 points are not good. Referring back to fig. 6.2-7, the map of Euclidean distances between plume irradiance vectors, four vectors, *C1, C2, C3, C8* and *DB1,* have large euclidean distances when compared to the other propellants. From 6.2-8, *C9, DB3, DB5* and *DB6* are the propellants which do not correlate with the other inputs. These identified propellants lie in a sparsely populated area of either the input or the output of the variable space, and have been found unsuited as test sets. On the account of fig.6.3-1 it is not possible to evaluate the model properly. Another way of evaluating the model is by using statistical tests. Note that the euclidean distance for *DB3, DB5* and *DB6* show small values, even though the correlation to the measured values is not as good as projected here. This is due to the low level of the spectral irradiance; the level is two orders smaller than most of the irradiance measured and therefore the error is also smaller.

6.3.1. Statistical Tests

To show that the model is unique and not just an average of the variable space, it will be compared to the 'static model' (the mean of the variable space), using several statistical tests. The mean squared error *(mse)* will be used to test for correlation in evaluating whether the NN model or the static model show better correlation to the measured irradiance.

$$mse = \frac{\sum_{i=1}^{146} \left(Model_i - Measured_i \right)^2}{146} \tag{6-4}$$

Table 6-11 Mean squared error for NN model and Static Model

	NN Model	***Static Model***
DB1	0.000397	0.0128
DB2	0.000345	0.0022
DB3	0.0000698	0.0173
DB4	0.0000240	0.0161
DB5	0.0000359	0.0160
DB6	0.0000718	0.0143
C1	0.00214	0.0534
C2	0.0880	0.0240
C3	0.0114	0.0145
C4	0.000165	0.0054
C5	0.000100	0.0074
C6	0.000520	0.0001
C7	0.000203	0.0063
C8	0.00185	0.0757
C9	0.00118	0.0022
C10	0.0000420	0.0017
C11	0.0000638	0.0024
C12	0.000221	0.0020
Average	**0.0059**	**0.0152**

From table 6-11 the *mse* for the NN model indicates a better fit of the measured data than that of the static model. This is also reflected in fig. 6.3-2 and fig. 6.3-3.

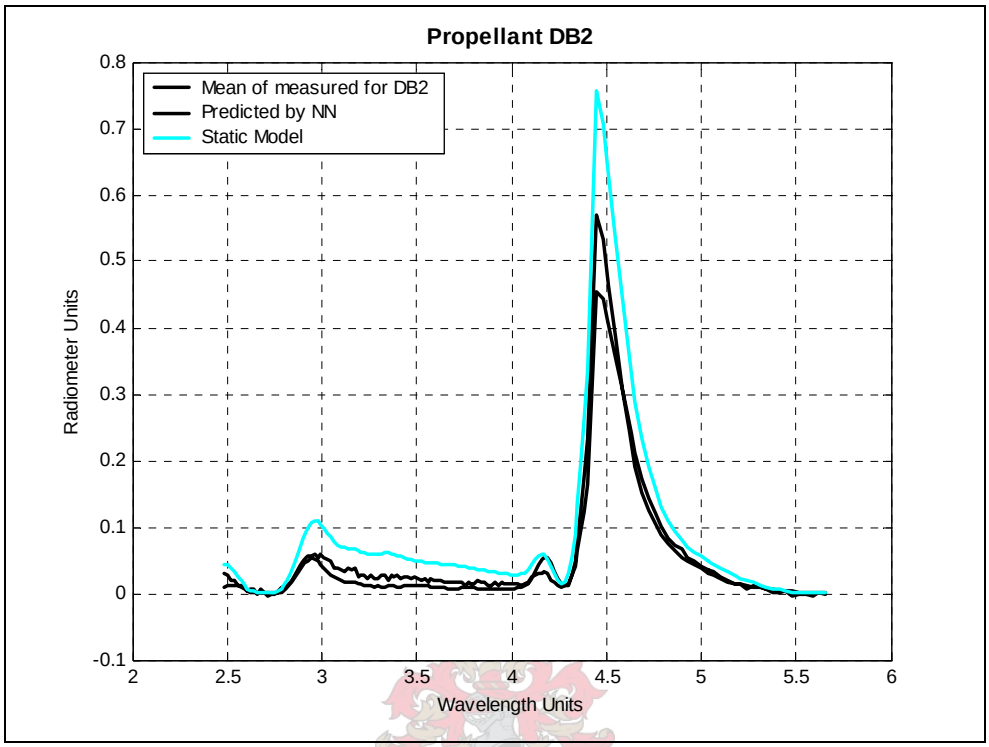

Figure 6.3-2Comparing the *mse* for the NN and static model for DB2

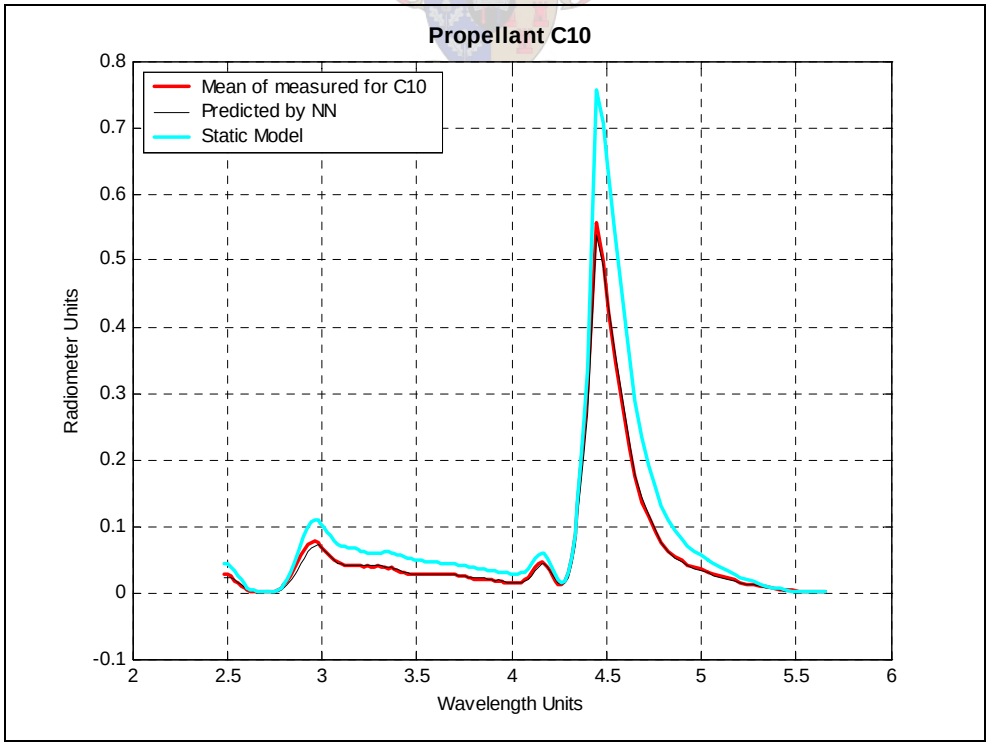

Figure 6.3-3 Comparing the *mse* for the NN and static model for C10

Two further tests were done: a t-test on the residuals of two models and the measured spectra, and a Wilcoxon signed-rank test (non-parametric test). The residuals, which are the difference between the model and the measured spectral points, were calculated and used for a t-test, to test the hypothesis that the mean of the residuals of the NN model is smaller than that of the static model. Two t-tests were done for the two test sets, at a confidence level of $\alpha = 0.05$ [8].

The null hypothesis is H_0: $\mu_{NN} = \mu_{static}$ ($\mu \equiv$ mean of residuals)
Alternative hypothesis is H_a: $\mu_{NN} < \mu_{static}$
$t_\alpha = 1.645$

Table 6-12 T-test statistic for test sets

	DB2	***C10***
t	-10.0330	-8.3354

The null hypothesis is rejected when $t < -t_\alpha$ and then the alternative hypothesis is accepted, which states that the error of the NN model will be smaller than that of the static model.

Non-parametric tests depend on the order of relationships among observations. For the given problem, it has to be decided whether two populations (residuals) are the same or whether one is likely to produce larger observations than the other. The null hypothesis to be tested proposes that the two sample populations (NN and static model), come from the same populations, thus the means or the sums of the ranking positions should be fairly similar [2].

Table 6-13 Wilcoxon ranksum test statistic for test sets

	DB2	***C10***
Z	-9.6766	-13.0379
p	0	0

Again the null hypothesis is rejected if $z < -z_{\alpha} = -1.645$ and the alternative hypothesis is accepted, stating that the two populations are not even remotely the same. The large value of the z statistic indicates that the residuals of the static model are much larger than that of the NN model. The statistic, p, is the probability of observing a result equally or more extreme than the one using the data (NN and static) if the null hypothesis is true. If p is near zero, it casts doubt on this hypothesis.

These statistical tests confirm the results from the correlation tests. The model is not an average of the variable space and is able to dynamically predict the propellant irradiance spectra. The model is also able to predict the correct change of the IR spectra (in the correct wavelength band) for a change in the input vector.

6.4. Reversing the neural network

In order to determine if it would be possible for the neural network to predict the chemical composition and motor parameters of the solid propellant rockets, the neural network was reversed. The input now consisted of 146 spectral points and the output of 14 chemical elements and 4 motor working parameters.

Table 6-14 Neural network setup for reverse network

Feature	***NN_{16}***	***Matlab function***
No. neurons in Input layer	146	
No. neurons in Hidden layer	16	
No. neurons in Output layer	18	
Training Function	Scaled conjugate gradient backpropagation [3]	trainscg
Performance function	Mean squared error	mse
Hidden layer Transfer function	Hyperbolic tangent sigmoidal	tansig
Output layer Transfer function	Linear	purelin

The reversed network was investigated to see whether it is possible to predict the composition of the solid propellants and the motor design, by using the infrared spectra as input. This result has many applications in the battlefield: if one could predict what the propellant and motor design of a rocket is, it would be possible to classify the rocket and the correct countermeasure would be taken. This model, however, is only a conceptual model and not optimised, yet already the predicted values hold promise where the accuracy of the prediction is concerned.

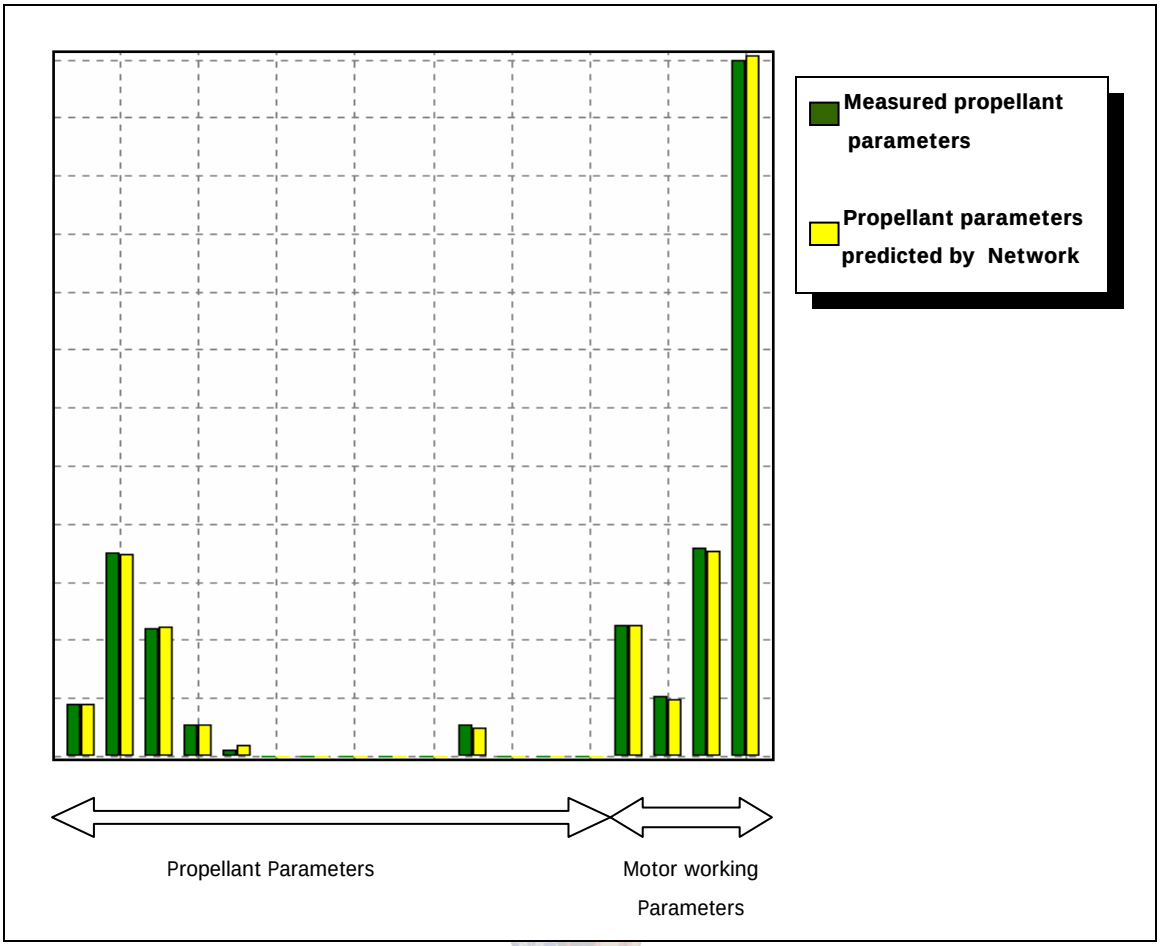

Figure 6.4-1 Results for test set C10

The results from the reversed network are shown in figures 6.4-1 to 6.4-5. It is clear that the network could predict the solid propellant composition values and the motor working parameters to high degree of accuracy. The network could also predict the correct composition for both double-base and composite solid propellants. The network was trained for 200 epochs, which agreed with the number of iterations in the forward problem.

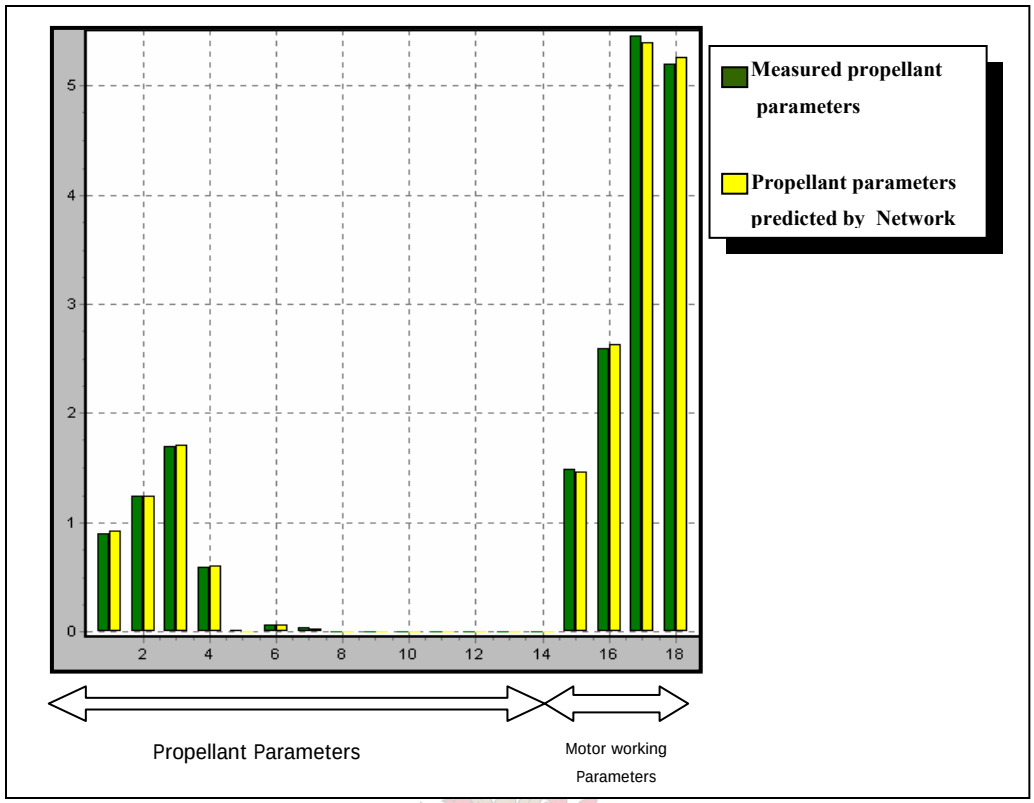

Figure 6.4-2 Results for test set DB3

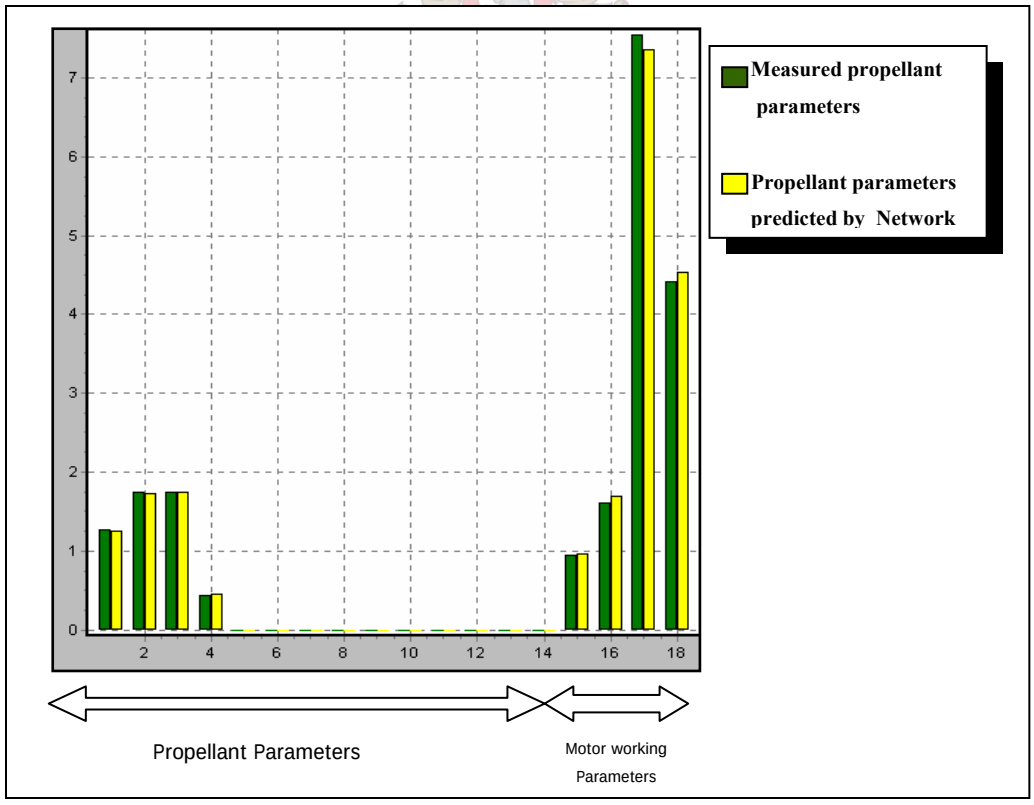

Figure 6.4-3 Results for test set DB4

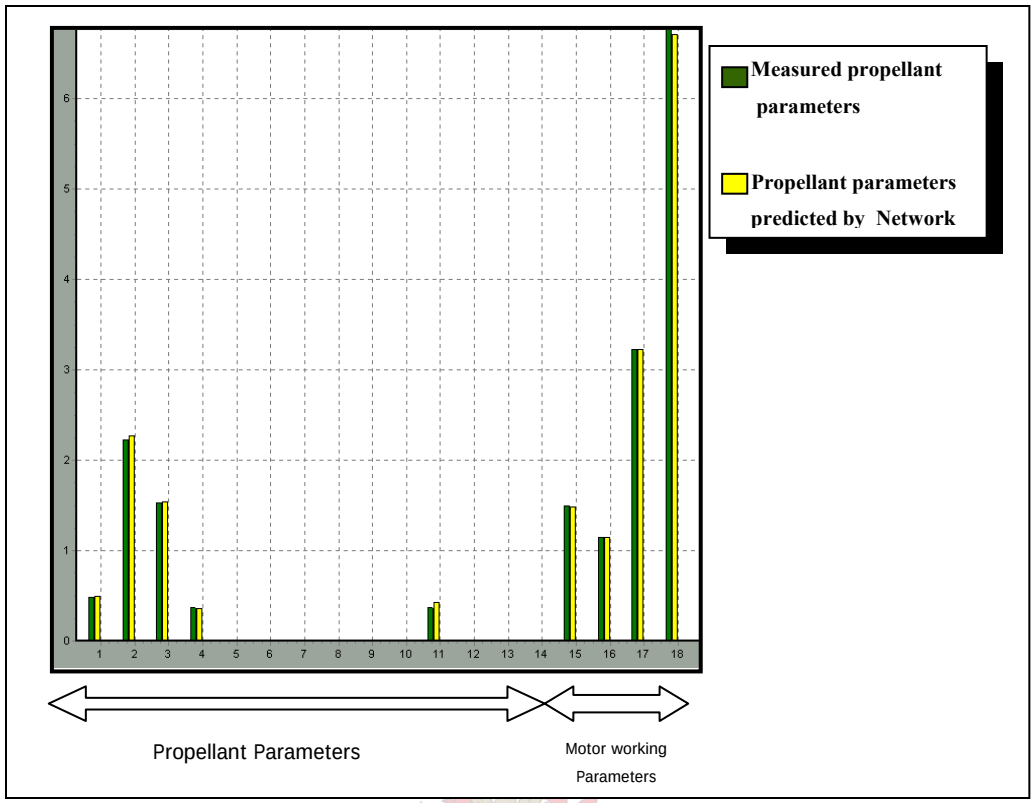

Figure 6.4-4 Results for test set C5

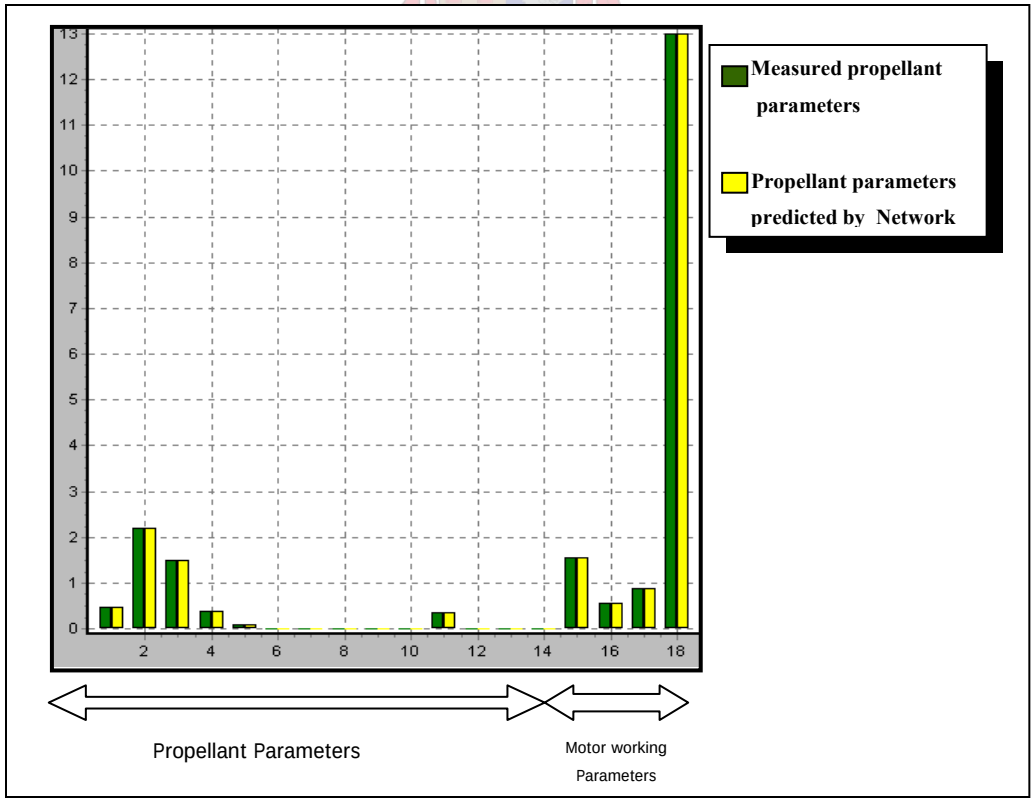

Figure 6.4-5 Results for test set C9

6.5. Reference:

1. Roodt, J., *The Prediction of the emission spectra of solid rocket propellants*, Ph.D. dissertation, Dept. Chemical Engineering, University of Stellenbosch, Chapter 7, (1998).

2. Mendenhall, W., *Introduction to Probability and Statistics,* 7th Edition, PWS Publishers, United States of America, Chapter 11, (1987).

3. Demuth, H., Beale, M., *Neural Network Toolbox User's Guide,* Version 3, The MathWorks, Inc., Chapter 2, (1998).

4. The MathWorks, *Statistics Toolbox User's Guide*, The MathWorks, Inc., Natick, United States, Multivariate Statistics, (2002).

5. Cherkassky, V., *Statistical, Neural Network and Fuzzy Methods for function Estimation,* Presented at WCNN-96, San Diego, (1996).

6. Sutton, G.P., *Rocket Propulsion Elements – An introduction to the engineering of rockets - 6 th Editio*n, John Wiley & Sons, New York, Chapter 3, (1992).

7. Zupan, J., Gasteiger, J., *Neural Networks for Chemists*, VCH Verlagsgesellschaft, Weinheim, Chapter 2, (1993).

8. Mendenhall, W., Scheaffer, R.L., Wackerly, D.D., *Mathematical Statistics with Applications,* 3rd edition, PWS Publishers, United States of America, Chapter 10, (1986).

7. Modelling of Flare Infrared Spectra

The same principle used in predicting the infrared spectra of the rocket plumes will be utilised here. The only known parameters in this scenario are the molecular composition of the flares. The flare data used here had never been modelled before and the aim is to develop a conceptual working model to show that it could be feasible to predict the flare spectra.

7.1. Defining a Model

Employing the same setup for predicting the radiation spectra of the rocket propellants, it was possible to predict the spectra for the flares. To start with a feedforward neural network with 13 input nodes, 16 hidden nodes and the 146 output nodes were used for predicting the radiation spectra. The input to the network consists of the molecular composition of the flares. Training and testing such a network did not show good results, as seen in fig. 7.1-1. It is clear that the composition of the flares do not supply the NN with sufficient information to correctly predict the radiation spectra.

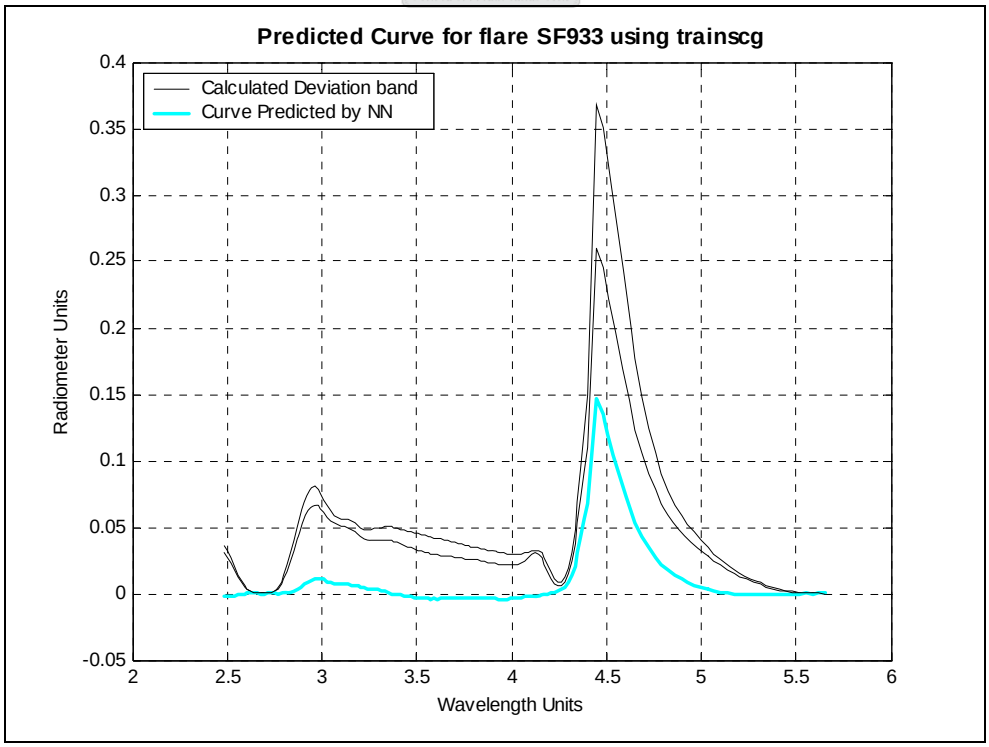

Figure 7.1-1 Predicted curve for SF933, using only the composition as input

Once again *Matlab's* neural network toolbox was used to train and evaluate the neural nets as shown in table

Table 7-1 Setup of neural network with only the composition as input

Feature	***NN_{16}***	***Matlab function***
No. neurons in Input layer	13 (composition)	
No. neurons in Hidden layer	16	
No. neurons in Output layer	146	
Training Function	Scaled conjugate gradient backpropagation	trainscg
Performance function	Mean squared error	mse
Hidden layer Transfer function	Hyperbolic tangent sigmoidal	tansig
Output layer Transfer function	Linear	purelin

Considering the radiation spectra graphs, it could be assumed that if the area underneath these graphs were to be known, enough information would be available for the NN to adequately predict the radiation spectra. A NN with the integrated area for each graph included in the input were then used to predict the spectra. Results for two different test sets show a very good solution. From fig.7.1-2 and fig.7.1-3, the predicted values are clearly lying in the variation space.

This integrated area however is not a known quantity and needs to be emulated by obtainable parameters, either by calculation or physical measurement. Since there are no physical parameters, as was the case for the rockets, parameters describing the intrinsic properties of the flares, need to be investigated.

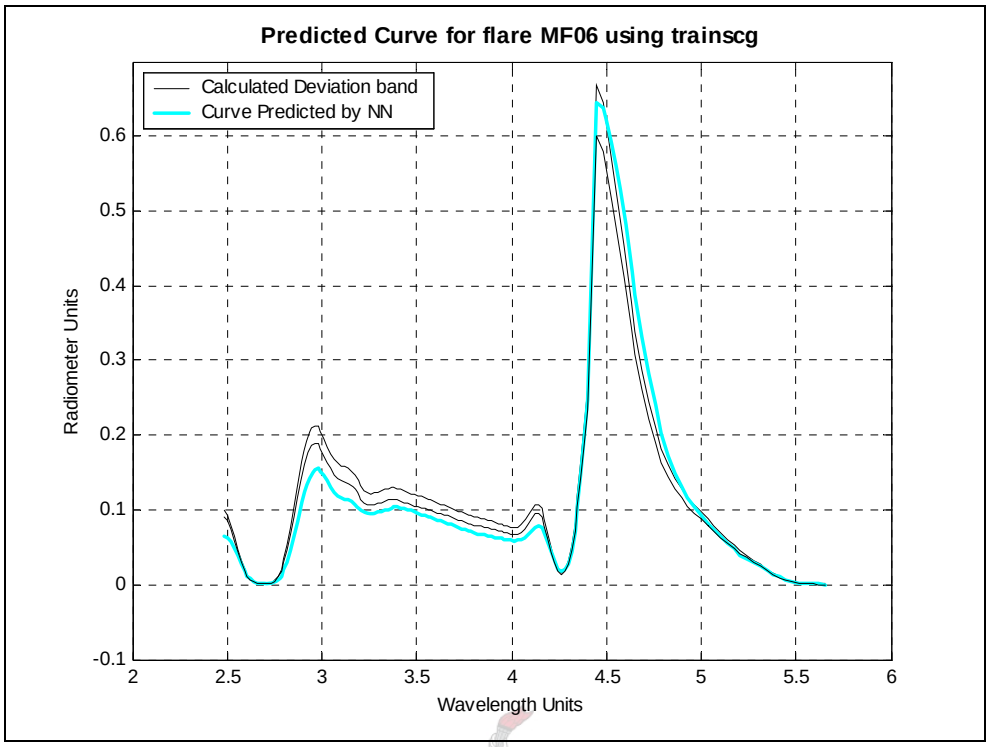

Figure 7.1-2 Predicted curve for MF06 with the area as added input

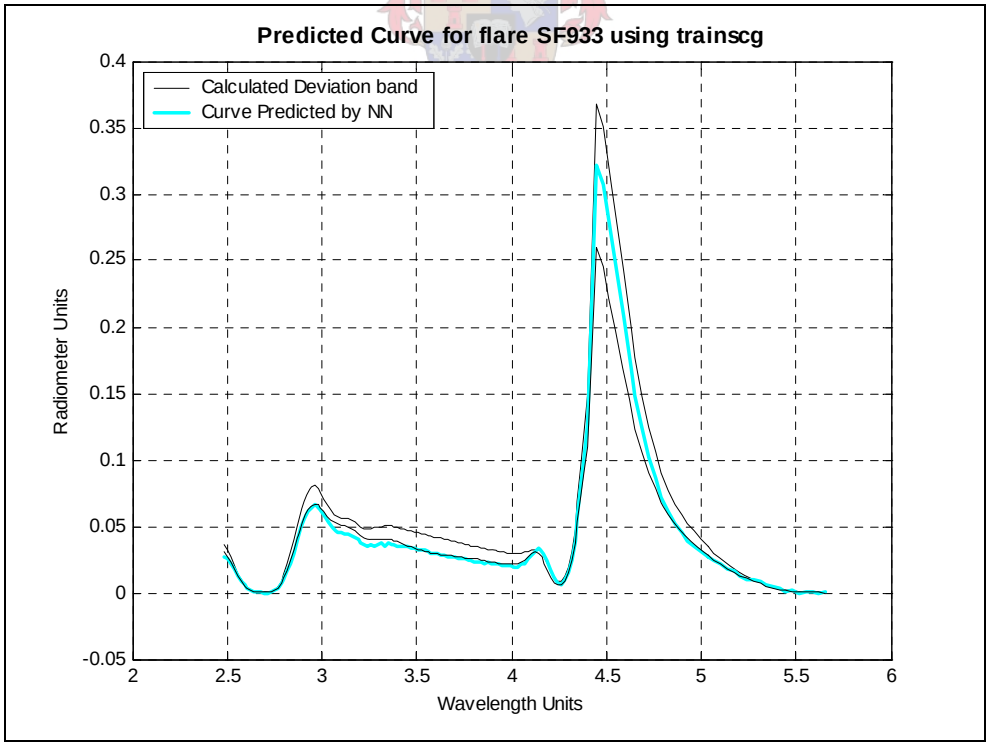

Figure 7.1-3 Predicted curve for SF933 with the area as added input

Thermodynamic properties of the flares are calculated using thermo-chemical calculations [1]. These thermo-chemical properties are listed in table 7-2. The thermo-chemical properties and the integrated area underneath the graphs were plotted on the same graph as shown in fig. 7.1-4. From fig. 7.1-4 it is possible to determine if there is any relation between these thermodynamic parameters and the area. The oxidant-fuel ratio, R,EQ.RATIO, mainly follows the same trend as that of the area for each of the flares. In fig. 7.1-4, the bold lines represent the area, the oxidant-fuel ratio, equilibrium temperature (T) and the molar mass (M). The oxidant-fuel ratio can now be used in the input, therefore substituting the area. The new input space was used for training a NN, of which the results are shown in fig.7.1-5.

Table 7-2 Thermodynamic Properties determined through thermo-chemical calculations

Thermodynamic Property	***Description***	***Thermodynamic Property***	***Description***
R,EQ.RATIO	Fuel : Air ratio	M	$1/n$
T	Temperature	$(\partial \ln V / \partial \ln p)_T$	
ρ	Density	$(\partial \ln V / \partial \ln T)_p$	
H	Enthalpy	C_p	Heat capacity
U	Internal Energy	GAMMAs	Ratio of specific heats at constant entropy
G	Gibbs free energy	SON VEL	Velocity of sound at T and p
S	Entropy		

The parameters shown in table 7-2 are not all independent of each other, but these are the most common thermo-chemical parameters evaluated when investigating combustion processes. It is interesting that the parameters that are eventually used in the input space of the network are all independent of each other, which suggests that the neural network anticipated the interdependencies.

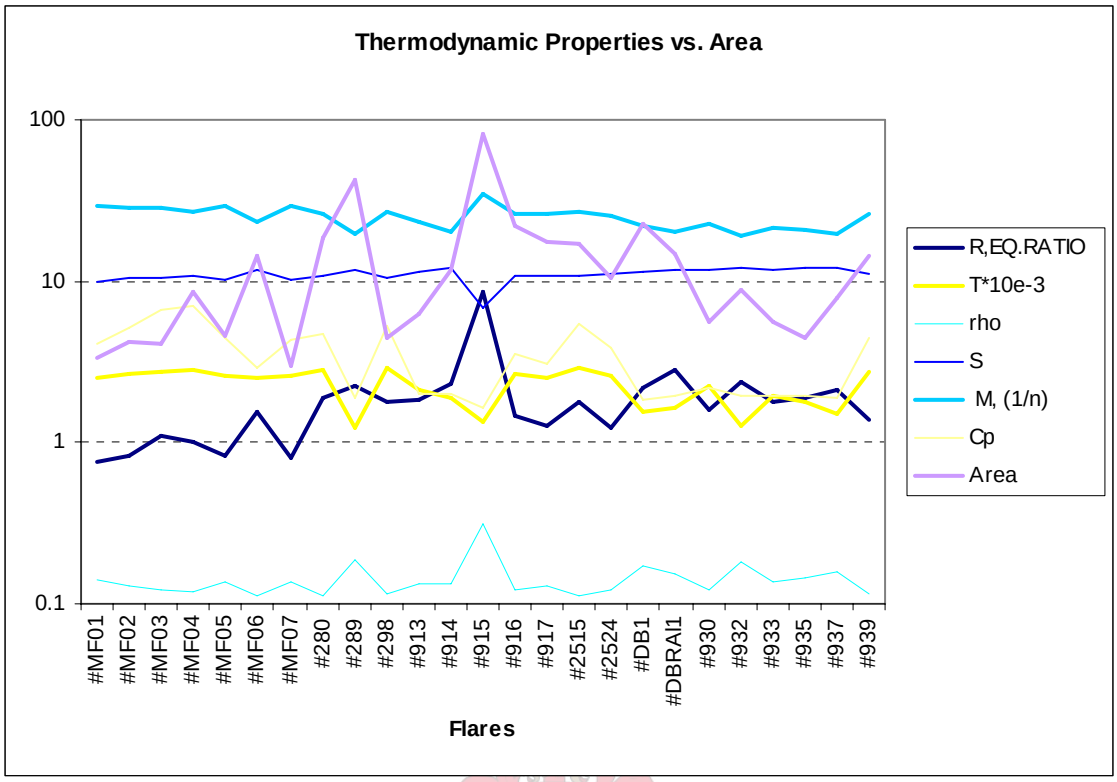

Figure 7.1-4 Thermodynamic Properties plotted against the Area underneath each graph

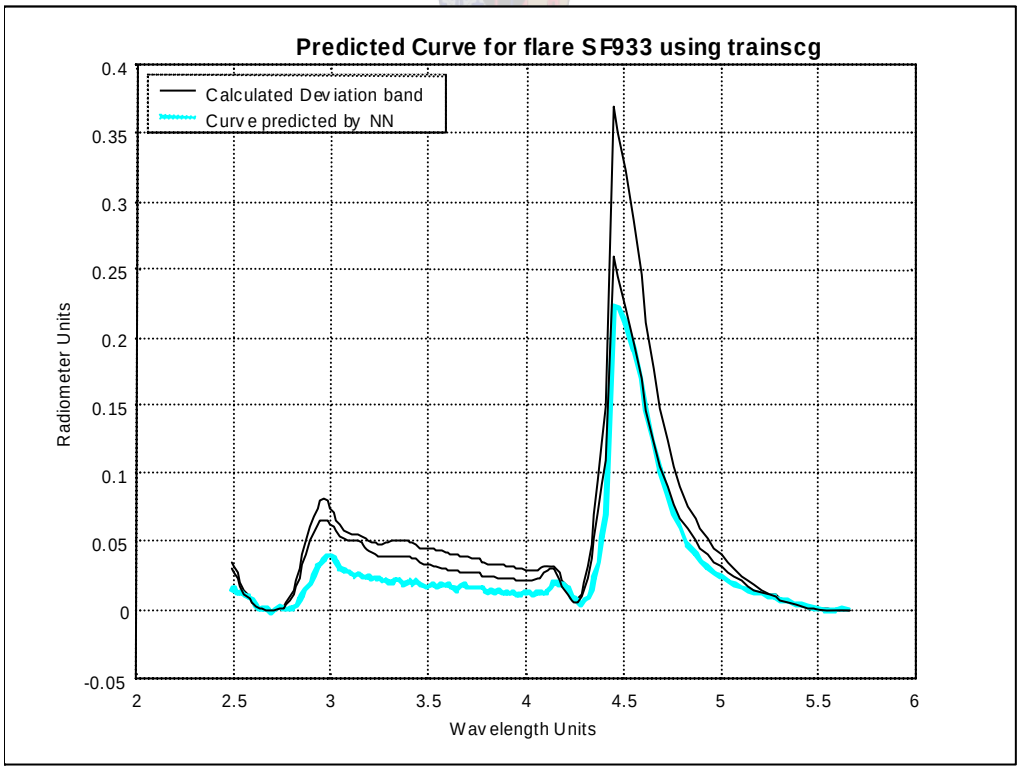

Figure 7.1-5 Predicted curve for SF933 with the oxidant-fuel ratio as added input

The predicted curve in fig. 7.1-5 is already a better approximation than the first run, where only the molar composition was used as input. The predicted curve is not yet an adequate approximation. The combustion temperature, for the equilibrium reaction of the flare with surrounding air, was next considered as an additional input. Replacing the oxidant-fuel ratio with the equilibrium temperature as input the resultant predicted curve is shown in fig.7.1-6. Compared to fig.7.1-5, the equilibrium temperature as additional input, does not greatly improve the Neural Net's capabilities.

The thermo-chemical parameters are calculated for different air : fuel ratios. The equilibrium reaction does not necessarily give rise to the highest combustion temperature. Thermo-chemical calculations were done at the following air: fuel ratios': 0.5, 0.75, 0.9, 1.0, 1.1, 1.25, 1.5, 2.0, 3.0. A plot of the temperature distribution over the range of oxidant-fuel ratios for flare SF935 are shown in fig. 7.1-7. The red dot represents the equilibrium combustion temperature and the top of the parabola curve the highest combustion temperature. Both the highest and equilibrium combustion temperatures could now be used as input to the NN.

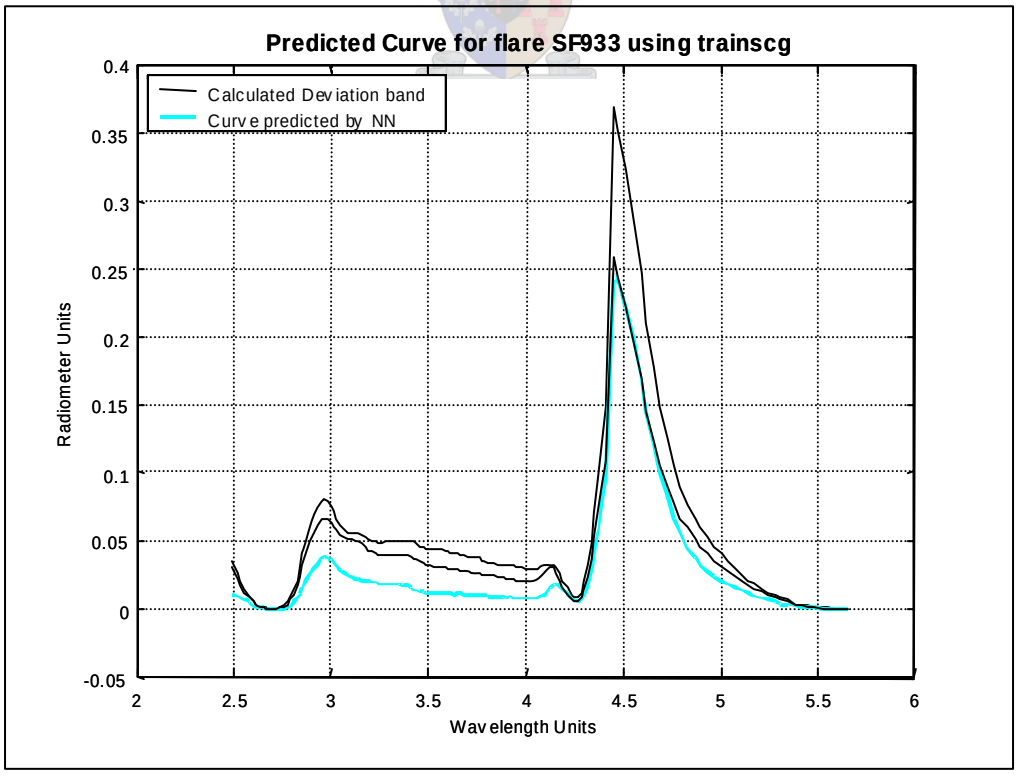

Figure 7.1-6 Predicted curve for SF933 with the equilibrium temperature as added input

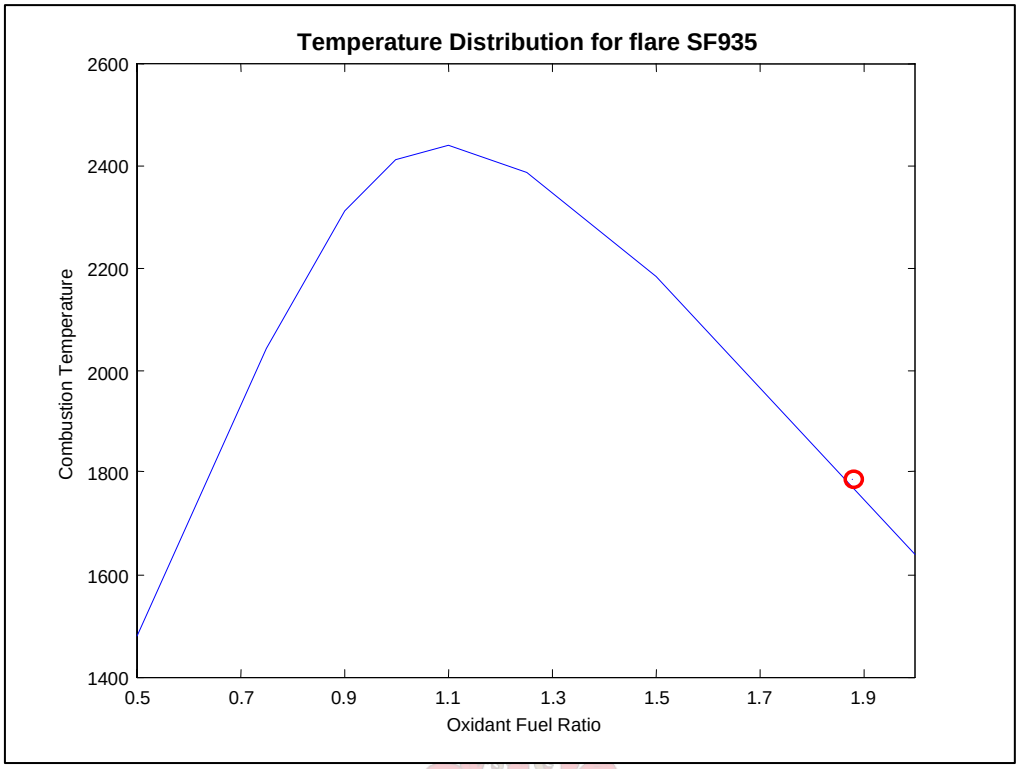

Figure 7.1-7 Temperature distribution over the range of oxidant-fuel ratios for flare SF935

The thermo-chemical parameters were used in a separate neural network to predict the area. From this simulation it was possible to distinguish the minimum of parameters that predicts the integrated area correctly. The oxidant-fuel ratio (OF), equilibrium temperature (T), the molar mass (M = 1/n) and the maximum combustion temperature (HT), accurately predicts the integrated area. Using these parameters in conjunction with molar composition as input, the predictive capability of the NN greatly improved. The input space with the thermo-chemical parameters is shown in Appendix D. In fig. 7.1-8 the predicted output for the OF-T-M-HT neural net shows a good correlation to the measured output. The phases of development for the flare input vector is shown in table7-3.

Table 7-3 Development of a model for predicting the radiation spectra of flares

Parameters	Number of Inputs
Molar Composition	13
Molar Composition Oxidant-Fuel Ratio	14
Molar Composition Equilibrium Temperature	14
Molar Composition Oxidant-Fuel Ratio Equilibrium Temperature Molar Mass Highest Combustion Temperature	17

In all cases 16 hidden nodes were used with the 146 output nodes in training the neural networks. The scaled conjugate gradient backpropagation algorithm was again used as the training function. The scaled conjugate gradient backpropagation algorithm proved to perform well for the solid propellants and as a starting point; it was used for the flares as well. A summary of the neural network architecture is shown in table7-4.

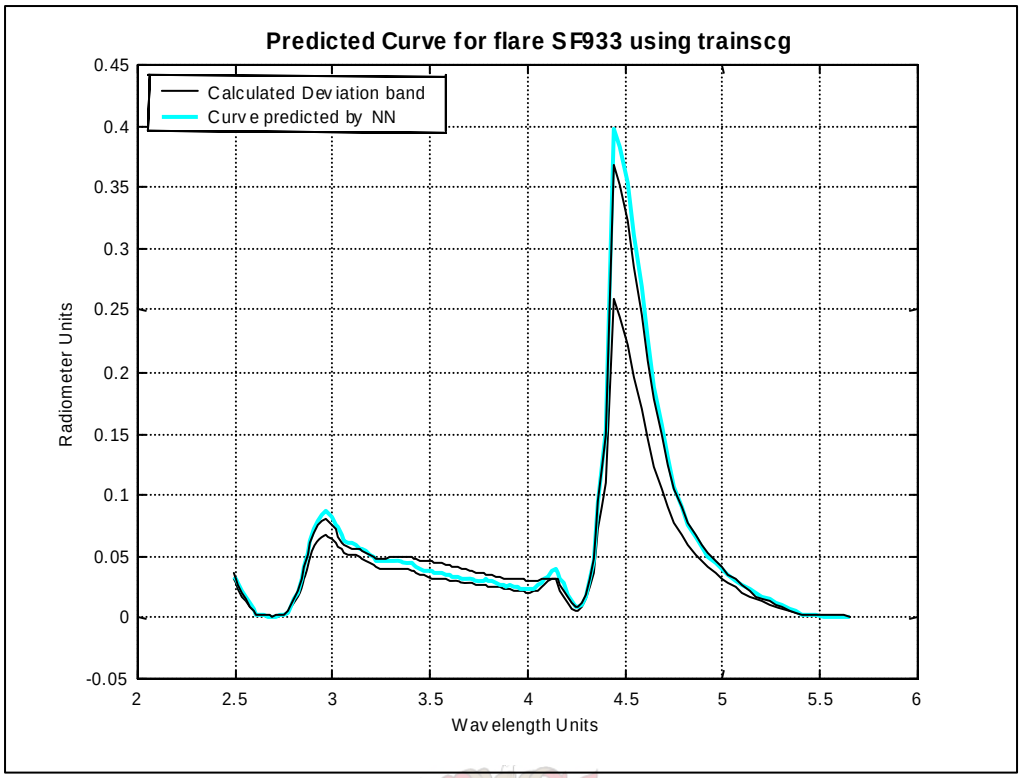

Figure 7.1-8 Predicted curve for SF933 from the OF-T-M-HT neural net

Table 7-4 Network configuration for OF-T-M-HT neural net

Feature	***NN_{16}***	***Matlab function***
No. neurons in Input layer	17	
No. neurons in Hidden layer	16	
No. neurons in Output layer	146	
Training Function	Scaled conjugate gradient backpropagation	trainscg
Performance function	Mean squared error	mse
Hidden layer Transfer function	Hyperbolic tangent sigmoidal	tansig
Output layer Transfer function	Linear	purelin

7.2. Refining the Model

7.2.1. Measure of Correlation

The two evaluation parameters defined in chapter 6 to evaluate the strength of correlation between the predicted and measured line spectra will again be used as criteria. *Pearson's product moment of coefficient of correlation* gives a good indication of how good the predicted line spectra follow the profile of the measured spectral line. The second parameter is measures relative distance between a target and a predicted spectral point and is defined as follows:

$$R^2 = 1 - \frac{\Sigma(X-Y)^2}{(n-1)(\sigma_{target})^2} \tag{6-2}$$

σ = standard deviation

Six different training functions, in table 7-5, were used to train the feedforward network. Along with 2 performance functions, namely the mean squared error *(mse)* and sum squared error *(sse);* the training functions were tested for each flare. This was done in order to see if there is one training function to model the whole variable space.

Table 7-5 Training functions tested for all

Matlab function	***Training Function***
traincgb	Powell-Beale conjugate gradient backpropagation
traincgf	Fletcher-Powell conjugate gradient backpropagation
traincgp	Polak-Ribiere conjugate gradient backpropagation
traingdx	Gradient descent, momentum & adaptive learning backpropagation
trainoss	One step secant backpropagation
trainscg	Scaled conjugate gradient backpropagation

The two correlation coefficients were then used to measure the correlation between the predicted and measured values. In table 7-6 the darker shading represents a strong correlation for both coefficients, while the cells lightly shaded present a weak correlation with one of the correlation coefficients. Since the weights of the network are initialised with a random function, each test was repeated three times.

Table 7-6 Testing the different training functions for each flare

MF01		***Trainscg***			***traincgb***			***traincgf***			***traincgp***			***traingdx***			***trainoss***			***Maximum***
mse	*Rsq2*	0.718	0.348	0.446	0.737	0.867	0.955	0.271	0.879	0.953	0.847	0.929	0.818	0.933	0.555	0.956	0.531	0.483	0.754	0.956
	rsquare	-2.538	-0.422	-0.215	0.260	0.661	0.576	-1.714	0.688	0.735	0.496	0.791	0.288	0.550	0.160	0.454	-2.255	-0.748	0.122	0.791
sse	*Rsq2*	0.076	0.945	0.727	0.039	0.138	0.796	0.940	0.166	0.932	0.214	0.016	0.883	0.928	0.910	0.971	0.683	0.032	0.192	0.971
	rsquare	-0.959	0.492	0.413	-0.997	-0.787	0.354	0.141	-3.987	0.834	-0.624	-2.624	0.450	-0.225	0.885	0.090	-2.322	-2.012	-0.879	0.885

MF02		***trainscg***			***traincgb***			***traincgf***			***traincgp***			***traingdx***			***trainoss***			***Maximum***
mse	***Rsq2***	0.991	0.991	0.993	0.988	0.981	0.991	0.998	0.974	0.993	0.994	0.986	0.989	0.981	0.981	0.986	0.983	0.997	0.989	0.998
	rsquare	0.237	-0.404	-1.767	-0.852	-1.103	0.149	0.308	-1.141	-0.185	-0.331	0.414	-0.236	0.591	0.807	0.868	-0.260	-0.326	-0.717	0.868
sse	***Rsq2***	0.991	0.988	0.990	0.988	0.992	0.989	0.978	0.983	0.990	0.980	0.993	0.993	0.929	0.955	0.992	0.980	0.988	0.973	0.993
	rsquare	-1.490	-0.811	-1.539	-0.897	0.566	0.316	0.516	0.662	-0.295	-0.831	-1.070	-0.666	0.718	0.816	0.918	-0.510	0.976	0.000	0.976

MF03		***trainscg***			***traincgb***			***traincgf***			***traincgp***			***traingdx***			***trainoss***			***Maximum***
mse	*Rsq2*	0.819	0.927	0.968	0.835	0.875	0.970	0.889	0.933	0.962	0.944	0.920	0.899	0.867	0.915	0.913	0.817	0.786	0.961	0.970
	Rsquare	0.292	-0.248	-1.203	-3.109	-0.545	0.546	-0.101	0.861	0.727	-0.738	0.260	0.450	-0.654	0.609	0.795	-1.236	-0.072	0.722	0.861
sse	*Rsq2*	0.963	0.947	0.962	0.914	0.957	0.819	0.946	0.948	0.628	0.822	0.613	0.877	0.919	0.839	0.971	0.561	0.875	0.812	0.971
	Rsquare	-3.275	0.916	0.106	-0.915	0.762	0.477	0.742	0.402	-1.692	-1.396	-0.661	0.404	0.626	0.053	0.641	0.100	0.240	-0.002	0.916

MF04		***trainscg***			***traincgb***			***traincgf***			***traincgp***			***traingdx***			***trainoss***			***Maximum***
mse	*Rsq2*	0.972	0.989	0.992	0.975	0.837	0.980	0.933	0.977	0.980	0.984	0.976	0.989	0.925	0.932	0.843	0.979	0.956	0.889	0.992
	Rsquare	0.696	0.901	0.558	0.650	0.513	0.686	0.823	0.614	0.395	0.739	0.570	0.683	0.771	0.552	0.792	0.835	0.802	0.106	0.901
sse	*Rsq2*	0.962	0.985	0.985	0.985	0.963	0.951	0.950	0.973	0.979	0.924	0.979	0.989	0.710	0.851	0.982	0.987	0.884	0.843	0.989
	Rsquare	0.267	0.375	0.834	0.538	0.612	0.449	0.820	0.386	0.414	0.633	0.471	0.512	0.446	0.698	0.789	0.712	0.645	0.290	0.834

MF05		***trainscg***			***traincgb***			***traincgf***			***traincgp***			***traingdx***			***trainoss***			***Maximum***
mse	*Rsq2*	0.915	0.028	0.898	0.161	0.907	0.960	0.879	0.985	0.989	0.760	0.003	0.487	0.922	0.873	0.363	0.897	0.988	0.981	0.989
	Rsquare	-13.572	-1.625	-45.210	-8.033	-4.550	0.894	-6.191	0.981	0.392	0.733	-1.007	-1.251	0.556	-0.672	-8.930	0.598	0.904	-1.489	0.981
sse	*Rsq2*	0.834	0.658	0.899	0.536	0.861	0.635	0.980	0.976	0.888	0.915	0.230	0.262	0.971	0.916	0.978	0.980	0.928	0.693	0.980
	Rsquare	0.335	0.455	-7.083	-6.223	-9.103	-4.056	-0.120	-1.824	0.606	-41.610	-3.344	0.136	-0.376	0.353	-1.833	-0.305	-0.781	-0.121	0.606

MF06		***trainscg***			***traincgb***			***traincgf***			***traincgp***			***traingdx***			***trainoss***			***Maximum***
mse	*Rsq2*	0.936	0.809	0.996	0.953	0.986	0.975	0.932	0.966	0.969	0.813	0.936	0.957	0.406	0.955	0.908	0.900	0.984	0.799	0.996
	Rsquare	0.358	0.077	0.813	0.581	0.839	0.604	-0.132	0.760	0.309	0.791	0.837	0.878	-0.912	0.513	0.048	0.470	0.510	-0.206	0.878
sse	*Rsq2*	0.954	0.983	0.962	0.863	0.981	0.829	0.994	0.935	0.988	0.985	0.498	0.387	0.970	0.903	0.953	0.705	0.955	0.340	0.994
	Rsquare	0.595	0.873	0.515	0.708	0.685	0.689	0.624	0.472	0.958	0.480	0.255	-1.652	0.188	0.222	0.532	-0.018	0.229	-1.053	0.958

MF07		***trainscg***			***traincgb***			***traincgf***			***traincgp***			***traingdx***			***trainoss***			***Maximum***
mse	*Rsq2*	0.995	0.984	0.976	0.970	0.910	0.988	0.993	0.977	0.993	0.947	0.986	0.986	0.914	0.906	0.975	0.977	0.901	0.952	0.995
	Rsquare	-0.195	-0.944	0.625	0.498	-9.517	0.843	0.247	0.599	-0.323	0.937	0.853	0.292	-0.944	-1.045	-0.242	0.835	-0.323	-0.929	0.937
sse	*Rsq2*	0.974	0.962	0.996	0.914	0.972	0.962	0.972	0.976	0.991	0.990	0.980	0.960	0.967	0.948	0.981	0.902	0.970	0.933	0.996
	rsquare	-0.542	0.691	0.610	0.684	0.530	0.764	-2.400	-0.204	0.713	0.727	0.419	0.615	-2.939	-1.414	-3.786	0.623	0.497	-1.347	0.764

SF280		***trainscg***			***traincgb***			***traincgf***			***traincgp***			***traingdx***			***trainoss***			***Maximum***
mse	*Rsq2*	0.953	0.949	0.970	0.953	0.897	0.958	0.929	0.915	0.940	0.912	0.940	0.961	0.926	0.920	0.927	0.907	0.958	0.897	0.969
	rsquare	0.941	0.274	0.360	0.402	0.532	0.794	0.637	0.714	0.734	0.441	0.910	0.791	0.503	0.530	0.603	0.824	0.835	0.282	0.941
sse	*Rsq2*	0.951	0.944	0.948	0.218	0.958	0.950	0.864	0.951	0.912	0.945	0.943	0.945	0.936	0.930	0.919	0.972	0.950	0.948	0.972
	rsquare	0.148	0.840	0.914	-1.132	0.469	0.882	0.290	0.492	0.235	0.571	0.890	0.550	0.674	0.629	0.632	0.862	0.661	0.511	0.913

SF289		***trainscg***			***traincgb***			***traincgf***			***traincgp***			***traingdx***			***trainoss***			***Maximum***
mse	*Rsq2*	0.430	0.885	0.427	0.299	0.619	0.619	0.352	0.855	0.489	0.779	0.905	0.114	0.434	0.560	0.645	0.864	0.772	0.887	0.905
	rsquare	-0.991	-1.055	0.215	-1.104	-0.858	-0.858	-1.283	-1.248	-0.962	-1.089	-0.859	-1.422	-1.331	-0.978	-1.043	-1.207	-1.124	-1.136	0.215
sse	*Rsq2*	0.053	0.936	0.097	0.271	0.619	0.851	0.506	0.545	0.916	0.420	0.377	0.831	0.679	0.619	0.580	0.972	0.777	0.722	0.972
	rsquare	-3.063	-1.074	-3.138	-1.575	-0.858	-0.988	-1.237	-0.998	-0.503	-1.334	-0.835	-1.158	-0.866	-1.134	-0.913	-0.765	-0.546	-1.340	-0.503

SF298		***trainscg***			***traincgb***			***traincgf***			***traincgp***			***traingdx***			***trainoss***			***Maximum***
mse	*Rsq2*	0.956	0.981	0.886	0.172	0.444	0.870	0.888	0.953	0.574	0.380	0.775	0.587	0.621	0.918	0.857	0.950	0.858	0.963	0.981
	rsquare	0.423	-1628	-2.957	-1.134	-1.997	-90.483	0.764	0.433	-0.086	-24.111	-27.082	-10.689	-72.797	-50.773	-3.577	-4.086	-66.420	-2.272	0.764
sse	*Rsq2*	0.977	0.504	0.718	0.574	0.105	0.945	0.985	0.929	0.582	0.465	0.943	0.329	0.953	0.770	0.797	0.934	0.974	0.539	0.985
	rsquare	-7.996	-1.779	-622.601	-38.149	-187.246	-83.433	-5.753	0.688	-0.033	-39.546	-76.484	-4.015	-264.818	-5.797	-48.410	-32.235	-17.010	-2.473	0.688

SF913		***trainscg***			***traincgb***			***Traincgf***			***traincgp***			***traingdx***			***trainoss***			***Maximum***
mse	*Rsq2*	0.898	0.958	0.784	0.970	0.923	0.927	0.953	0.983	0.974	0.101	0.912	0.830	0.870	0.938	0.956	0.922	0.975	0.972	0.983
	Rsquare	0.061	0.805	-9.316	0.402	0.350	0.387	0.289	0.972	0.880	-0.723	0.627	0.490	0.075	0.455	0.631	0.803	0.863	0.887	0.972
sse	*Rsq2*	0.505	0.899	0.982	0.161	0.959	0.986	0.844	0.964	0.993	0.943	0.978	0.890	0.961	0.938	0.976	0.966	0.983	0.970	0.993
	Rsquare	-1.480	0.775	0.916	-5.912	0.523	0.822	0.040	0.814	0.807	0.822	0.909	0.736	0.175	0.413	0.879	0.806	0.958	0.603	0.958

SF914		***trainscg***			***traincgb***			***Traincgf***			***traincgp***			***traingdx***			***trainoss***			***Maximum***
mse	*Rsq2*	0.989	0.150	0.948	0.850	0.981	0.987	0.985	0.988	0.968	0.907	0.247	0.983	0.938	0.812	0.982	0.981	0.986	0.977	0.989
	Rsquare	0.988	-5.727	0.662	0.407	0.947	0.987	0.859	0.878	0.761	0.436	0.222	0.957	0.917	0.784	0.981	0.970	0.881	0.581	0.988
sse	*Rsq2*	0.975	0.996	0.984	0.509	0.995	0.756	0.914	0.986	0.912	0.969	0.983	0.976	0.974	0.903	0.969	0.946	0.918	0.972	0.996
	Rsquare	0.791	0.626	0.982	-0.815	0.789	0.111	0.865	0.945	0.845	0.875	0.789	0.836	0.933	0.718	0.936	0.761	0.448	0.970	0.982

SF915		***trainscg***			***traincgb***			***Traincgf***			***traincgp***			***traingdx***			***trainoss***			***Maximum***
mse	*Rsq2*	0.027	0.241	0.726	0.001	0.009	0.054	0.040	0.237	0.004	0.349	0.003	0.069	0.180	0.056	0.024	0.061	0.057	0.073	0.726
	Rsquare	-46.685	-15.960	-549.056	-33.760	-64.730	-25.186	-14.030	-693.168	-126.705	-43.038	-22.409	-46.200	-25.384	-20.823	-28.747	-24.534	-11.188	-34.920	-11.188
sse	*Rsq2*	0.007	0.356	0.098	0.223	0.443	0.012	0.048	0.191	0.385	0.104	0.003	0.062	0.017	0.021	0.006	0.008	0.050	0.001	0.443
	Rsquare	-24.377	-243.182	-16.012	-75.313	-150.684	-18.608	-25.252	-363.803	-793.448	-30.779	-23.565	-18.668	-25.185	-67.768	-27.045	-22.863	-20.859	-24.851	-16.012

SF916		***trainscg***			***traincgb***			***Traincgf***			***traincgp***			***traingdx***			***trainoss***			***Maximum***
mse	*Rsq2*	0.818	0.921	0.989	0.863	0.970	0.972	0.979	0.962	0.978	0.843	0.034	0.931	0.673	0.333	0.937	0.965	0.979	0.940	0.989
	Rsquare	-2.998	0.538	0.970	0.793	0.809	0.815	0.970	0.781	0.616	0.736	-0.585	-3.251	0.207	0.051	0.529	0.932	0.859	0.775	0.970
sse	*Rsq2*	0.964	0.963	0.967	0.828	0.930	0.975	0.963	0.975	0.985	0.922	0.973	0.986	0.916	0.788	0.957	0.974	0.934	0.969	0.986
	Rsquare	0.802	0.795	0.706	0.774	0.539	0.894	0.692	0.515	0.974	0.255	0.927	0.984	0.405	0.683	0.364	0.830	0.674	0.867	0.984

SF917		***trainscg***			***traincgb***			***Traincgf***			***traincgp***			***traingdx***			***trainoss***			***Maximum***
mse	*Rsq2*	0.452	0.991	0.825	0.987	0.987	0.988	0.956	0.995	0.969	0.880	0.898	0.972	0.652	0.663	0.940	0.978	0.867	0.904	0.995
	Rsquare	-1.218	0.943	0.782	-26.119	0.834	0.926	0.897	0.935	-206.491	-0.835	-180.983	0.193	-1.091	0.273	0.730	0.936	-5.259	-4.671	0.943
sse	*Rsq2*	0.990	0.988	0.983	0.712	0.282	0.979	0.863	0.988	0.990	0.990	0.972	0.986	0.799	0.901	0.322	0.976	0.940	0.869	0.990
	Rsquare	0.715	0.391	0.281	-0.269	-29.589	0.610	-6825.36	0.752	0.984	0.738	0.816	0.753	-3.291	0.525	-1.289	0.617	0.915	-0.062	0.984

SF2515		***trainscg***			***traincgb***			***Traincgf***			***traincgp***			***traingdx***			***trainoss***			***Maximum***
mse	*Rsq2*	0.732	0.980	0.880	0.209	0.981	0.792	0.556	0.976	0.026	0.774	0.782	0.859	0.827	0.848	0.861	0.865	0.002	0.963	0.981
	Rsquare	-208.852	0.914	-5.432	-13.403	0.951	0.197	-1.010	0.610	-0.896	-0.007	-0.104	-0.208	0.244	0.204	0.358	-4.959	-0.407	0.739	0.951
sse	*Rsq2*	0.986	0.995	0.673	0.252	0.698	0.978	0.973	0.956	0.975	0.995	0.829	0.899	0.959	0.933	0.977	0.925	0.924	0.977	0.995
	Rsquare	-13.808	-7.156	-4.613	-5.951	-1.706	-13.040	0.494	0.434	0.279	0.988	0.670	0.342	0.720	0.211	0.350	0.272	-0.066	0.201	0.988

SF2524		***trainscg***			***traincgb***			***Traincgf***			***traincgp***			***traingdx***			***trainoss***			***Maximum***
mse	*Rsq2*	0.756	0.042	0.995	0.655	0.937	0.989	0.981	0.983	0.973	0.725	0.981	0.979	0.596	0.623	0.542	0.984	0.065	0.938	0.995
	Rsquare	-2.348	-15.518	0.627	-5.061	0.880	0.921	0.600	0.935	0.824	-34.801	-3.541	-0.155	-28.754	0.536	0.040	0.962	-3.207	0.869	0.962
sse	*Rsq2*	0.994	0.990	0.992	0.993	0.443	0.781	0.936	0.973	0.976	0.999	0.779	0.988	0.980	0.197	0.997	0.827	0.949	0.676	0.999
	rsquare	-2.453	0.706	0.973	-20.443	-4.270	0.213	0.859	-0.179	0.917	0.997	0.497	0.005	0.765	-16.233	0.962	-9.980	0.861	-10.064	0.997

SFDB1		***trainscg***			***traincgb***			***Traincgf***			***traincgp***			***traingdx***			***trainoss***			***Maximum***
mse	*Rsq2*	0.716	0.466	0.579	0.588	0.588	0.706	0.938	0.421	0.211	0.856	0.786	0.952	0.308	0.089	0.002	0.982	0.986	0.895	0.986
	rsquare	-3.635	-1.590	-37.713	0.008	0.008	-0.826	0.831	-5.501	-1095.55	-0.069	0.700	-29.932	-0.807	-2.115	-4.540	-25.020	-2.532	-63.812	0.831
sse	*Rsq2*	0.109	0.022	0.045	0.002	0.588	0.032	0.638	0.908	0.909	0.553	0.840	0.870	0.008	0.211	0.697	0.044	0.656	0.482	0.909
	rsquare	-2.171	-2.009	-354.726	-5.029	0.007	-3.107	-0.104	0.512	-0.265	0.065	-69.530	0.839	-5.057	-96.215	0.463	-46.805	-46.365	-1.453	0.839

SFDBRAI1		***trainscg***			***traincgb***			***Traincgf***			***traincgp***			***traingdx***			***trainoss***			***Maximum***
mse	*Rsq2*	0.127	0.922	0.090	0.899	0.671	0.012	0.702	0.931	0.820	0.882	0.175	0.002	0.947	0.760	0.690	0.992	0.231	0.993	0.993
	Rsquare	-123.292	-38.247	-86.581	-18.062	-12.628	-76.404	0.097	-35.645	-203.563	-160.761	-8.394	-4.040	-8.463	-0.631	-1.492	-24.391	-1.071	-13.497	0.097
sse	*Rsq2*	0.990	0.331	0.987	0.827	0.645	0.934	0.994	0.883	0.988	0.397	0.861	0.982	0.982	0.914	0.900	0.962	0.967	0.656	0.994
	Rsquare	-103.001	-18.917	-2582.59	-215.533	-0.444	-81.379	0.589	0.348	-4.421	-20.584	-7.011	-11.666	-2.718	-4.208	0.365	-18.239	-7.850	-4.155	0.589

SF930		***trainscg***			***traincgb***			***Traincgf***			***traincgp***			***traingdx***			***trainoss***			***Maximum***
mse	*Rsq2*	0.856	0.984	0.989	0.978	0.991	0.987	0.983	0.977	0.988	0.923	0.984	0.951	0.992	0.987	0.980	0.978	0.989	0.995	0.995
	Rsquare	0.456	0.960	0.712	0.906	0.943	0.664	0.860	0.346	0.903	0.669	0.978	0.874	0.979	0.956	0.971	0.956	0.948	0.946	0.979
sse	*Rsq2*	0.994	0.992	0.995	0.981	0.974	0.973	0.954	0.923	0.948	0.986	0.977	0.990	0.980	0.981	0.961	0.984	0.984	0.965	0.995
	Rsquare	0.813	0.754	0.947	0.466	0.681	0.904	0.875	0.772	0.845	0.730	0.902	0.984	0.967	0.955	0.758	0.904	0.984	0.684	0.984

SF932		***trainscg***			***traincgb***			***Traincgf***			***traincgp***			***traingdx***			***trainoss***			***Maximum***
mse	*Rsq2*	0.722	0.922	0.663	0.727	0.869	0.766	0.966	0.881	0.497	0.771	0.809	0.802	0.672	0.952	0.923	0.905	0.954	0.833	0.966
	Rsquare	-6.781	-2.582	-2.256	0.132	-3.915	-4.155	-9.513	-4.587	-21.038	-4.344	-1.295	-4.061	-1.118	-9.361	-18.387	-4.760	-11.272	-3.897	0.132
sse	*Rsq2*	0.725	0.870	0.673	0.864	0.844	0.828	0.868	0.828	0.808	0.917	0.976	0.934	0.966	0.779	0.951	0.938	0.823	0.617	0.976
	Rsquare	-3.223	-5.728	-7.794	-2.691	-4.683	-4.889	-1.246	-3.362	-1.647	-3.456	-11.371	-2.215	-5.300	-3.471	-9.172	-12.389	-1.700	-3.540	-1.246

SF933		***trainscg***			***traincgb***			***Traincgf***			***traincgp***			***traingdx***			***trainoss***			***Maximum***
mse	*Rsq2*	0.996	0.970	0.995	0.992	0.989	0.993	0.991	0.986	0.988	0.994	0.988	0.983	0.916	0.921	0.925	0.937	0.948	0.966	0.996
	Rsquare	0.938	0.910	0.899	0.959	0.719	0.973	0.985	0.974	0.873	0.960	0.978	0.952	0.302	-0.001	0.132	0.313	0.560	0.703	0.985
sse	*Rsq2*	0.992	0.993	0.994	0.996	0.997	0.995	0.998	0.988	0.990	0.986	0.974	0.995	0.875	0.886	0.897	0.971	0.951	0.909	0.998
	Rsquare	0.978	0.911	0.819	0.688	0.976	0.923	0.992	0.810	0.964	0.887	0.925	0.979	0.666	-0.491	-0.483	0.698	0.612	-0.865	0.992

SF935		***trainscg***			***traincgb***			***Traincgf***			***traincgp***			***traingdx***			***trainoss***			***Maximum***
mse	*Rsq2*	0.965	0.998	0.994	0.990	0.962	0.970	0.974	0.993	0.984	0.982	0.989	0.999	0.905	0.945	0.937	0.937	0.981	0.900	0.999
	Rsquare	0.842	0.788	0.783	0.880	-0.259	0.844	0.883	0.859	0.755	0.882	0.855	0.623	-0.207	-0.883	-2.214	0.864	0.848	-0.035	0.883
sse	*Rsq2*	0.998	0.997	0.995	0.997	0.995	0.984	0.984	0.987	0.978	0.978	0.998	0.988	0.898	0.909	0.892	0.963	0.985	0.957	0.998
	Rsquare	0.967	0.958	0.855	0.639	0.704	0.783	0.306	-0.430	0.934	0.866	0.914	0.876	-0.723	-0.815	-1.333	0.641	0.437	-0.352	0.967

SF937		***trainscg***			***traincgb***			***Traincgf***			***traincgp***			***traingdx***			***trainoss***			***Maximum***
mse	*Rsq2*	0.964	0.903	0.917	0.864	0.992	0.917	0.938	0.996	0.999	0.980	0.982	0.928	0.940	0.948	0.879	0.882	0.832	0.873	0.999
	Rsquare	0.673	0.534	0.614	0.605	0.979	0.594	0.723	0.858	0.923	0.761	0.688	0.508	0.709	0.772	0.303	0.426	0.617	0.845	0.979
sse	*Rsq2*	0.934	0.965	0.955	0.949	0.993	0.907	0.999	0.993	0.943	0.917	0.919	0.923	0.819	0.868	0.884	0.914	0.939	0.804	0.999
	Rsquare	0.625	0.673	0.716	0.484	0.968	0.550	0.900	0.992	0.648	0.498	0.554	0.716	0.726	0.419	0.431	0.892	0.478	0.652	0.992

SF939		***trainscg***			***traincgb***			***Traincgf***			***traincgp***			***traingdx***			***trainoss***			***Maximum***
mse	*Rsq2*	0.557	0.790	0.179	0.194	0.254	0.308	0.155	0.263	0.230	0.318	0.254	0.276	0.226	0.139	0.186	0.245	0.308	0.282	0.790
	Rsquare	0.012	-2.802	-1.110	-1.039	-0.609	-0.355	-1.110	-0.660	-1.454	-0.283	-0.567	-0.511	-0.711	-1.261	-1.153	-0.690	-0.378	-0.431	0.012
sse	*Rsq2*	0.257	0.171	0.289	0.281	0.252	0.369	0.652	0.332	0.231	0.217	0.245	0.368	0.354	0.311	0.228	0.482	0.427	0.445	0.652
	Rsquare	-0.524	-1.126	-0.382	-0.437	-0.544	-0.089	-85.321	-0.407	-0.690	-0.738	-0.613	-0.120	-0.307	-0.349	-0.655	-0.010	-0.156	0.019	0.019

Again it has to be noted that the goal of this thesis was to find a conceptual working model and not necessarily the optimum network model, especially where the flares are concerned. The aim was to investigate whether it was possible to build a model that would be able to predict the infrared spectra of the flares.

The average mean squared error for each of the training algorithms under evaluation is shown in table 7-7. These averages were taken over all the flares and all three trained networks. The training function with the best overall correlation is the Fletcher-Powell conjugate gradient *(traincgf)* backpropagation function.

Table 7-7 Average sse values for training algorithms

trainscg	traincgb	traincgf	traincgp	traingdx	trainoss
0.792	0.729	0.864	0.782	0.804	0.794

Again the performance of all the training functions are comparable, which suggests that the training function does not have such a great influence on the performance of the net. Further optimisation could be done by increasing the number of hidden nodes or further optimising the training function parameters.

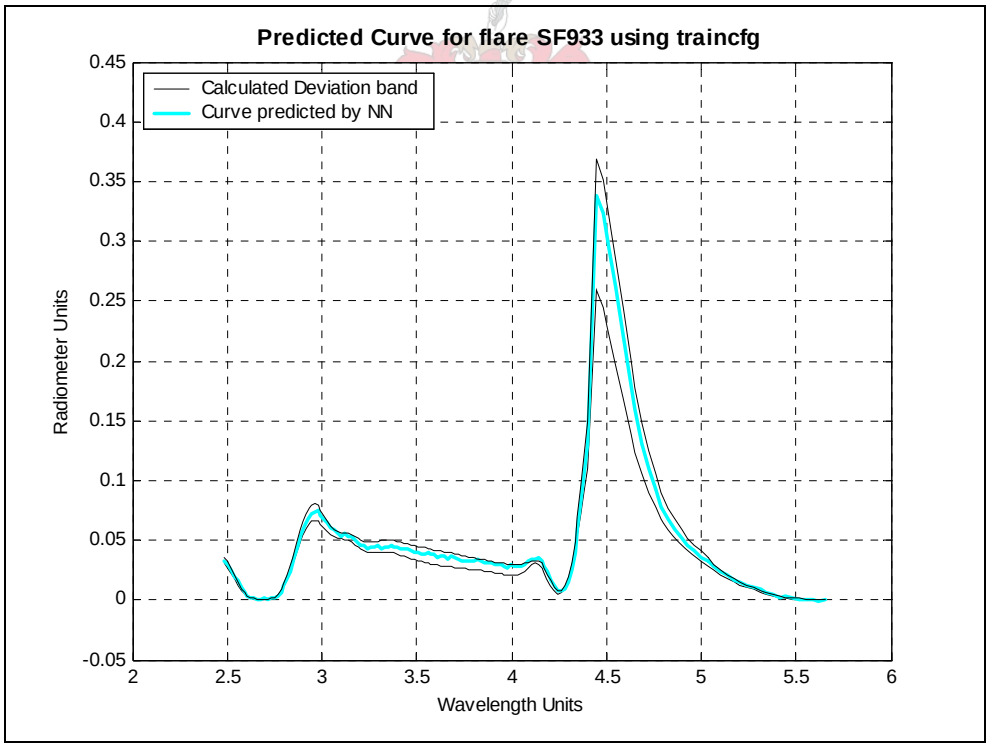

Figure 7.2-1 Predicted curve for SF933 using the Fletcher-Powell conjugate function.

The predicted curve in fig. 7.2-1 is again an improvement on the correlation of the scaled conjugate gradient method used in fig. 7.1-8. It has to be noted that not all the flare line spectra would show such a good correlation, as did SF933. This is due to the fact that

some of the flares' data lie on the edge of the variation space, fig. 7.2-3, (discussed in chapter 4), and this data would not be predicted with the same accuracy as seen here. Flare SF933 was used as an example to illustrate the development of a suitable model.

Another way of visualising the variation space of all the flare data is to express it in terms of the Euclidean distance between the various flares. The Euclidean distance was defined in chapter 6 as

$$d_{ij} = \left\{ \sum_{k=1}^{p} \left| x_{ik} - x_{jk} \right|^2 \right\}^{1/2} \tag{7-1}$$

where d_{ij} denotes the distance between objects i and j [2], x_{ik}, the data point k of propellant i and p the number of observations .

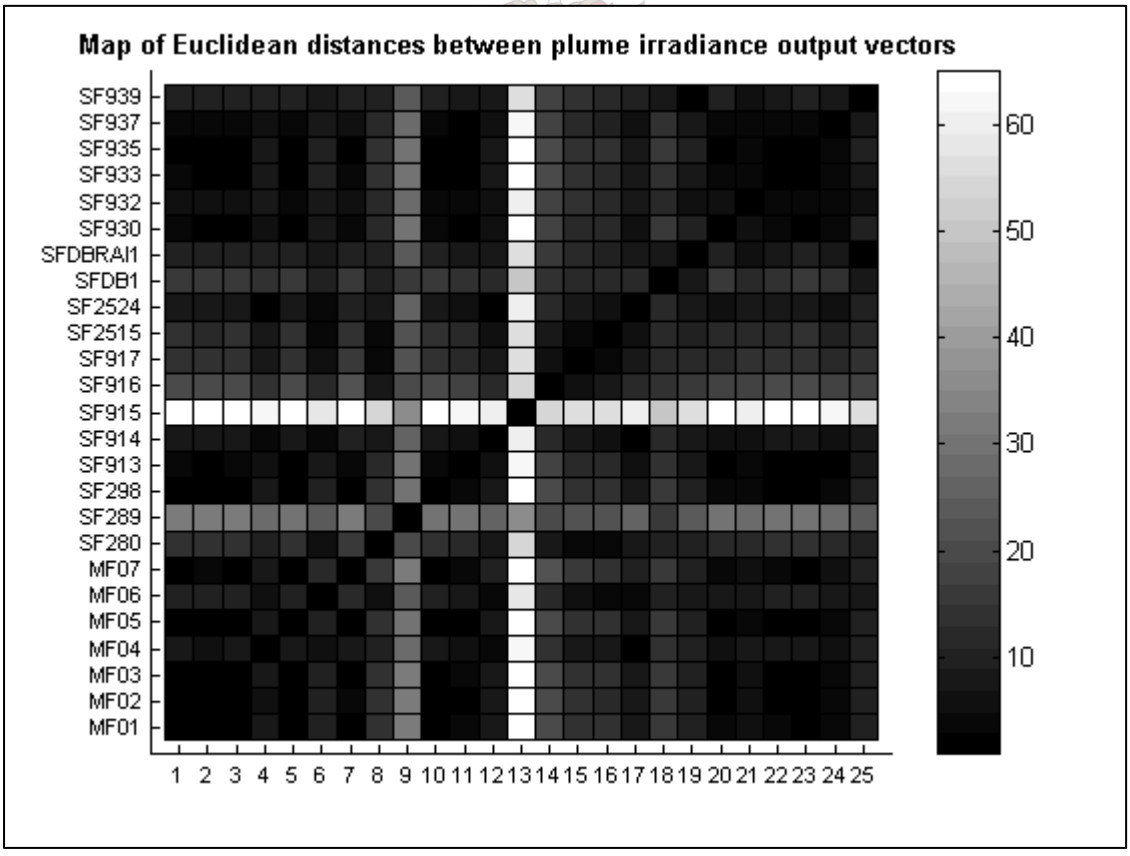

Figure 7.2-2 Map of Euclidean distances between plume irradiance output vectors

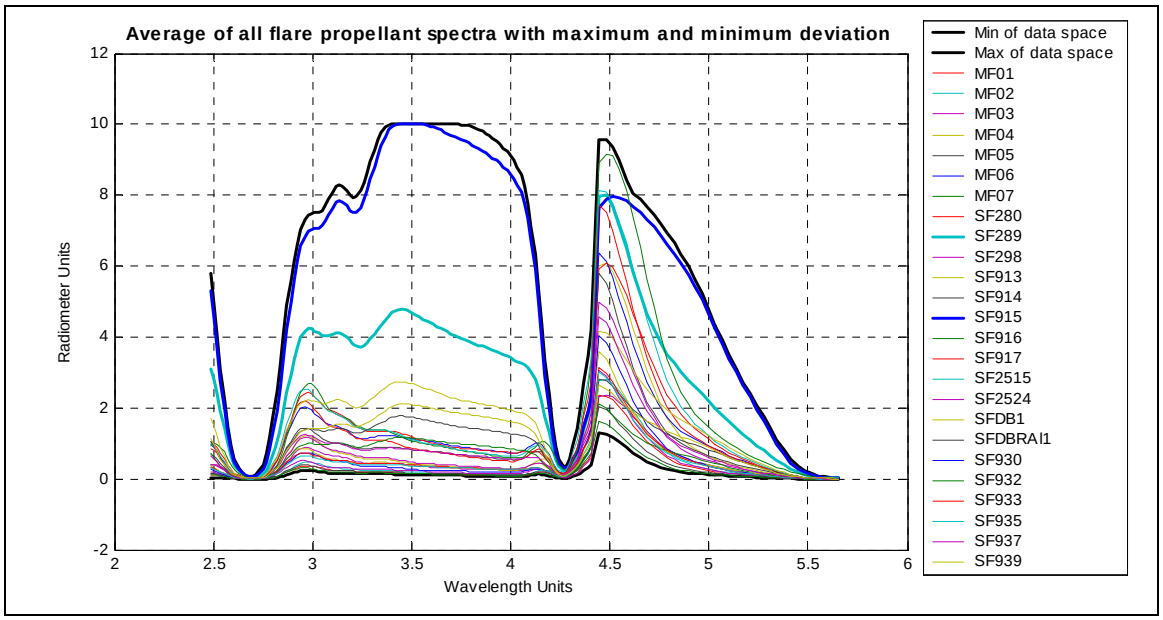

Figure 7.2-3 Average spectra signatures of all the flares, i.e. variation space

The relationship between the two visualisations is easily explained. The topmost bold curve in fig. 7.2-3, which lies on the edge of the variation space, can be identified in fig.7.2-2 as the flare SF915, of which the Euclidean distances are the greatest. The same could be said for SF289, which also lies far from the rest of the flares (second bold curve from the top) in fig. 7.2-3, which is reflected in fig. 7.2-2 and the corresponding graph of the flare, comparing the predicted curve with the measured values. The graphs depicting the predicted curve, generated by the NN, compared to the measured values for all the flares are shown in figures 7.2-4 to 7.2-27.

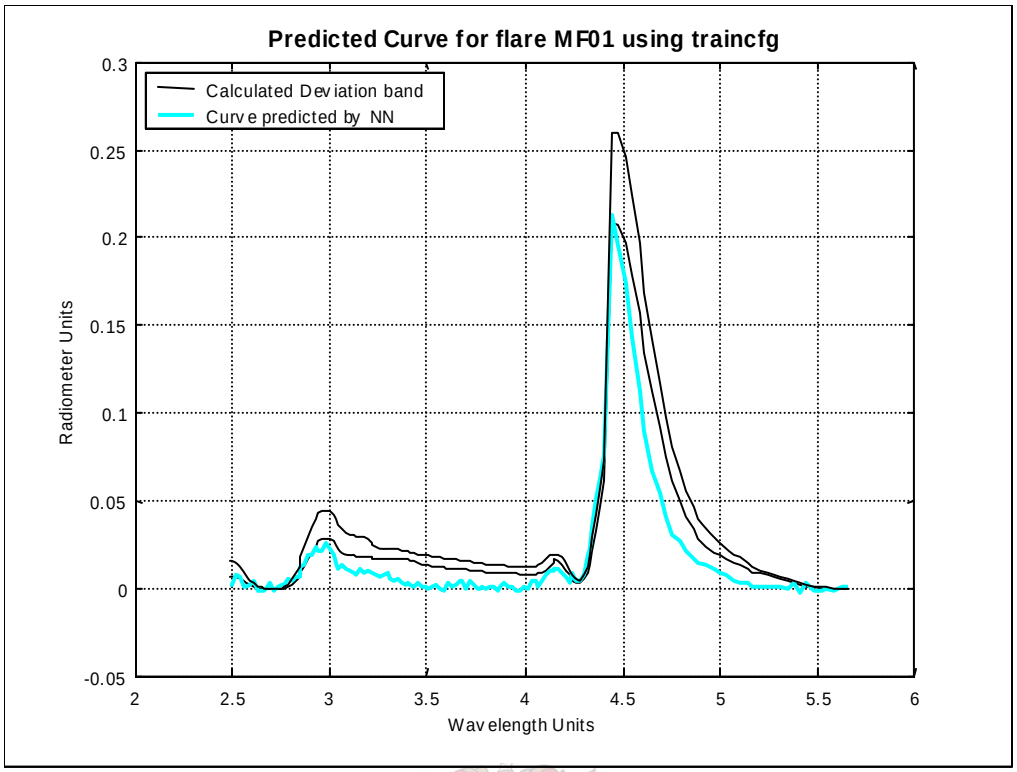

Figure 7.2-4 Irradiance predicted for flare MF01

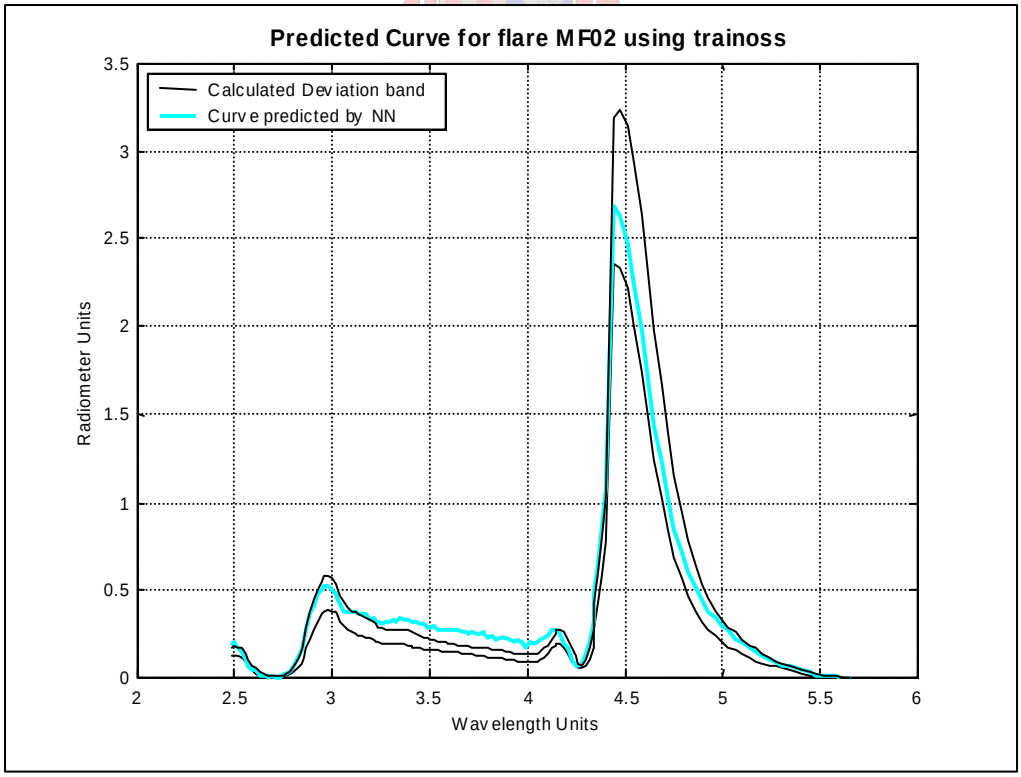

Figure 7.2-5 Irradiance predicted for flare MF02

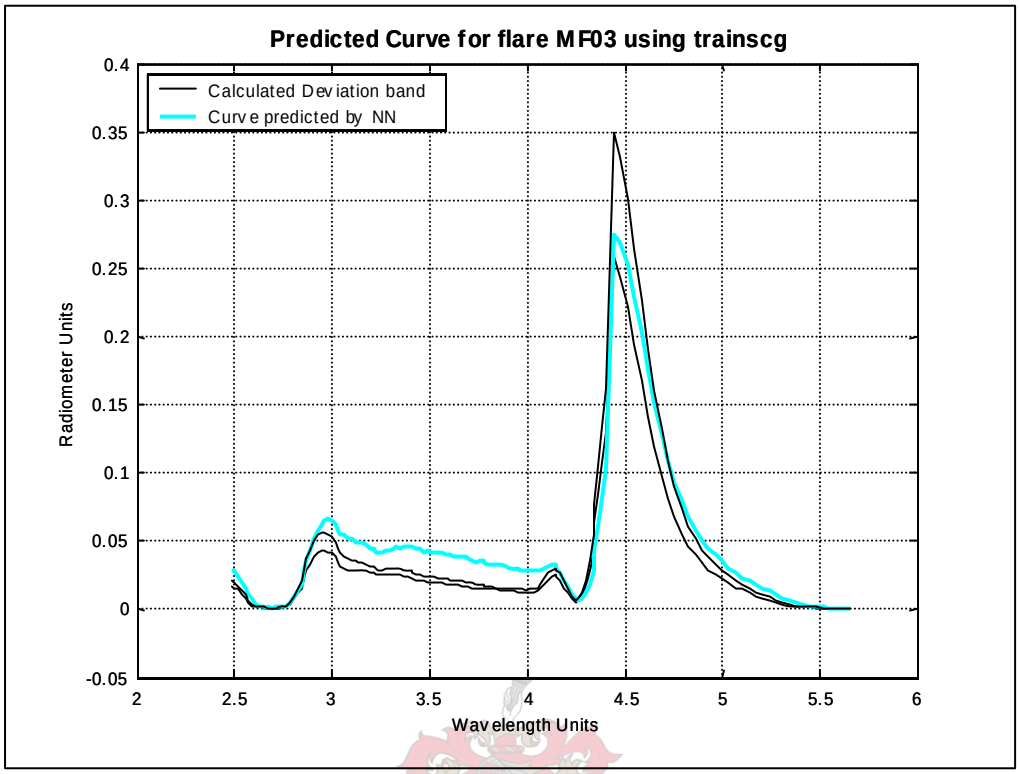

Figure 7.2-6 Irradiance predicted for flare MF03

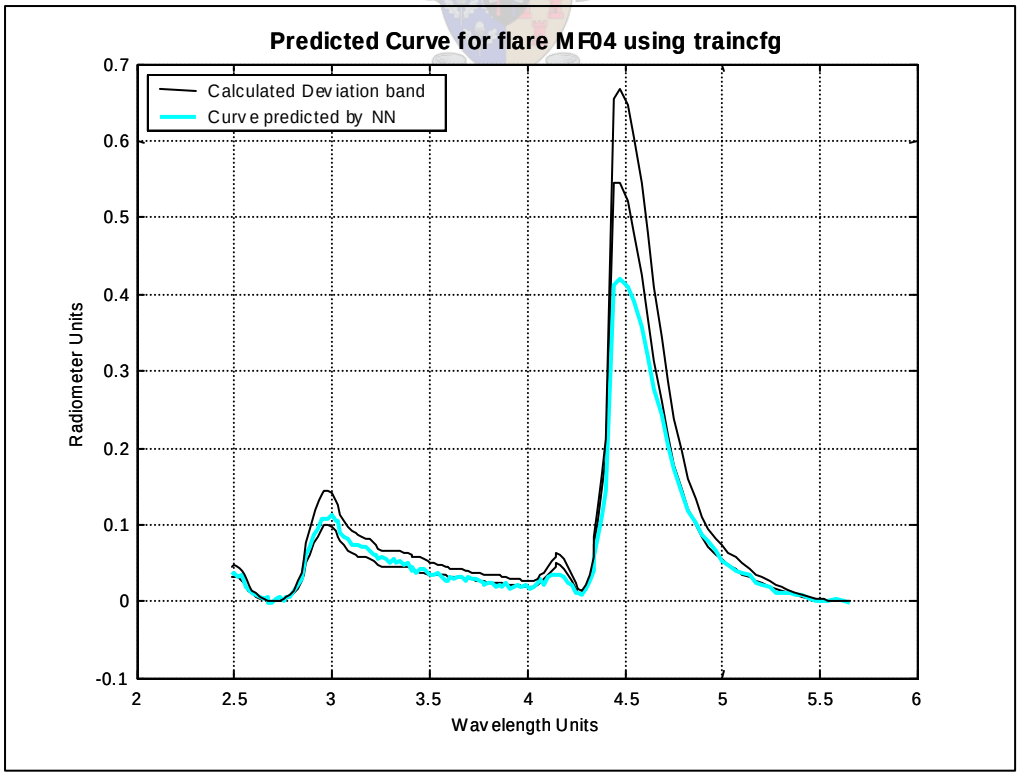

Figure 7.2-7 Irradiance predicted for flare MF04

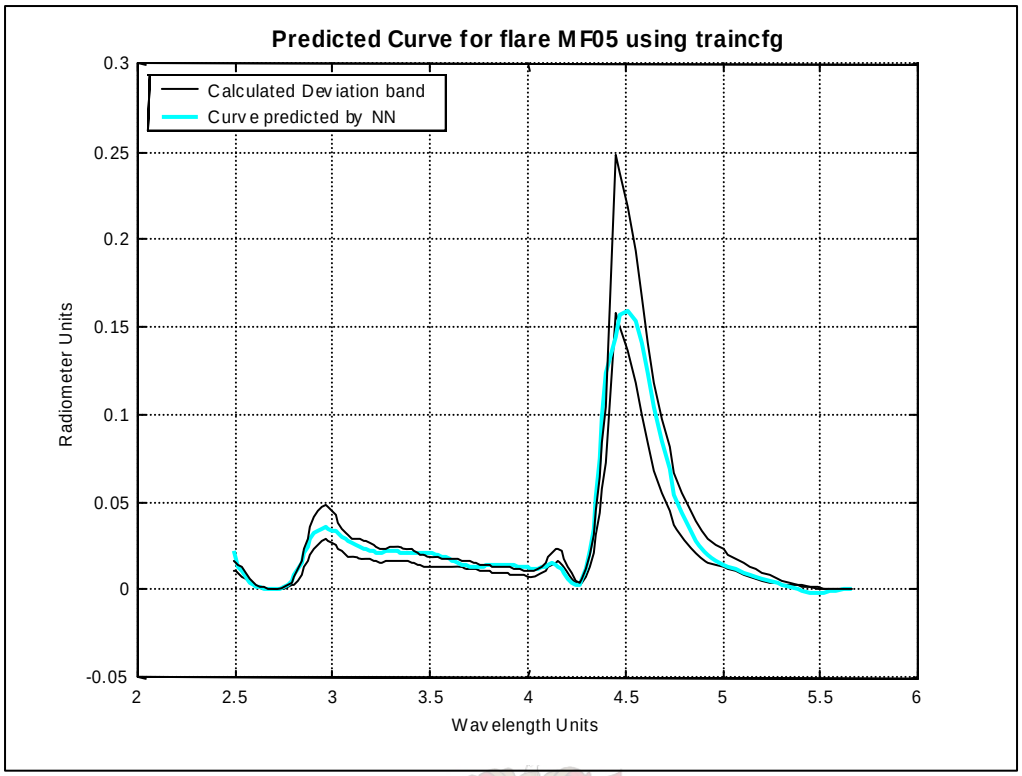

Figure 7.2-8 Irradiance predicted for flare MF05

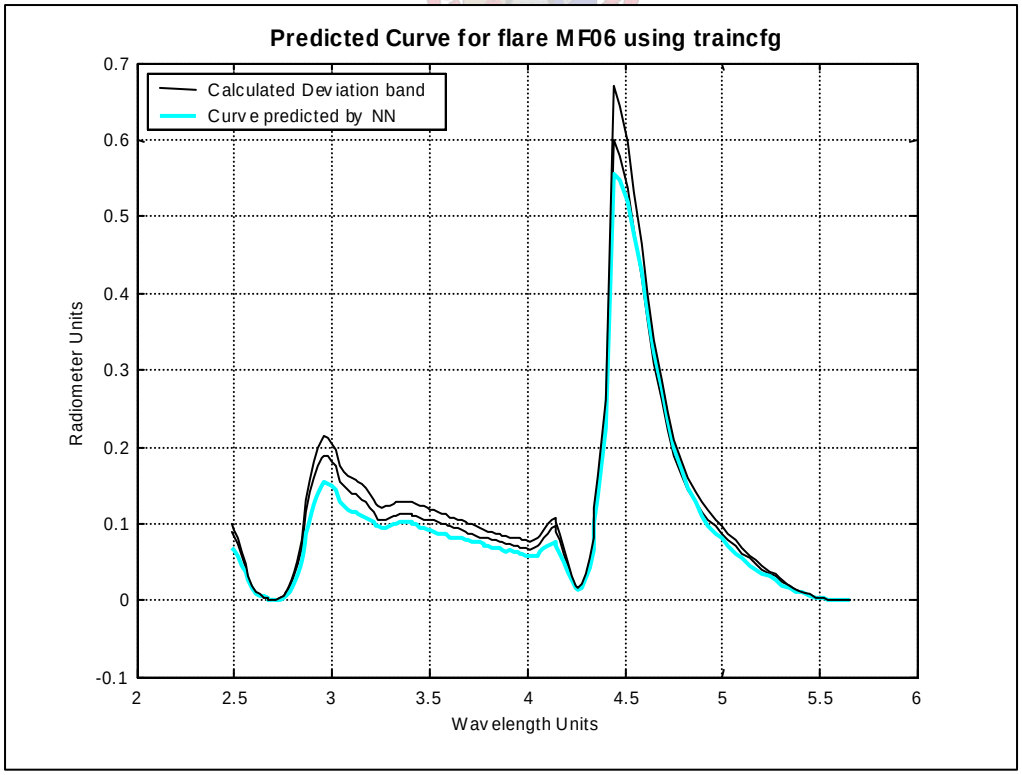

Figure 7.2-9 Irradiance predicted for flare MF06

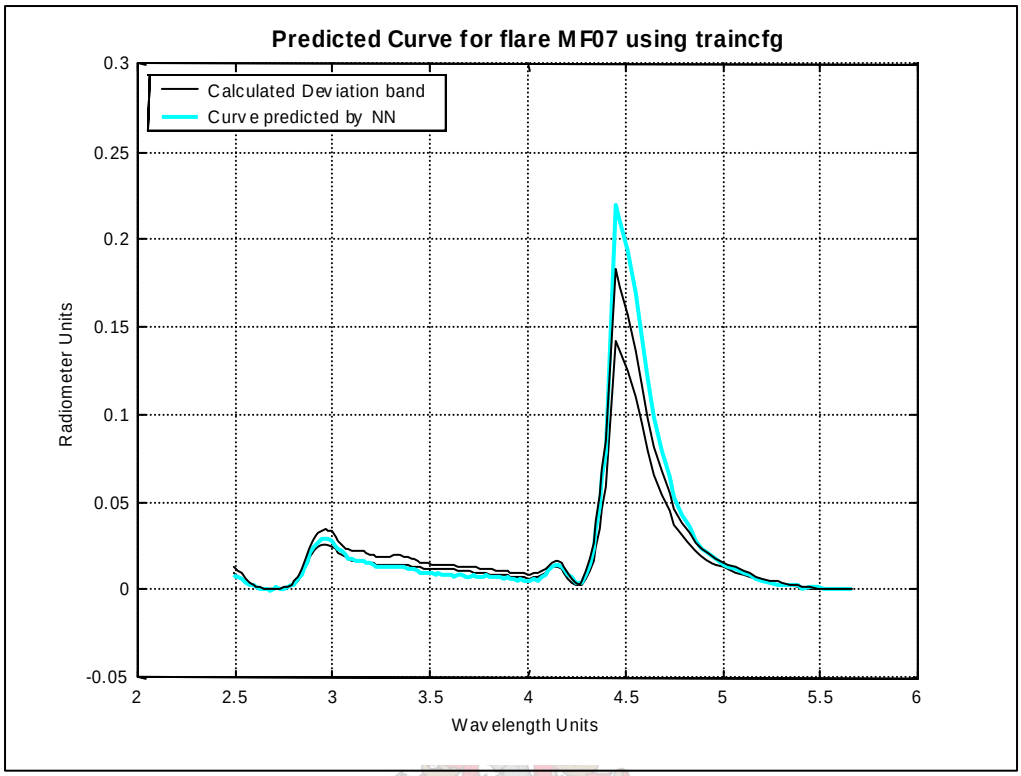

Figure 7.2-10 Irradiance predicted for flare MF07

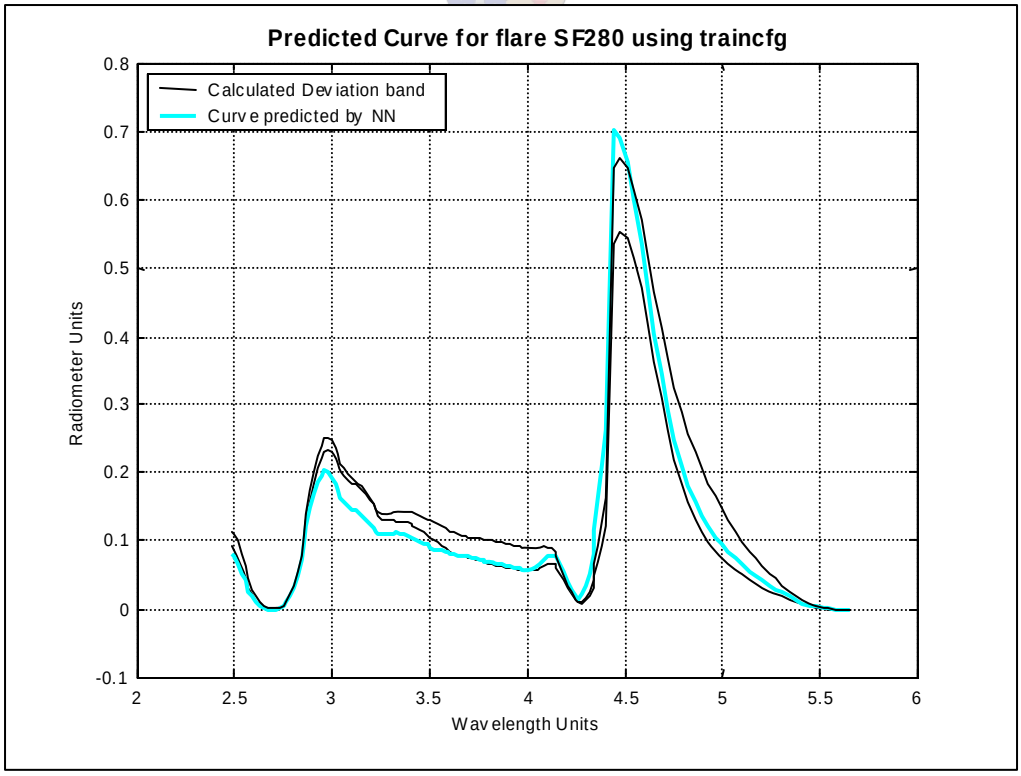

Figure 7.2-11 Irradiance predicted for flare SF280

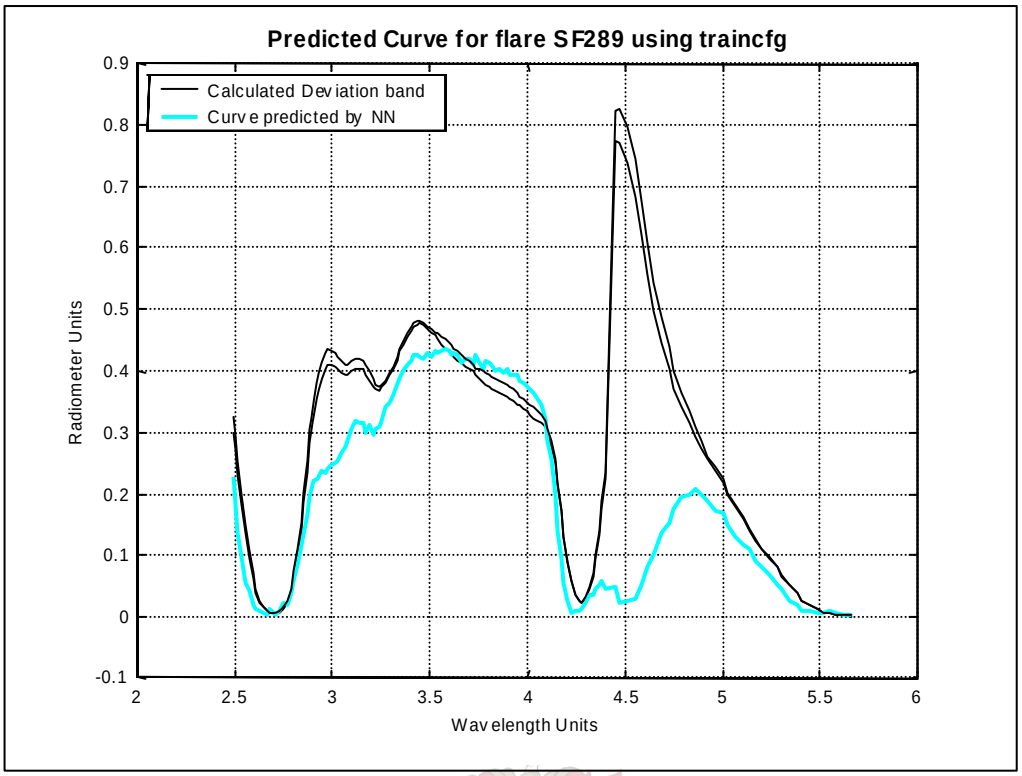

Figure 7.2-12 Irradiance predicted for flare SF289

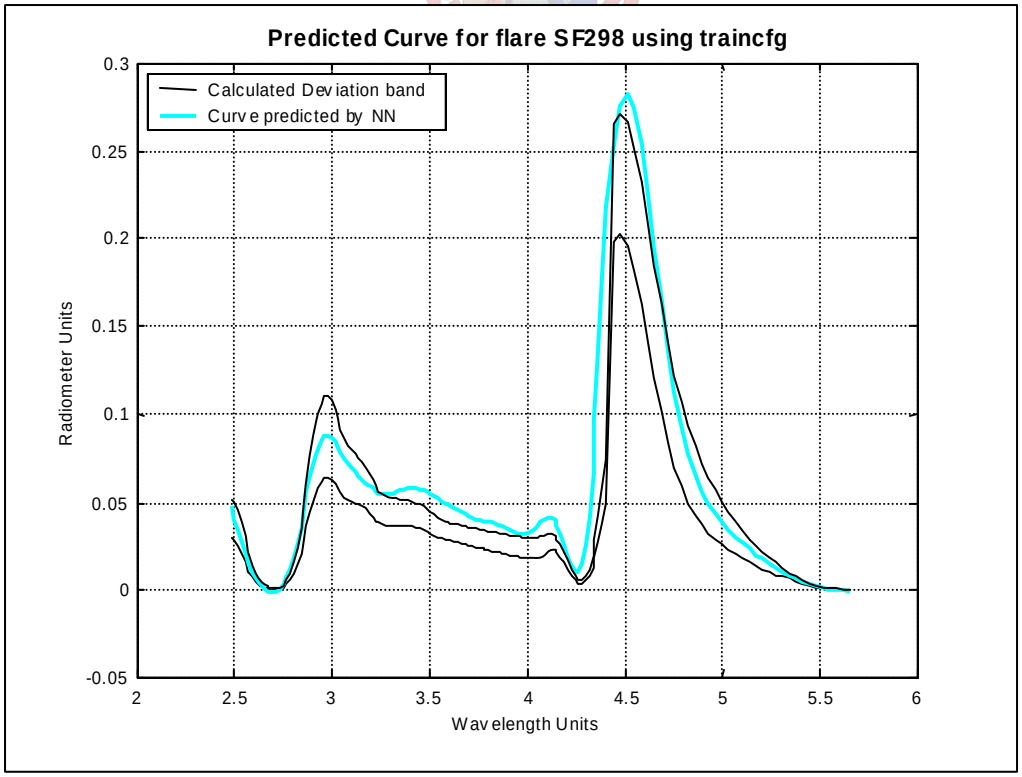

Figure 7.2-13 Irradiance predicted for flare SF298

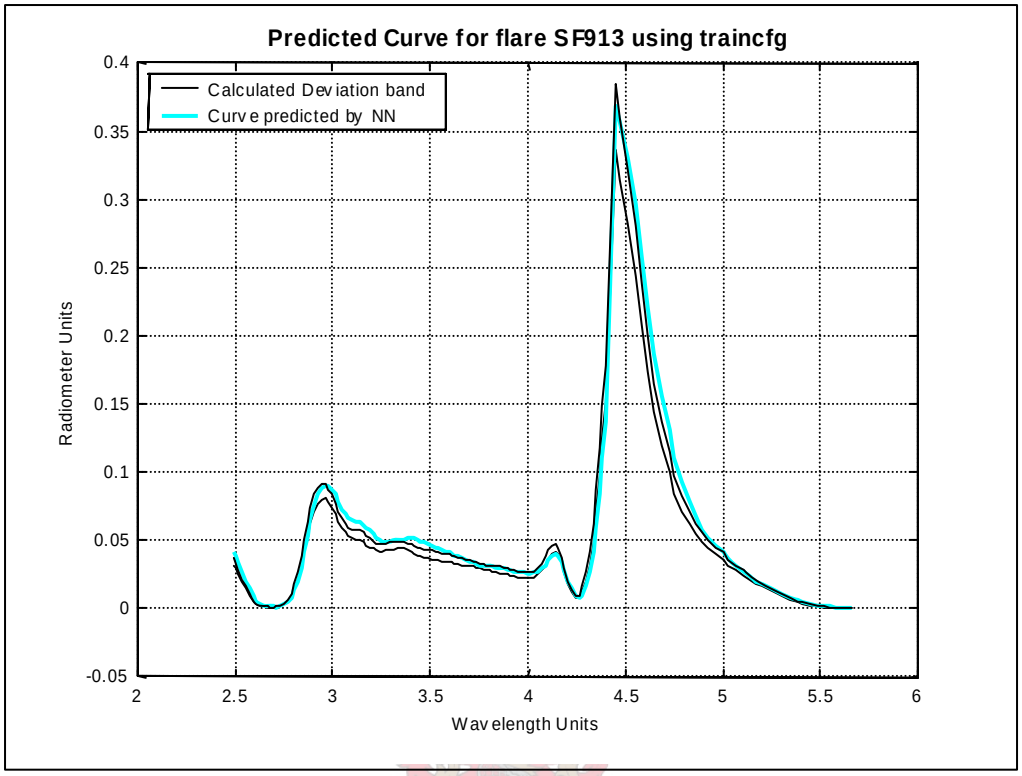

Figure 7.2-14 Irradiance predicted for flare SF913

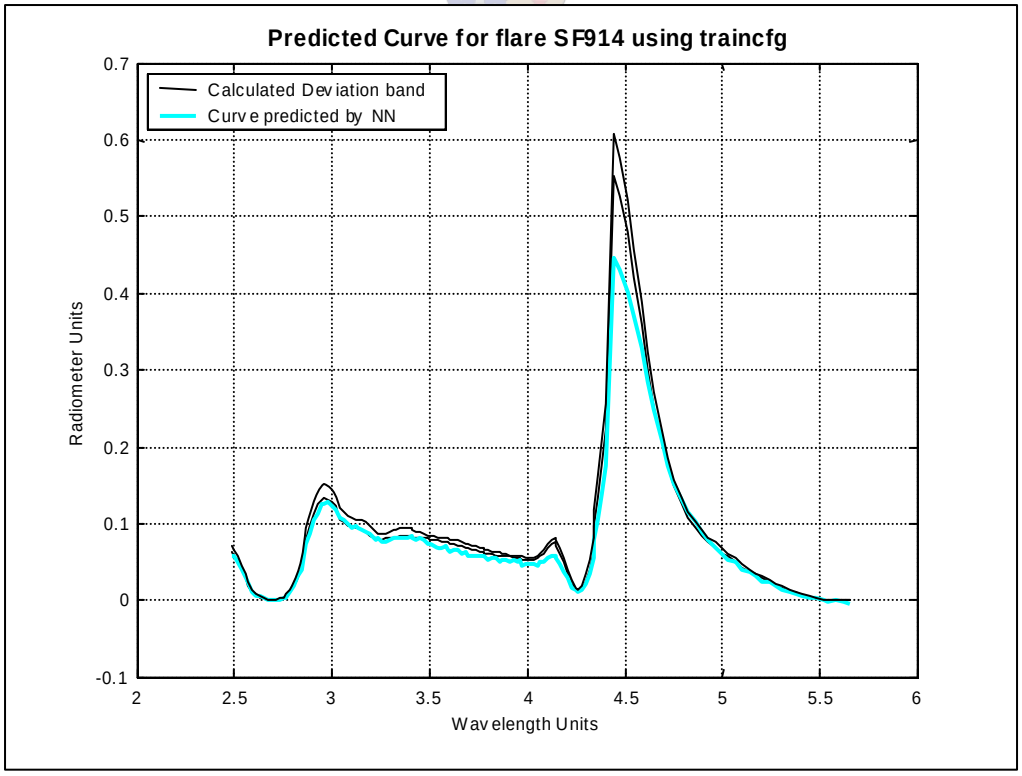

Figure 7.2-15 Irradiance predicted for flare SF914

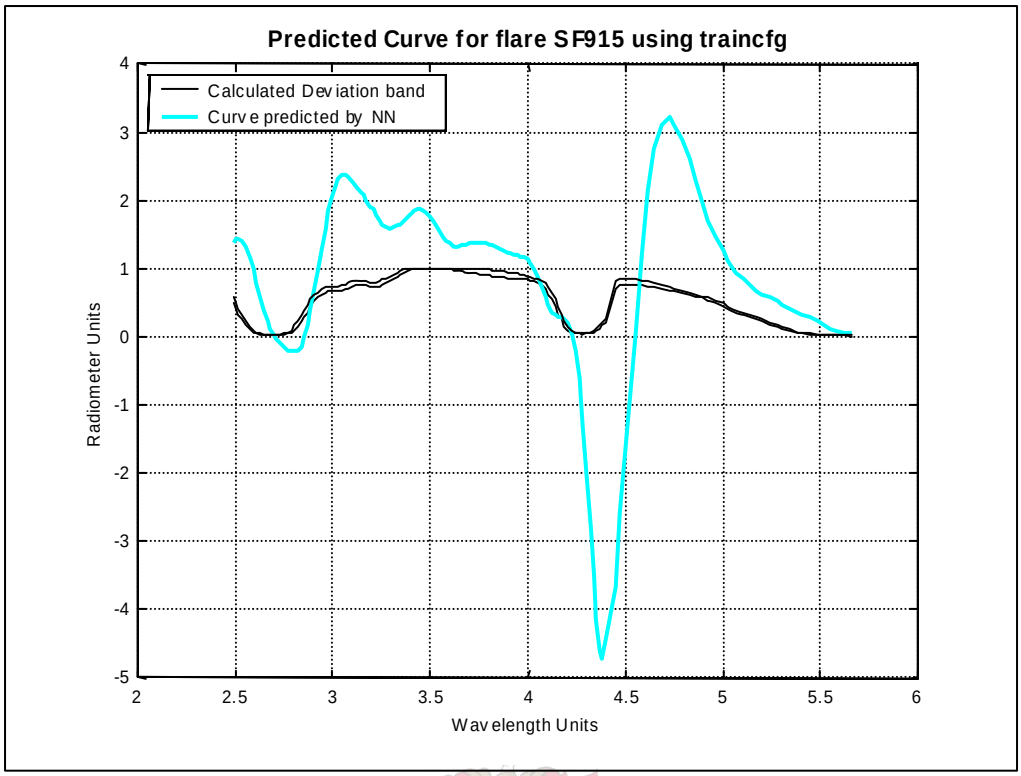

Figure 7.2-16 Irradiance predicted for flare SF915

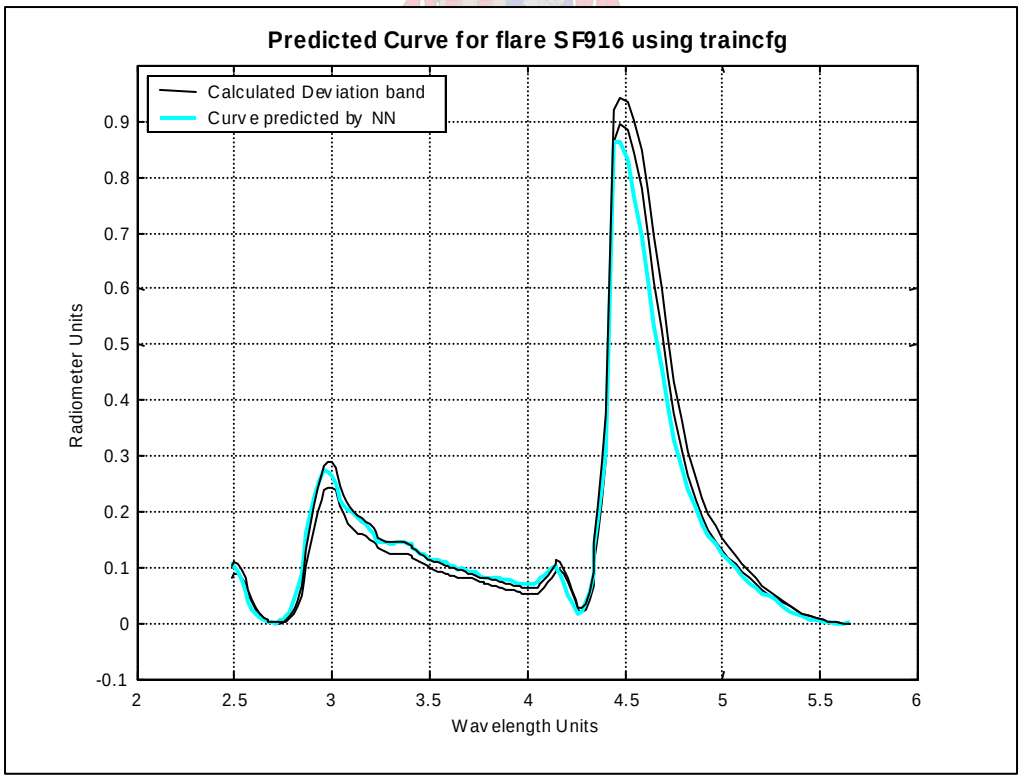

Figure 7.2-17 Irradiance predicted for flare SF916

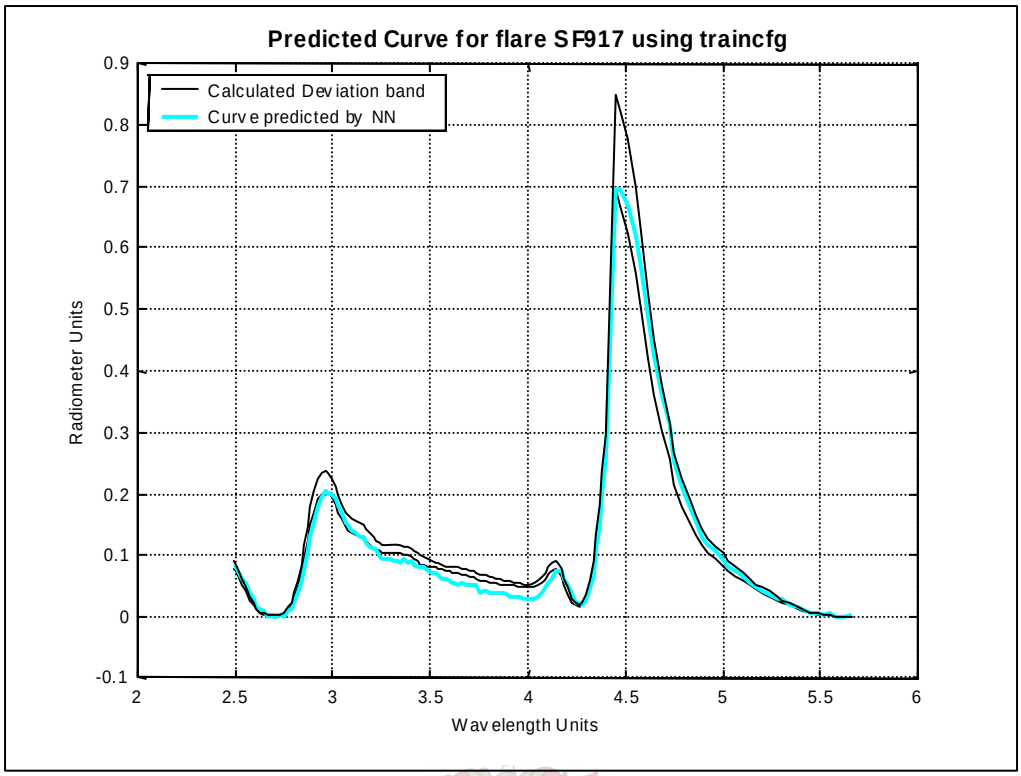

Figure 7.2-18 Irradiance predicted for flare SF917

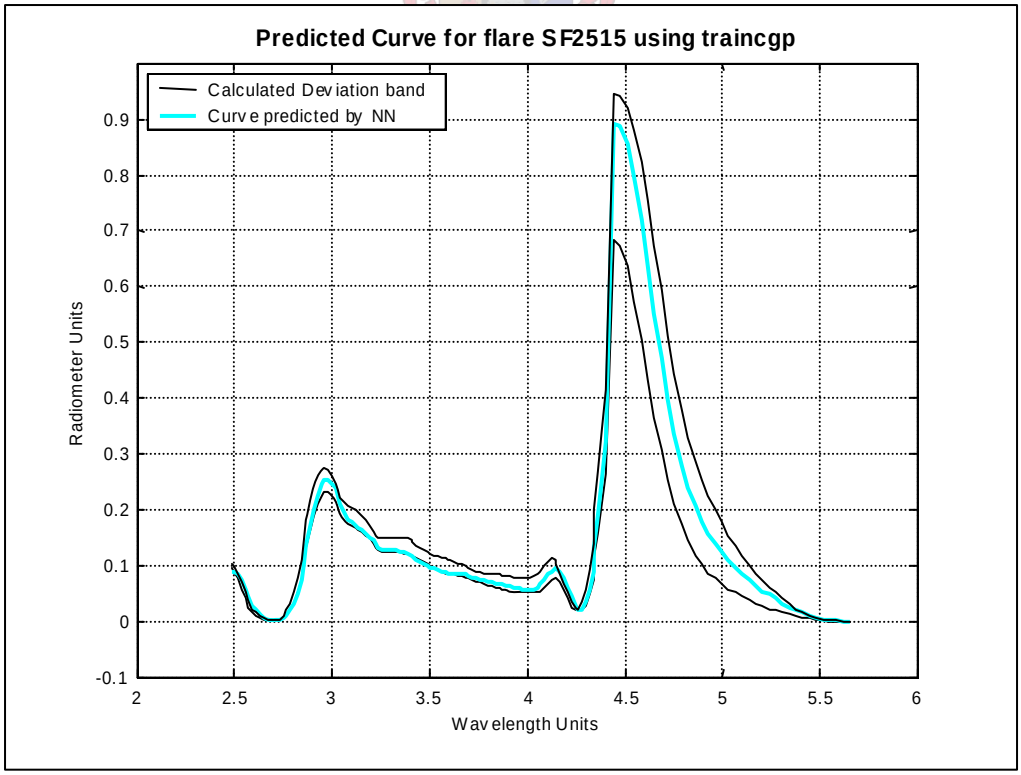

Figure 7.2-19 Irradiance predicted for flare SF2515

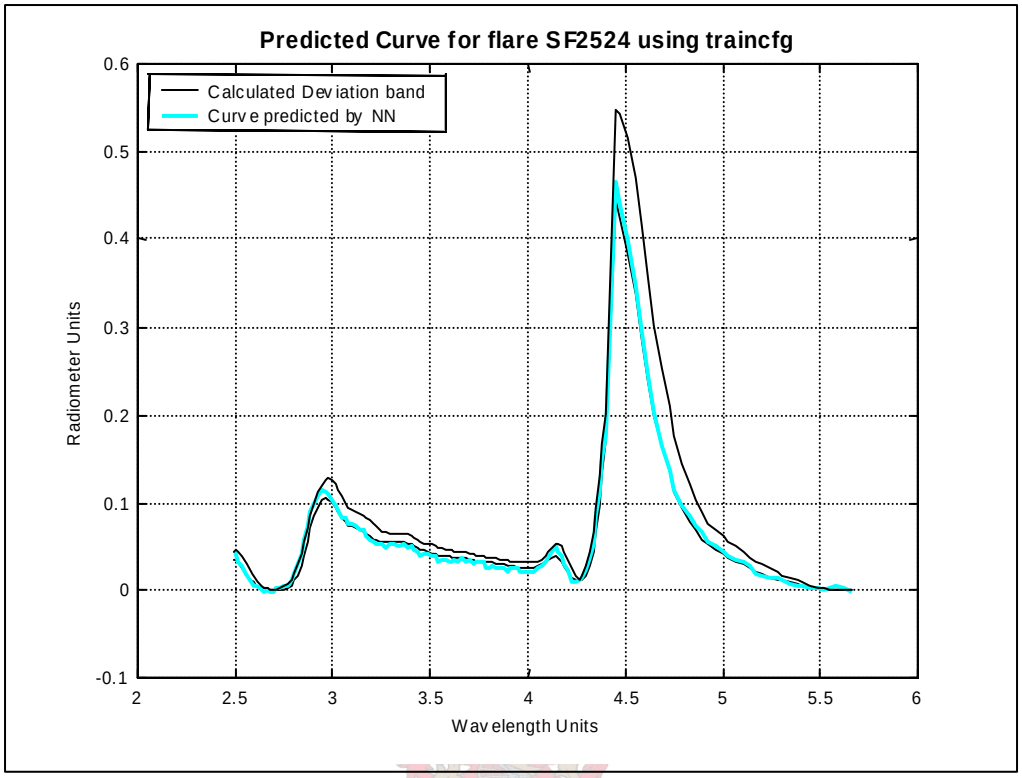

Figure 7.2-20 Irradiance predicted for flare SF2524

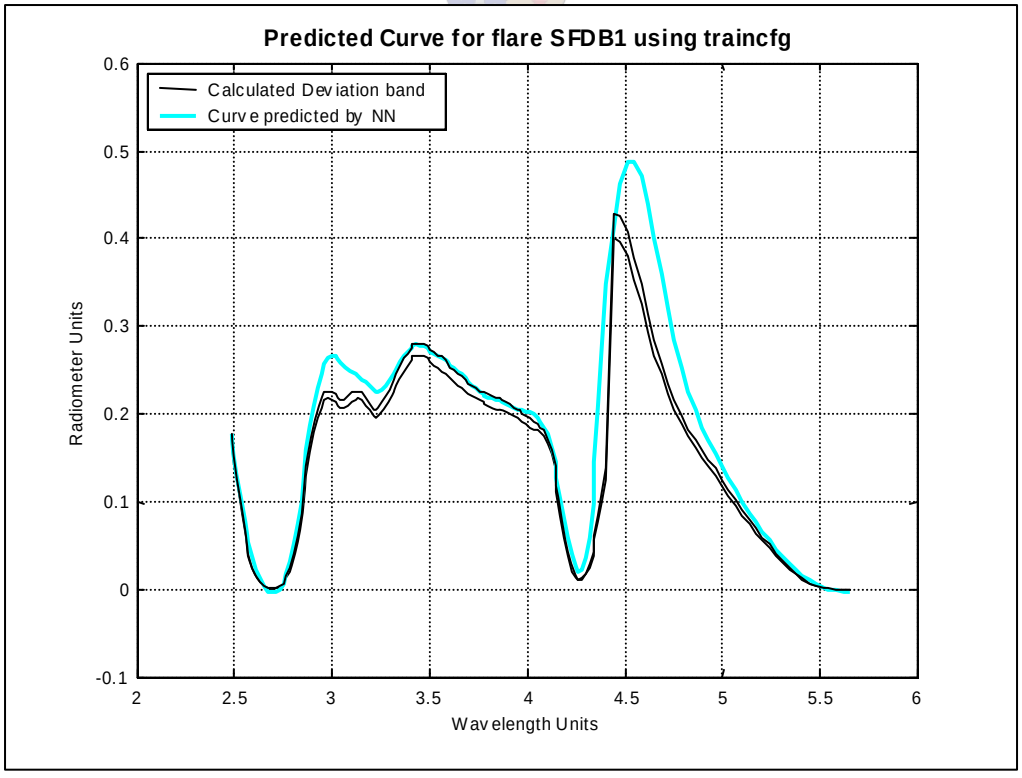

Figure 7.2-21 Irradiance predicted for flare SFDB1

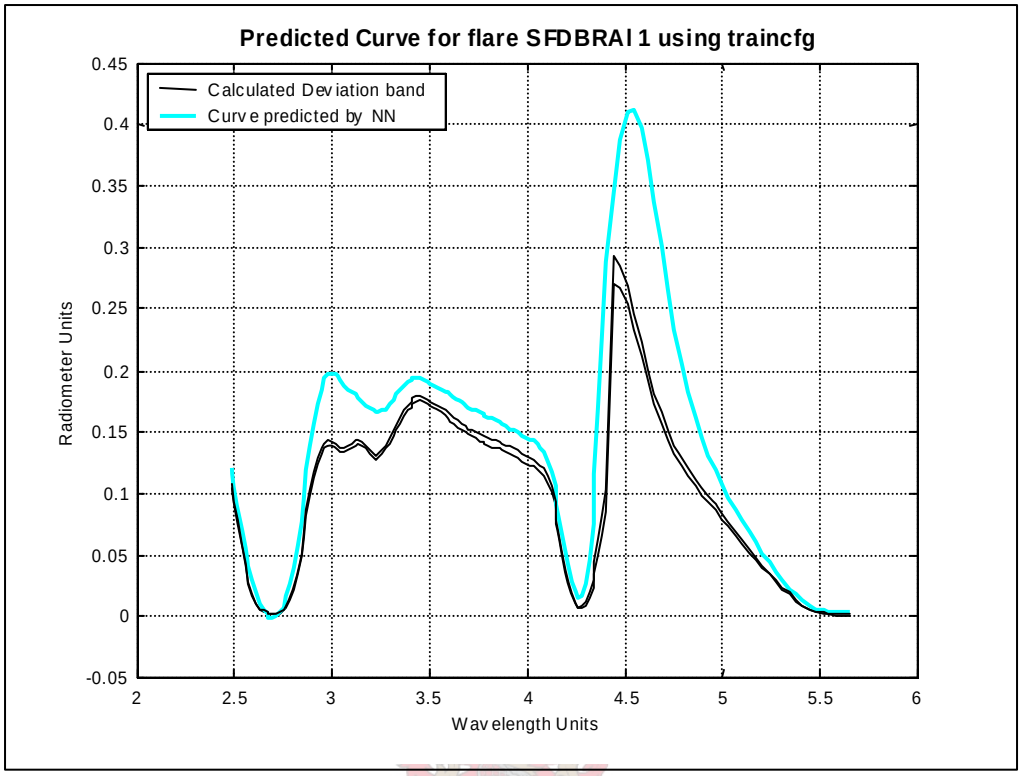

Figure 7.2-22 Irradiance predicted for flare SFDBRAI 1

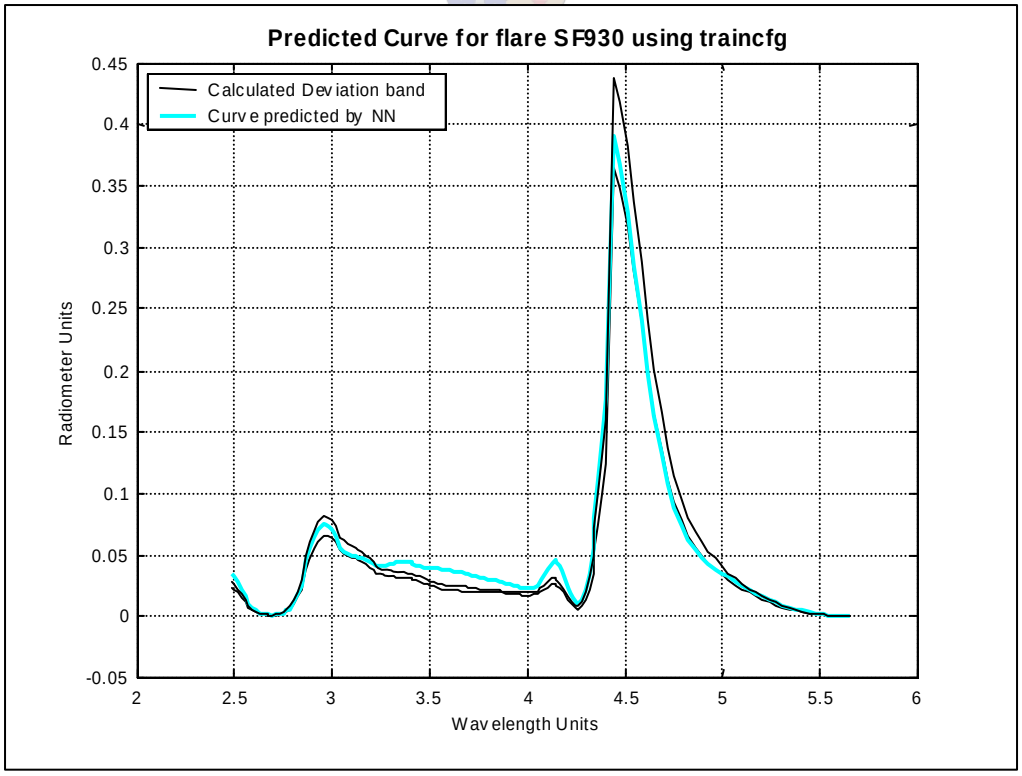

Figure 7.2-23 Irradiance predicted for flare SF930

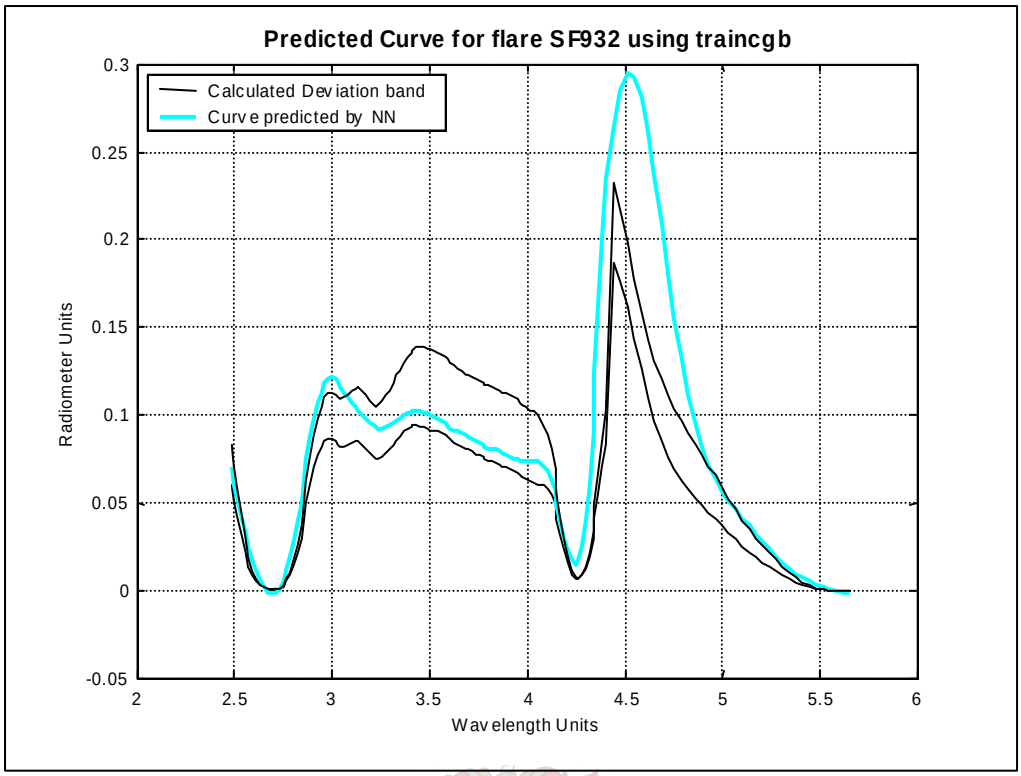

Figure 7.2-24 Irradiance predicted for flare SF932

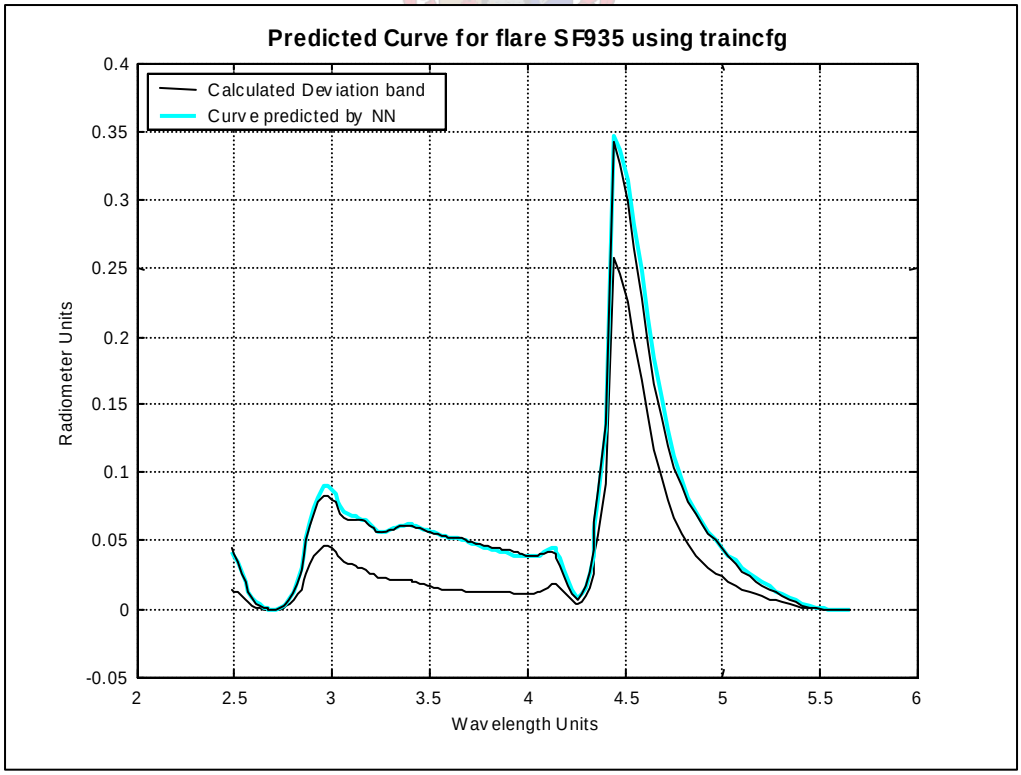

Figure 7.2-25 Irradiance predicted for flare SF935

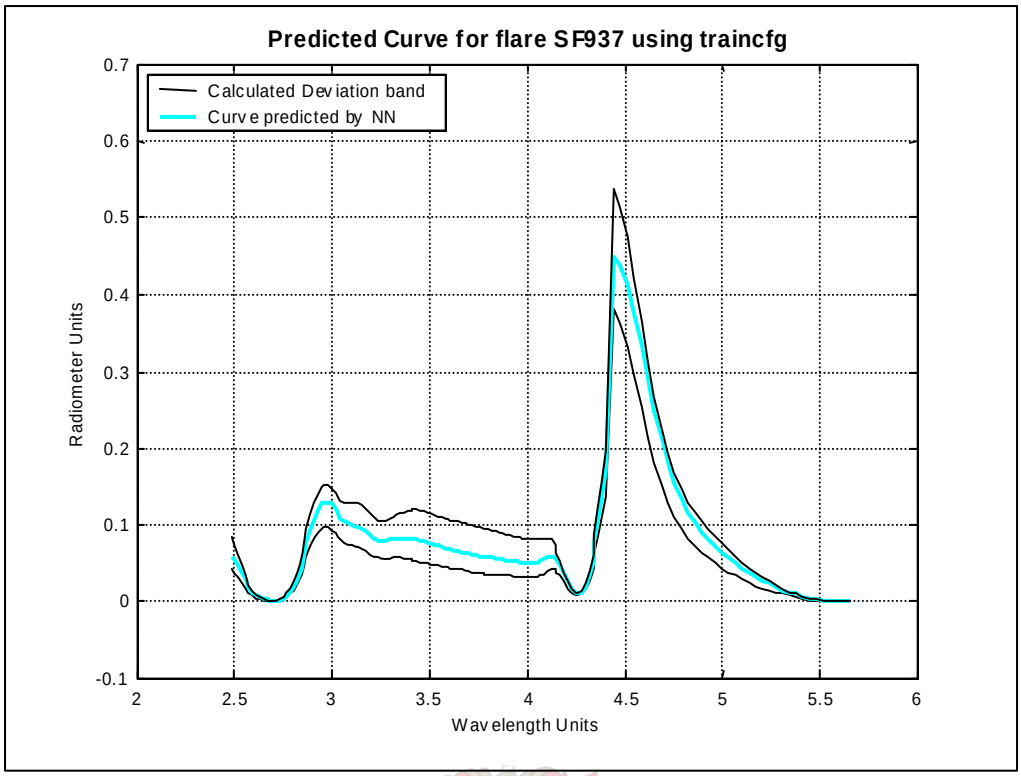

Figure 7.2-26 Irradiance predicted for flare SF937

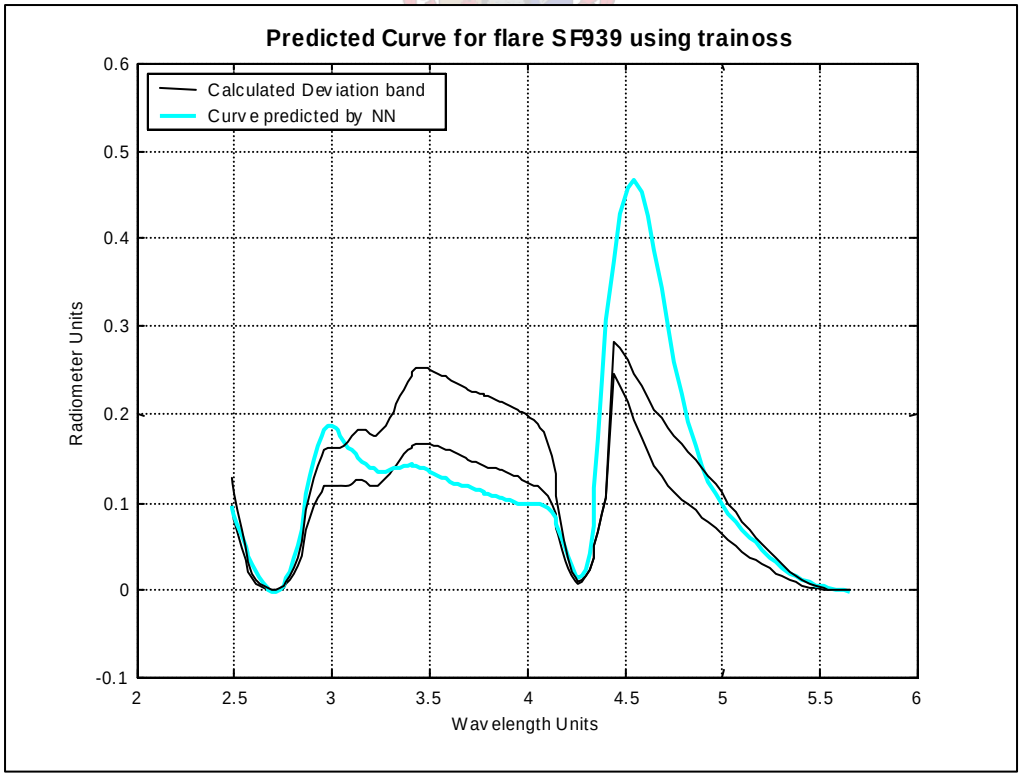

Figure 7.2-27 Irradiance predicted for flare SF939

7.2.2. Characteristics of Spectra

The two major transmission windows in the wavelength band considered, is the CO_2 window at 4.4 μm and the H_2O window around 2.5 μm. In these respective windows, these specific molecules radiate strongly coupled with less absorption by the atmosphere at these wavelengths. In the 2.5 – 4 μm region the radiation is mainly due to metals present in the composition. The two main outliers in the variable space are SF915 and SF289. In both cases there are high radiation in the 2.5 – 4 μm regions. For SF915 this is due to Magnesium present in the composition. A comparative content of elements in the flares are shown in fig. 7.2-28. As was shown in fig. 7.1-4, the fuel:air ratio follows the trend of the area underneath the spectral curves of the flares. Assuming that the more radiation measured in the 2.5 – 4 μm region, the bigger the area enclosed by the curve, it follows that the fuel:air ratio indicates higher radiation in the 2.5 – 4 μm region. In fig. 7.2-28 this assumption is confirmed. In all the cases where high radiation is measured in the 2.5 – 4 μm region a bigger C:O ratio can be seen.

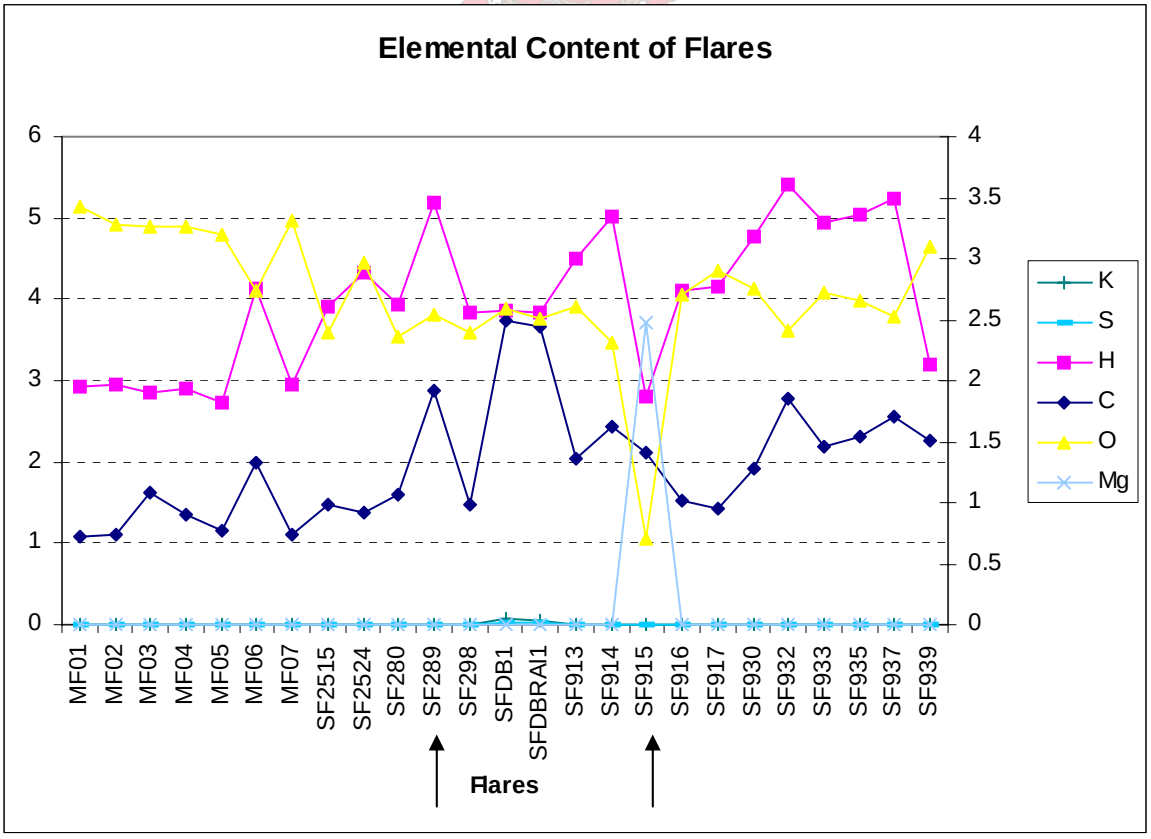

Figure 7.2-28 Elemental Content of Flares

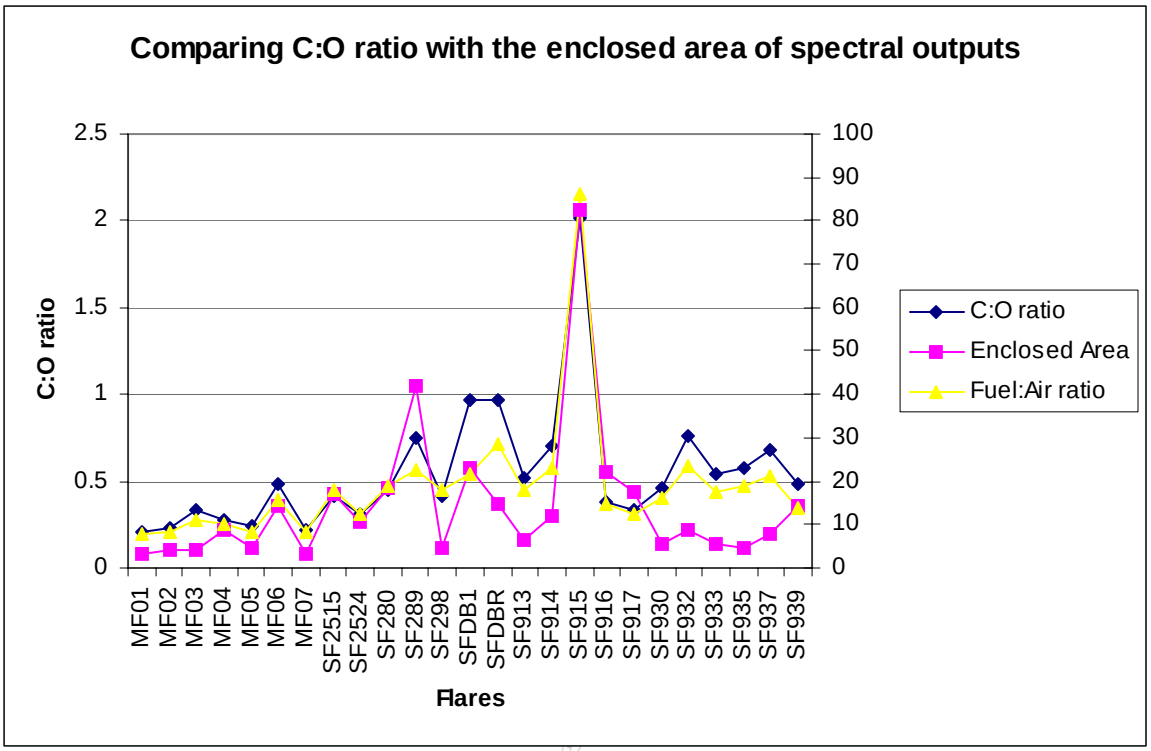

Figure 7.2-29 Comparing the C:O ratio with the Fuel:Air ratio and Enclosed area of spectral outputs

Fig.7.2-29 shows that the C:O ratio is a good measure of the Fuel:Air ratio for the different flares. The predicted spectra for SF915 return some negative values. The transfer function used in the training of the neural net was a tangential function. Before the neural is trained, the input and output data is normalised. The training data is normalised and returns a vector signifying the normalisation. The vector is then used to normalise the test data. Since SF915 is the only flare with the large amount of Mg present, the normalisation vector did not scale the input data of the SF915 flare properly. This coupled with a tangential transfer function could have led to the negative values seen in fig. 7.2-16.

Another way of viewing the input space is again using the Euclidean distance as a measure, shown in fig.7.2-30. Again a direct comparison can be made: The flares with the comparatively larger Euclidean distances are the same flares with a bigger C:O ratio and thus radiate strongly in the 2.5-4 micron waveband.

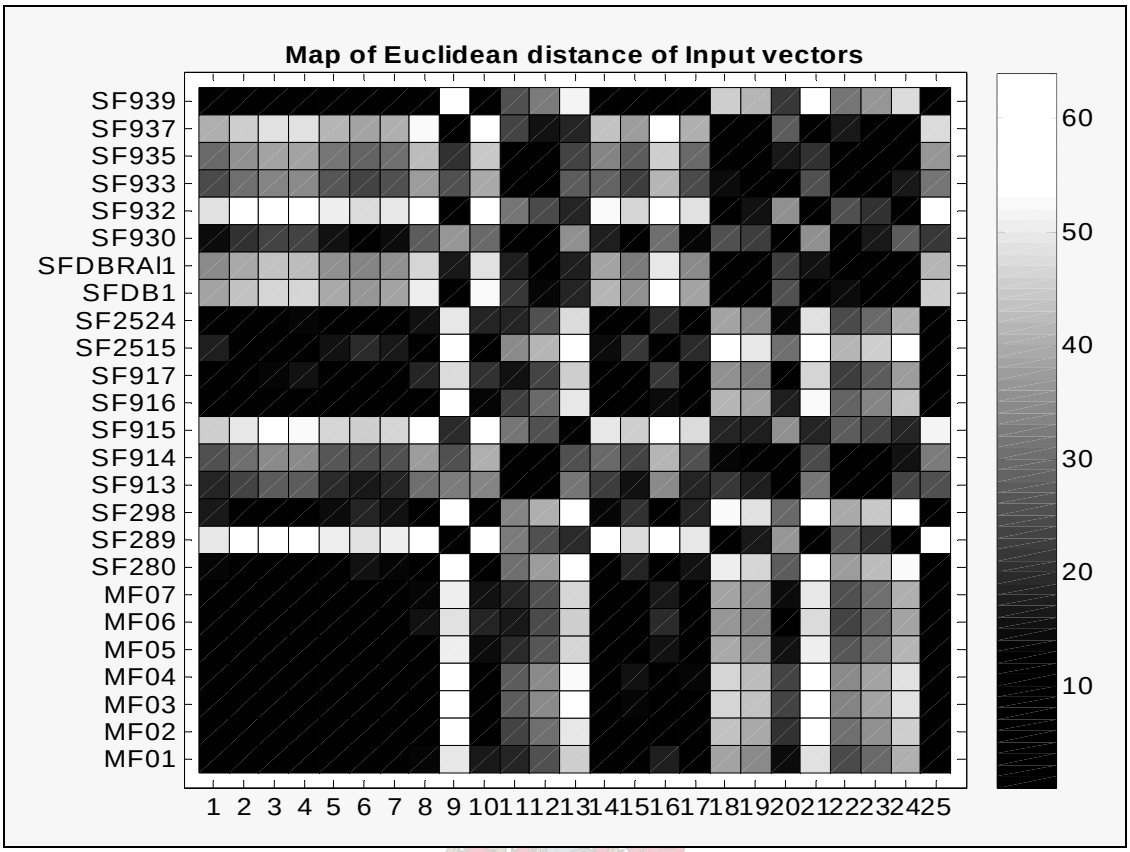

Figure 7.2-30 Map of Euclidean distances between plume irradiance input vectors

In conclusion, it would be necessary to have a more densely populated variable space in order to correctly model these particular radiance spectra. However the model still gives the impression as being a working model, which will be tested for in the next section.

7.3. Discussion of Results

As with the prediction of the rocket spectra it was again shown that the neural network could "sufficiently" predict the measured spectra, except for the spectra on the edge of the variable space. In order to qualify the neural network it is necessary to evaluate the neural network's performance according to several statistical measures. The statistical tests will determine if the solution is just an average of the variable space or whether it is a unique solution.

The R^2 evaluation parameters for each of the flares test sets are shown in table 7-8. The average R^2 for all the test sets is 0.829. After inspection of the values, there are certain flares' prediction that did not perform well. This poor performance can be ascribed to not enough hidden nodes used in the net or that the net is not fully optimised yet. It is also shown in fig.7.2-3 that the flares that show poor correlation are also the flares on the edge of the variable space or in sparsely populated areas. This would imply that the ability of this net to extrapolate is not that good, which could be due to the small amount of data that was available for training the net.

Table 7-8 R2 values for each of the test sets

	R^2		R^2
MF01	0.8846	***SF916***	0.98408
MF02	0.9757	***SF917***	0.984
MF03	0.9159	***SF2515***	0.98799
MF04	0.90086	***SF2524***	0.99737
MF05	0.981	***SFDB1***	0.83936
MF06	0.95847	***SFDBRAl1***	0.58851
MF07	0.937	***SF930***	0.98433
SF280	0.94074	***SF932***	0.13162
SF289	0.21525	***SF933***	0.99177
SF298	0.7637	***SF935***	0.96729
SF913	0.97177	***SF937***	0.99174
SF914	0.98779	***SF939***	0.019037
SF915	-11.188		

The plot of the Euclidean distances between the predicted and measured spectra confirms the conclusions made after comparing the area plot of the Euclidean distances of the different flares in fig. 7.2-2 and the variable space in fig. 7.2-3. The spectra of flares SF915 and SF289 could not be predicted due to their spectral signature lying on the edge of the variable space, which means that there were not enough data in that region of the variable space to properly populate the model, before training the neural network.

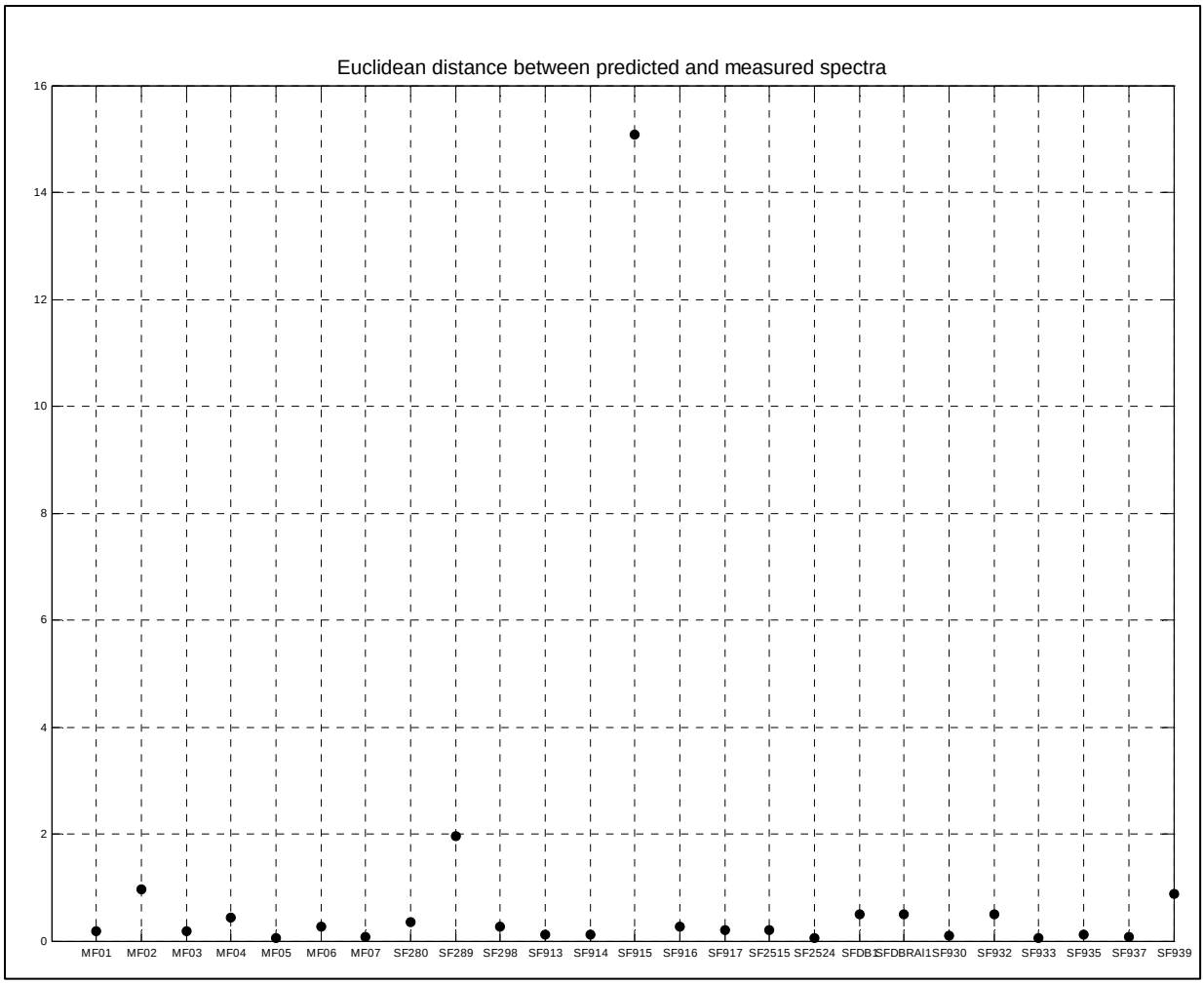

Figure 7.3-1 Comparing the predicted and measured IR spectra in terms of Euclidean distance

The plot of the fractional energy difference between the measured and predicted spectra confirms the result from fig.7.3-1. Once again the two main culprits are SF915 and SF289, but some other flares are also identified to have larger fractional energy differences. It has to be noted that in fig.7.3-1 the results are not scaled according to the maximum irradiance each flare exhibited. This means that if a flare exhibits a low

irradiance level, the euclidean distance between the predicted and measured spectra could show a good result relative to other flares even though the solution is actually quite bad.

7.3.1. Statistical Tests

It was shown that the response of the model could be interpreted by using plots such as Euclidean distances and fractional energy differences, but in order to prove that the neural network model is unique and not just an average solution relative to the variable space, it is important to statistically verify the model. As with the rocket propellants in the previous chapter the "static model", or the mean of the variable space will be evaluated against two test sets for several statistical tests. Only the results of two test sets are shown here, since it was only necessary to prove that the neural net worked for future work to continue.

The mean squared error *(mse)* will be used to determine the strength of correlation in evaluating whether the NN model or the static model show better correlation to the measured irradiance for the two test sets, MF06 and SF933. The *mse* is defined as:

$$mse = \frac{\sum_{i=1}^{146} \left(Model_i - Measured_i \right)}{146} \tag{6-4}$$

Table 7-9 Mean squared error for NN model and Static Model

	MF06	***SF933***
NN Model	0.0167	0.00179
Static Model	0.102	0.0582

A graphical representation of the comparison the NN model and the static model is shown in fig.7.3-3 and fig.7.3-4. Even though the static model seems to be a fairly good model of the measured data the difference is notable when considering table 7-9.

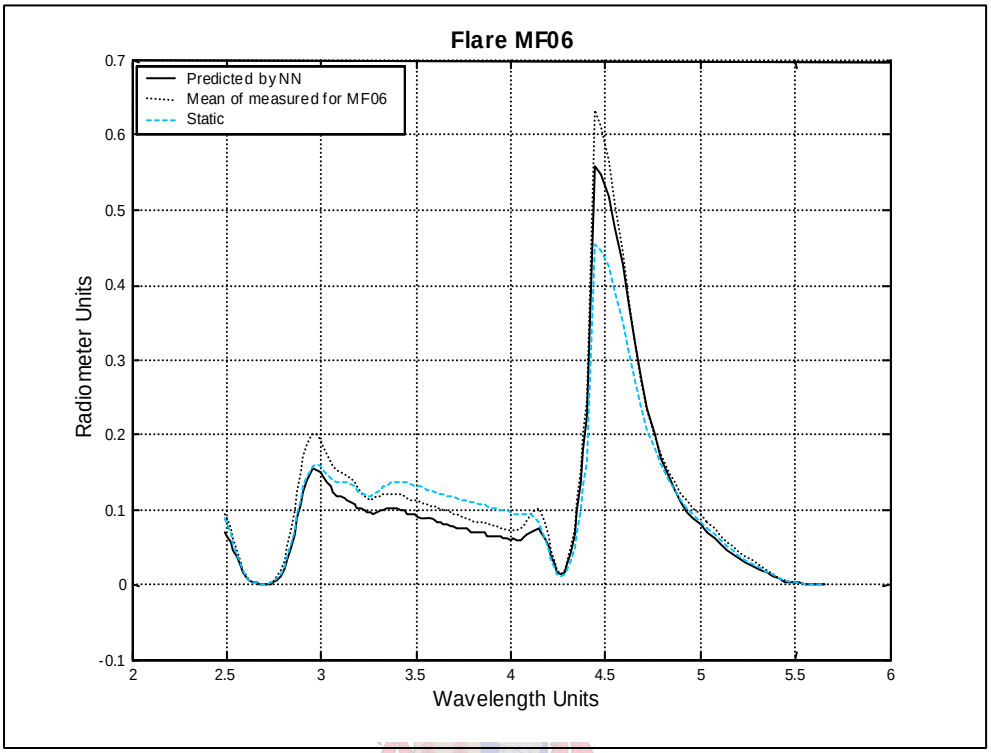

Figure 7.3-2 Comparing the mse between the NN and static model for MF06

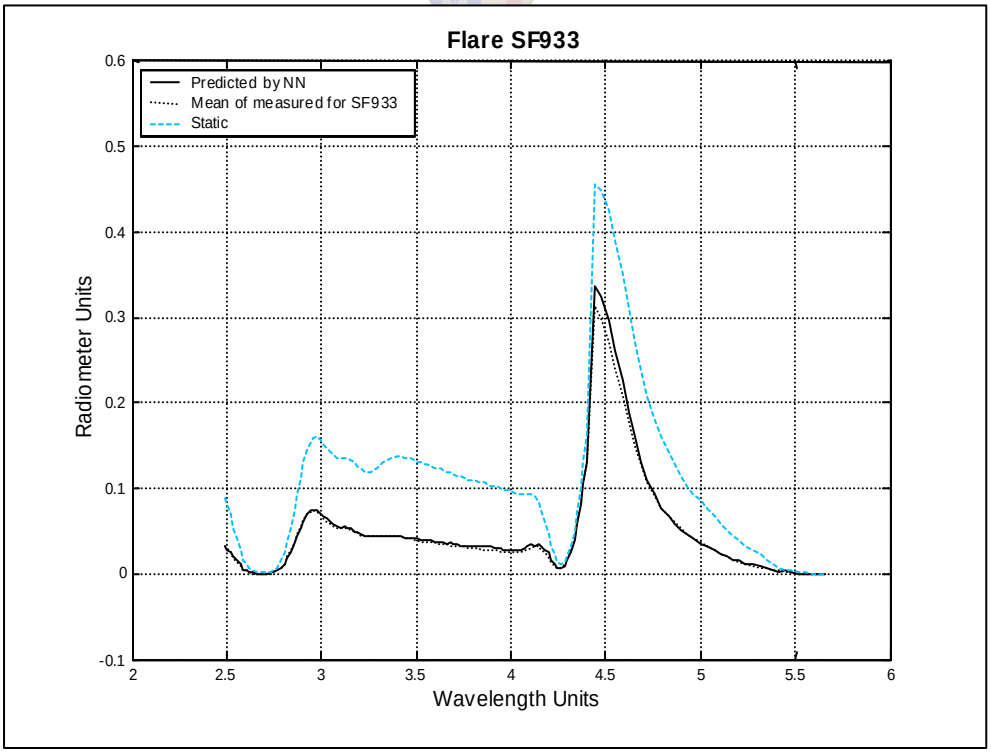

Figure 7.3-3 Comparing the mse between the NN and static model for SF933

In order to complete the evaluation, two further tests were done: a t-test on the residuals of the two models and the measured spectra, and a Wilcoxon signed-rank test (non-parametric test). The t-test is done in order to test the hypothesis that the mean of the residuals of the NN model is smaller than that of the static model. Two t-tests were done for the two test sets, at a confidence level of $\alpha = 0.05$ [8].

The null hypothesis is H_0: $\mu_{NN} = \mu_{static}$ ($\mu \equiv$ mean of residuals)
Alternative hypothesis is H_a: $\mu_{NN} < \mu_{static}$
$t_\alpha = 1.645$

Table 7-10 T-test statistic for test sets

	MF06	***SF933***
t	-2.71	-19.01

The null hypothesis is rejected when $t < -t_\alpha$ and then the alternative hypothesis is accepted, which states that the error of the NN model will be smaller than that of the static model. From table 7-10 it is now possible to conclude with greater confidence that the NN model outperforms the static model, even though the NN model for flare *MF06* and static model seem to be closely correlated in fig.7.3-3.

Non-parametric tests depend on the order relationships of among observations. For the given problem, it has to be decided whether two populations (residuals) are the same or whether one is likely to produce larger observations than the other. The null hypothesis to be tested proposes that the two sample populations (NN and static model), come from the same populations, thus the means or the sums of the ranking positions should be fairly similar [9].

Table 7-11 Wilcoxon ranksum test statistic for test sets

	MF06	***C10***
Z	-11.9886	-13.283
p	0	0

Again the null hypothesis is rejected if $z < -z_{\alpha} = -1.645$ and the alternative hypothesis is accepted, stating that the two populations are not even remotely the same. The large value of the z statistic indicates that the residuals of the static model are much larger than that of the NN model. The statistic p, is the probability of observing a result equally or more extreme than the one using the data (NN and static) if the null hypothesis is true. If p is near zero, it casts doubt on this hypothesis.

It is interesting to note that the static model and the predicted spectral values do not differ much for *MF06*, as can be seen in fig.7.3-3, yet with the use of these statistical tests, it is clearly not the fact. The NN model indeed does dynamically predict the spectra in question correctly and is not an average of the variable space. The model is also able to predict the correct change of the IR spectra (in the correct wavelength band) for a change in the input vector.

7.4. Reference:

1. Gordon, S. and McBride, B., *Computer program for Calculation of Complex Chemical Equilibrium Compositions and Applications,* NASA SP-273, 1971, NASA Lewis Research Center, NASA Reference Publication 1311, (1994).

2. The MathWorks, *Statistics Toolbox User's Guide*, The MathWorks, Inc., Natick, United States, Multivariate Statistics, (2002).

8. Conclusions

8.1. Scope of the Problem

The main objective of the study was to predict the infrared emission spectra of a combustion process. Two datasets were available namely the solid propellant rocket emission spectra and the flare emission data. A neural network was used to model the data, since Roodt[1] successfully used a feedforward neural network to train solid propellant data on. During the study it was also shown that an optimised neural network structure could improve the performance of the model. The data used by Roodt was subsequently used for developing an optimised solution, which is complemented by the results in chapter 6. The same procedure for optimising the NN structure was used to determine the optimal structure to train the flares on.

The results from the subsequent testing of these models seemed to be positive, but in order to verify the graphical results, statistical testing of these models were done. In both cases the model outperformed the average solution to the problem. The statistical tests verify that the neural network is a valid model and the solutions yielded are unique.

8.2. Results

8.2.1. Input data

The neural network needed an input vector that would activate as many nodes as possible. If too large a zero vector exists within the network it would be difficult to generate a proper solution. The physical parameters that can be used to describe the infrared signature of the plume from the countermeasure flare are the propellant composition and combustion temperature, i.e.

Plume signature = f { T, fuel composition}

From the thermochemical calculations done it was possible to discern four thermodynamic properties that improved the performance of the neural network. The infrared spectra of the plume are then a function of the fuel composition and these thermodynamic properties.

Plume signature = f {fuel composition, oxidant-fuel ratio, equilibrium temperature, the molar mass and the maximum combustion temperature}

Combining the propellant composition and thermodynamic information about the combustion products, there now exists a sufficient description of the plume's infrared signature.

The same procedure was followed for the solid propellant rockets, except that the mass flow dynamics in the rocket motor also have an effect on the plume, i.e.

Plume signature = f {fuel composition, chamber temperature, chamber pressure, nozzle expansion ratio, nozzle throat diameter}

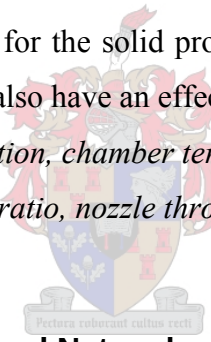

8.2.2. Optimisation of Neural Network architecture

The optimisation of the NN used for training of the data, was an iterative process. As a start the simplest possible NN is used for training. By adding hidden nodes the performance of the net improved. The number of hidden nodes determines the number of relationships between the input and output nodes of the net. If too many relationships are present the model could be training "noise" or unimportant information, which do not add to the solution. There is no real way of evaluating this, but in adding hidden nodes a plateau was reached in the solution space, which suggested that further adding of hidden nodes or relationships will not improve the solution.

The proposed NN for the training of the rocket signatures showed a structure with 16 hidden nodes. This dramatically reduces the number of variables or weights in the

model. The model suggested by Roodt [1], had 23944 variables, but with the reduced number of hidden nodes the number of variables dropped to 2624, which improved the training time of the NN. In reducing the number of variables (nodes) in the system the number of unused nodes becomes less. Such a network is more efficient and the smaller the zero vector in the network the higher the probability of getting a reasonable solution. When comparing the new NN against the old NN the results confirm the assumptions made in selecting an optimised NN.

The results from the t-test are shown in table 8-1. t-tests were done for the two test sets at a confidence level of $\alpha = 0.05$ [2] as was shown in chapter 6.3.1. The t-test states that the null hypothesis is rejected when $t < -t_\alpha$ and then the alternative hypothesis is accepted, which states that the error of the NN model will be smaller than that of the static model. The static model is the average of the data space used in the model.

$t_\alpha = 1.645$

Table 8-1 t-test statistic for test sets

	New Results		***Roodt's Results***	
	DB2	***C10***	***DB2***	***C10***
T	-10.0330	-8.3354	-9.225	-8.986

Table 8-2 Wilcoxon ranksum test statistic for test sets

	New Results		***Roodt's Results***	
	DB2	***C10***	***DB2***	***C10***
Z	-9.6766	-13.0379	-10.007	-9.657
p	0	0	0	0

The results from the Wilcoxon ranksum test are shown in table 8-2. The null hypothesis to be tested proposes that the two sample populations (NN and static model), come from the same populations. Again the null hypothesis is rejected if $z < -z_\alpha = -1.645$ and the alternative hypothesis is accepted, stating that the two populations are not even remotely the same. The large value of the *z* statistic indicates that the residuals of the static model

are much larger than that of the NN model. The statistic *p*, is the probability of observing a result equally or more extreme than the one using the data (NN and static) if the null hypothesis is true. If *p* is near zero, it casts doubt on this hypothesis.

The same approach was utilised to find the optimal solution for the training of the flares, with the same result.

8.2.3. Spectral Emission Prediction Results

The results for predicting the spectral emissions of rocket motors and the flares have been shown in chapters 6&7. During the training of the neural networks, the mean squared error was used as measure for the performance of the net. Once the final model for the NN was obtained several geometrical and statistical tests were done, by comparing the model against an average solution for the variable space. These include the plotting of the Euclidean distance and fractional energy. Analysing these graphs it was clear that the NN model closely predicts the measured infrared spectra. Only in the case where a measured value was on the edge of the variable space and the density of data was low did the model not predict the measured values accurately. The Euclidean distance plot for the flares is shown in fig 8-1. Flare SF915 shows a relatively big Euclidean distance compared to the other predicted values. In fig 8-2, the variable space for the flares is shown, with SF 915 being the topmost curve. It seems that during the measurement of the emission spectra the spectra radiometer may have saturated, but nevertheless the measured value lies on the edge of the variable space in a less dense region. This shows that the NN can only predict values where enough training data was available to correctly fill the variables in the model.

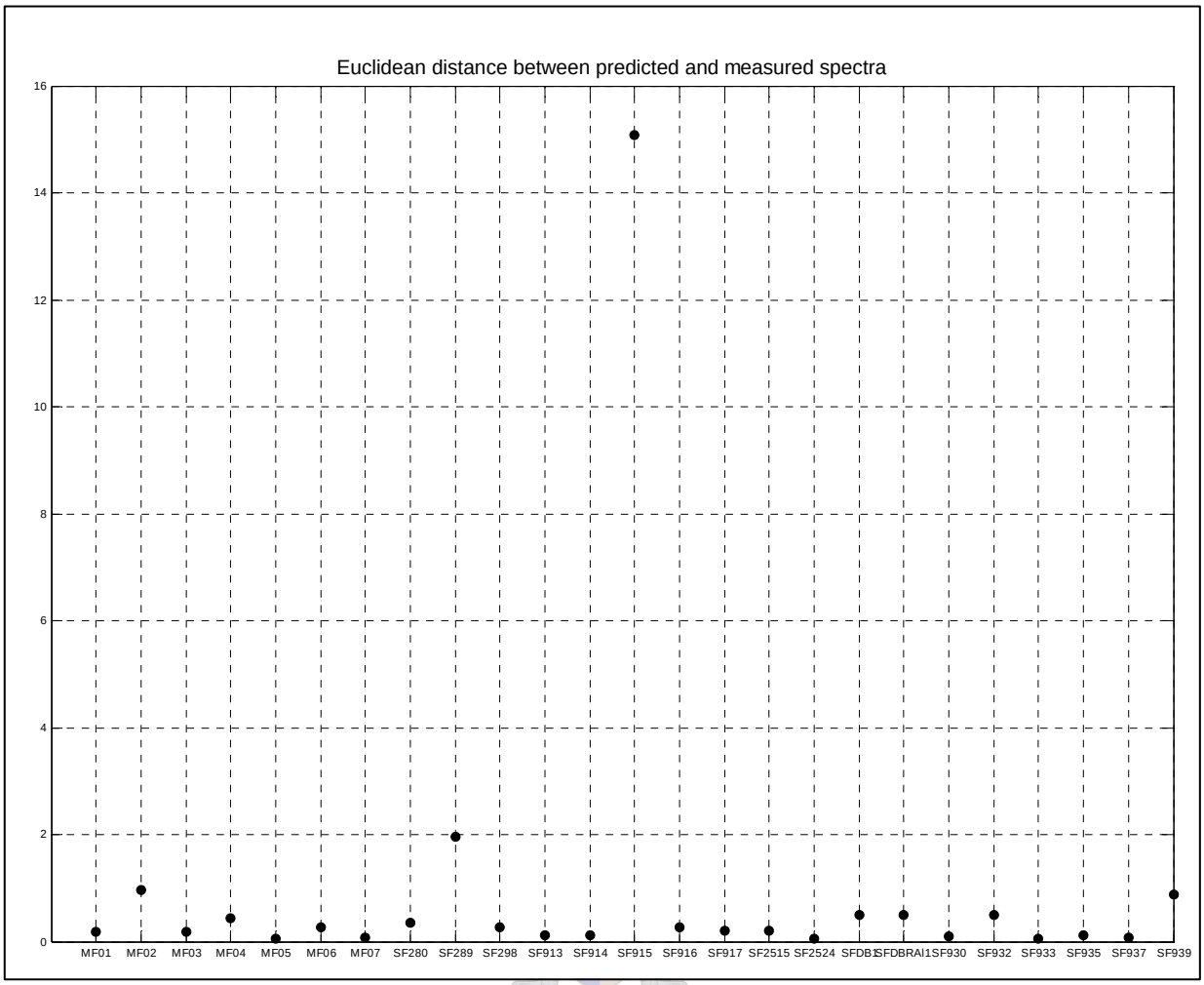

Figure 8.2-1 Comparing the predicted and measured IR spectra in terms of Euclidean distance

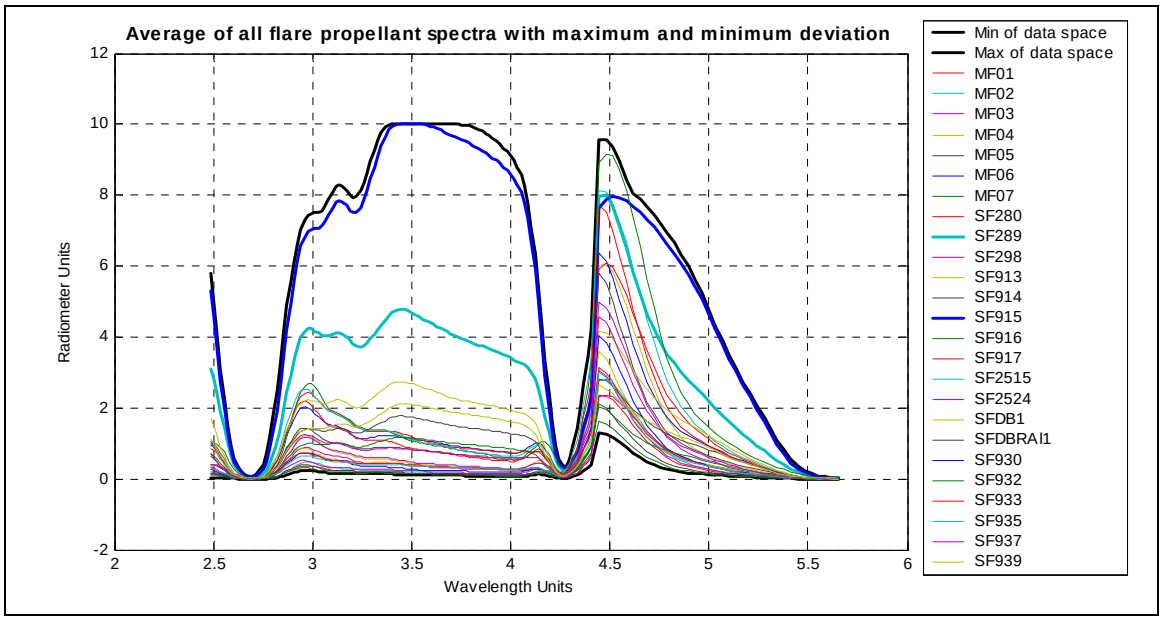

Figure 8.2-2 Average spectra signatures of all the flares, i.e. variation space

Further statistical testing was done, by comparing the performance of the static model or the average solution to that of the NN model, in predicting the measured values. These tests included a t-test and a Wilcoxon ranksum test, of which the results of the flares are shown in tables 8-3 and 8-4. In both cases the NN model outperformed the static model (a negative number shows a unique solution), which proves that the NN model is a unique solution for this variable space.

Table 8-3 T-test statistic for test sets

	MF06	***SF933***
T	-2.71	-19.01

Table 8-4 Wilcoxon ranksum test statistic for test sets

	MF06	***C10***
Z	-11.9886	-13.283
P	0	0

8.3. Future Work

8.3.1. New data

In all the cases where a solid propellant or flare did not show good predicted values, the input or output vector lies in a sparsely populated area of the data space. The only way of solving this is by doing more testing. It has to be taken into account that such testing is an expensive exercise, but using the current data and model it would be easy to pinpoint the tests that need to be run in order the fill the variable space.

The study should also be extended to new kinds of flare materials, such as pyrophorics or more complex mixtures. The development of flares is an expensive operation and this tool could help in not only reducing cost, but also getting to the answer faster.

8.3.2. Investigation of model

The feedforward neural network used here is a non-linear solution. The chemical and thermodynamic equations that represent the combustion reactions are also non-linear. The interesting thing is that the neural network model approached a linear solution. This became apparent when the network was switched around and the input vector could be predicted using the output vector as input. The neural net was reversible, which suggests that the model is less complex than first anticipated.

The network should be analysed to see how it responds to "new data". The "new data" should be such that it would be necessary for the model to extrapolate or interpolate in order to find a solution. This will illustrate whether the model is dynamic or not.

Grouping some of the chemical element inputs could further reduce the size of the input vector of the model. The grouping could happen in different ways: The elements could be grouped according to their function in the reactants, or according to their position in the periodic table. This grouping will essentially represent the functionality of compounds in the fuels, which could improve the neural net's performance.

8.3.3. New techniques

It is also necessary to search for new or improved techniques of predicting emission spectra for combustion reactions. The neuro-computing field is growing rapidly and there is no knowing of what tools may be available for use.

It has come to the attention of the author that certain new techniques could be used on small data sets to optimise some modern training algorithms and it should be investigated.

8.4. Reference:

1. Roodt, J., *The Prediction of the emission spectra of solid rocket propellants*, Ph.D. dissertation, Dept. Chemical Engineering, University of Stellenbosch, Chapter 7, (1998).

2. Mendenhall, W., Scheaffer, R.L., Wackerly, D.D., *Mathematical Statistics with Applications,* 3rd edition, PWS Publishers, United States of America, Chapter 10, (1986).

Appendix A Components of solid propellant

Components of solid rocket propellant		
Shortcut	**Name**	**Function**
NC25	Nitrocellulose	Energetic binder
AP	Ammonium Perchlorate	Oxidizer
SiC	Silicon Carbide	Particles
TiO_2	Titanium Oxide	Particles
DOP	Di-octyl-phthalate	Energetic plasticizer
Fe_2O_3	Iron Oxide	Burning rate modifier
KAFI	Potassium Floride	Flame supressant
Al	Aluminum	Fuel
DOA	Di-octyle-adipate	Binder / Plasticizer
IPDI	Isophoron	Curing Catalyst
CuO	Copper Oxide	Balastic modifier
KNO_3	KNO_3	Flame supressant / Oxidizer
RDX	Cyclotrimethylene trinitramine	Energetic Fuel / Oxidizer
Compound 7	Compound 7	Balastic modifier
EC	Ethyl Centralite	Stabilizer
HTPB	Hydroxy-terminated polybutadiene	Energetic binder
Pb-Steorate	Lead Sterate	Balastic modifier / Extrusion agent
K_2SO_4	Potassium Sulphate	Flame supressant
C-Black	Carbon Black	Pigment / Opacifier / Burning rate enhancer
DEP	Diethyl Phthalate	Inert plasticizer
Cu-SAL-CU	Copper Saleselate	Balistic modifier
TA	Triacetin	Inert plasticizer
NGU	Nitroguanidine	Energetic Fuel / Oxidizer
NG	Nitroglycerin	Energetic plasticizer

Solid propellant components used in Flares		
Shortcut	***Name***	***Function***
HTPB	Hydroxy-terminated polybutadiene	Energetic binder
IPDI	Isophoron	Curng Catalyst
DOA	Di-octyle-adipate	Binder / Plasticizer
DTBHQ	2,5-Di-tert-butylhydroquinone	
Tepa	Tetraethylenepentamine	Bonding agent
Tepan	Cyanoethylated tetraethylenepantamine	Bonding agent
Tepanol	Dihydroxypropyl cyanoethyl tetraethylenepentamine	Bonding agent
HX752	Di-[isophthaloyl-1-(2methyl)-aziridine	Bonding agent
AP	Ammonium Perchlorate	Oxidizer
AN	Ammonium Nitrate	Oxidizer
Al	Aluminum	Fuel
Mg	Magnesium	Fuel
SiC	Silicon Carbide	Fuel
Fe_2O_3	Iron Oxide	Burning rate modifier / Oxidizer
$SrCO_3$	Zirconium Oxide	Burning rate modifier
Oksamide	Oxamide	
Hexamine	Hexamine	
Tetrasicline	Tetrasicline	
Fe(AA)		Balistic modifier
Aerosil	Silicon dioxide colloid with amorphous structure	Fuel / Oxidiser
TMP	Trimethylolpropane	Bonding agent
AO 2246	Plastonox 2246	
MgO	Magnesium oxide	
C-Black	Carbon Black	Pigment / Opacifier / Burning rate enhancer
MA	Maleic Anhydride	

TPB	Triphenylbismuth	
NG/TA (80:20)	Nitroglycerin / Triacetin	Energetic plasticizer
RDX	Cyclotrimethylene trinitramine	Energetic Fuel / Oxidizer
MP200	Ball powder	
Prussian Blue	Ferrocyanide	
Lecithin	Lecithin phosphtidylcholine	
Polylite	Polyester	Binder / Inhibitor
TNT	Trinitro-toluene	Energetic plasticizer
NTO	3-nitro-1,2,4-triazole	
Cianuric acid	Cyanuric acid anhydrous	

Appendix B Radiation Spectra of Solid Rocket Propellants

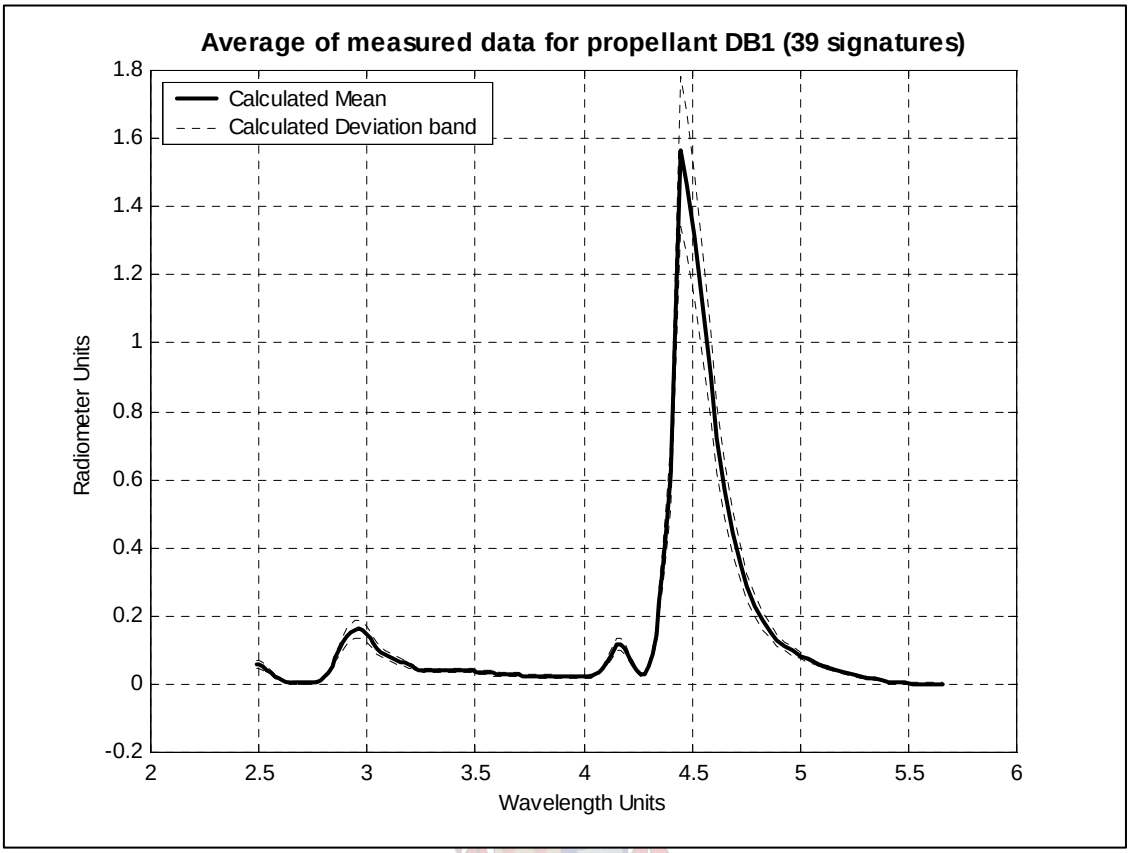
Average of measured data for propellant DB1 (39 signatures)
Calculated Mean
Calculated Deviation band
Radiometer Units
Wavelength Units
1.8
1.6
1.4
1.2
1
0.8
0.6
0.4
0.2
0
-0.2
2
2.5
3
3.5
4
4.5
5
5.5
6

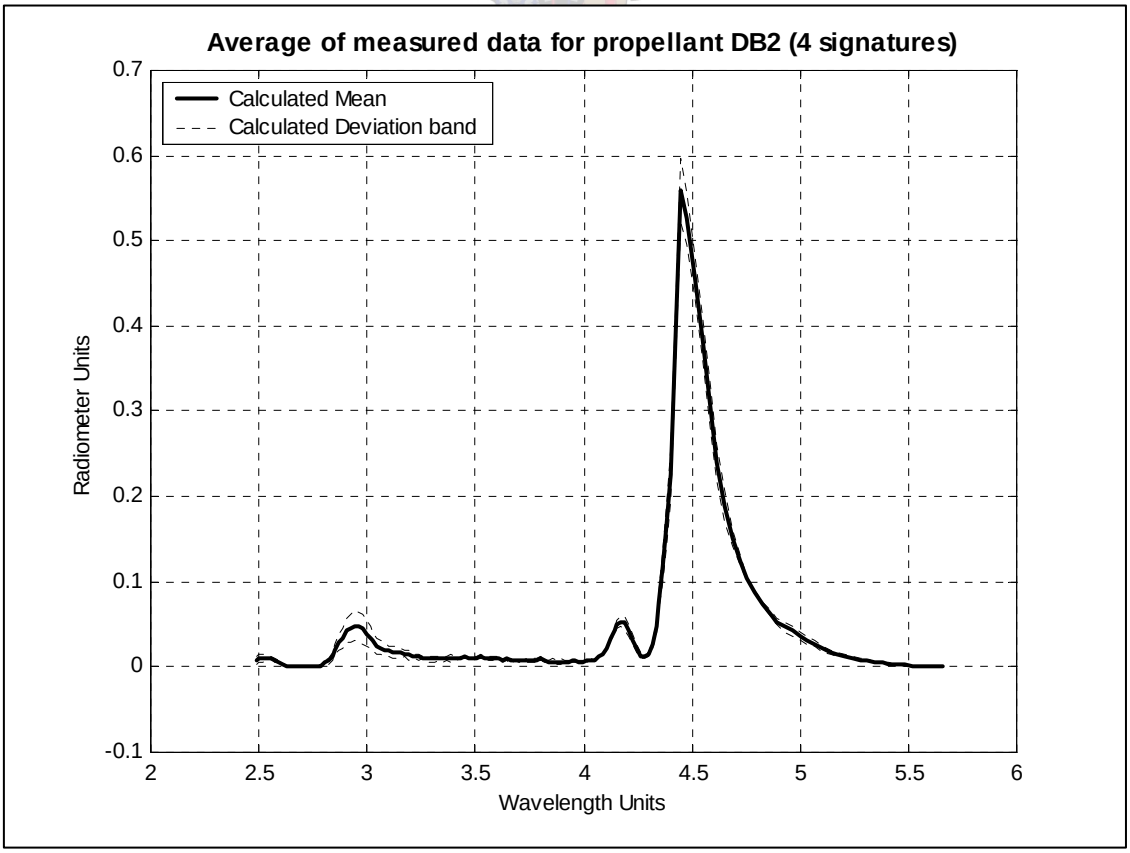
Average of measured data for propellant DB2 (4 signatures)
Calculated Mean
Calculated Deviation band
Radiometer Units
Wavelength Units
0.7
0.6
0.5
0.4
0.3
0.2
0.1
0
-0.1
2
2.5
3
3.5
4
4.5
5
5.5
6

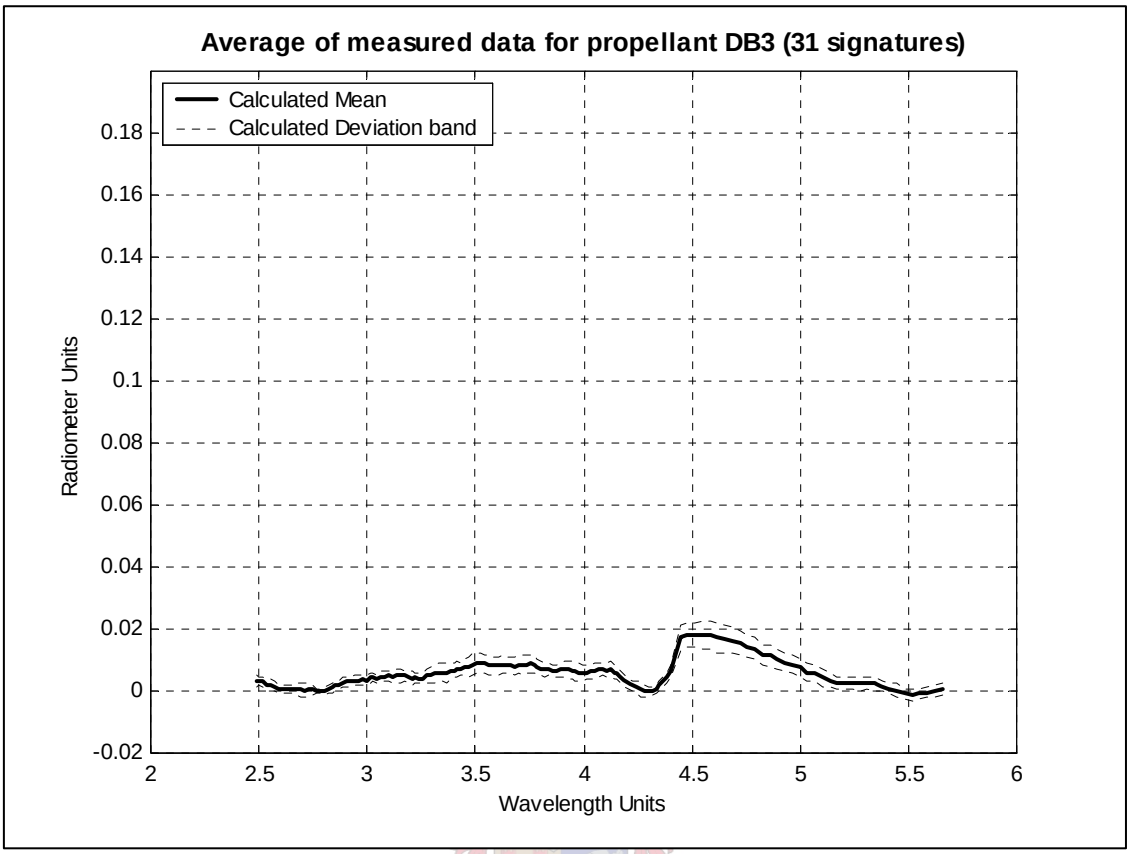
Average of measured data for propellant DB3 (31 signatures)
Calculated Mean
Calculated Deviation band
Radiometer Units
Wavelength Units
0.18
0.16
0.14
0.12
0.1
0.08
0.06
0.04
0.02
0
-0.02
2
2.5
3
3.5
4
4.5
5
5.5
6

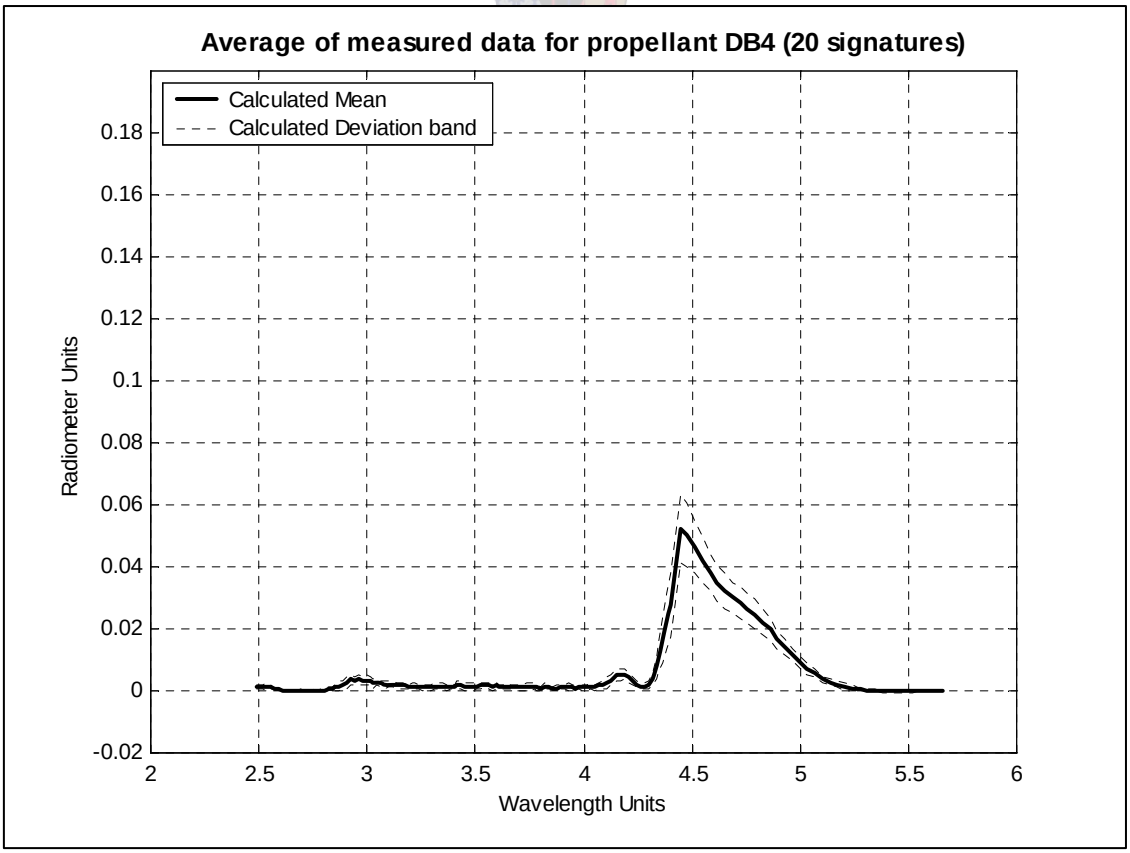
Average of measured data for propellant DB4 (20 signatures)
Calculated Mean
Calculated Deviation band
Radiometer Units
Wavelength Units
0.18
0.16
0.14
0.12
0.1
0.08
0.06
0.04
0.02
0
-0.02
2
2.5
3
3.5
4
4.5
5
5.5
6

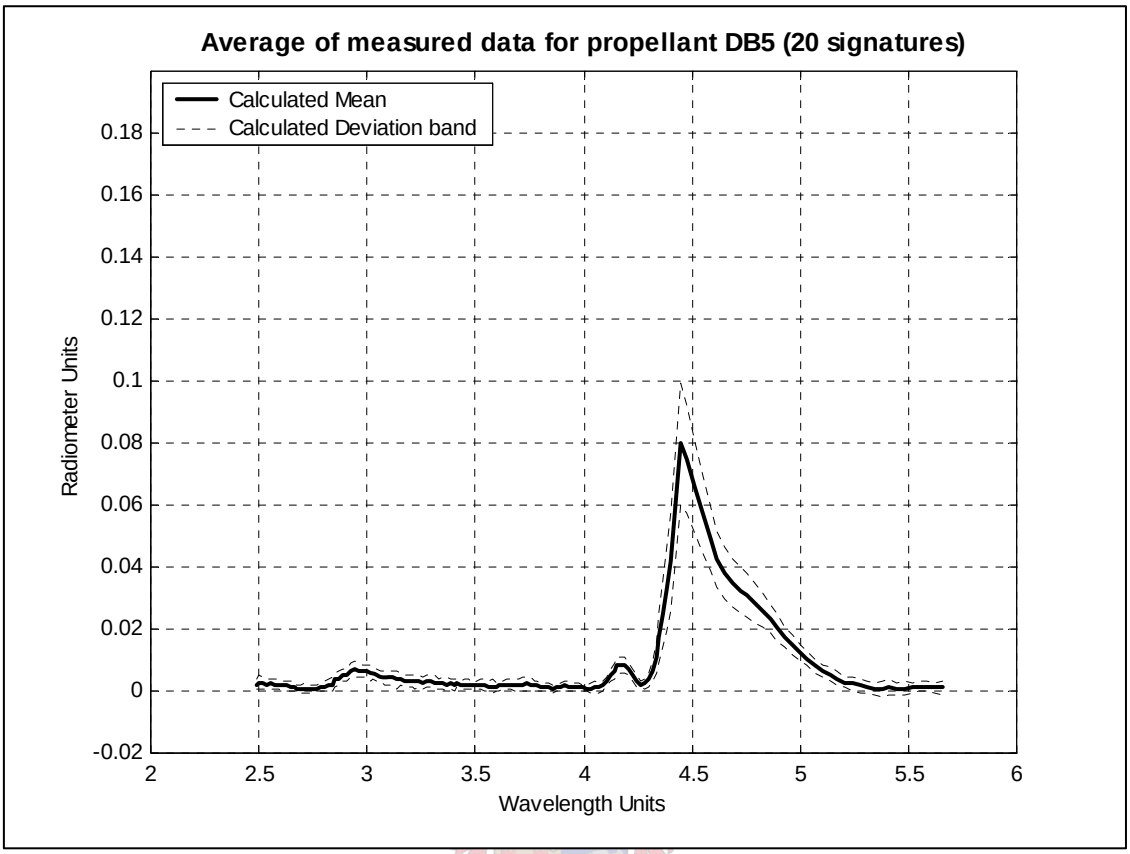
Average of measured data for propellant DB5 (20 signatures)
Calculated Mean
Calculated Deviation band
Radiometer Units
Wavelength Units
0.18
0.16
0.14
0.12
0.1
0.08
0.06
0.04
0.02
0
-0.02
2
2.5
3
3.5
4
4.5
5
5.5
6

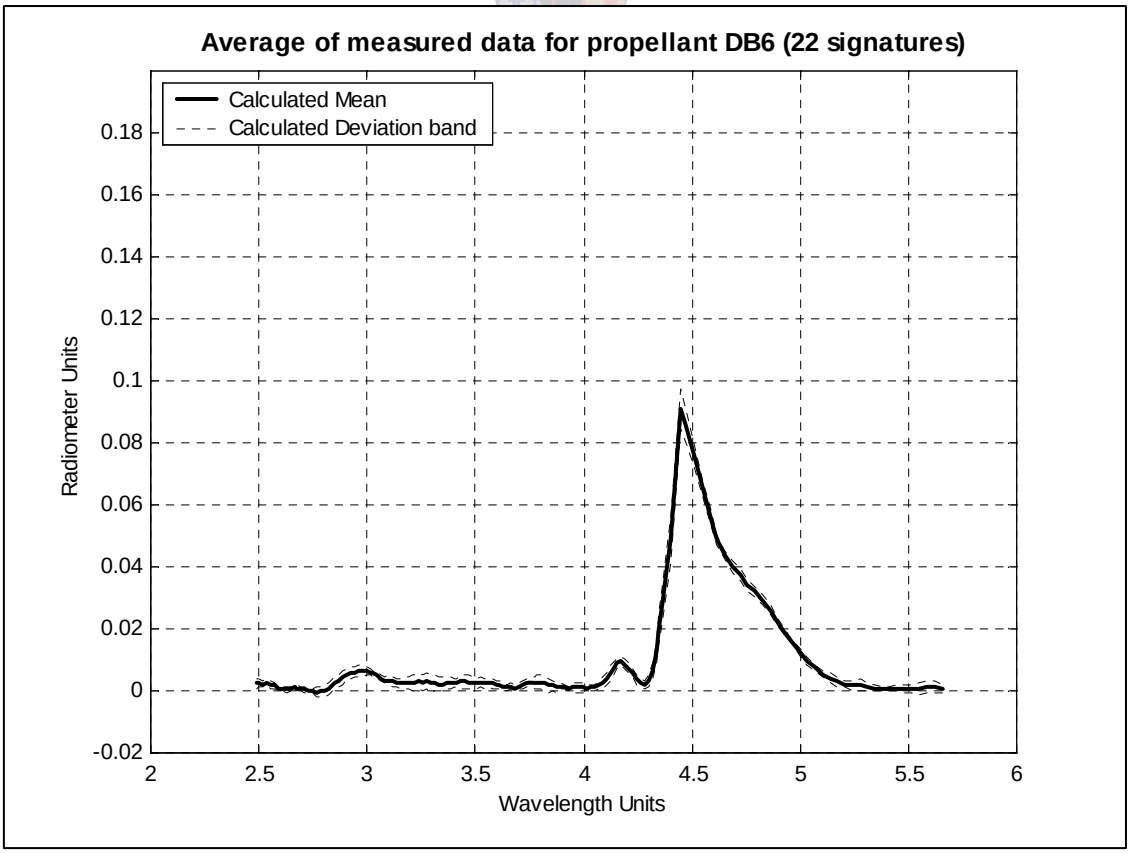
Average of measured data for propellant DB6 (22 signatures)
Calculated Mean
Calculated Deviation band
Radiometer Units
Wavelength Units
0.18
0.16
0.14
0.12
0.1
0.08
0.06
0.04
0.02
0
-0.02
2
2.5
3
3.5
4
4.5
5
5.5
6

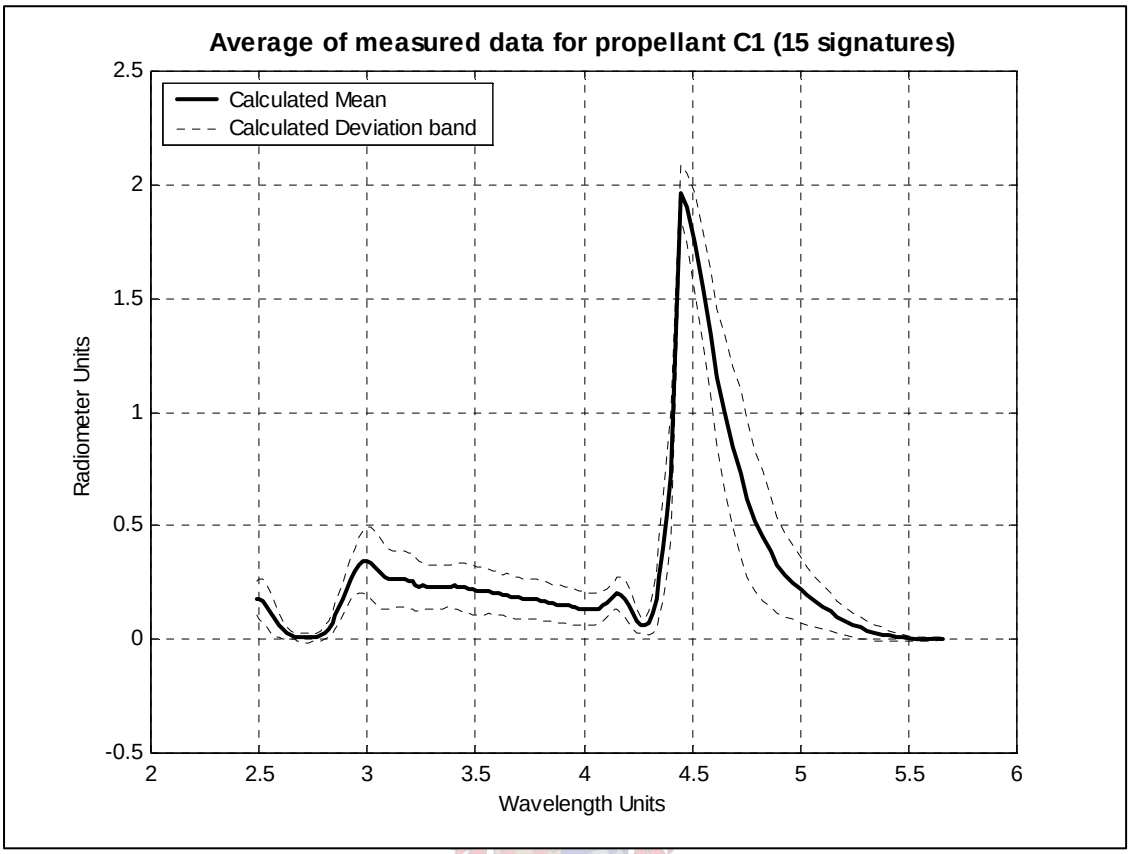
Average of measured data for propellant C1 (15 signatures)
Calculated Mean
Calculated Deviation band
Radiometer Units
Wavelength Units
2.5
2
1.5
1
0.5
0
-0.5
2
2.5
3
3.5
4
4.5
5
5.5
6

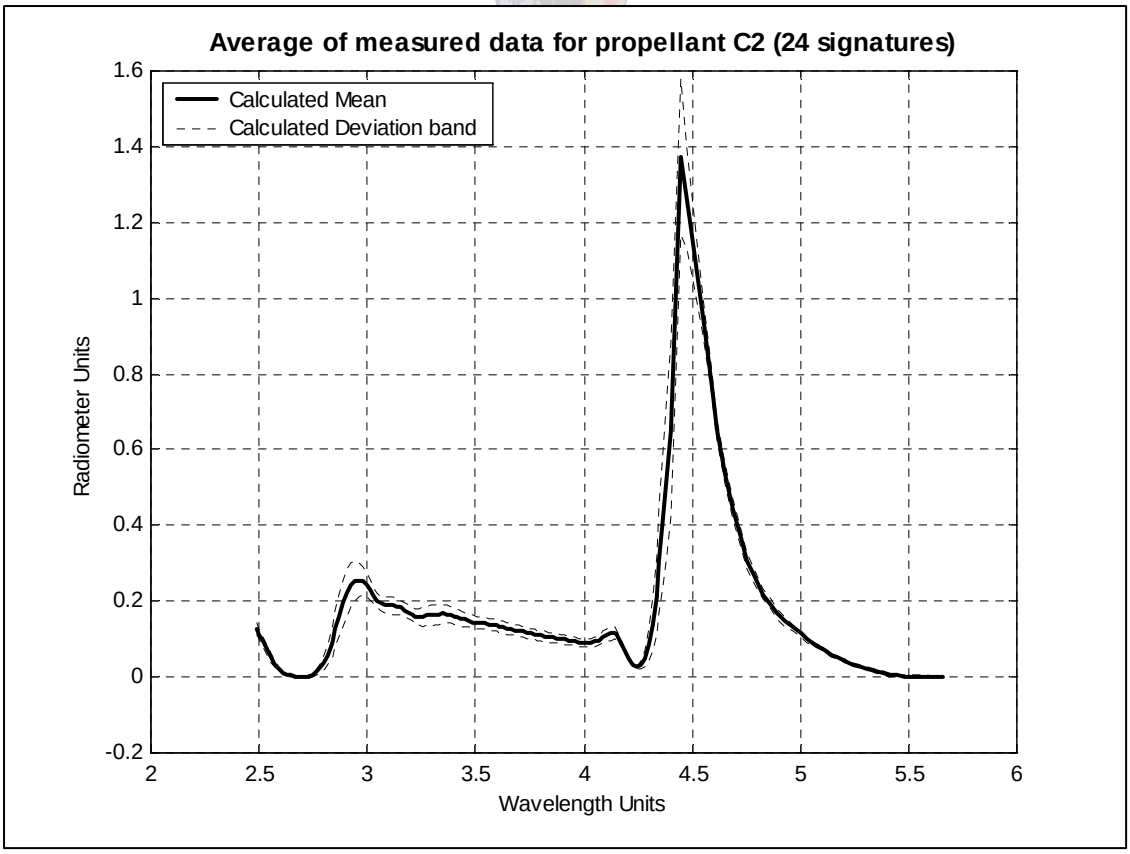
Average of measured data for propellant C2 (24 signatures)
Calculated Mean
Calculated Deviation band
Radiometer Units
Wavelength Units
1.6
1.4
1.2
1
0.8
0.6
0.4
0.2
0
-0.2
2
2.5
3
3.5
4
4.5
5
5.5
6

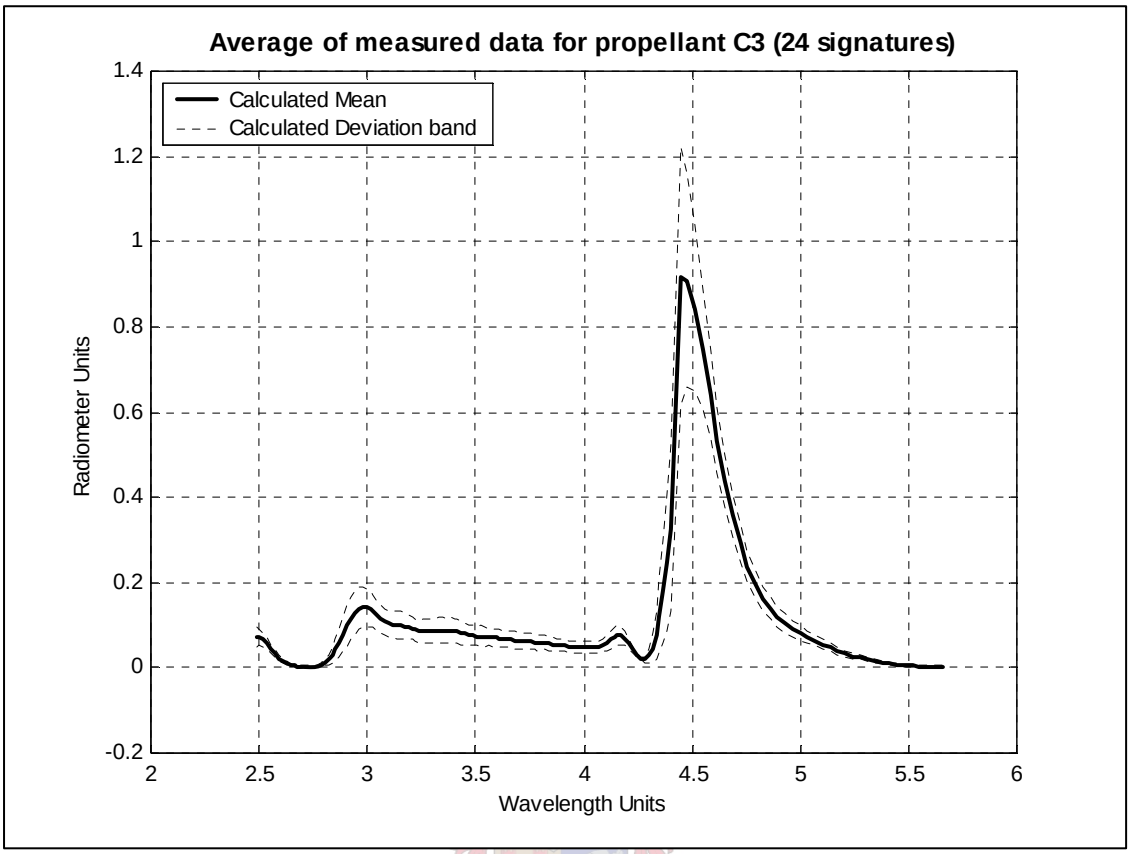
Average of measured data for propellant C3 (24 signatures)
Calculated Mean
Calculated Deviation band
Radiometer Units
Wavelength Units
1.4
1.2
1
0.8
0.6
0.4
0.2
0
-0.2
2
2.5
3
3.5
4
4.5
5
5.5
6

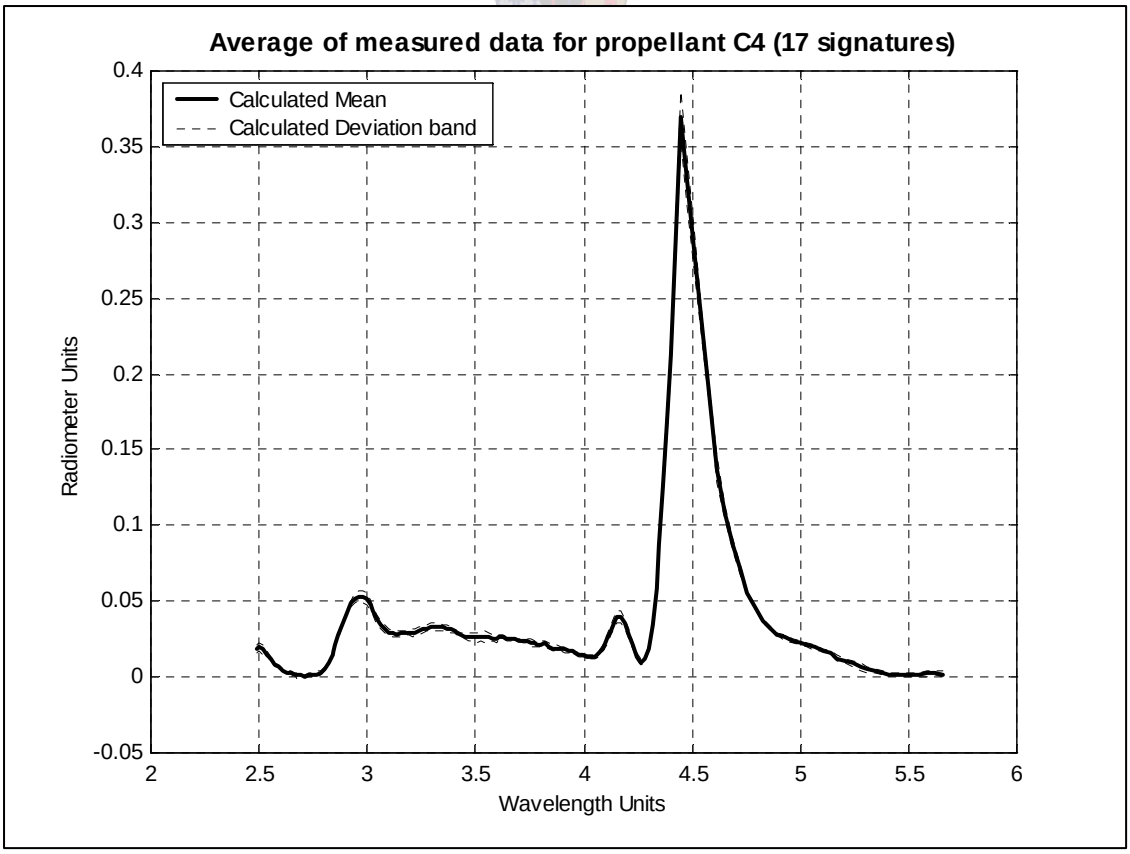
Average of measured data for propellant C4 (17 signatures)
Calculated Mean
Calculated Deviation band
Radiometer Units
Wavelength Units
0.4
0.35
0.3
0.25
0.2
0.15
0.1
0.05
0
-0.05
2
2.5
3
3.5
4
4.5
5
5.5
6

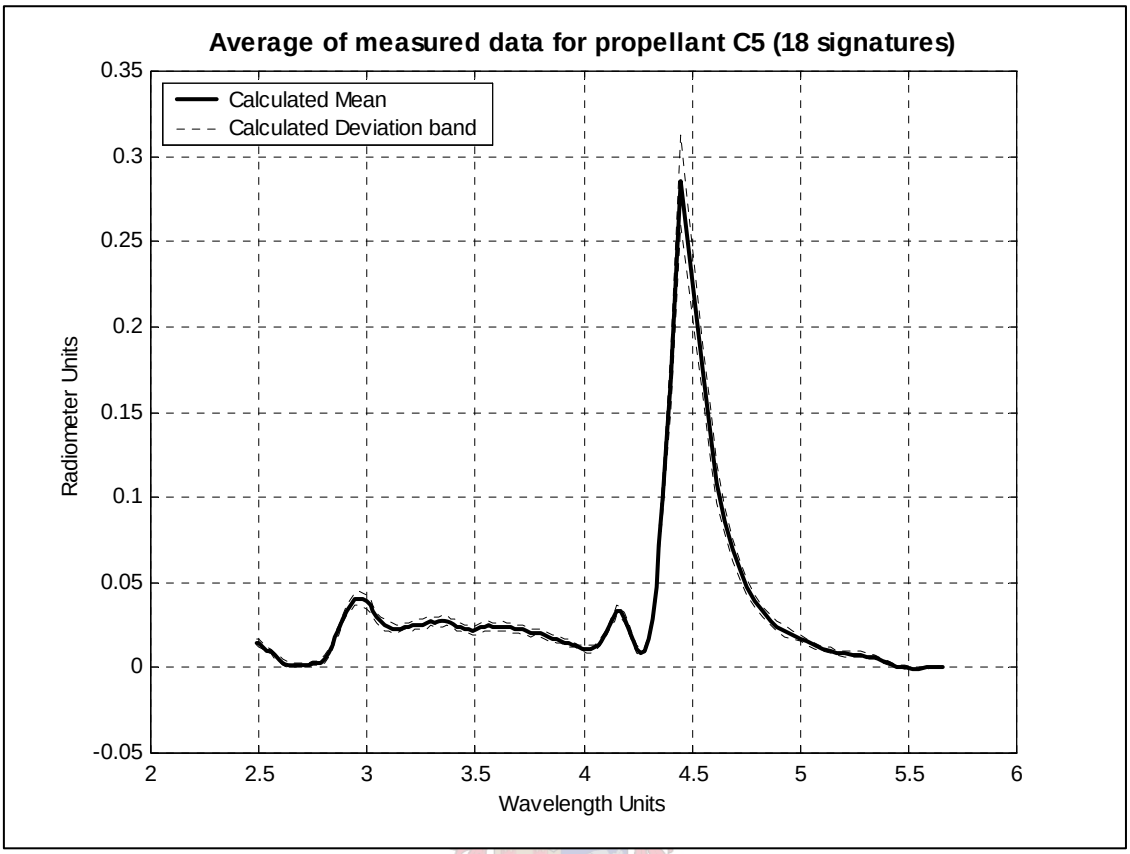
Average of measured data for propellant C5 (18 signatures)
Calculated Mean
Calculated Deviation band
Radiometer Units
Wavelength Units
0.35
0.3
0.25
0.2
0.15
0.1
0.05
0
-0.05
2
2.5
3
3.5
4
4.5
5
5.5
6

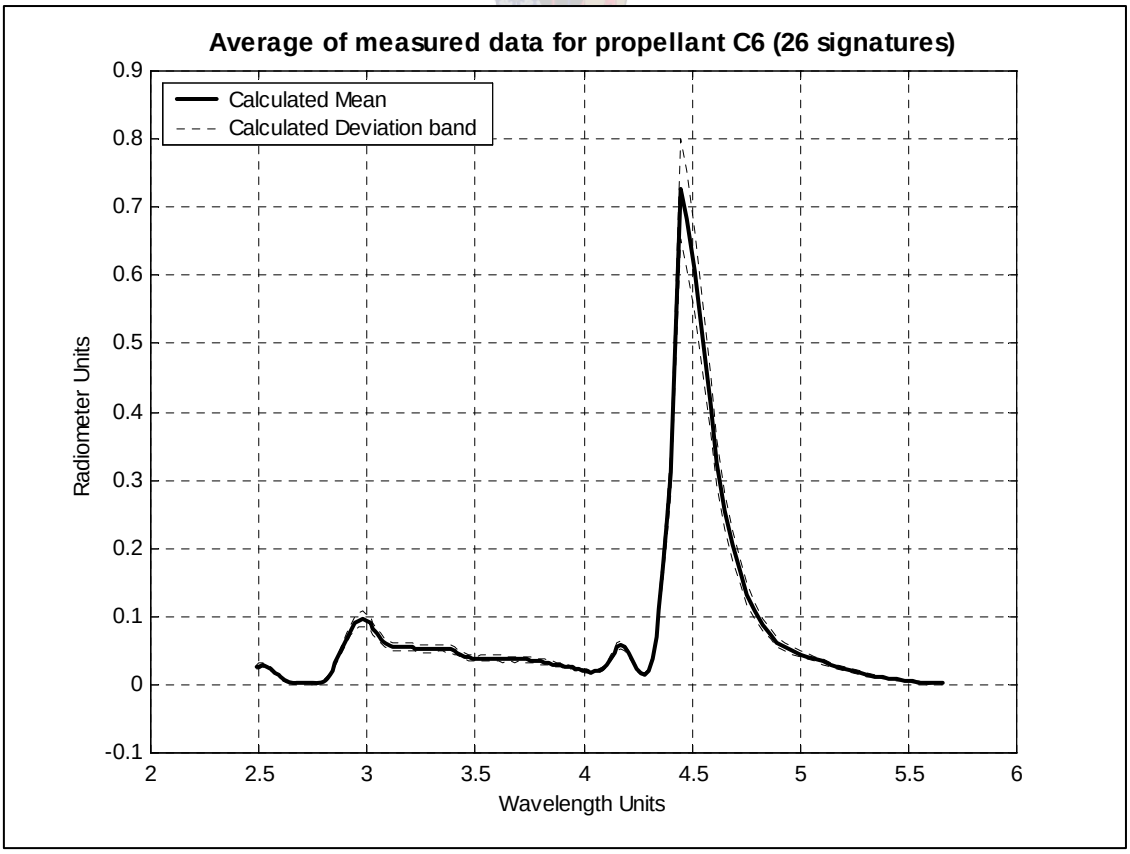
Average of measured data for propellant C6 (26 signatures)
Calculated Mean
Calculated Deviation band
Radiometer Units
Wavelength Units
0.9
0.8
0.7
0.6
0.5
0.4
0.3
0.2
0.1
0
-0.1
2
2.5
3
3.5
4
4.5
5
5.5
6

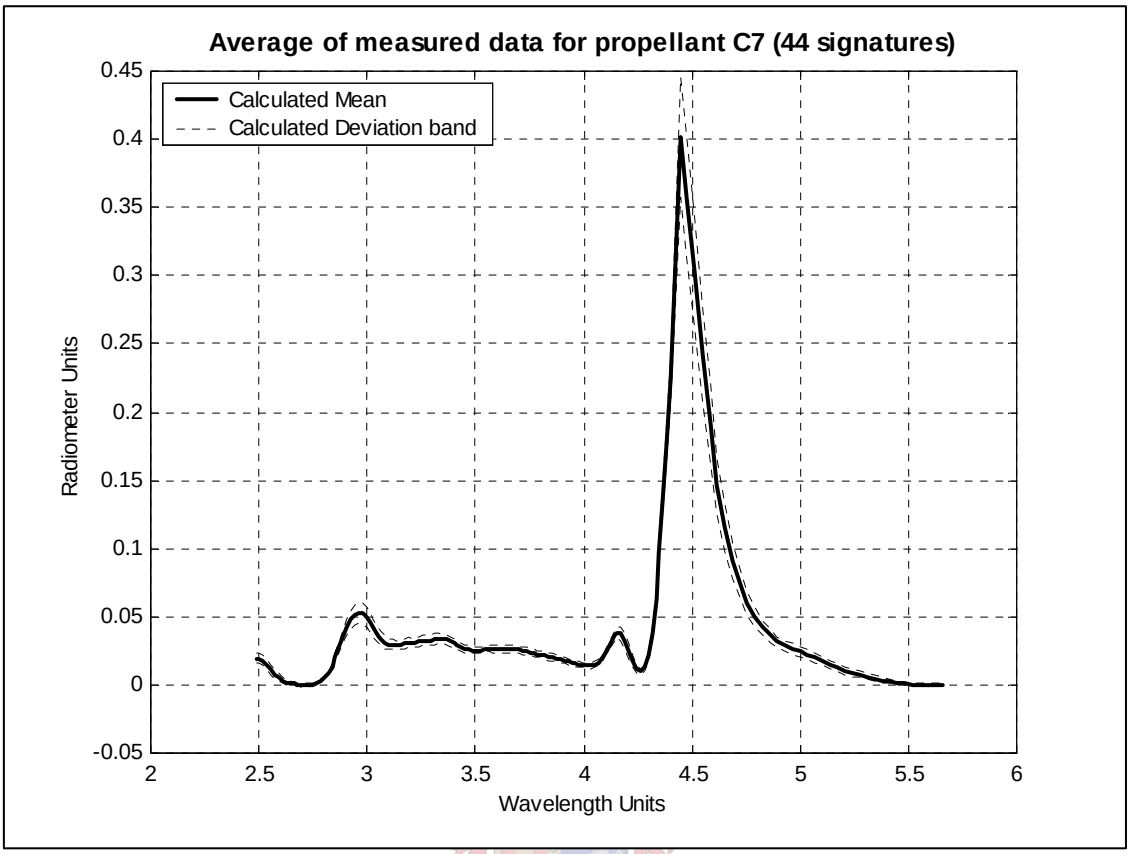
Average of measured data for propellant C7 (44 signatures)
Calculated Mean
Calculated Deviation band
Radiometer Units
Wavelength Units
0.45
0.4
0.35
0.3
0.25
0.2
0.15
0.1
0.05
0
-0.05
2
2.5
3
3.5
4
4.5
5
5.5
6

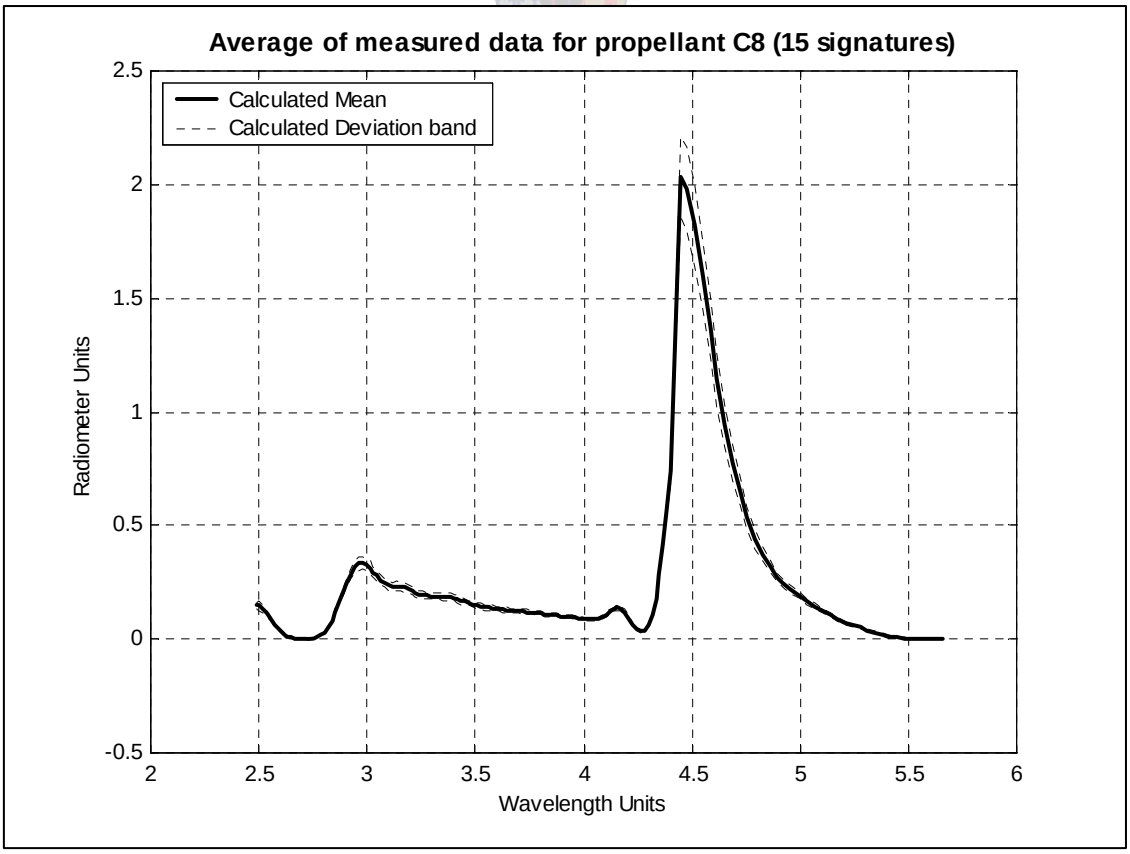
Average of measured data for propellant C8 (15 signatures)
Calculated Mean
Calculated Deviation band
Radiometer Units
Wavelength Units
2.5
2
1.5
1
0.5
0
-0.5
2
2.5
3
3.5
4
4.5
5
5.5
6

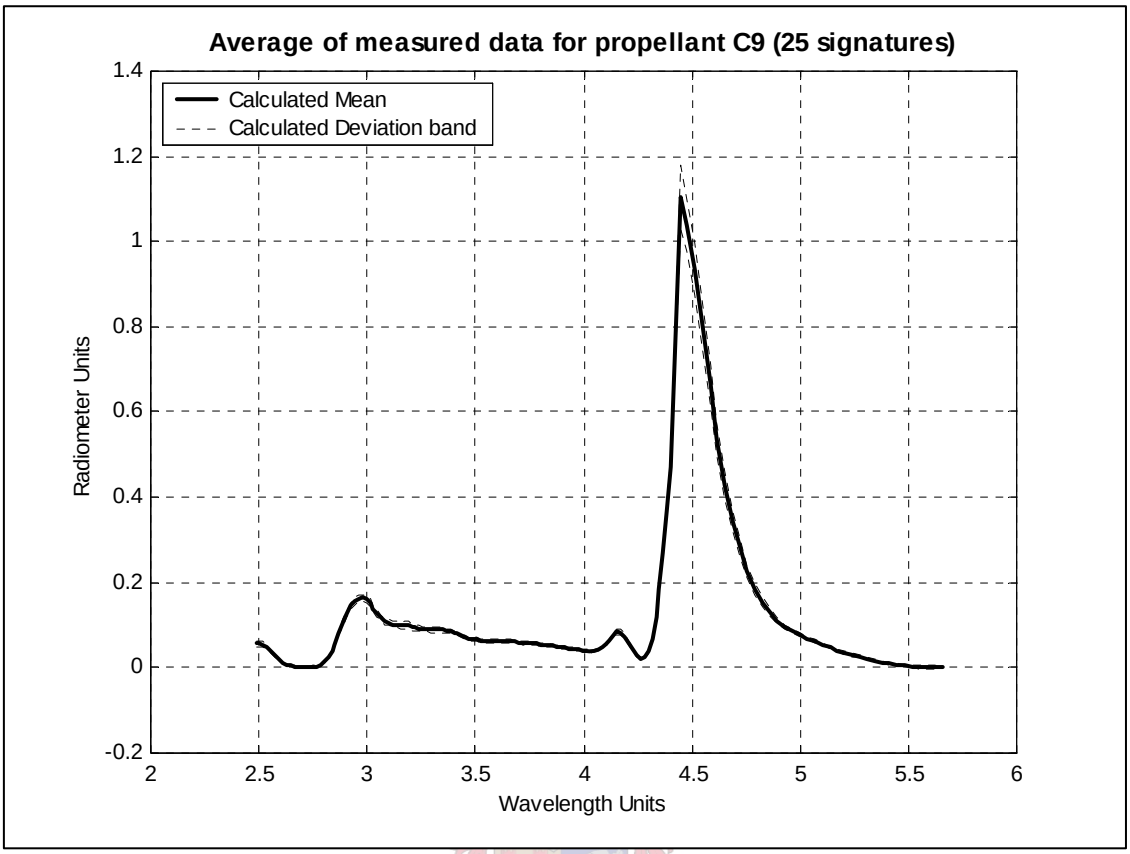
Average of measured data for propellant C9 (25 signatures)
Calculated Mean
Calculated Deviation band
Radiometer Units
Wavelength Units
1.4
1.2
1
0.8
0.6
0.4
0.2
0
-0.2
2
2.5
3
3.5
4
4.5
5
5.5
6

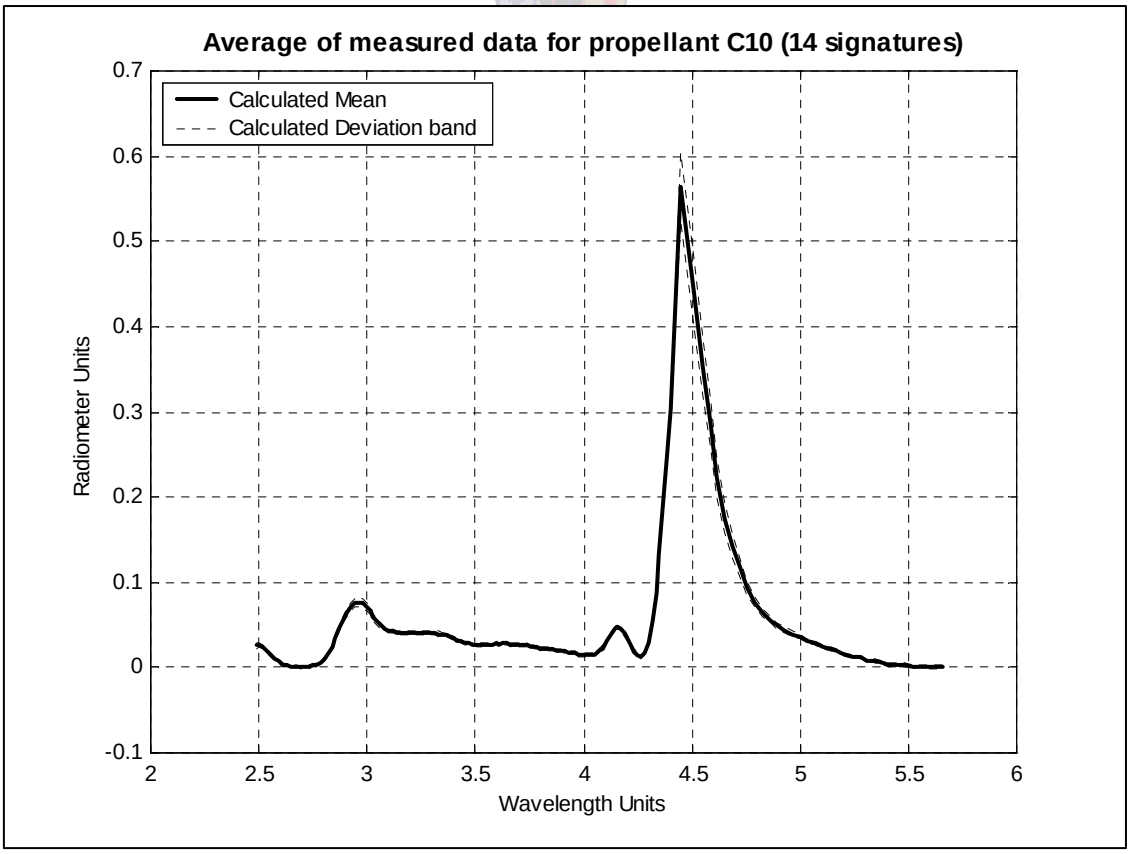
Average of measured data for propellant C10 (14 signatures)
Calculated Mean
Calculated Deviation band
Radiometer Units
Wavelength Units
0.7
0.6
0.5
0.4
0.3
0.2
0.1
0
-0.1
2
2.5
3
3.5
4
4.5
5
5.5
6

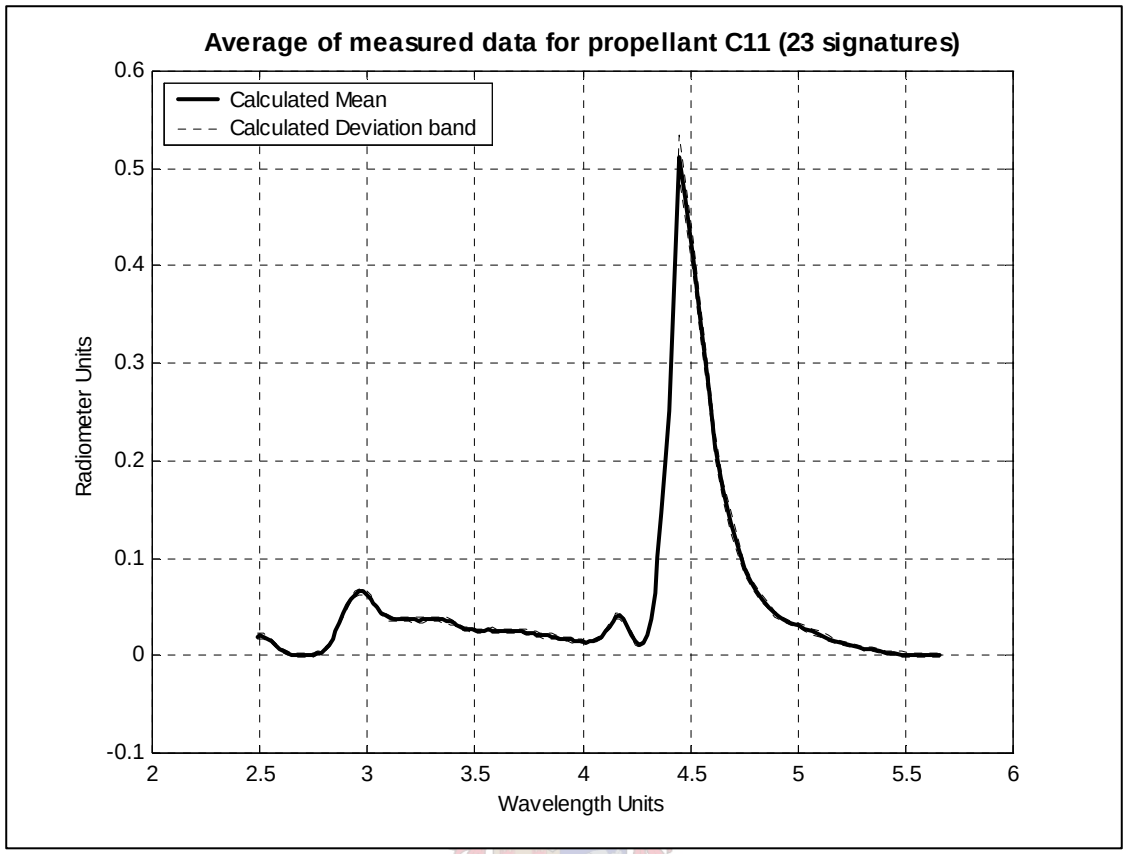
Average of measured data for propellant C11 (23 signatures)
Calculated Mean
Calculated Deviation band
Radiometer Units
Wavelength Units
0.6
0.5
0.4
0.3
0.2
0.1
0
-0.1
2
2.5
3
3.5
4
4.5
5
5.5
6

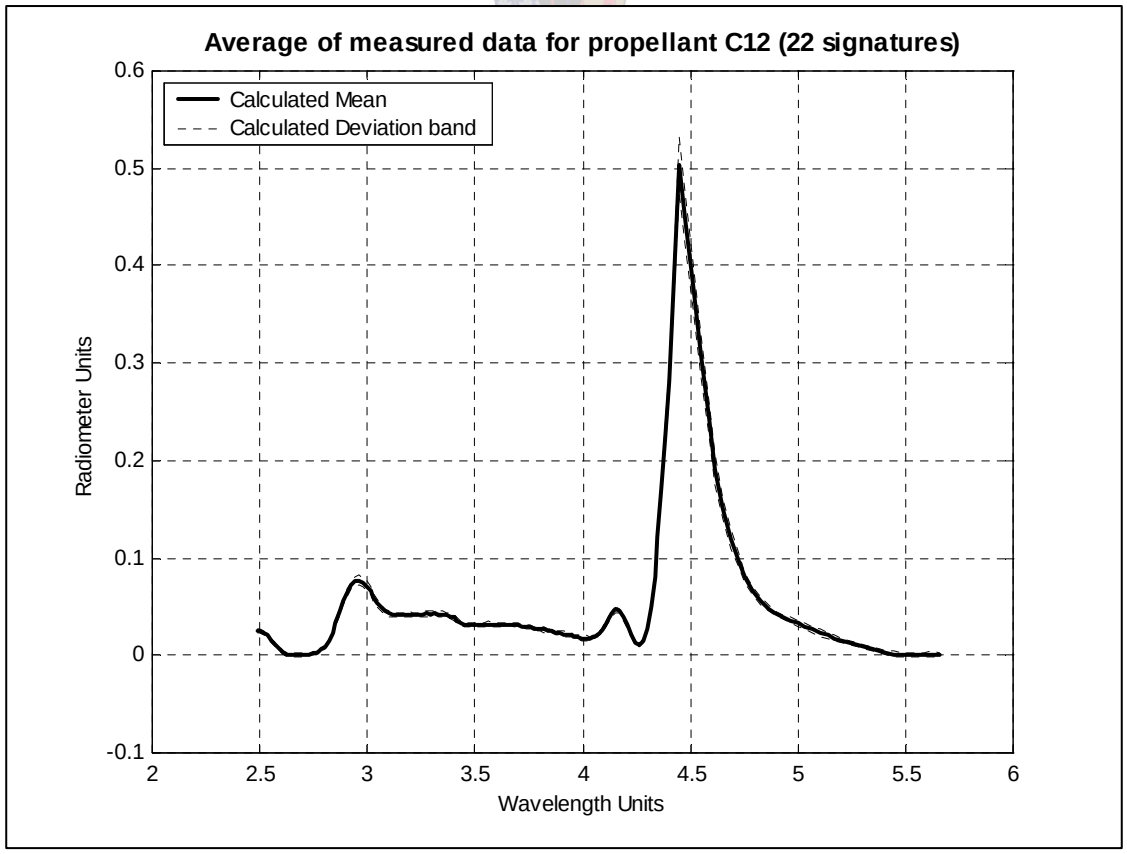
Average of measured data for propellant C12 (22 signatures)
Calculated Mean
Calculated Deviation band
Radiometer Units
Wavelength Units
0.6
0.5
0.4
0.3
0.2
0.1
0
-0.1
2
2.5
3
3.5
4
4.5
5
5.5
6

Appendix C Radiation Spectra of Flares

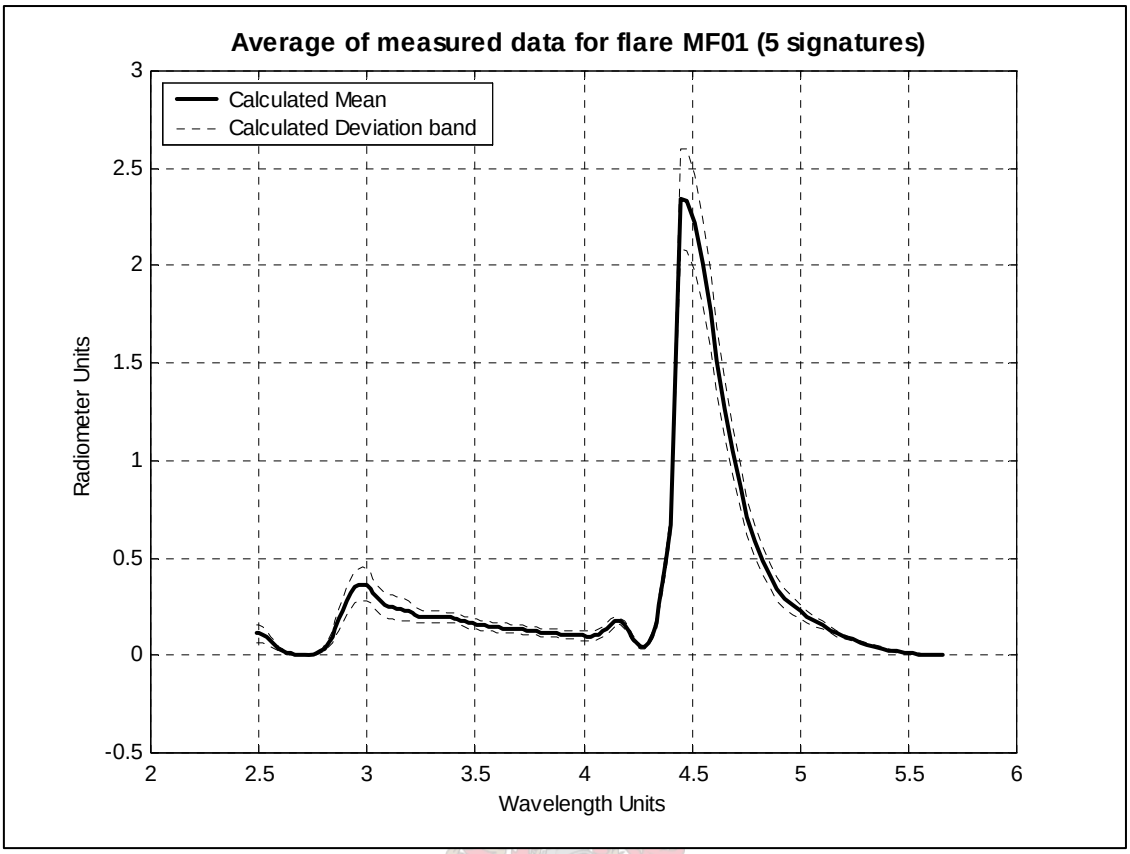
Average of measured data for flare MF01 (5 signatures)
Calculated Mean
Calculated Deviation band
Radiometer Units
Wavelength Units
3
2.5
2
1.5
1
0.5
0
-0.5
2
2.5
3
3.5
4
4.5
5
5.5
6

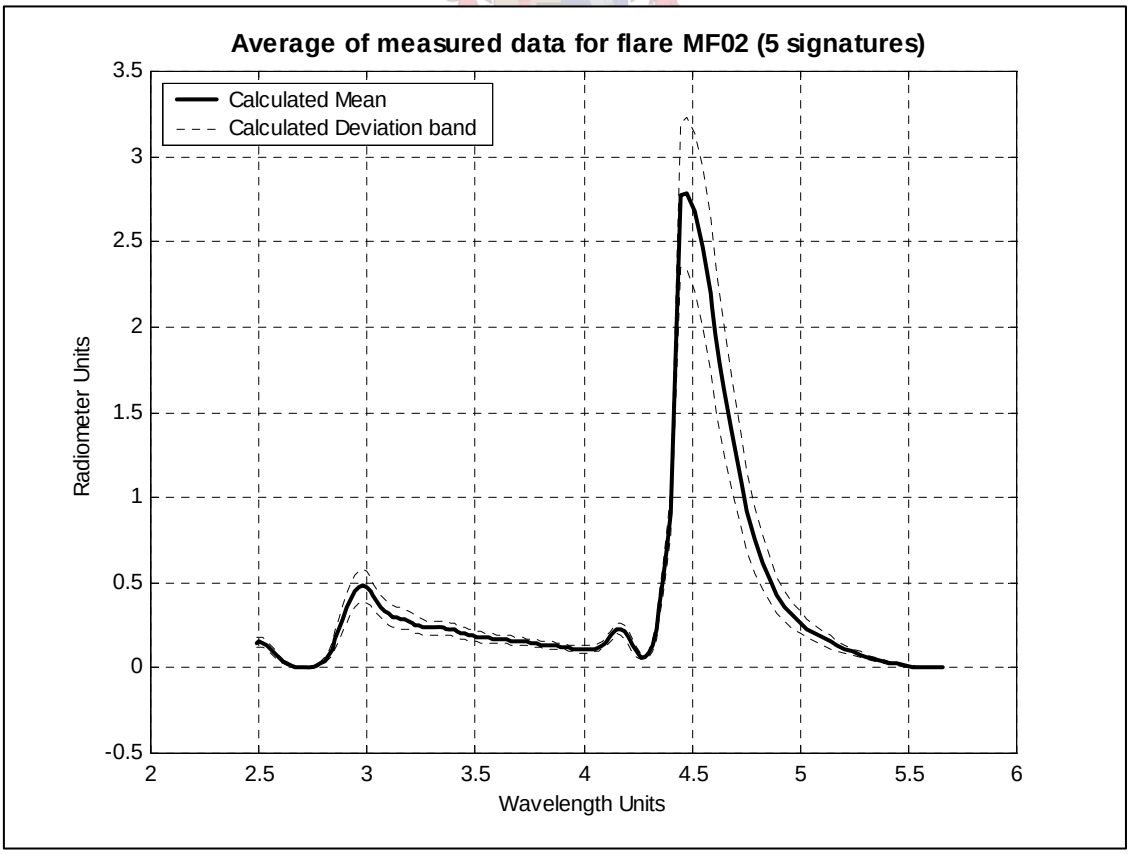
Average of measured data for flare MF02 (5 signatures)
Calculated Mean
Calculated Deviation band
Radiometer Units
Wavelength Units
3.5
3
2.5
2
1.5
1
0.5
0
-0.5
2
2.5
3
3.5
4
4.5
5
5.5
6

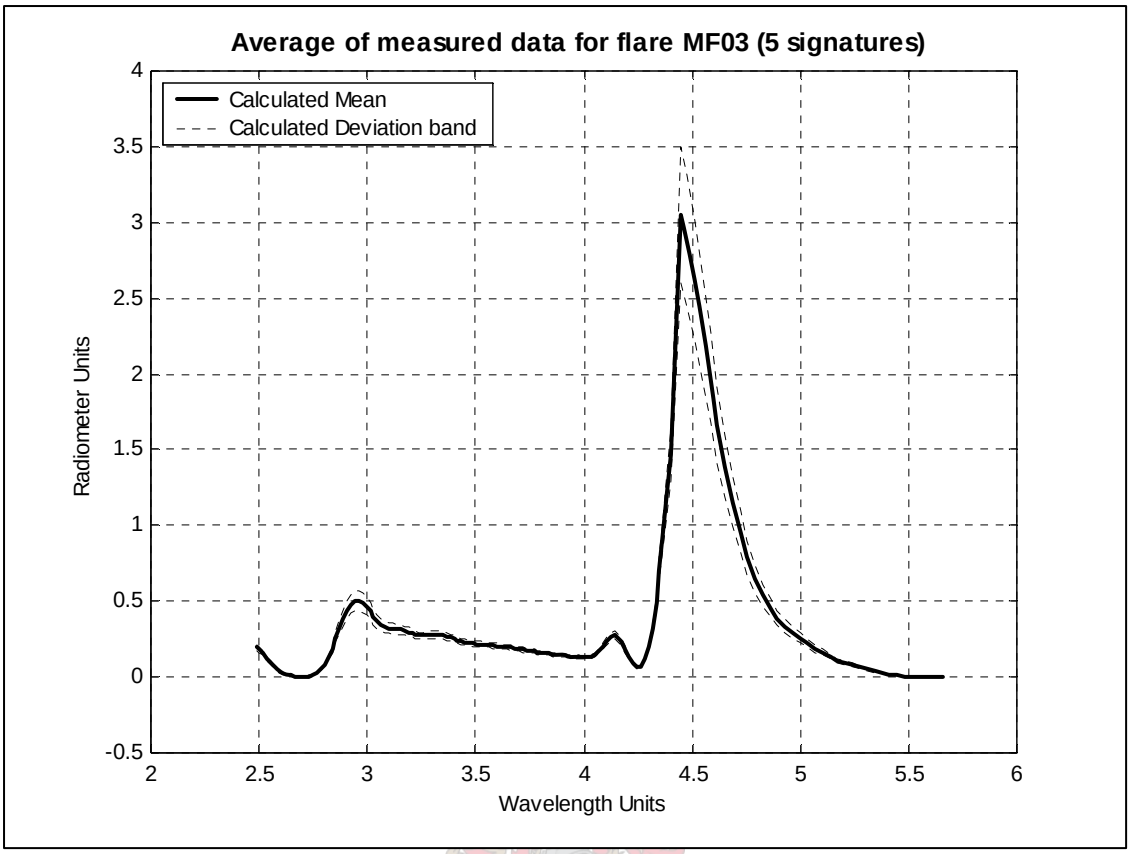
Average of measured data for flare MF03 (5 signatures)
Calculated Mean
Calculated Deviation band
Radiometer Units
Wavelength Units
4
3.5
3
2.5
2
1.5
1
0.5
0
-0.5
2
2.5
3
3.5
4
4.5
5
5.5
6

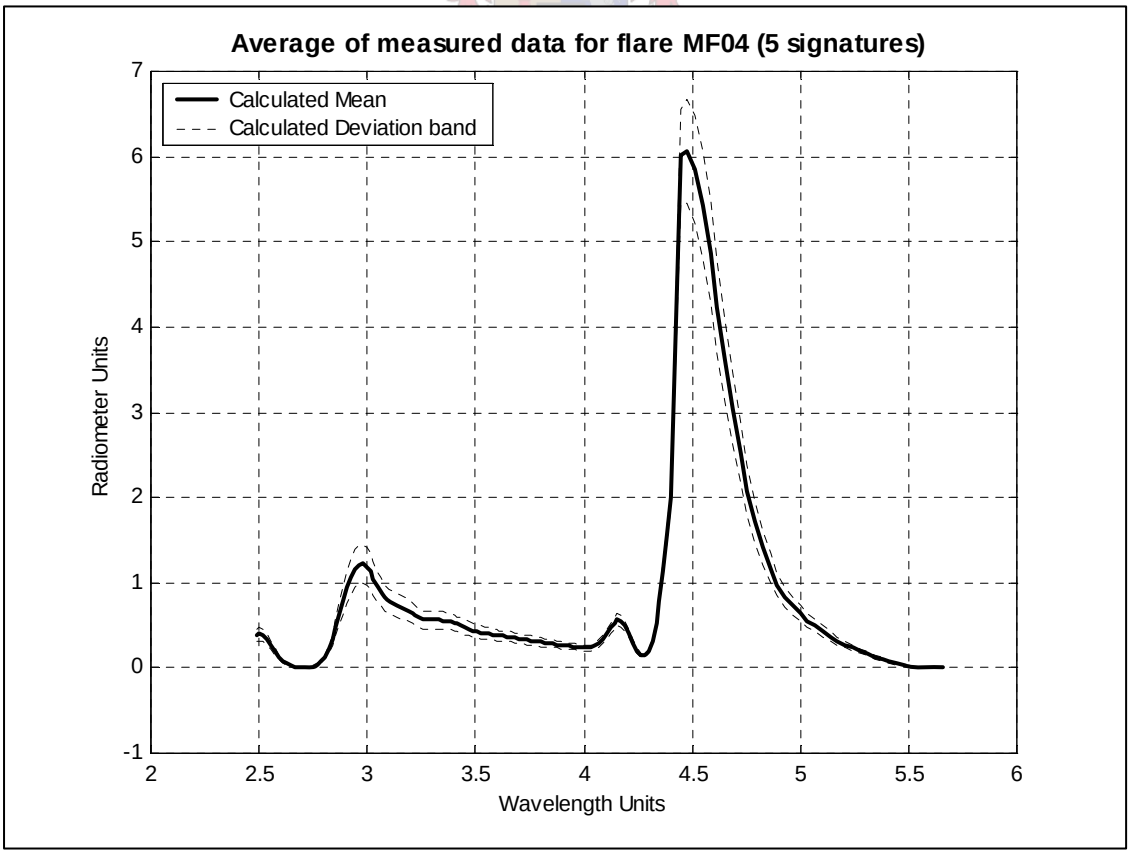
Average of measured data for flare MF04 (5 signatures)
Calculated Mean
Calculated Deviation band
Radiometer Units
Wavelength Units
7
6
5
4
3
2
1
0
-1
2
2.5
3
3.5
4
4.5
5
5.5
6

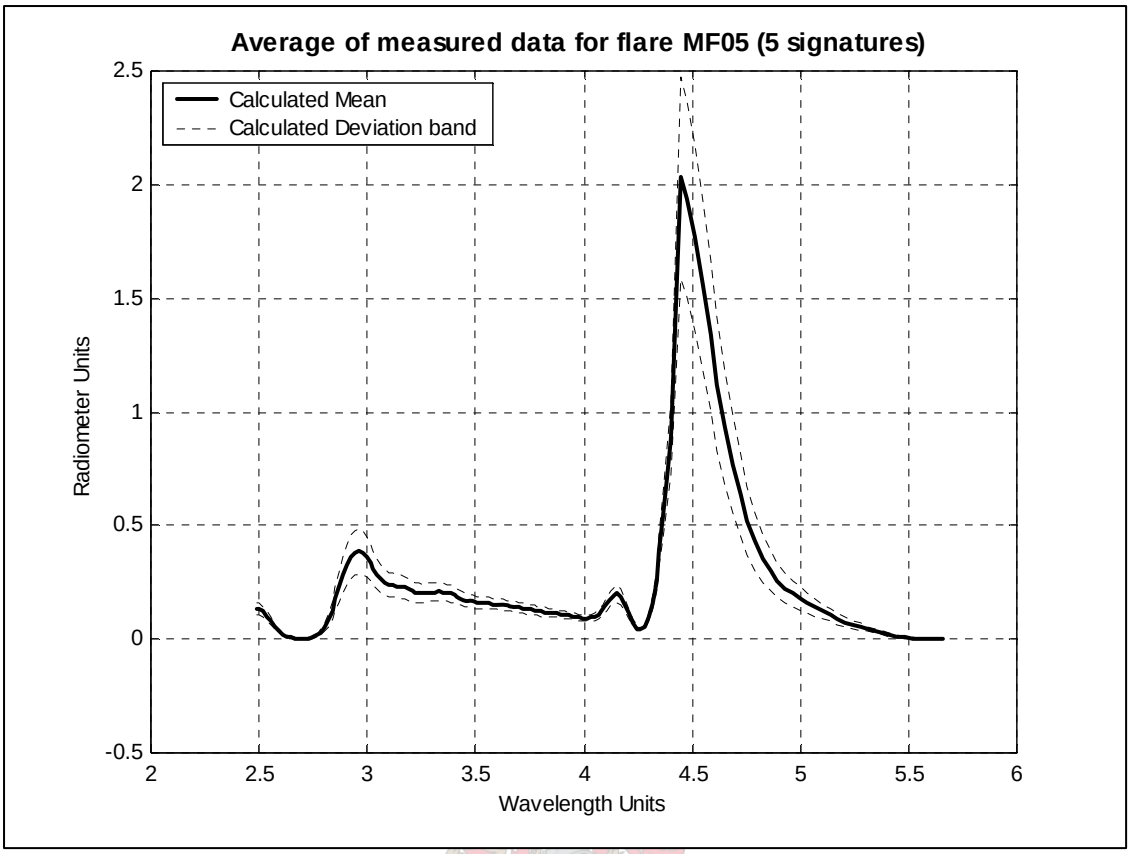
Average of measured data for flare MF05 (5 signatures)
Calculated Mean
Calculated Deviation band
Radiometer Units
Wavelength Units
2.5
2
1.5
1
0.5
0
-0.5
2
2.5
3
3.5
4
4.5
5
5.5
6

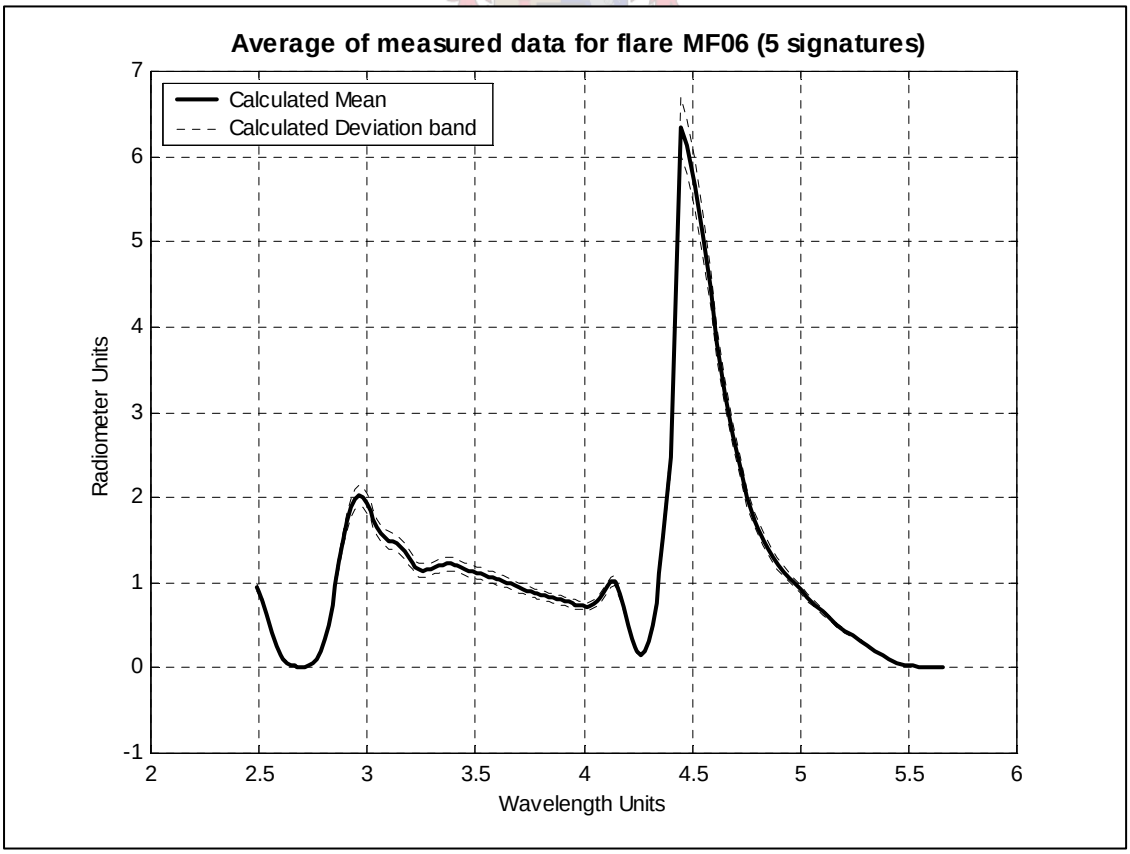
Average of measured data for flare MF06 (5 signatures)
Calculated Mean
Calculated Deviation band
Radiometer Units
Wavelength Units
7
6
5
4
3
2
1
0
-1
2
2.5
3
3.5
4
4.5
5
5.5
6

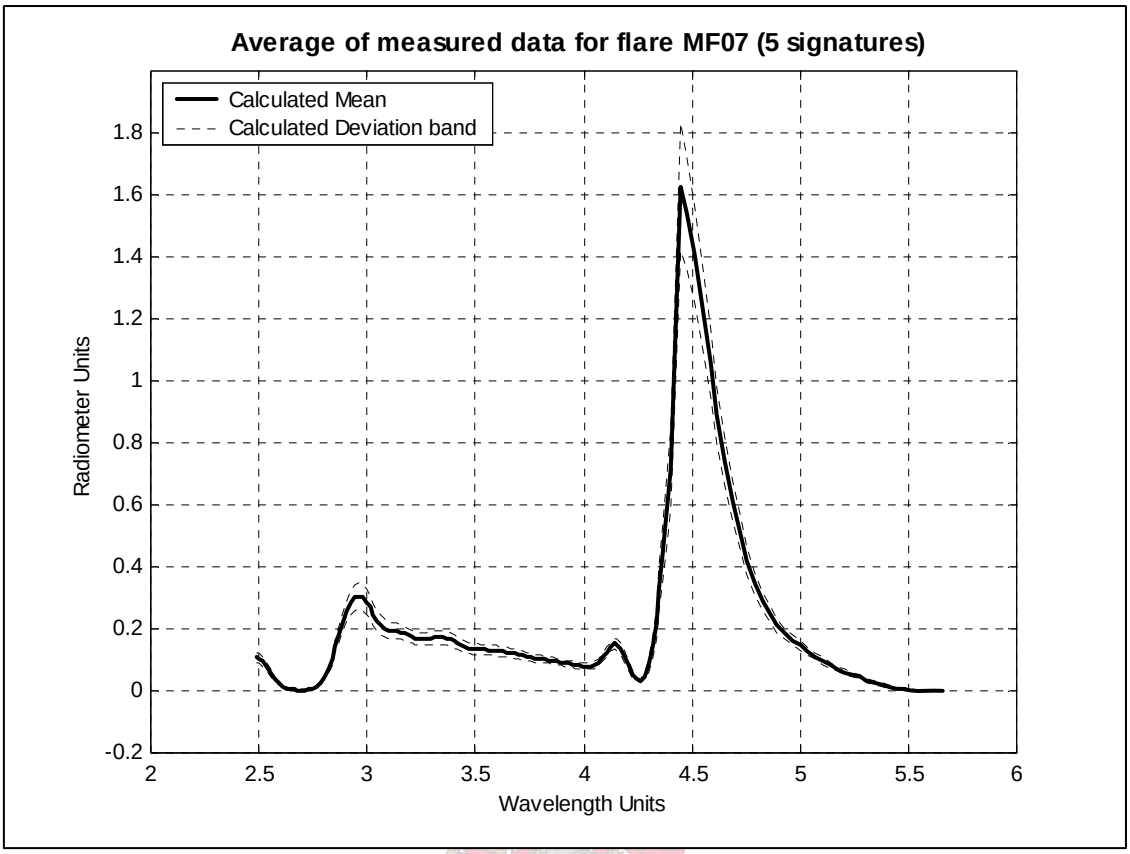
Average of measured data for flare MF07 (5 signatures)
Calculated Mean
Calculated Deviation band
Radiometer Units
Wavelength Units
1.8
1.6
1.4
1.2
1
0.8
0.6
0.4
0.2
0
-0.2
2
2.5
3
3.5
4
4.5
5
5.5
6

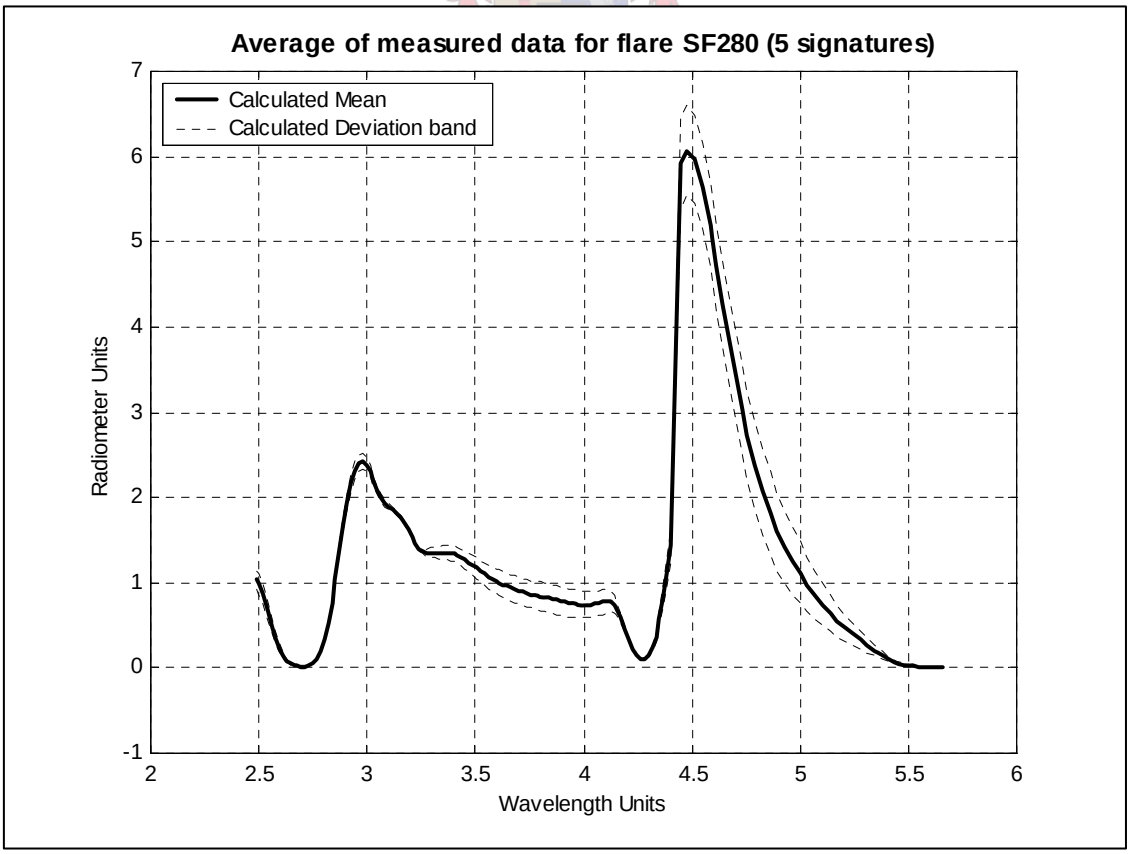
Average of measured data for flare SF280 (5 signatures)
Calculated Mean
Calculated Deviation band
Radiometer Units
Wavelength Units
7
6
5
4
3
2
1
0
-1
2
2.5
3
3.5
4
4.5
5
5.5
6

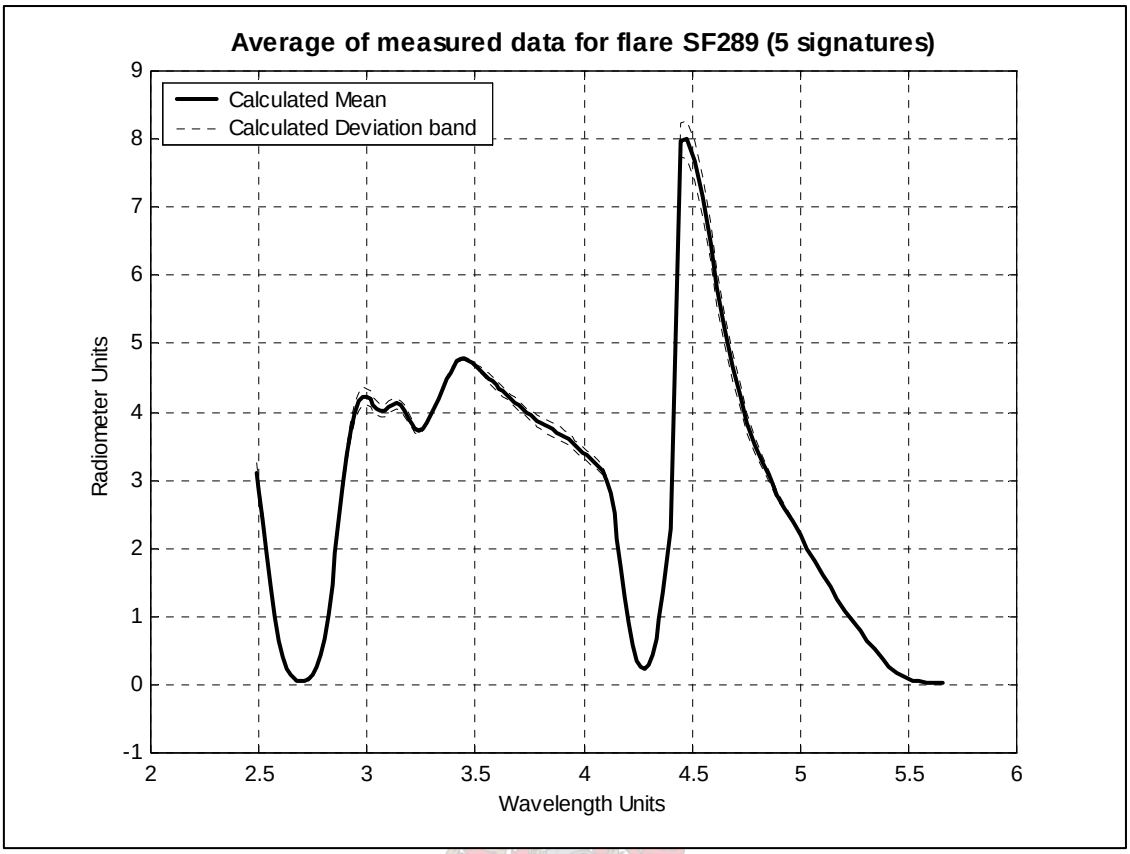
Average of measured data for flare SF289 (5 signatures)
Calculated Mean
Calculated Deviation band
Radiometer Units
Wavelength Units
9
8
7
6
5
4
3
2
1
0
-1
2
2.5
3
3.5
4
4.5
5
5.5
6

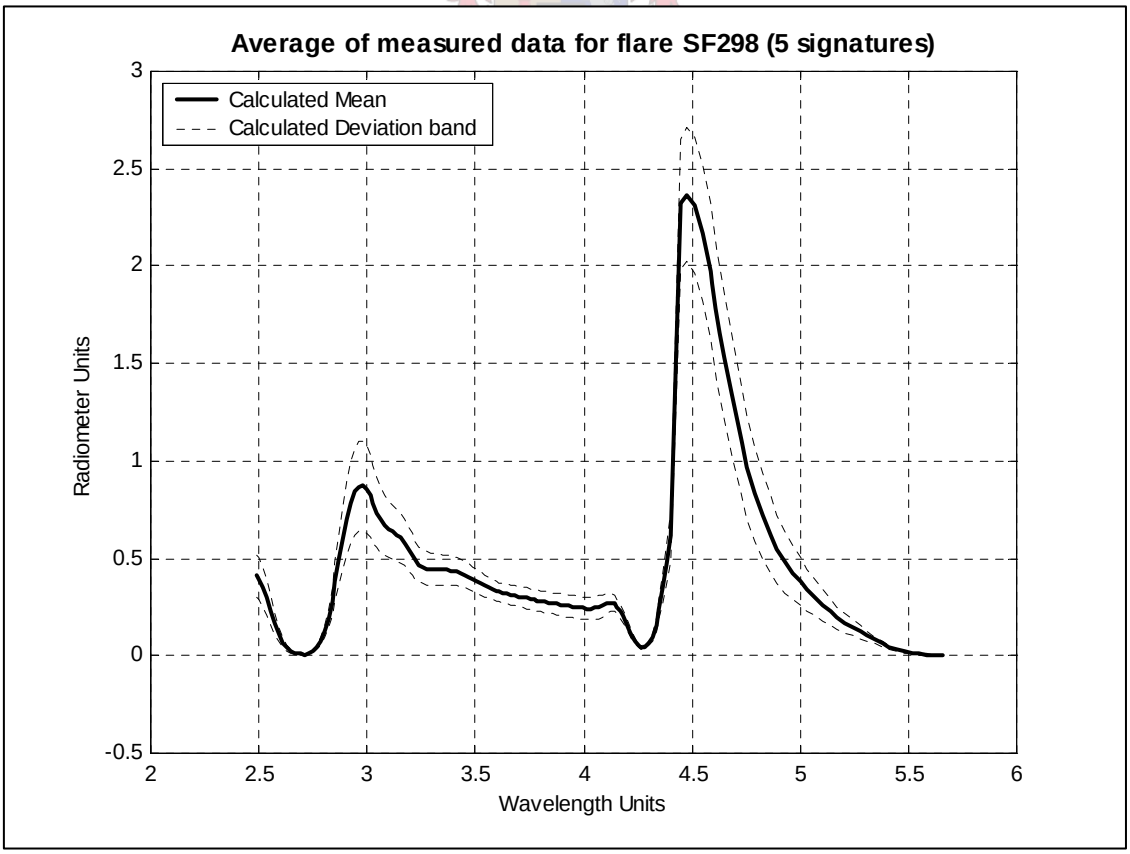
Average of measured data for flare SF298 (5 signatures)
Calculated Mean
Calculated Deviation band
Radiometer Units
Wavelength Units
3
2.5
2
1.5
1
0.5
0
-0.5
2
2.5
3
3.5
4
4.5
5
5.5
6

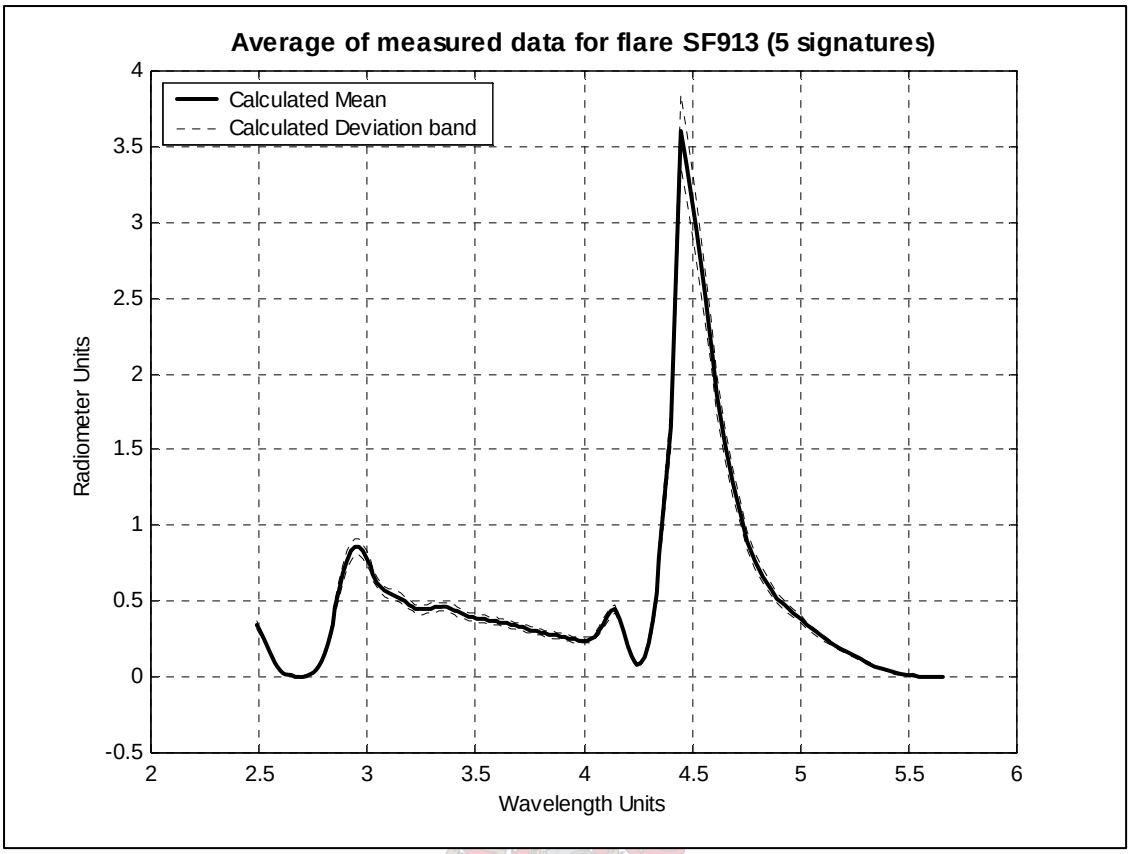
Average of measured data for flare SF913 (5 signatures)
Calculated Mean
Calculated Deviation band
Radiometer Units
Wavelength Units
4
3.5
3
2.5
2
1.5
1
0.5
0
-0.5
2
2.5
3
3.5
4
4.5
5
5.5
6

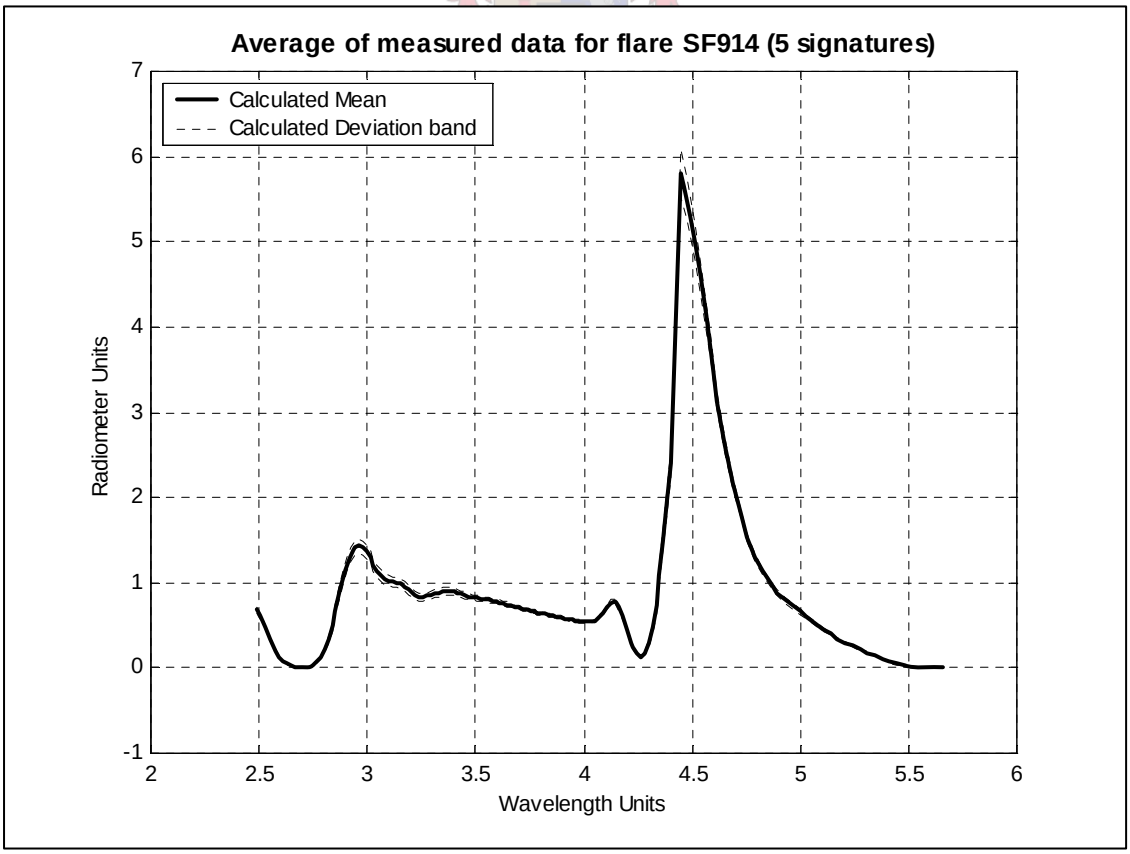
Average of measured data for flare SF914 (5 signatures)
Calculated Mean
Calculated Deviation band
Radiometer Units
Wavelength Units
7
6
5
4
3
2
1
0
-1
2
2.5
3
3.5
4
4.5
5
5.5
6

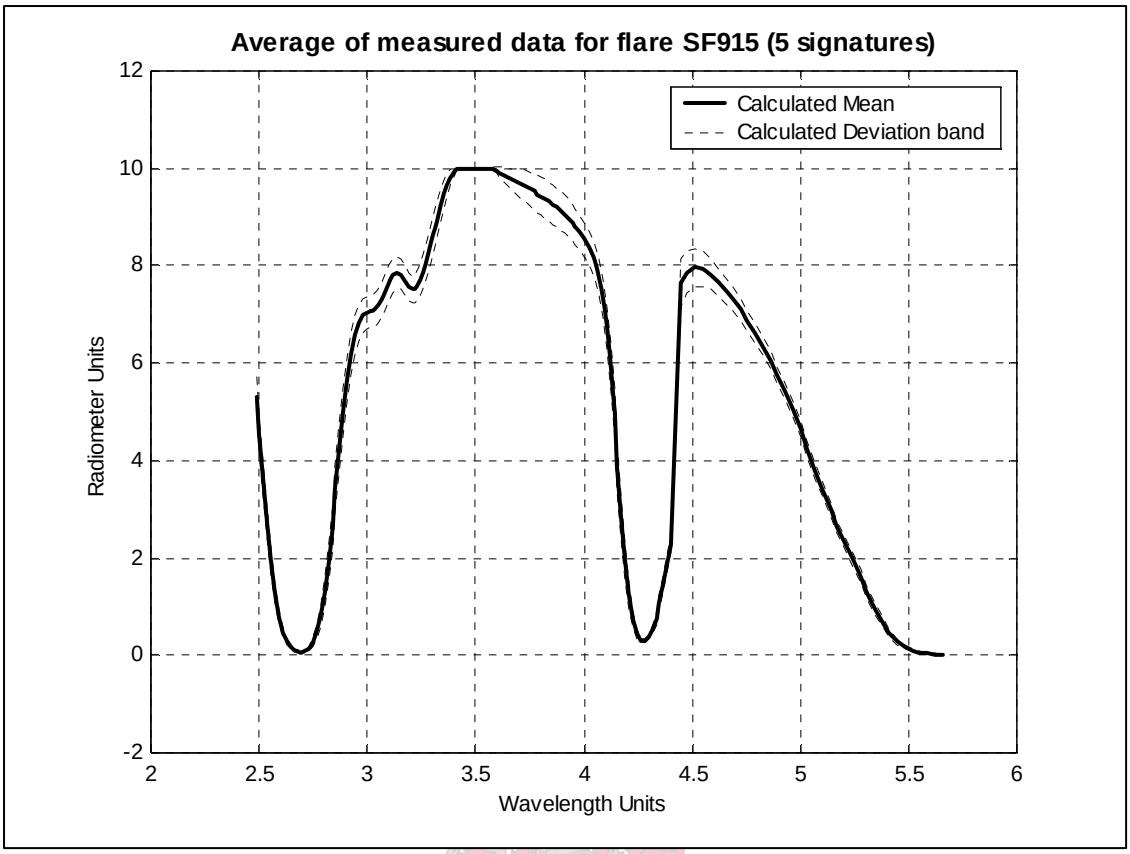
Average of measured data for flare SF915 (5 signatures)
Calculated Mean
Calculated Deviation band
Radiometer Units
Wavelength Units
12
10
8
6
4
2
0
-2
2
2.5
3
3.5
4
4.5
5
5.5
6

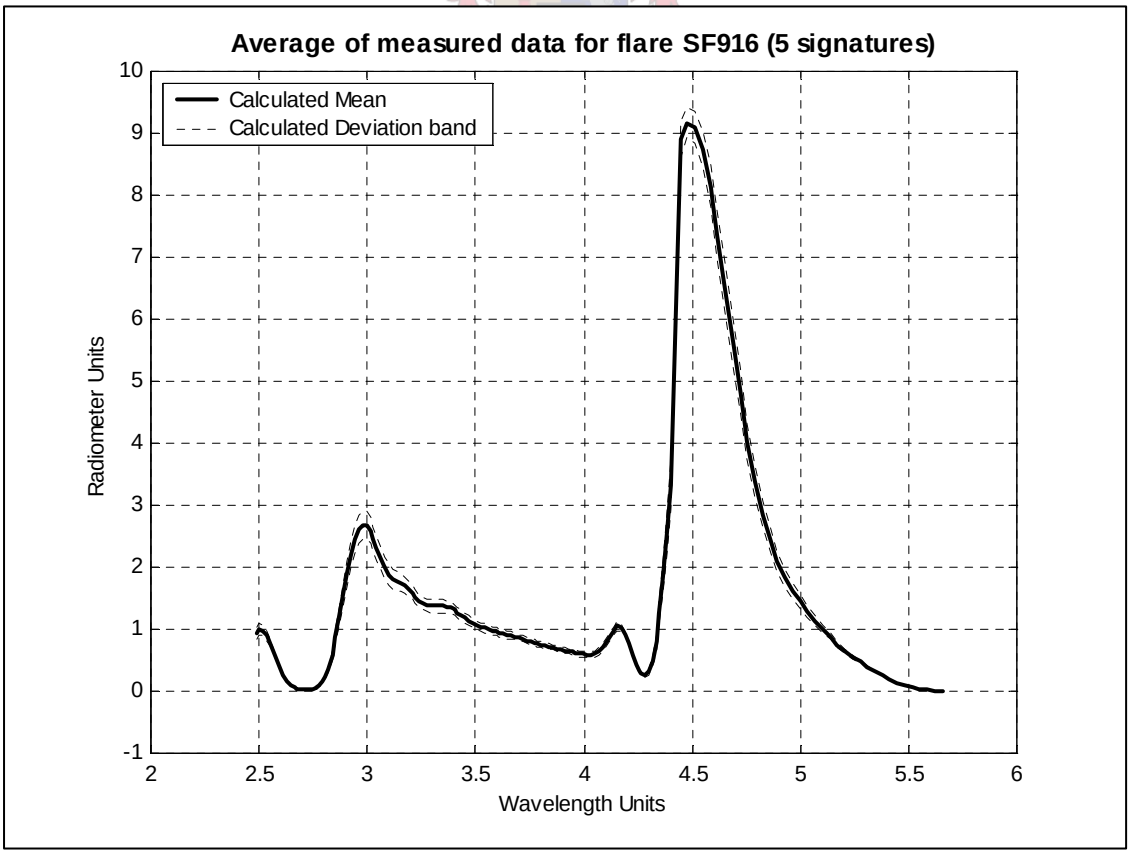
Average of measured data for flare SF916 (5 signatures)
Calculated Mean
Calculated Deviation band
Radiometer Units
Wavelength Units
10
9
8
7
6
5
4
3
2
1
0
-1
2
2.5
3
3.5
4
4.5
5
5.5
6

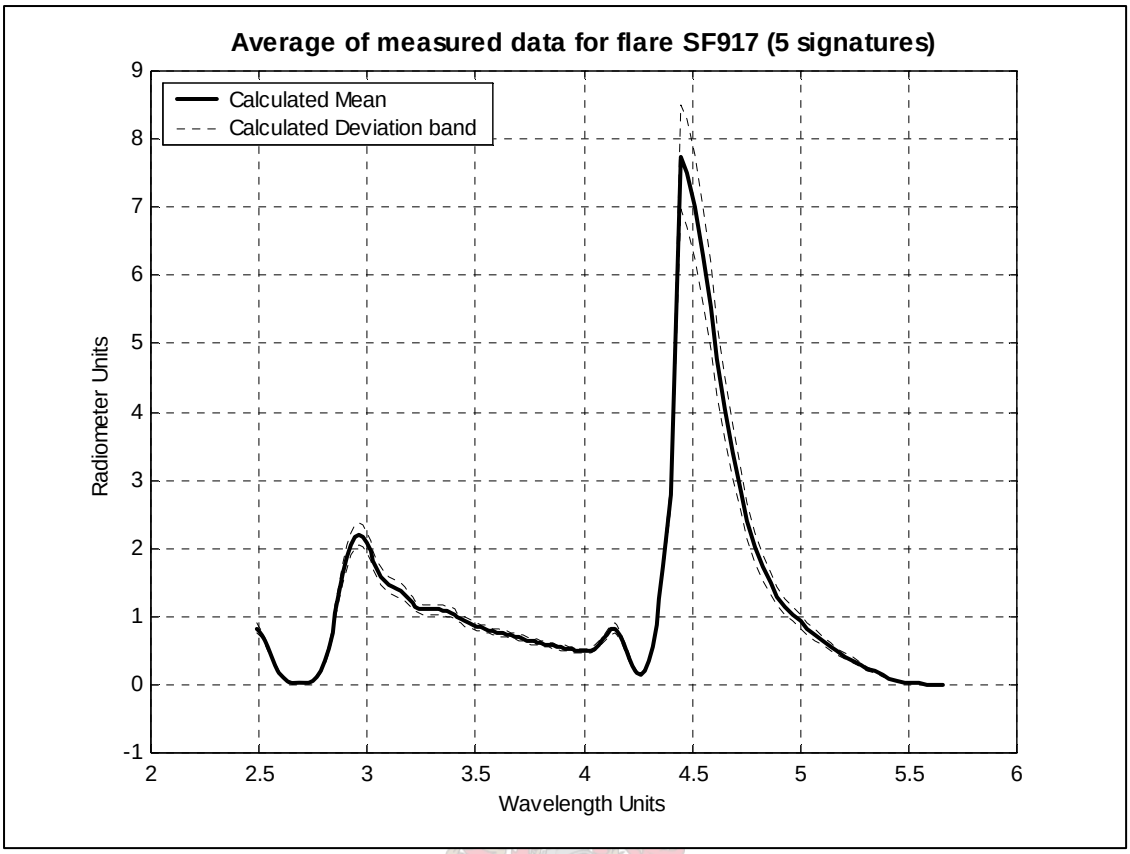
Average of measured data for flare SF917 (5 signatures)
Calculated Mean
Calculated Deviation band
Radiometer Units
Wavelength Units
9
8
7
6
5
4
3
2
1
0
-1
2
2.5
3
3.5
4
4.5
5
5.5
6

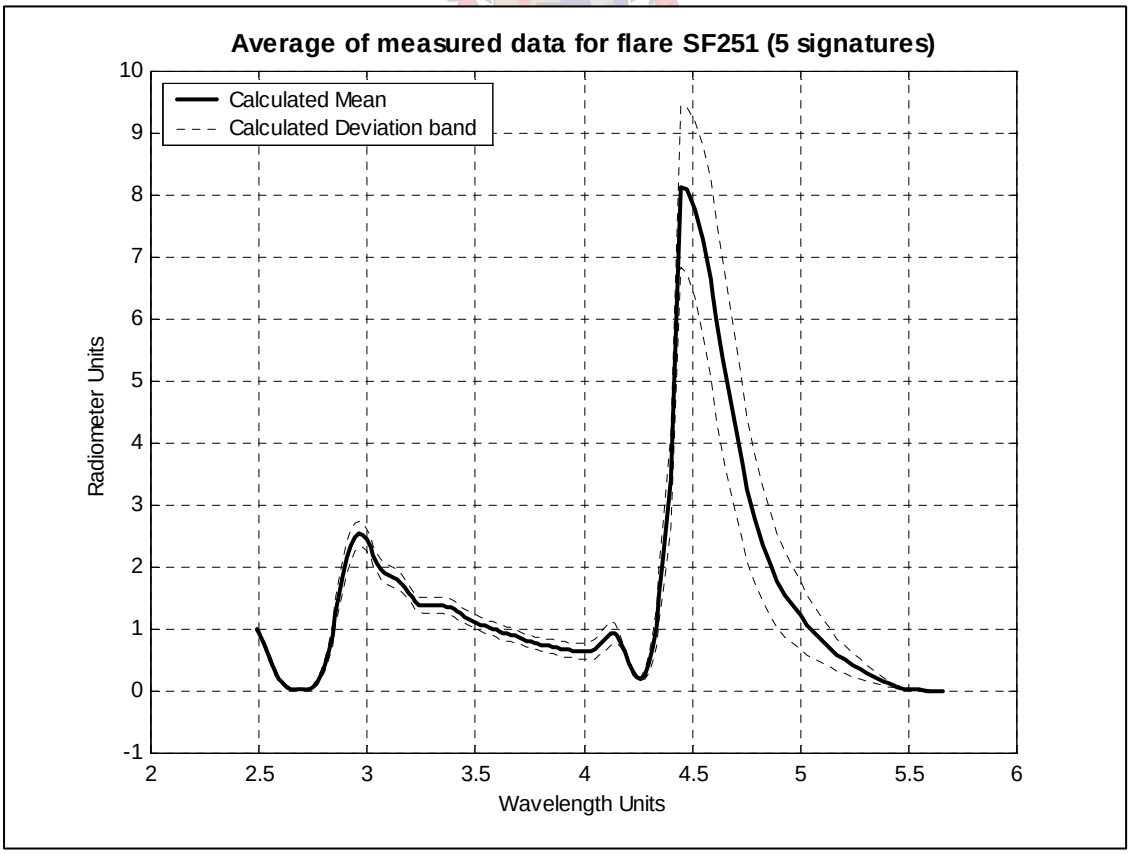
Average of measured data for flare SF251 (5 signatures)
Calculated Mean
Calculated Deviation band
Radiometer Units
Wavelength Units
10
9
8
7
6
5
4
3
2
1
0
-1
2
2.5
3
3.5
4
4.5
5
5.5
6

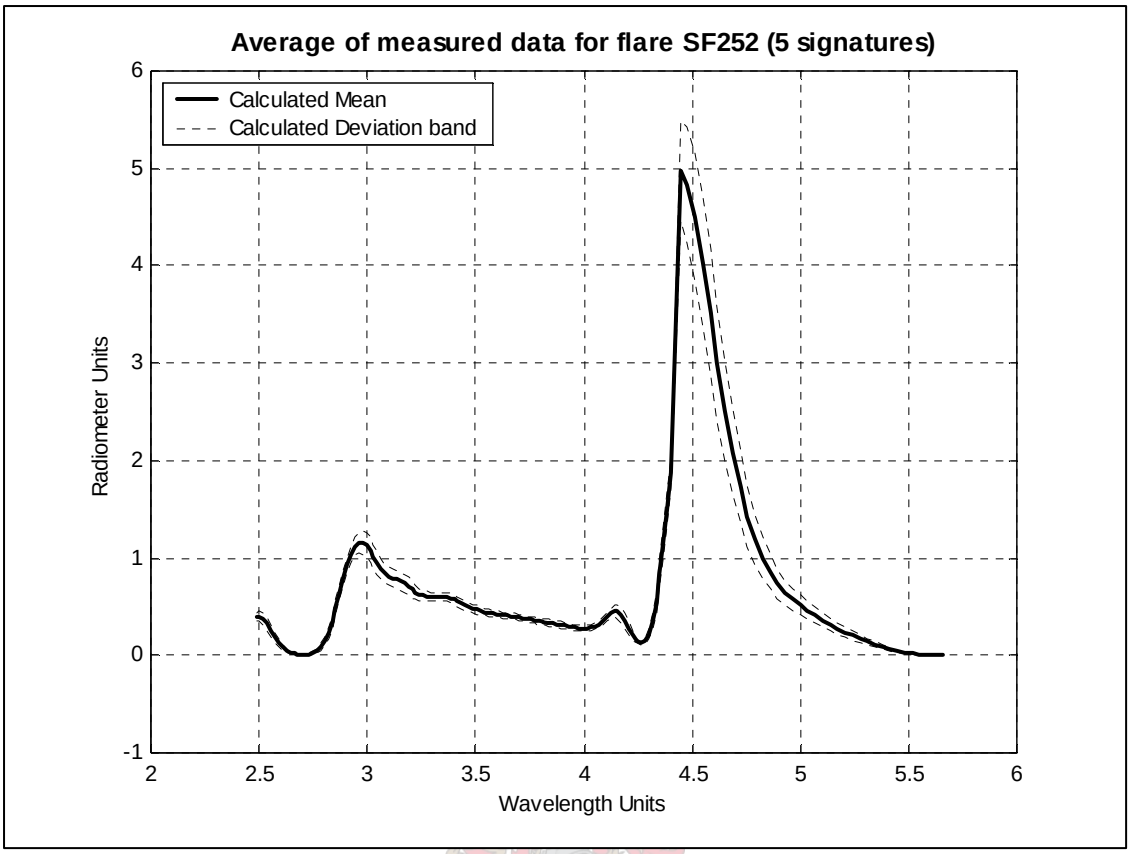
Average of measured data for flare SF252 (5 signatures)
Calculated Mean
Calculated Deviation band
Radiometer Units
Wavelength Units
6
5
4
3
2
1
0
-1
2
2.5
3
3.5
4
4.5
5
5.5
6

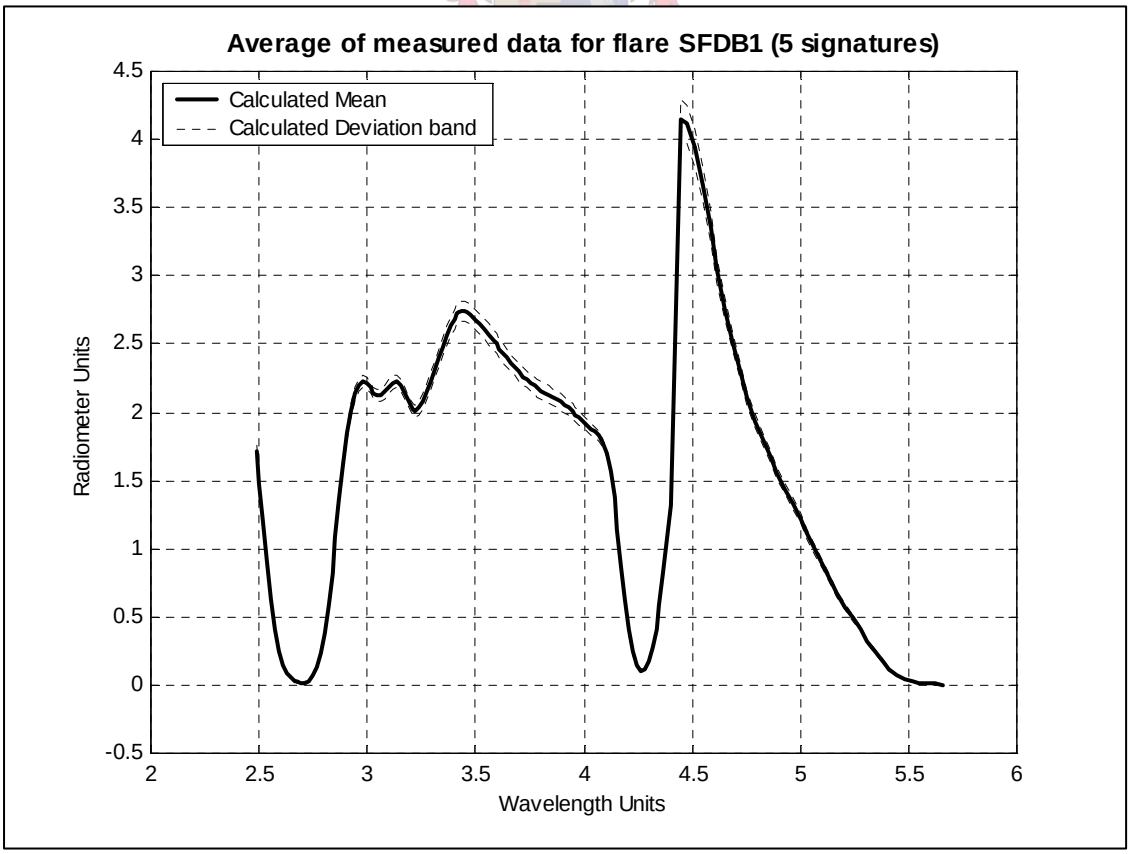
Average of measured data for flare SFDB1 (5 signatures)
Calculated Mean
Calculated Deviation band
Radiometer Units
Wavelength Units
4.5
4
3.5
3
2.5
2
1.5
1
0.5
0
-0.5
2
2.5
3
3.5
4
4.5
5
5.5
6

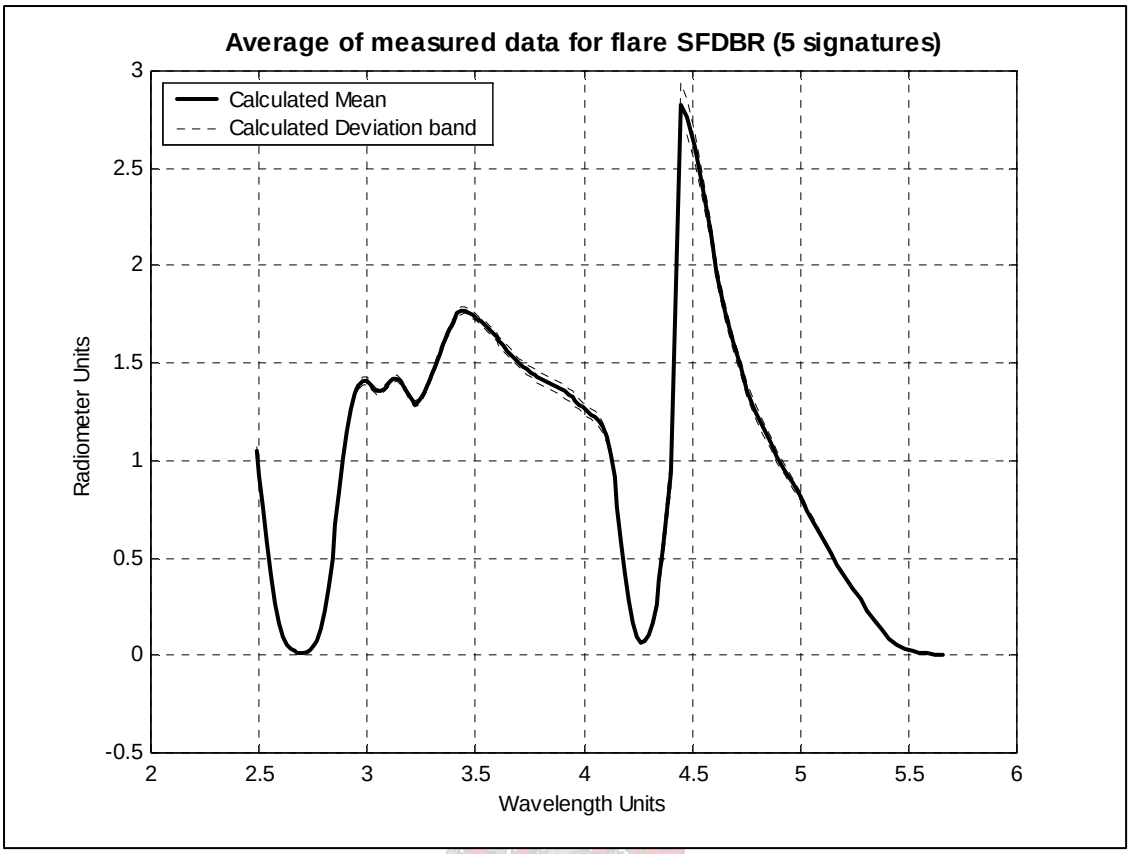
Average of measured data for flare SFDBR (5 signatures)
Calculated Mean
Calculated Deviation band
Radiometer Units
Wavelength Units
3
2.5
2
1.5
1
0.5
0
-0.5
2
2.5
3
3.5
4
4.5
5
5.5
6

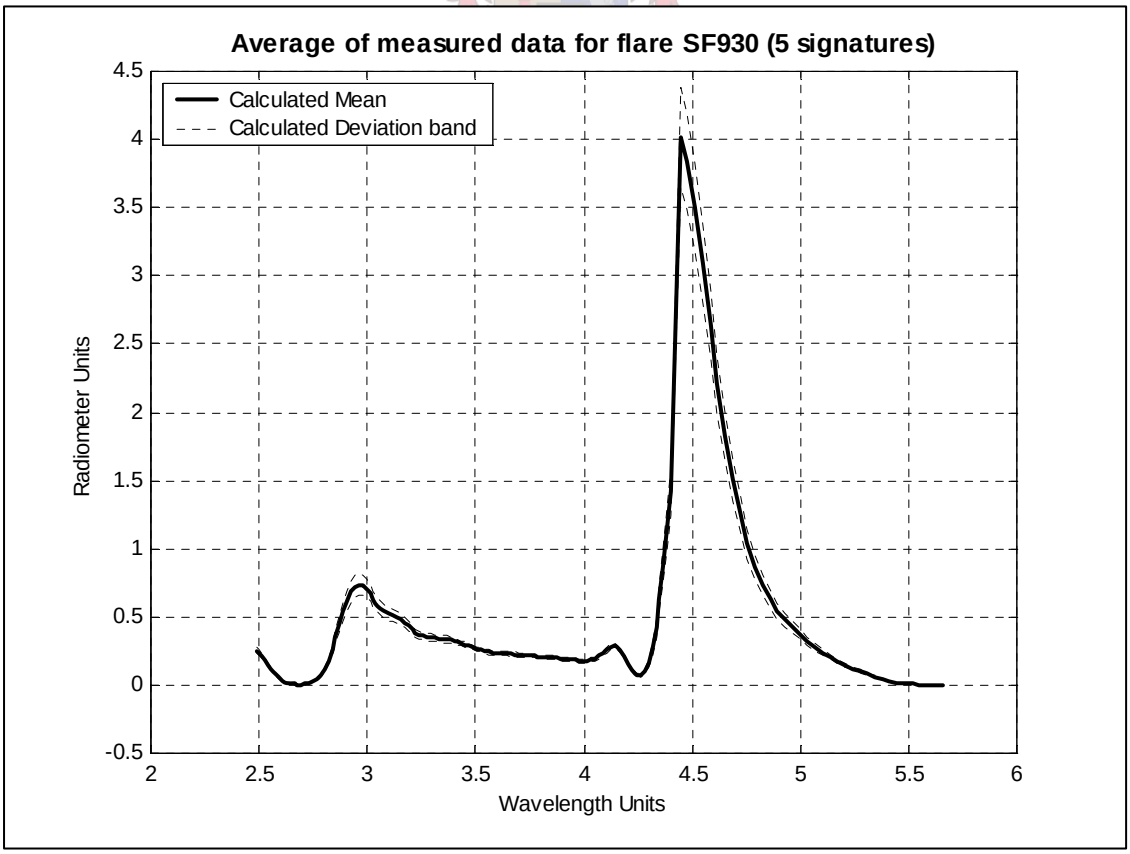
Average of measured data for flare SF930 (5 signatures)
Calculated Mean
Calculated Deviation band
Radiometer Units
Wavelength Units
4.5
4
3.5
3
2.5
2
1.5
1
0.5
0
-0.5
2
2.5
3
3.5
4
4.5
5
5.5
6

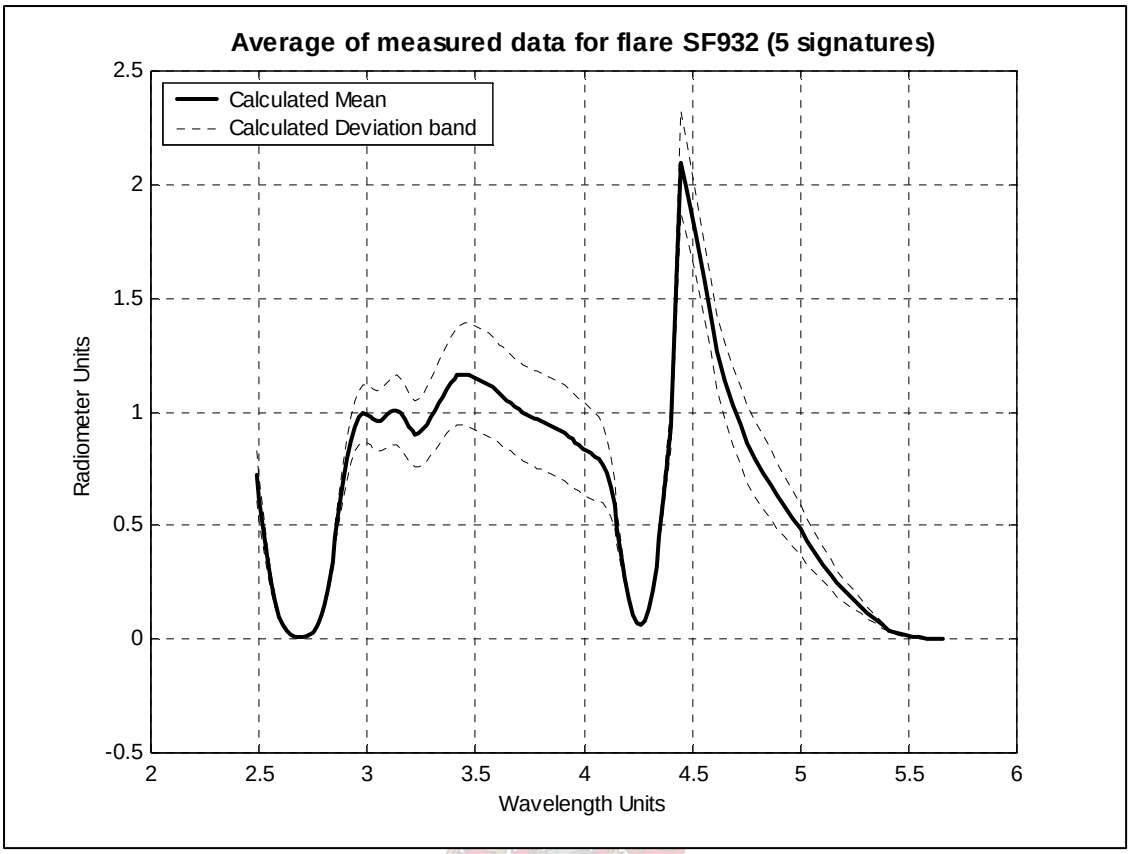
Average of measured data for flare SF932 (5 signatures)
Calculated Mean
Calculated Deviation band
Radiometer Units
Wavelength Units
2.5
2
1.5
1
0.5
0
-0.5
2
2.5
3
3.5
4
4.5
5
5.5
6

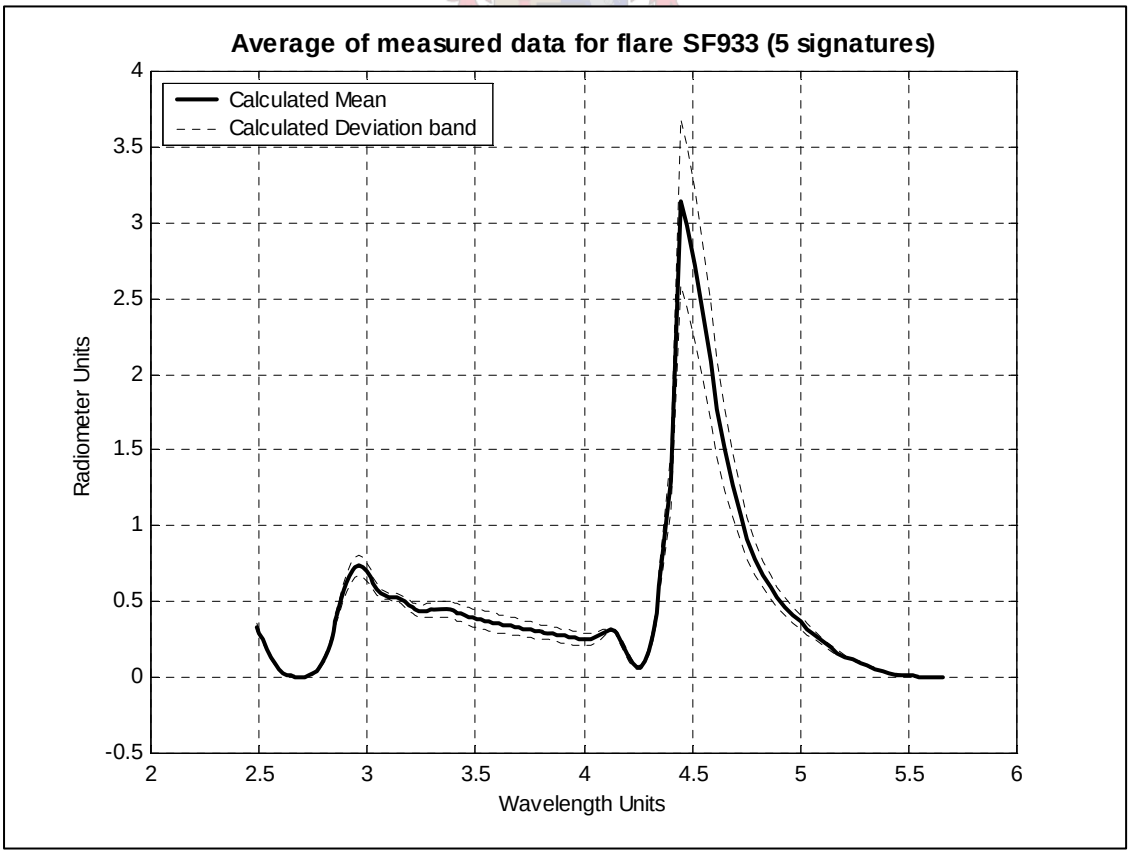
Average of measured data for flare SF933 (5 signatures)
Calculated Mean
Calculated Deviation band
Radiometer Units
Wavelength Units
4
3.5
3
2.5
2
1.5
1
0.5
0
-0.5
2
2.5
3
3.5
4
4.5
5
5.5
6

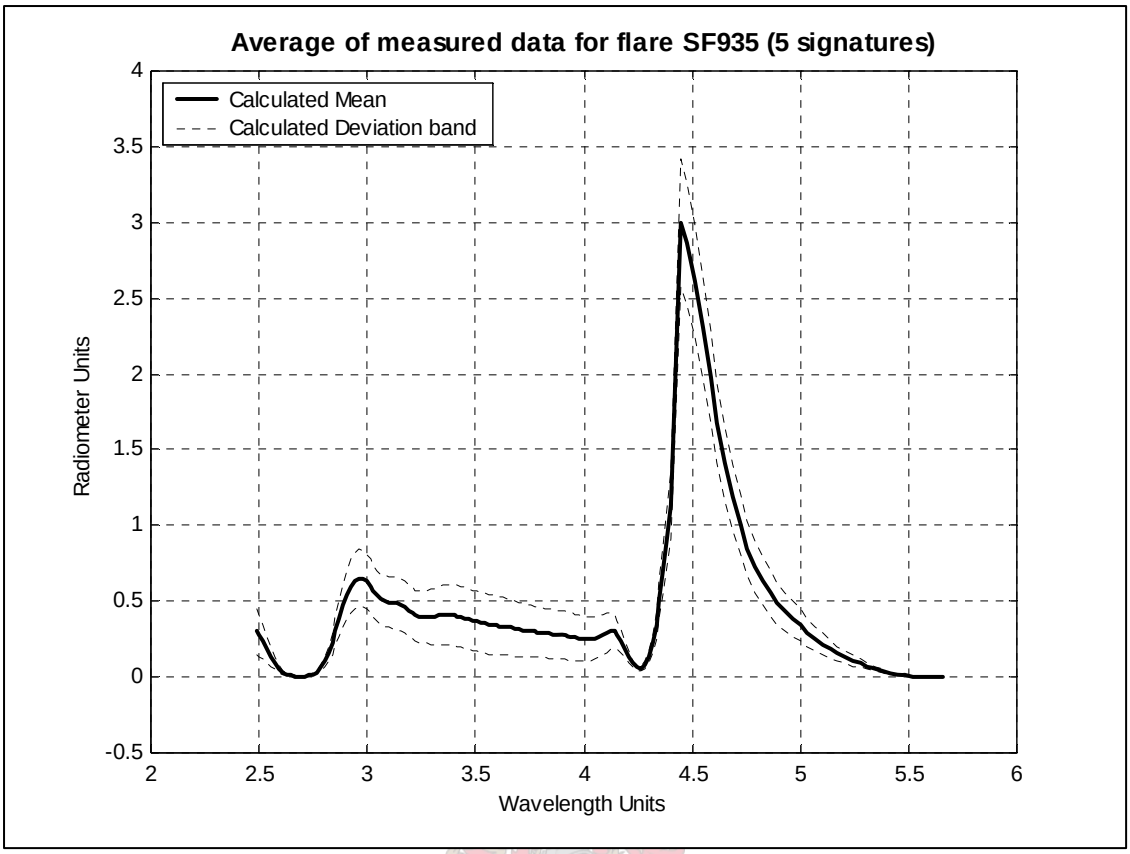
Average of measured data for flare SF935 (5 signatures)
Calculated Mean
Calculated Deviation band
Radiometer Units
Wavelength Units
4
3.5
3
2.5
2
1.5
1
0.5
0
-0.5
2
2.5
3
3.5
4
4.5
5
5.5
6

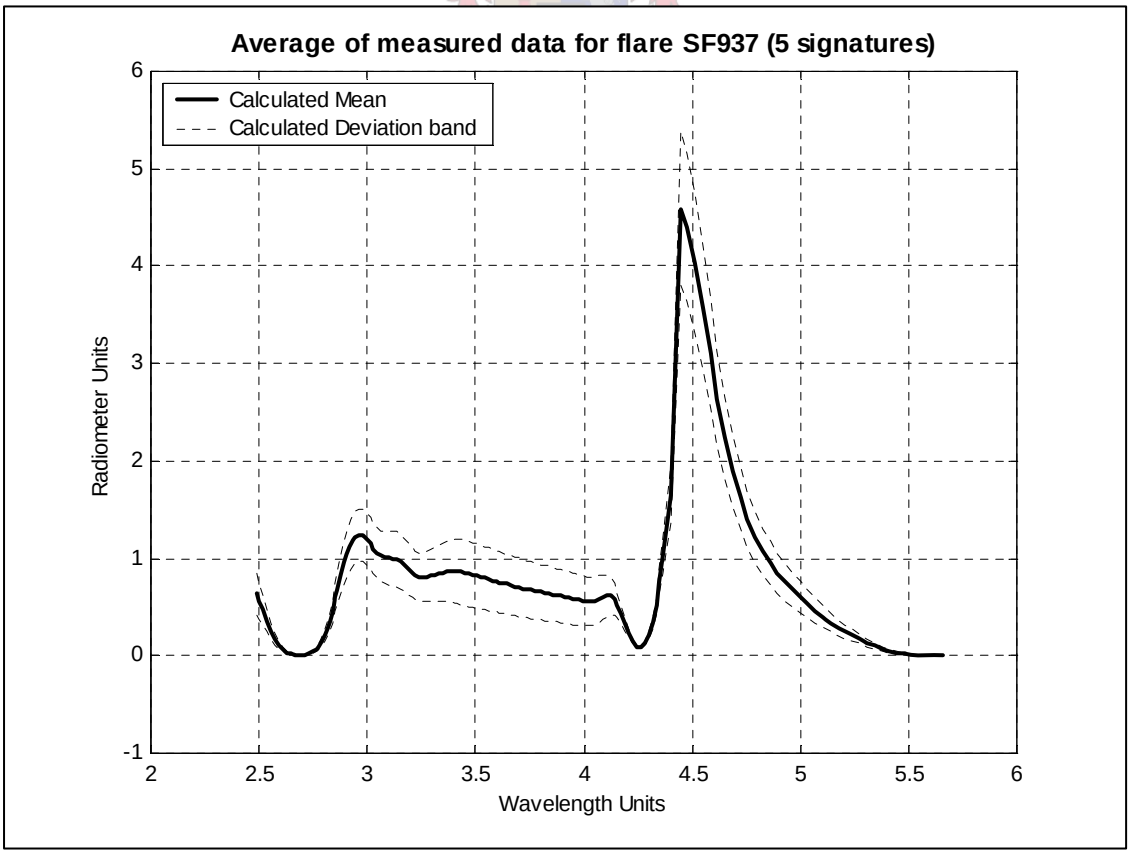
Average of measured data for flare SF937 (5 signatures)
Calculated Mean
Calculated Deviation band
Radiometer Units
Wavelength Units
6
5
4
3
2
1
0
-1
2
2.5
3
3.5
4
4.5
5
5.5
6

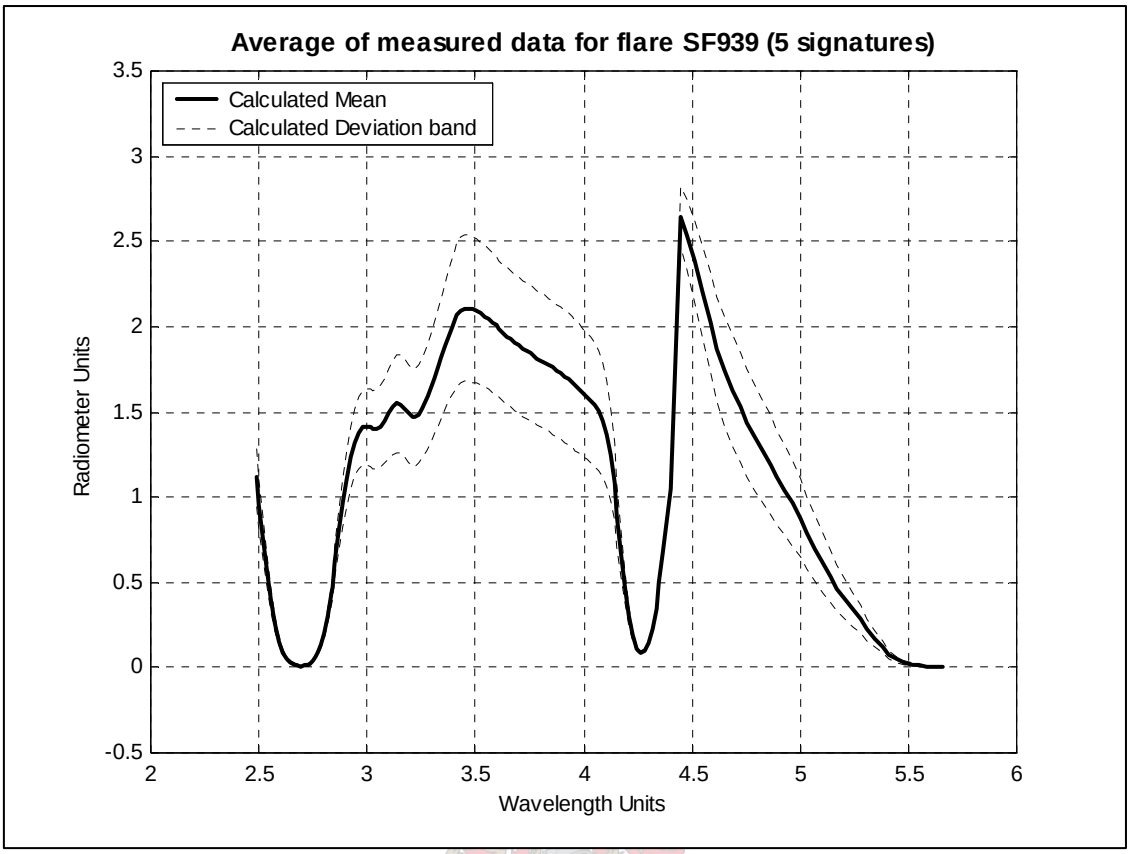
Average of measured data for flare SF939 (5 signatures)
Calculated Mean
Calculated Deviation band
Radiometer Units
Wavelength Units
3.5
3
2.5
2
1.5
1
0.5
0
-0.5
2
2.5
3
3.5
4
4.5
5
5.5
6

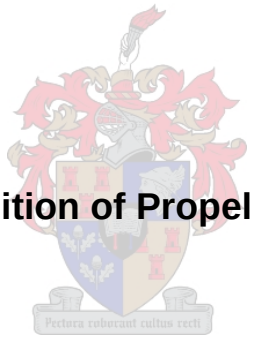

Appendix D Composition of Propellant Components

	MF01	MF02	MF03	MF04	MF05	MF06	MF07	SF280	SF289	SF298	SF913	SF914	SF915	SF916	SF917	SF2515	SF2524	SFDB1	SFDBRAI1	SF930	SF932	SF933	SF935	SF937	SF939
HTPB								10.56	20.24	10.78	12.84	12.84	16.51	11.91	10.02	11.85	10.06	15	15	12.71	17.34	17.28	17.05	16.79	
IPDI								0.84	2.77	0.82	0.91	0.91	1.29	0.84	0.71	0.9	0.67	1.4	1.4	1.04	1.41	1.47	1.7	1.96	
DOA								3	1	2	1	1	1.9	1	1.92	1	1.92			1	1	1	1	1	
DTBHQ								0.1		0.1			0.1												
Tepa									0.3																
Tepan											0.25	0.25		0.25		0.25				0.25	0.25	0.25	0.25	0.25	
Tepanol															0.15		0.15								
HX752								0.3		0.3			0.1												
AP coarse (1)	80	67	67	67	67	67	76										34.48								
AP coarse (2)								24	36.5	28	44.22	46.9	5	53.2	56.84	49	30.17			54.5	56	56	53.9	51.1	60
AP fine								44	36.5	40	22.78	20.1	13.5	22.8	24.36	20.8	21.55			25.5	14	23	23.1	21.9	
AN																									
Al								15		16	5	5		5		16			5						
Mg													60												
SiC															1		1								
Fe_2O_3										2			1.5												
$SrCO_3$														5	5										
Oksamide											13														
Hexamine						20						13								5	10	1	3	7	10
Tetrasicline													0.1												
Fe(AA)																0.0001									
Aerosil																0.02									
TMP									0.45																
AO 2246									0.24																
MgO									0.09																
C-Black									2																
MA									0.07																
TPB									0.05																
NG/TA (80:20)																			18						
RDX		20		10														43	35.6						
MP200																		40.6	25						
Prussian Blue								2																	
Lecithin								0.2																	
Polylite	20	13	13	13	13	13	14																		30
TNT			20	10																					
NTO					20																				
Cianuric acid							10																		
Σ	100	100	100	100	100	100	100	100	100	100	100	100	100	100	100	100	100	100	100	100	100	100	100	100	100

	C	H	O	N	Al	Cl	K	P	S	Si	Fe	Sr	Mg	Bi	Molar mass of Components
HTPB	**1**	**1.506**	**0.006**												**13.62**
IPDI	**12**	**18**	**2**	**2**											**222.29**
DOA	**22**	**42**	**4**												**370.57**
DTBHQ	**14**	**22**	**2**												**222.33**
Tepa	**8**	**35**		**5**											**201.40**
Tepan	**11**	**26**		**6**											**242.37**
Tepanol	**17**	**35**	**2**	**7**											**369.51**
HX752	**14**	**16**	**2**	**2**											**244.29**
AP coarse (1)		**4**	**4**	**1**		**1**									**117.49**
AP coarse (2)		**4**	**4**	**1**		**1**									**117.49**
AP fine		**4**	**4**	**1**		**1**									**117.49**
AN		**3.84**	**2.92**	**1.92**											**79.83**
Al					**1**										**26.98**
Mg													**1**		**24.31**
SiC	**1**									**1**					**40.10**
Fe_2O_3			**3**								**2**				**159.70**
$SrCO_3$	**1**		**3**									**1**			**147.63**
Oksamide	**2**	**4**	**2**	**2**											**88.07**
Hexamine	**6**	**12**		**4**											**140.19**
Tetrasicline	**22**	**30**	**11**	**2**											**498.49**
Fe(AA)	**15**	**21**	**6**								**1**				**353.18**
Aerosil			**2**							**1**					**60.09**
TMP	**6**	**14**	**3**												**134.18**
AO 2246	**22**	**32**	**2**												**328.50**
MgO			**1**										**1**		**40.30**
C-Black	**1**														**12.01**
MA	**4**	**2**	**3**												**98.06**
TPB	**18**	**15**												**1**	**441.30**
NG/TA (80:20)	**4.2**	**6.8**	**8.4**	**2.4**											**225.31**
RDX	**3**	**6**	**6**	**6**											**222.12**
MP200	**4.251**	**5.349**	**8.091**	**2.046**			**0.358**		**0.179**						**234.29**
Prussian Blue	**18**			**18**							**7**				**859.27**
Lecithin	**12**	**23**	**8**	**1**				**1**							**340.29**
Polylite	**10**	**2.824**	**9.765**												**279.19**
TNT	**7**	**5**	**6**	**3**											**227.13**
NTO	**2**	**2**	**3**	**4**											**130.06**
Cianuric acid	**3**	**3**	**3**	**3**											**129.08**

SF289	C	H	O	N	Al	Cl	K	P	S	Si	Fe	Sr	Mg	Bi	Fraction	Molar mass of Components
HTPB	**1**	**1.5058**	**0.0058**												**20.24**	**13.62**
IPDI	**12**	**18**	**2**	**2**											**2.77**	**222.29**
DOA	**22**	**42**	**4**												**1**	**370.57**
DTBHQ																**222.33**
Tepa	**8**	**35**		**5**											**0.3**	**201.40**
Tepan																**242.37**
Tepanol																**369.51**
HX752																**244.29**
AP coarse (1)																**117.49**
AP coarse (2)		**4**	**4**	**1**		**1**									**36.5**	**117.49**
AP fine		**4**	**4**	**1**		**1**									**36.5**	**117.49**
AN																**79.83**
Al																**26.98**
Mg																**24.31**
SiC																**40.10**
Fe2O3																**159.70**
SrCO3																**147.63**
Oksamide																**88.07**
Hexamine																**140.19**
Tetrasicline																**498.49**
Fe(AA)																**353.18**
Aerosil																**60.09**
TMP	**6**	**14**	**3**												**0.45**	**134.18**
AO 2246	**22**	**32**	**2**												**0.24**	**328.50**
MgO			**1**										**1**		**0.09**	**40.30**
C-Black	**1**														**2**	**12.01**
MA	**4**	**2**	**3**												**0.07**	**98.06**
TPB	**18**	**15**												**1**	**0.05**	**441.30**
NG/TA (80:20)																**225.31**
RDX																**222.12**
MP200																**234.29**
Prussian Blue																**859.27**
Lecithin																**340.29**
Polylite																**279.19**
TNT																**227.13**
NTO																**130.06**
Cianuric acid																**129.08**
Σ	**94**	**167.51**	**23.01**	**9**		**2**							**1**	**1**	**100**	
Σ of Fraction	**1.914**	**5.186**	**2.546**	**0.654**		**0.621**							**0.002**	**0.0001**		

	DB1	DB2	DB3	DB4	DB5	DB6	C1	C2	C3	C4	C5	C6	C7	C8	C9	C10	C11	C12
Chemical Composition																		
C	1.869	2.01	2.44	1.96	1.73	1.73	1	1	1	0.94	0.94	0.89	0.92	1	0.89	1.12	1.05	0.92
H	2.658	2.99	3.36	2.86	2.39	2.66	3.91	3.84	3.84	4.35	4.28	4.14	4.33	3.91	4.2	4.4	4.38	4.33
O	3.362	3.32	3.36	3.35	3.27	3.27	2.41	2.38	2.39	2.96	2.94	2.81	2.97	2.41	2.86	2.77	2.8	2.96
N	1.335	1.28	0.84	1.18	1.12	1.39	0.6	0.59	0.59	0.74	0.72	0.71	0.74	0.6	0.71	0.7	0.7	0.74
Al	0	0	0	0	0.02	0	0.59	0.59	0.59	0	0	0.15	0	0.59	0.15	0.15	0.15	0
K	0	0	0	0.05	0.12	0.06	0	0	0.02	0	0.02	0	0	0	0	0	0	0
F	0	0	0	0	0.06	0	0	0	0	0	0	0	0	0	0	0	0	0
Cu	0.007	0.01	0	0.01	0.01	0.01	0	0	0	0	0	0	0	0	0	0	0	0
Pb	0.008	0.01	0.01	0.01	0.01	0.01	0	0	0	0	0	0	0	0	0	0	0	0
S	0	0	0	0	0	0	0	0	0.01	0	0.01	0	0	0	0	0	0	0
Cl	0	0	0	0	0	0	0.6	0.58	0.58	0.73	0.72	0.7	0.73	0.6	0.7	0.68	0.69	0.73
Si	0	0	0	0	0	0	0	0	0	0.03	0.03	0	0.03	0	0	0	0	0.03
Ti	0.008	0	0	0	0.01	0.01	0	0	0	0	0	0	0	0	0	0	0	0
Fe	0	0	0	0	0	0	0	0.03	0	0	0	0	0	0	0.01	0	0	0
Motor Working Paramters																		
Tc	2.92	2.53	1.82	2.56	2.86	2.78	3.27	3.26	3.26	2.93	2.87	3.07	2.9	3.3	2.98	2.81	2.86	2.9
Pc	4.9	4.4	3.1	4.1	5	7.4	2.7	2.8	2.5	6.2	2.2	3.4	3	4	1.06	1.29	1	3
ε	6.2	8.7	14.5	8.7	10.5	10.5	6.2	4.7	6.2	6.2	6.2	4.7	7.3	7.3	1.7	4.5	4.5	6.2
ϕ	13	11	8.5	11	10	10	13	15	13	13	13	15	12	12	25	15	15	13

	MF01	MF02	MF03	MF04	MF05	MF06	MF07	SF280	SF289	SF298	SF913	SF914	SF915	SF916	SF917	SF2515	SF2524	SFDB1	SFDBRAll	SF930	SF932	SF933	SF935	SF937	SF939
Chemical Composition																									
C	0.716	0.736	1.082	0.909	0.773	1.322	0.734	1.071	1.914	0.978	1.358	1.619	1.411	1.024	0.954	0.989	0.921	2.494	2.447	1.274	1.848	1.461	1.543	1.709	1.503
H	2.926	2.953	2.853	2.903	2.720	4.125	2.962	3.934	5.186	3.829	4.505	5.027	2.797	4.112	4.162	3.899	4.333	3.860	3.847	4.781	5.410	4.945	5.041	5.240	3.202
O	3.423	3.276	3.264	3.270	3.197	2.736	3.310	2.368	2.546	2.390	2.601	2.306	0.701	2.713	2.898	2.401	2.967	2.583	2.515	2.749	2.414	2.721	2.655	2.521	3.092
N	0.681	1.111	0.834	0.972	1.185	1.141	0.879	0.631	0.654	0.589	0.880	0.956	0.170	0.661	0.700	0.608	0.743	1.529	1.384	0.839	0.900	0.720	0.762	0.845	0.796
Al	0	0	0	0	0	0	0	0.556	0	0.593	0.185	0.185	0	0.185	0	0.593	0	0	0.185	0	0	0	0	0	0
Cl	0.681	0.570	0.570	0.570	0.570	0.570	0.647	0.579	0.621	0.579	0.570	0.570	0.157	0.647	0.691	0.594	0.734	0.000	0.000	0.681	0.596	0.672	0.655	0.621	0.511
K	0	0	0	0	0	0	0	0	0	0	0	0	0	0	0	0	0	0.062	0.038	0	0	0	0	0	0
P	0	0	0	0	0	0	0	0.001	0	0	0	0	0	0	0	0	0	0	0	0	0	0	0	0	0
S	0	0	0	0	0	0	0	0	0	0	0	0	0	0	0	0	0	0.031	0.019	0	0	0	0	0	0
Si	0	0	0	0	0	0	0	0	0	0	0	0	0	0	0.025	0.000	0.025	0	0	0	0	0	0	0	0
Fe	0	0	0	0	0	0	0	0.016	0	0.025	0	0	0.019	0	0	0.000	0	0	0	0	0	0	0	0	0
Sr	0	0	0	0	0	0	0	0	0	0	0	0	0	0.034	0.034	0	0	0	0	0	0	0	0	0	0
Mg	0	0	0	0	0	0	0	0	0.002	0	0	0	2.469	0	0	0	0	0	0	0	0	0	0	0	0
Bi	0	0	0	0	0	0	0	0	0.000	0	0	0	0	0	0	0	0	0	0	0	0	0	0	0	0
Ox Ratio	7.69	8.27	11.0	10.1	8.34	15.5	8.11	18.7	22.5	17.9	18.1	23.2	86.1	14.5	12.5	17.8	12.21	21.5	28.4	15.9	23.6	17.6	18.8	21.3	13.7
Temp	2543	2660	2767	2747	2578	2518	2559	2834	1249	2890	2101	1896	1349	2647	2500	2915	2565	1554	1644	2219	1270	1924	1787	1506	2725
M, (1/n)	29.2	28.14	28.08	27.25	29.02	23.33	28.93	26.28	19.47	27.23	23.04	20.42	34.40	26.23	26.27	26.71	25.39	21.77	20.47	22.54	18.86	21.59	20.95	19.75	25.80
Tmax	2657	2783	2756	2827	2686	2611	2672	2858	2395	2898	2501	2520	2876	2675	2531	2914	2552	2450	2524	2499	2406	2454	2443	2422	2717

Pectora roborant cultus recti